THE EFFECT OF PLATINUM GROUP METALS

ON DUPLEX STAINLESS STEELS

A thesis submitted for the degree of
Doctor of Philosophy
in the University of London

by

STEPHEN GEORGE McKENZIE

Department of Metallurgy and
Materials Science,
Imperial College of Science
and Technology,
London, SW7 2BP.

February, 1985.

If the world were mine, and all its store,
And were it of crystal gold,
Could I reign on its throne for evermore
From the ancient days of old,
An empress noble and fair as day,
Oh gladly might it be -
That I might cast it all away:
Christ, only Christ for me!

(Matilda of Hefta, 13th Century)

ABSTRACT

The objectives of the present work were to investigate the metallurgical effects of three platinum group metals (PGMs), namely Pt, Pd and Ru on duplex stainless steels in terms of structure and certain properties; strength and ductility, corrosion and oxidation resistance. Two base compositions were chosen, namely Fe-18Cr-6Ni and Fe-21Cr-6Ni (wt%). These compositions lie in the ferrite + austenite region of the ternary system in the range 1000°C to 1300°C. Additions of 2 wt% and 8 wt% PGMs were made to these base alloys. Results show that PGM additions notably affect as-cast structures promoting an austenitic mode of solidification. Microstructural and microchemical studies of duplex alloys solution treated between 1000°C and 1300°C have enabled tie-lines to be established, and show the partitioning of PGMs to the austenite phase, and the movement of ferrite and austenite boundaries.

After solution treatment of the ternary alloys at 1250°C and quenching the duplex structures contained up to 70% martensite. The PGM additives significantly reduced the martensite content, in the case of Pd, down to levels of 10%. Solution treated alloys were refrigerated to -196°C and rolled at room temperature and -196°C to study the kinetics of martensite formation, a significant reduction in martensite content was found for Pd-containing alloys, e.g. 21Cr-6Ni-2Pd, for deformations of up to 70%.

Samples of three alloys, 21/6, 21/6/2Ru and 21/6/2Pd, were aged in the temperature range 650°C to 950°C for times of up to 5 days to determine the TTT curves for precipitation. Some acceleration of sigma formation was found in the relatively early times of ageing, but after longer times, e.g. 2 days, differences in sigma content were small. The effect of sigma formation on the tensile properties in these alloys has also been investigated - the effect of sigma being most significant on reduction in room temperature ductility.

Additions of 2 wt%Pd and Ru to the 21Cr-6Ni alloy series have only a marginal effect on isothermal oxidation at 1000°C. However, their effect on anodic polarisation characteristics, is a reduction in the current density over the potential range of passivity and at the critical passivation potential in 1N.H_2SO_4 at 25°C. Additionally, tensile measurements show the Pd containing alloys to have a slight improvement in the 0.2% proof stress, whilst the Ru containing alloys have increased ductility.

TABLE OF CONTENTS

	Page
Abstract	3
List of Figures	8
CHAPTER 1 INTRODUCTION	14
CHAPTER 2 LITERATURE REVIEW	17
2.1. Constitution	18
2.1.1. Elements	18
2.1.2. Binary Systems	19
2.1.3. Ternary System	28
2.1.4. Austenite Stability	32
2.1.5. Intermetallic Compounds	34
2.1.6. Carbide Formation	37
2.2. Solidification Modes	39
2.3. Corrosion	42
2.3.1. General	42
2.3.2. Austenitic Steels	42
2.3.3. Duplex Steels	42
2.3.4. Pitting Attack	43
2.3.5. Effect of PGMs - general	46
2.3.6. Stress Corrosion Cracking (SCC)	49
2.3.7. Effect of PGMs on SCC	51
2.4. Oxidation	52
2.4.1. General	52
2.4.2. Effect of PGMs	54
2.5. Mechanical Properties	55
2.5.1. General Effects	55
2.5.2. Temperature Dependence	58
2.5.3. Toughness and Fracture Behaviour	58
2.5.4. Effect of PGMs	58
2.5.5. Hot Workability	61
2.6. Deformation Induced Structure	66
2.6.1. Deformation Induced Strength	68
CHAPTER 3 EXPERIMENTAL PROCEDURE	69
3.1. Preparation of Materials	70
3.2. Deformation and Heat Treatments	72
3.3. Microscopy	73
3.4. Magnetic Balance Measurements	75
3.5. Dilatometry Studies	79

	Page
3.6. Potentiodynamic Polarisation Studies	79
3.7. Thermogravimetric Studies	85
CHAPTER 4 SOLIDIFICATION MODES	87
4.1. Results	90
4.1.1. Solidification Modes	90
4.1.2. α-ferrite Solidification Route	93
4.1.3. γ-austenite Solidification Route	101
4.1.4. SEM Chemical Analysis	110
4.2. Discussion	110
4.2.1. Significance of Solidification Mode and Composition	110
4.2.2. Microstructural Features	112
4.2.3. Microchemical Features	113
4.2.4. Implications of PGM Additions	116
CHAPTER 5 PHASE CONSTITUTION	117
5.1. Introduction	119
5.2. Results	119
5.2.1. Microstructural Characterisation	119
5.2.2. 21Cr-6Ni Alloy Series	119
5.2.3. 18Cr-6Ni Alloy Series	126
5.2.4. Sigma Precipitation	130
5.2.5. γ_2-Austenite Precipitation	130
5.2.6. Microchemical Characterisation	130
5.3. Discussion	147
5.3.1. Microstructural Characterisation	147
5.3.2. 21Cr-6Ni Alloy Series	147
5.3.3. 18Cr-6Ni Alloy Series	149
5.3.4. Microchemical Characterisation	149
5.3.5. γ_2-Austenite Precipitation	152
5.3.6. σ-sigma Precipitation	154
CHAPTER 6 SIGMA PRECIPITATION	155
6.1. Results	156
6.1.1. Microchemical Features	156
6.1.2. Microstructural Features	156
6.1.3. Sigma Precipitation Kinetics	165
6.1.4. TEM Studies	170
6.1.5. Hardness Variations	170

	Page
6.2. Discussion	180
6.2.1. Phase Constitution	180
6.2.2. Compositional Effects	184
6.2.3. Sigma Precipitation Kinetics	186
6.2.4. Substructural Transformations	190
6.2.5. Hardness Variations	191
6.2.6. Effect of Thermal History and Strain	192
CHAPTER 7 MARTENSITE: STRUCTURE AND FORMATION	194
7.1. Results	195
7.1.1. Effect of PGMs on Bulk Martensite	195
7.1.2. Microstructural Features	196
7.1.3. Effect of PGMs on Strain-induced α'	216
(i) Room Temperature Deformation	216
(ii) -196°C Deformation	216
7.2. Discussion	223
7.2.1. Effect of PGMs on Bulk Martensite	223
7.2.2. Martensite: Structure, Morphology and Orientation	225
7.2.3. Strain-Induced Martensite	227
(i) Introduction	227
(ii) Effect of PGMs, Pt, Pd and Ru	227
7.2.4. Martensite Kinetics	230
7.2.5. Microstructural Features	235
CHAPTER 8 PHYSICAL PROPERTIES	237
8.1. Results	238
8.1.1. Tensile Properties	238
8.1.2. Hardness Variations	249
(i) As-Cast Alloys	249
(ii) Annealed Alloys	249
8.1.3. Isothermal Oxidation Behaviour	254
8.1.4. Anodic Polarisation Behaviour	260
8.2. Discussion	264
8.2.1. Tensile Behaviour	264
(i) Variables Affecting Stress-Strain Characteristics	264
(ii) Effect of Composition and Microstructure	264
(iii) Effect of Prior α' and Solid Solution Strengthening.	266

	Page
(iv) Effect of PGMs on Proof Stress	267
(v) Effect of PGMs on Tensile Strength	272
(vi) Effect of PGMs on the Strain-Hardening Exponent	273
(vii) Ageing Characteristics	275
(viii) Mode of Failure	278
8.2.2. Hardness Variations	281
(i) As-cast Alloys	281
(ii) Annealed Alloys	281
8.2.3. Anodic Polarisation Characteristics	282
8.2.4. Isothermal Oxidation Behaviour	282
(i) Effect of Alloy Composition	282
(ii) Effect of Pd and Ru	283
CHAPTER 9 CONCLUSIONS AND PROPOSALS FOR FUTURE WORK	286
REFERENCES	291
ACKNOWLEDGEMENTS	301
APPRNDIX: Determination of %α' From Magnetic Balance Measurements	302

NUMBER	LIST OF FIGURES	Page
1	Fe-Cr Binary Diagram.	20
2	Cr-Ni Binary Diagram.	21
3	Fe-Ni Binary Diagram.	21
4	Fe-Ru Binary Diagram.	22
5	Fe-Pd Binary Diagram.	24
6	Fe-Pt Binary Diagram.	25
7	Fe-Pt Binary Diagram	25
8	Fe-Ni-Cr Liquidus Projection.	26
9	Fe-Ni-Cr Solidus Projection.	26
10	3-D Schematic Diagram of Fe-Ni-Cr System.	27
11	Invariant Points in the Fe-Ni-Cr System.	29
12	Schaeffler Diagram.	29
13	Fe-Ni-Cr 1300°C Isotherm.	30
14	Fe-Ni-Cr 1200°C Isotherm.	30
15	Fe-Ni-Cr 1100°C Isotherm.	31
16	Fe-Ni-Cr 1000°C Isotherm.	31
17	Variation of T_o and M_s with Nickel Content in an Fe (17-18)%Cr Alloy.	33
18	Temperature-Time-Precipitation Curves for Various Phases in Uranus 50 Alloy.	35
19	Fe-Ni-Cr 650°C Isotherm.	36
20	Effect of Time and Temperature on Sigma Formation in an 26Cr-6Ni Stainless Steel.	36
21	The Partitioning of Cr and C Across an α/γ Boundary.	38
22	Schematic Chromium Concentration Profile at a γ/α Interface Containing $M_{23}C_6$.	38
23	Schematic Pseudobinary Diagram for 70%Fe Showing the Structures Developed in Fe-Ni-Cr Alloys.	40
24	Effect of Alloy Additions on Polarisation Characteristics of AISI 430 in 1N.H_2SO_4 at Room Temperature.	44
25	Effect of Alloy Additions on Polarisation Characteristics of AISI 430 in 1N.H_2SO_4 + 0.5N.NaCl at Room Temperature.	44
26	Mean Corrosion Rates of Steels in HCl at 80°C.	45
27	Potential-time Curves in 3%HCl at 25°C.	45
28	Potential-time Curves in 3%HCl at 50°C.	45
29	Potential-time Curves in 3%HCl at 100°C.	45
30	Effect of Noble Metal Additions on the Corrosion of a Fe-28Cr-4Mo Alloy.	47

LIST OF FIGURES

NUMBER		Page
31	Corrosion Rates of Various Steels in HCl Solution.	48
32	Time to Passivation of a Pd-Containing Steel in HCl Solution at 100°C.	48
33	Effect of Various Alloying Elements on Resistance to SCC in Chloride Environments.	50
34	Percent of Specimens Broken, Containing PGMs, with Time in Boiling $MgCl_2$.	50
35	Fe-Ni-Cr-O Phase Diagram at 1000°C Showing Oxides in Equilibrium with Varying Alloy Compositions.	53
36	Fe-Ni-Cr-O System at 1000°C, Defining the Limit of Stability of Chromic Oxide and Internal Oxidation.	53
37	True Stress-True Strain Behaviour of a Duplex Alloy.	56
38	Temperature Dependence of the Yield Strength of Duplex Stainless Steels.	56
39	Ferrite Dependence of the Yield Strength of Duplex Stainless Steels.	57
40	Ferrite Dependence of the UTS of Duplex Stainless Steels.	57
41	Tensile Properties, Product Forms and Recommended Environments for Some Duplex Steels.	59
42	Ferrite Dependence of the Impact Energy of Duplex Stainless Steels.	59
43	Effect of Ferrite Content on Mechanical Properties.	60
44	Effect of Ferrite Content on Cast FMN Material.	60
45	Mechanical Properties of Noble Metal Modified Alloys.	62
46	Effect of Ferrite Content on Hot-Workability.	63
47	Influence of Lead on Hot Ductility of a 7Cr-13Ni-1Mo Steel; As-cast Material	63
48	Thermomechanical Treatments Used to Produce a Microduplex, Superplastic Stainless Steel.	65
49	Analysed Alloy Compositions.	70
50	Fe, Ni, and Cr Purity.	70
51	PGM Purity.	71
52	Electro-polishing Characteristics of 21Cr-6Ni-8Ru Alloy..	74
53	Schematic Diagram of a Magnetic Ring Balance.	76
54	Pole Gap Characteristics.	77
55	Power Supply for Magnetic Balance.	78
56(a)	Specimen Position in Dilatometer.	80
56(b)	Specimen Heating Cycle.	81
57	Apparatus for Polarisation Curve Determination.	82

LIST OF FIGURES

NUMBER			Page
58		Close-up of Polarisation Cell.	83
59		Schematic Diagram of Apparatus for Polarisation Curve Determination.	84
60		Schematic Diagram of Thermogravimetric Balance.	86
61		Planar Section Through the Pipe of a 21Cr-6Ni-8Ru Alloy.	88
62		Effect of Alloy Composition on Solidification Modes.	91
63		Predicted Mode of Solidification for Experimental Alloys.	92
64		Schematic Pseudobinary Diagram for 70% Fe Showing the Structures Developed in Fe-Ni-Cr Alloys.	94
65		18Cr-6Ni Alloy Series As-cast Microstructures.	95
66		21Cr-6Ni Alloy Series As-cast Microstructures.	97
67		Effect of Cooling Rate on the Precipitation of Widmanstatten Austenite.	99
68		EDS Analysis of Alloy 21Cr-6Ni-8Pd wt%.	102
69		EDS Analysis of Alloy 18Cr-6Ni-8Pd wt%.	104
70		EDS Analysis of Alloy 21Cr-6Ni-8Ru wt%.	106
71		EDS Analysis of Alloy 18Cr-6Ni-8Pt wt%.	108
72		Fe-Ni-Cr Liquidus Projection.	111
73		Fe-Ni-Cr Solidus Projection.	111
74		Cross-Sections of the Fe-Cr-Ni System.	118
75		Modified Schaeffler Diagram.	120
76		Schaeffler Type Diagram for Wrought Alloys, Hot-Worked at 1150°C.	120
77		Widmanstatten Precipitation of ε-Martensite in a 18Cr-6Ni-8Pt Alloy.	121
78		Ferrite Volume Fraction as a Function of Annealing Temperature in the 21Cr-6Ni Alloy Series.	123
79		Microstructures of the 21Cr-6Ni Annealed Alloy Series.	124
80		Ferrite Volume Fraction as a Function of Annealing Temperature in the 18Cr-6Ni Alloy Series.	127
81		Microstructures of the 18Cr-6Ni Annealed Alloy Series.	128
82	(a)	γ_2 Precipitation in 21/6 Alloy Aged at 900°C.	131
	(b)	γ_2 Precipitation in an Alloy 21/6/8 Ru Aged at 650°C.	131
83		γ_2 Precipitation in Alloys 21/6/2Pd and 21/6/8Ru.	133
84		σ-Sigma Precipitation in an Alloy 21/6/8Ru Aged at 650°C.	135
85		Analysed Compositions of α and γ Phases at 1000°C.	137
86		Analysed Compositions of α and γ Phases at 1250°C.	137
87		Analysed Compositions of α and γ Phases at 1300°C.	138

LIST OF FIGURES

NUMBER			Page
88		PGM Partitioning Coefficients in Both 18/6 and 21/6 Alloy Series.	138
89		Cr and Ni Partitioning Coefficients for 2wt% PGM Additions at 1250°C.	139
90	(a)	21/6 - Cr and Ni Partitioning Coefficients - Bar Charts.	140
	(b)	18/6 - Cr and Ni Partitioning Coefficients - Bar Charts.	140
91		1300°C Isotherm - Effect of 2wt% PGMs on Tie-Lines.	142
92		1250°C Isotherm - Effect of 2wt% PGMs on Tie-Lines.	144
93		1000°C Isotherm - Effect of 2wt% PGMs on Tie-Lines.	146
94		Effect of 2wt% Noble Metal Additions on the Constitution of an Experimental Fe-26%Cr-8%Ni Alloy.	148
95		γ_2 Compositions in a 21Cr-6Ni Alloy.	153
96		σ and γ_2 Precipitation in Alloy 21Cr-6Ni-2Pd.	157
97		Microchemical Analysis of Aged Specimens.	159
98		Effect of Temperatures, 700°C and 900°C on Sigma Precipitation at 5 Minutes.	161
99		Effect of Times, 5 and 250 Minutes on Sigma Precipitation at 950°C.	163
100		Curves for σ Precipitation in Duplex Alloys, Varying Time and Temperature.	166
101		Time-Temperature-Transformation Curves for σ Precipitation.	167
102		σ Precipitation According to the Johnson-Mehl Equation.	168
103		n and k Values from the Johnson-Mehl Equation.	169
104		σ Precipitation in Alloy 21Cr-6Ni-8Ru Aged at 650°C.	171
105		σ Precipitation in Alloy 21Cr-6Ni-8Ru Aged at 650°C.	171
106		SADP of σ in (105).	171
107		Lamellar Precipitation of σ - TEM Micrograph.	171
108		Lamellar Precipitation of σ - TEM Micrograph.	173
109		SADP of σ Phase in (108)	173
110		σ Growth into α Grains - TEM Micrograph.	173
111		σ Growth into α Grains - TEM Micrograph.	173
112		TEM Micrographs of Alloy 21Cr-6Ni-8Ru Aged at 650°C, Showing the Partial Decomposition of $\gamma \rightarrow \varepsilon$.	175
113		Hardness Variations in Aged Duplex Alloys.	177
114		Light Micrographs of Alloy 21Cr-6Ni-2Pd Showing Coalesced and Discrete Grains of σ Phase.	178
115		Model for γ/σ Lamellar Formation.	181
116		Fe-Ni-Cr 650°C Isotherm.	181

LIST OF FIGURES

NUMBER		Page
117	Fe-Ni-Cr 800°C Isotherm.	182
118	Fe-Ni-Cr 900°C Isotherm.	183
119	Values of n in the Kinetic Law, $X = \exp(-Kt^n)$.	188
120	n and k Values from Beetge and Robinson.	188
121	Effect of Cooling Rate on σ Precipitation.	193
122	Percentage of $\gamma \rightarrow \alpha'$ in Annealed Experimental Alloys.	195
123	Micrographs of α'-Martensite in Alloy 21Cr-6Ni.	197
124	Micrographs of α'-Martensite Laths in 21Cr-6Ni.	199
125	Micrographs in Alloy 21Cr-6Ni-8Ru Showing Stacking Faults, ε and α'-Martensites.	201
126	TEM Micrographs of α', ε, α and γ Phases in Alloy 21Cr-6Ni-8Ru.	203
127	Micrographs of Faulted γ in Alloy 18Cr-6Ni-8Ru.	205
128	TEM Micrographs of α' and ε Martensites in 18Cr-6Ni-8Ru.	207
129	Micrographs of α' in Alloy 18Cr-6Ni-8Pd.	209
130	Micrographs of α' in Alloy 18Cr-6Ni-8Ru.	211
131	Micrographs of α' in Alloy 18Cr-6Ni-8Pd.	213
132	Dilatometry Measurements.	215
133	% $\gamma \rightarrow \alpha'$ Induced by Rolling Alloys at Room Temperature.	217
134	% $\gamma \rightarrow \alpha'$ Induced by Rolling Alloys at -196°C.	218
135	Light Micrographs of Alloy 21Cr-6Ni-2Pd Deformed at Room Temperature.	220
136(a)	M_s Temperatures of Fe-Based Binary Alloys.	222
(b)	M_s Temperatures of Fe-PGM Binary Alloys.	222
(c)	Effect of Alloy Composition on ΔH.	222
137	M_s Values, Measured and Calculated.	224
138	Effect of Pt, Pd and Ru on the % $\gamma \rightarrow \alpha'$ and Rate of Transformation of γ to α' with Strain.	229
139	Strain-Induced α' in 18Cr-6Ni Alloy Series According to Angel Equation.	232
140	Strain-Induced α' in 21Cr-6Ni Alloy Series According to Angel Equation.	234
141	Proof Stress, UTS, % Elongation Values in Annealed and Aged Alloys.	238
142	Stress-Strain Characteristics of Duplex Alloys Annealed at 1250°C.	239
143	The Effect of σ Precipitation, Ageing at 900°C, on Ductility and Proof Stress in Duplex Alloys.	240
144	Stress-Strain Characteristics of Aged Duplex Alloys.	241

NUMBER LIST OF FIGURES Page

145 The Effect of Ageing Temperature on Tensile Ductility. 243

146 Light Micrographs of Structures Generated in Tensile Specimens. 245

147 Fractography of Annealed and Aged Duplex Steels. 247

148 Hardness Values of As-Cast and Annealed Alloys. 249

149 18Cr-6Ni Alloy Series-Hardness Variations in Annealed Alloys. 250

150 21Cr-6Ni Alloy Series-Hardness Variations in Annealed Alloys. 251

151 Isothermal Oxidation Behaviour of Duplex Alloys at 1000°C in Air. 252

152 Schematic Section Through Oxide Films Developed at 1000°C in Air. 254

153 SEM Micrograph of Oxide Cross-Section with Accompanying X-ray EDS Analysis of Surface. 256

154 SEM Micrographs of Oxide Surfaces. 258

155 Anodic Polarisation Characteristics of Duplex Alloys Containing Pd and Ru in Deaerated 1N.H_2SO_4 at 25°C. 261

156 Anodic Polarisation Characteristics of Pd-Modified Uranus 50 Steel in Deaerated 1N.H_2SO_4 at 25°C. 262

157 Anodic Polarization Curve Showing the Effect of Noble Metals to the Corrosion Reaction of Chromium. 263

158 (a) Relation Between Ni and Cr Contents of Stainless Steels and Type of Steel. 265

(b) Tensile Stress-Strain Curves for Various Stainless Steels and Pure Iron. 265

159 Regression Analysis of 0.2% Proof Stress of Duplex Alloys. 266

160 TEM Micrographs of α-Ferrite Stringers and α'-Martensite Grains. 268

161 (a) Change in 0.2% Proof Stress per Atomic % Alloying Elements. 271

(b) Effect of γ/α Fraction on Proof Stress, UTS, and % Elongation. 271

162 Strain-Hardening Exponent Variations in Annealed and Aged Duplex Alloys. 273

163 Effect of Ageing on the Tensile Properties in Duplex Steels. 276

164 Variation of σ Phase Volume Fraction and Room Temperature Tensile Properties with Ageing Time at 1073K. 277

165 Proposed Mechanism of Failure in σ-Phase/Austenite Structures. 279

166 Diagramatic Classification of Oxidation Behaviour in Fe-Ni-Cr Alloys. 284

CHAPTER ONE

INTRODUCTION

They may be the best of alloys, or the worst of alloys;
They may possess all the desired properties
Or they may possess none of them;
Their use may mark our wisdom, or our foolishness

(Dickens)

Duplex stainless steels, consisting of fine grained mixtures of ferrite and austenite offer attractive combinations of properties (1). The presence of ferrite confers increased yield strength and improved resistance to the initiation of stress corrosion, while the austenite phase is beneficial in lowering the ductile/brittle transition temperature. Correctly fabricated and used in selected environments, they can be superior to competing materials (2). Recent interest in their applications has included the corrosive environments of heat exchangers, chemical process plants and flue-gas desulphurisation plants (3-5).

Several PGM enriched nickel based superalloys have been developed for specific industrial and aerospace applications (6,7) and experience to date suggests that such alloys have much to offer in many industrial applications where corrosion resistance in arduous high temperature environments is an important material selection criterion (8). It is hoped that PGM enriched Fe-based alloys in this study may show potential for industrial applications as outlined for the Ni-based alloys.

The objectives of the present work were therefore, to investigate the metallurgical effects of three platinum group metals (PGMs), namely Pt, Pd and Ru on duplex stainless steels in terms of structure and certain properties. The main reasons why PGMs may be advantageous is through their electrochemical nobility and their potential for enhancing passivity. However, studies of PGM alloying additions to stainless steels previously made, have lacked a sufficient basis of fundamental data on the specific structural and constitutional features.

The choice of duplex stainless steels as a base for PGM alloying is advantageous in providing a convenient route for elucidating key features of ferrite/austenite relationships and austenite stability. For the present work two base compositions were chosen, namely, Fe-18Cr-6Ni and Fe-21Cr-6Ni (wt%). These compositions lie in the ferrite + austenite region of the Fe-Cr-Ni system in the range 1000°C to 1300°C. Additions of 2 wt% and 8 wt% of the three PGMs were made to these base alloys.

Constitutional studies have been largely based upon the recent review of the Cr-Fe-Ni system by Rivlin and Raynor (9) who present the ternary system in the form of projections for the liquidus, solidus and isothermal sections for the solid phase equilibrium down to 550°C.

Data for the binary Fe-Pt (10,11), Fe-Pd (10-14) and Fe-Ru (10,15) systems demonstrate the γ-stabilizing role of these PGMs. Pt and Pd, being fcc, show a complete series of solid solution with austenite. Ru, which is hcp in structure, opens the γ-field giving rise to a eutectoid reaction $\gamma \rightarrow \alpha$ + Ru solid solution at $\simeq 500^{o}C$.

CHAPTER TWO

LITERATURE SURVEY

All men naturally desire to know,
but what doth knowledge avail,
without the fear of God?

(Thomas A. Kempis)

2.1. Constitution

2.1.1. Elements

Fe

Below the melting points of iron (1536°C) there are 3 allotropes:-

Temperature range °C	Symbol	Crystal Structure
1536-1392	δFe	bcc
1392- 911	γFe	fcc
911 and below	αFe	bcc

The ferromagnetic Curie temperature lies between 767-771°C (16). Phase equilibria in binary and higher systems of iron depend on whether the added elements are more soluble in bcc or fcc iron. Solid solutions in the fcc and bcc iron phases are usually designated γ and α respectively.

Cr

The element is bcc below its melting point. A review of the original literature places the value at a mean of 1878±22°C (17). Solid solutions in chromium are denoted α'. Claims for allotropy in chromium are reviewed by Pearson (18). However, the balance of evidence emphasises that the structure is bcc at all temperatures below its melting point.

Ni

The element is fcc below its melting point (1453°C) and has a ferromagnetic Curie temperature of between 352-360°C (16).

Pt

Platinum is fcc below its melting point of 1768°C and is paramagnetic (19).

Pd

Paladium is fcc below its melting point of 1552°C and as a pure metal is almost ferromagnetic with a very high paramagnetic susceptibility and polarizability (19).

Ru

Ruthenium is hcp below its melting point of 2310°C and is paramagnetic (19).

2.1.2. Binary Systems

Cr-Fe

(See Figure 1). Chromium and bcc iron are miscible in all proportions from Cr to Fe at elevated temperatures. The α and δ allotropes of Fe unite at over 12wt%Cr to form a continuous bcc solid solution, $\alpha\delta$Fe, stable at all temperatures up to the solidus. Consequently, the range of the fcc γ is restricted. The element Cr is therefore a stabilizer for $\alpha\delta$Fe but not for γFe.

The equilibria below 800°C are governed by the σ-phase. Sigma phase forms congruently from α at 820°C and 48%Cr. At lower temperatures a eutectoid decomposition to α and α' takes place. The sluggishness of all reactions involving σ, has made its bounding temperatures and compositions a matter of some dispute (9).

Cr-Ni

(See Figure 2). The simple eutectic version of the system is taken from Shunk (10). The liquidus and solidus are well established. The eutectic horizontal at 1345°C, extends from 41 to 53%Ni and the eutectic composition is reliably placed at 49%Ni.

Solubility in α' is very restricted at lower temperatures (<1000°C). Solubility in γ is less restricted and extends to at least 20%Cr, but a phase $CrNi_2$, with an orthorhombic structure, intervenes below 580°C.

Fe-Ni

(See Figure 3). Fcc nickel is totally miscible with fcc iron (γFe) so that the fcc phase, γ, extends across the diagram below the solidus and above the fcc → bcc Fe transition temperature except for the small δFe field close to the melting point of Fe. Solubility in the bcc allotropes of iron (α and δ) is very restricted.

Fe-Ru

(See Figure 4). As has been noted by Cottrell (15), Hume-Rothery (23) and Honeycombe (24), Ru belongs to a group of metals which 'open-up' the γ-field. The system reveals wide areas of solid solution based on ruthenium and γ-Fe. The solubility of Fe in Ru and that of Ru in γ-Fe at the peritectic temperature of 1590°C are respectively ∿64.5 and 29.5at%. The solubility of Ru in δFe at the peritectic temperature of 1536°C is 5.5at%. Some 4.8% of Ru dissolves in α-Fe at the eutectoid temperature of 500°C while the solubility of Fe in Ru at the same temperature is 76.5at%

Fe - Cr system

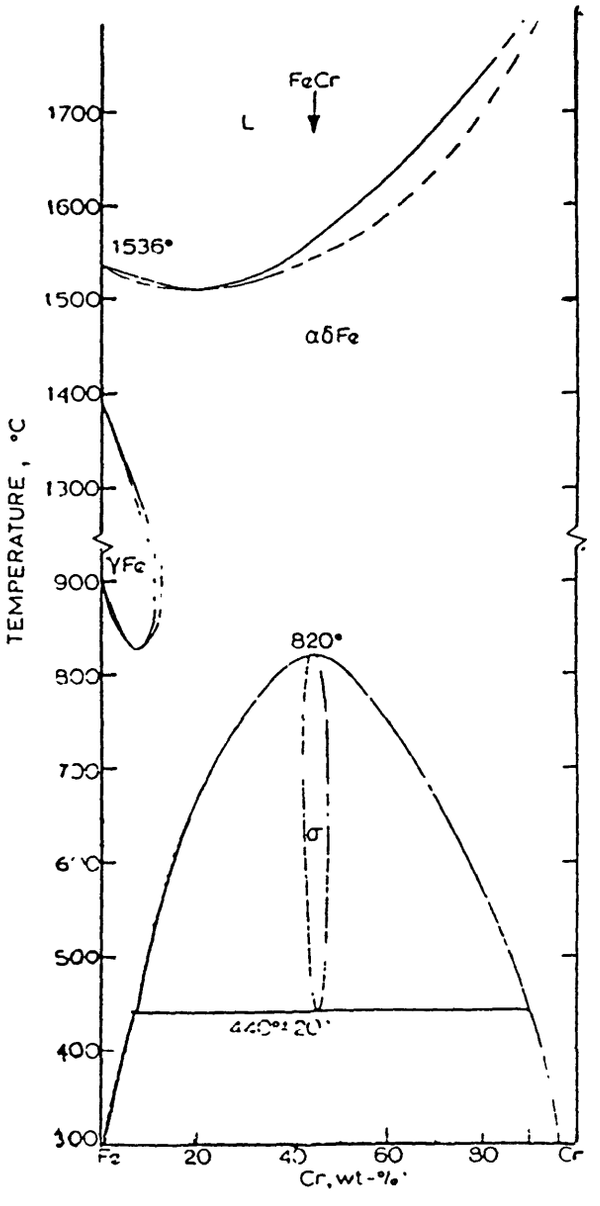

Figure 1.

Refs. 10-12, 20,21

Cr - Ni system

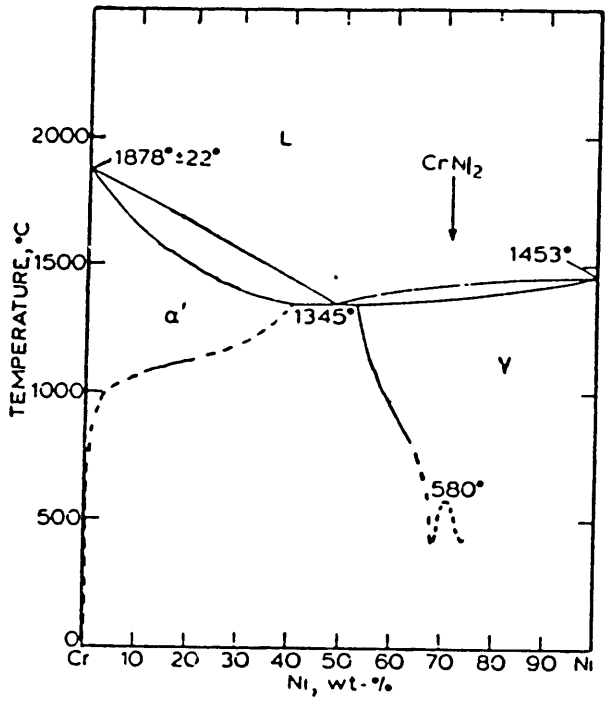

Figure 2. Refs. 10-12

Fe - Ni system

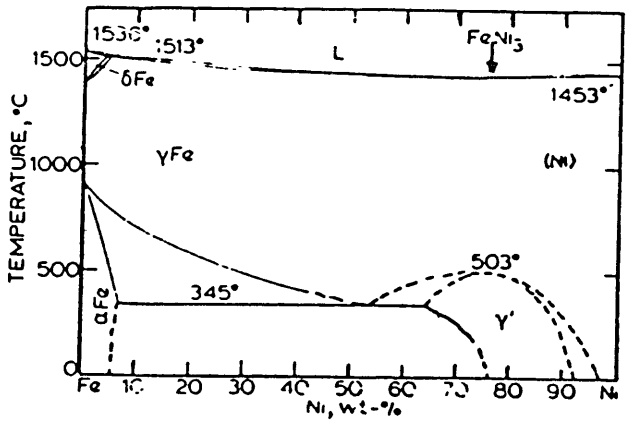

Figure 3. Refs. 10-12,22

Fe - Ru System

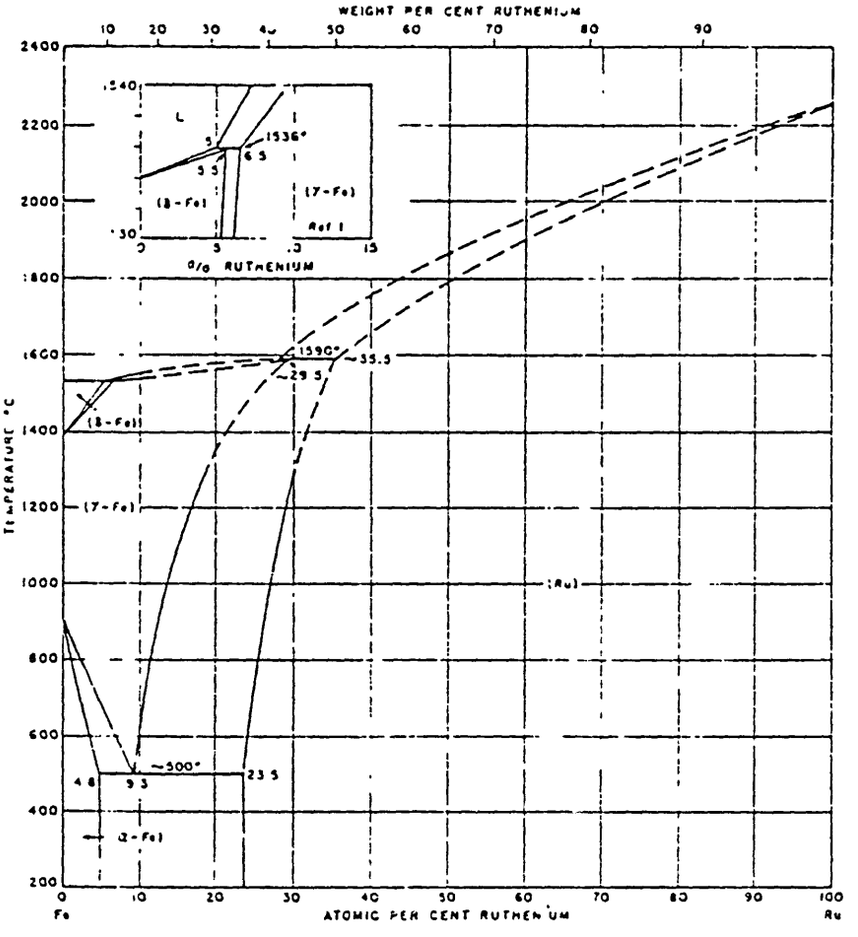

Figure 4.

Ref. 10

(25). As a consequence of an extremely sluggish eutectoid reaction in the system, diffusionless (shear) transformations from γ(fcc) to α(bcc) or Ru-ε (hcp) are possible at atmospheric pressure. (At higher pressures the diffusionless transformation $\alpha \not\rightleftarrows \varepsilon$-Ru, is possible). (10).

Fe-Pd

(See Figure 5). The constitutional diagram of Fe-Pd was first established by Grigoriev who used thermal and microstructural analysis and measured hardness and the temperature coefficient of electrical resistivity (26).

Additions of Pd to Fe 'open-up' the γ-field (15,23,24), and between $\sim$910 and 1300°C there is a continuous series of fcc solid solutions between γ-Fe and Pd. A miscibility gap however, exists in the fcc solid solution between 7-23 at%Pd (10). The solid solubility of Pd in Fe is $\sim$3at% (19,26).

Pd additions to Fe raise the $\delta \not\rightleftarrows \gamma$ transition temperature to a peritectic reaction of $\delta + L \not\rightleftarrows \gamma$ at 1478°C (11).

Fe-Pt

(See Figure 6). The phase diagram is taken from Hanson (12), Elliott (11) and Shunk (10). Sundaresen et al (27) determined the thermodynamic properties of the Fe-rich alloys from electrochemical data, and subsequently inferred the solid state equilibria: Fe_3Pt stable $\sim$600-740°C and three eutectoid reactions - $\gamma \not\rightleftarrows \alpha$ + (FePt) at $\sim$550°C, $Fe_3Pt \not\rightleftarrows \gamma$ + (FePt) at $\sim$600°C and $\gamma \not\rightleftarrows Fe_3Pt$ + (FePt) at >600°C. These equilibria are considered only tentative by Shunk (10), however, they are in good agreement with data presented by Hanson (12).

By high-temperature X-ray techniques, Crangle and Shaw (28) have determined the phase boundaries for ($FePt_3$) which is observed to exist over a wide composition range. Figure 7a shows these boundaries and incorporates the liquidus and solidus from Hanson.

By careful thermal analysis of alloys prepared from 99.99% Pt and high purity Fe, Buckley and Hume-Rothery (29), have ascertained that the $\delta \not\rightleftarrows \gamma$ transformation in Fe is raised with Pt additions. Their version of the peritectic reaction is shown in Figure 7 b.

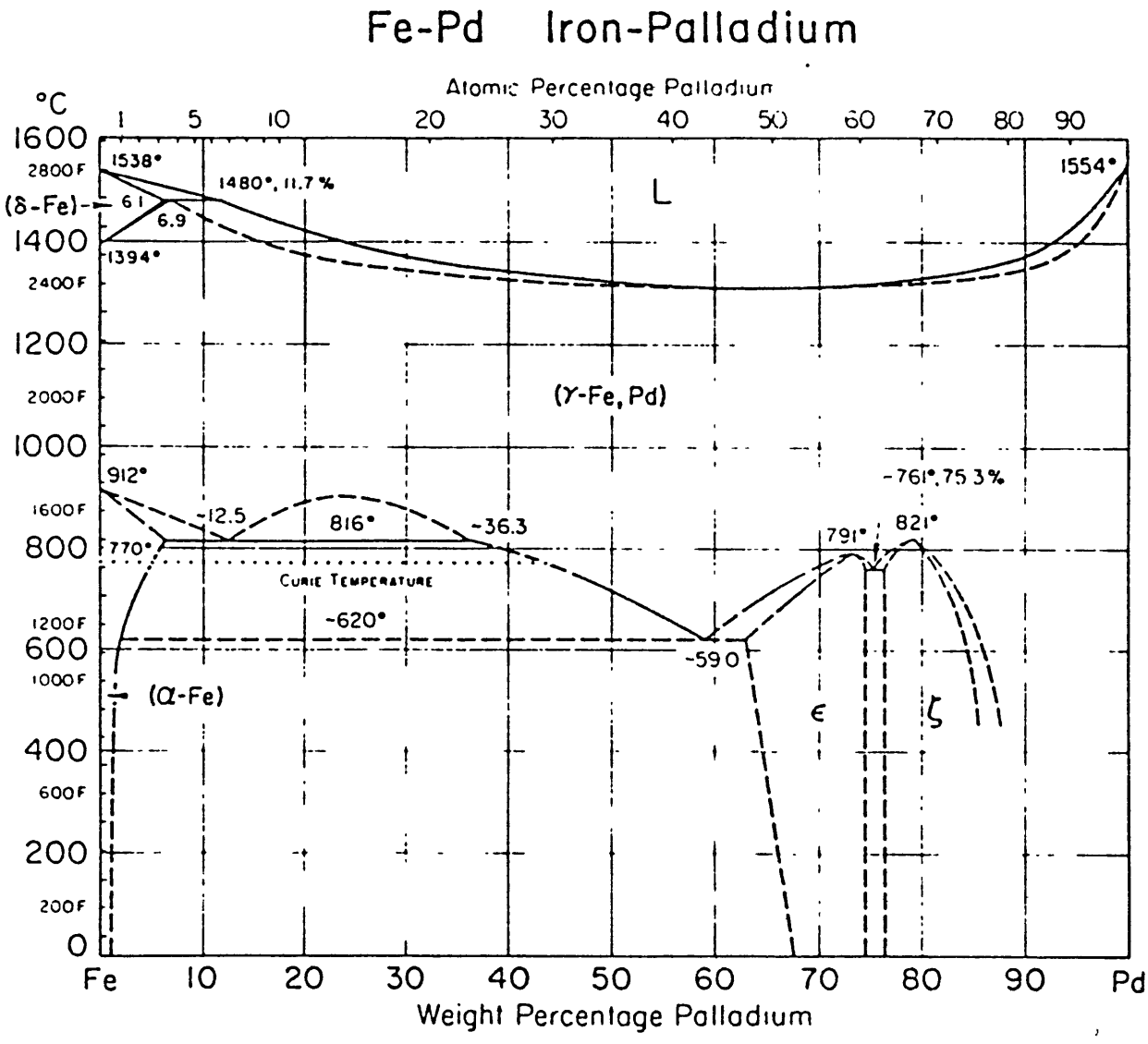

Figure 5.

Refs. 10-14

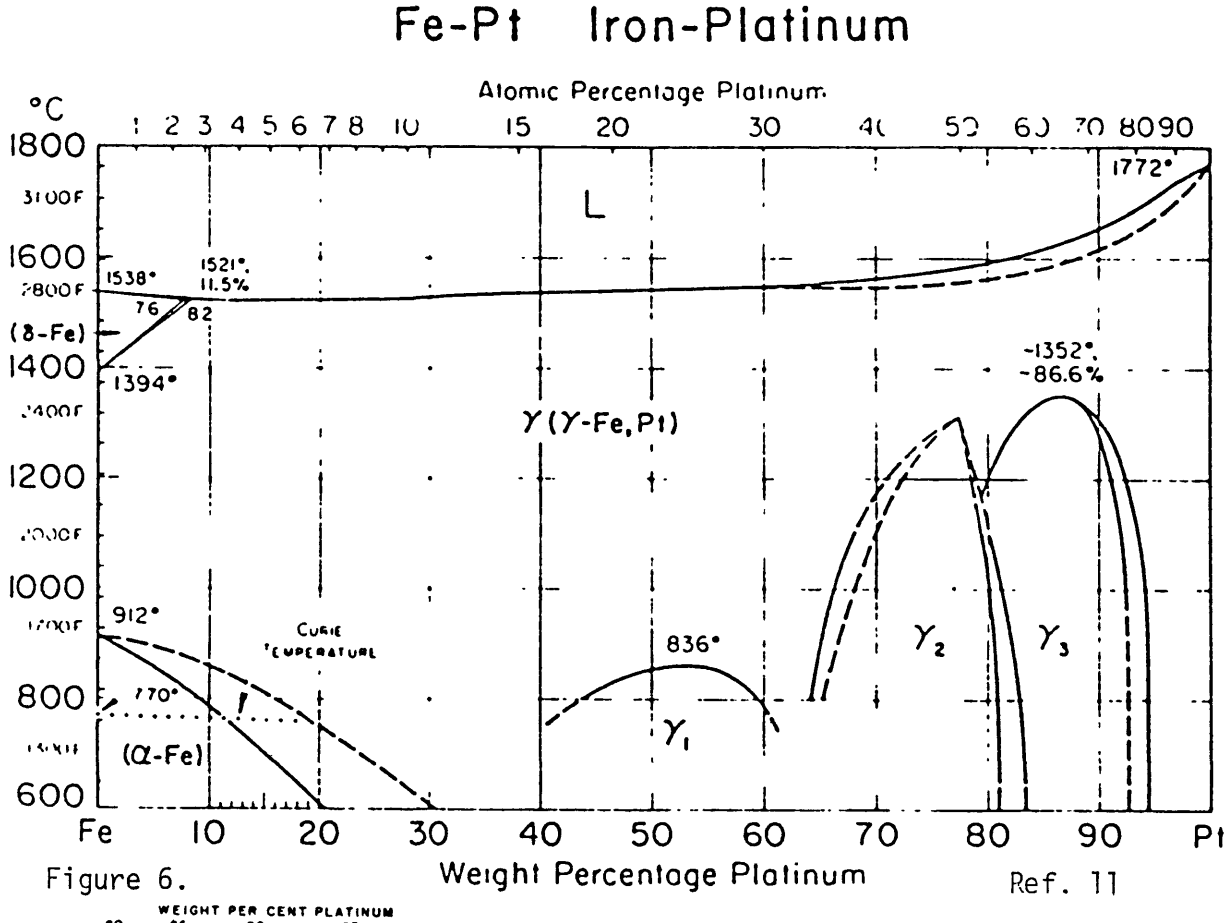

Figure 6. Ref. 11

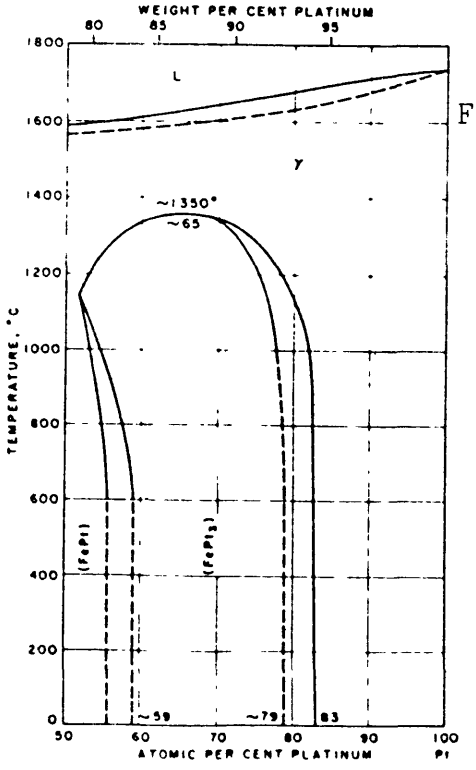

Figure 7a

Ref. 10

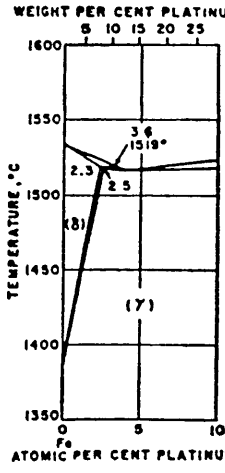

Figure 7b

Ref. 11

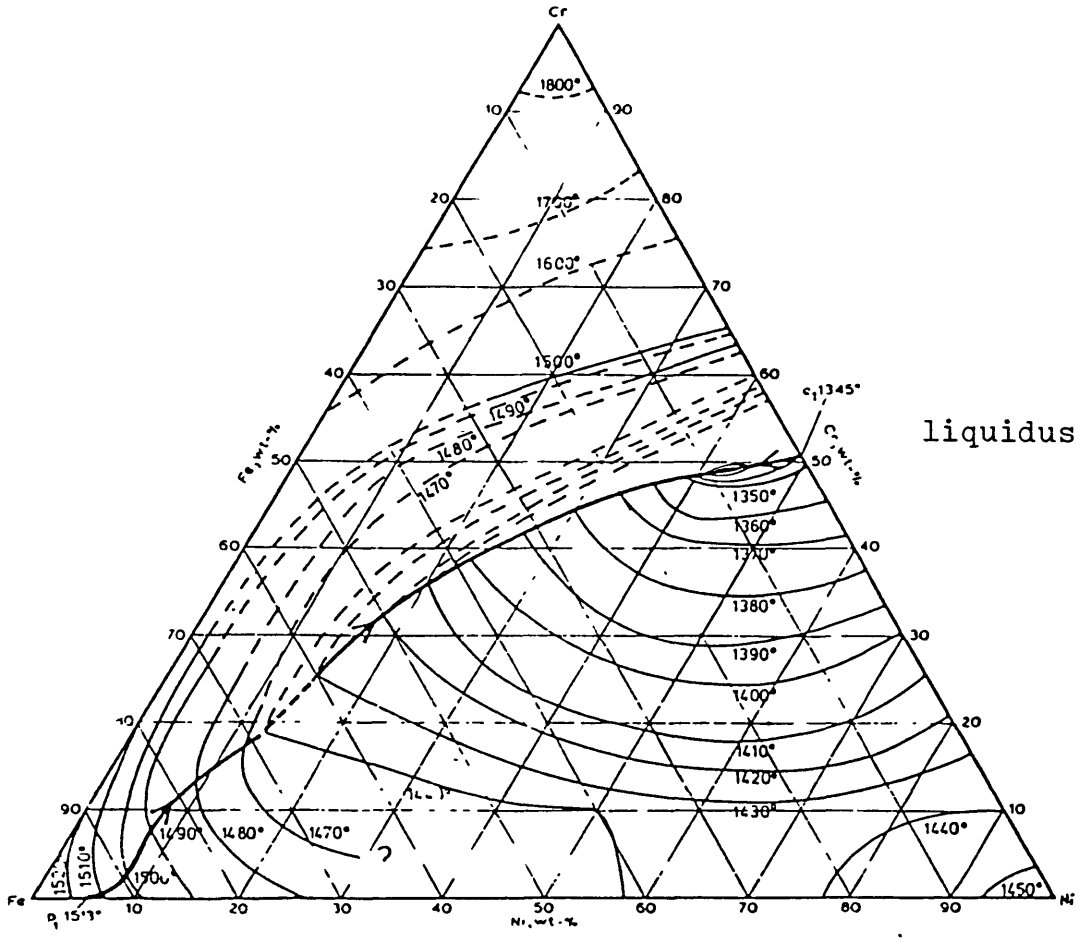

liquidus projection

Figure 8.

Refs. 22,40,41

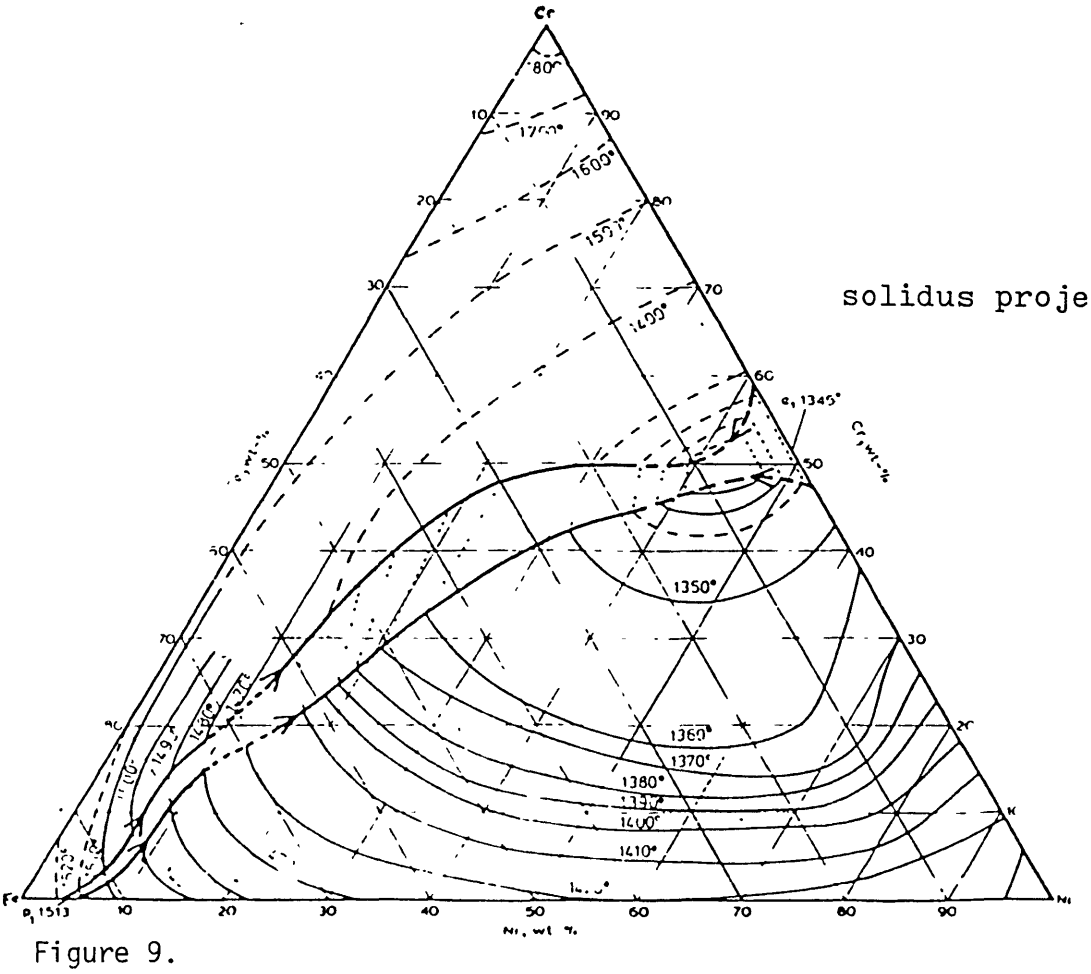

solidus projection

Figure 9.

Ref. 22

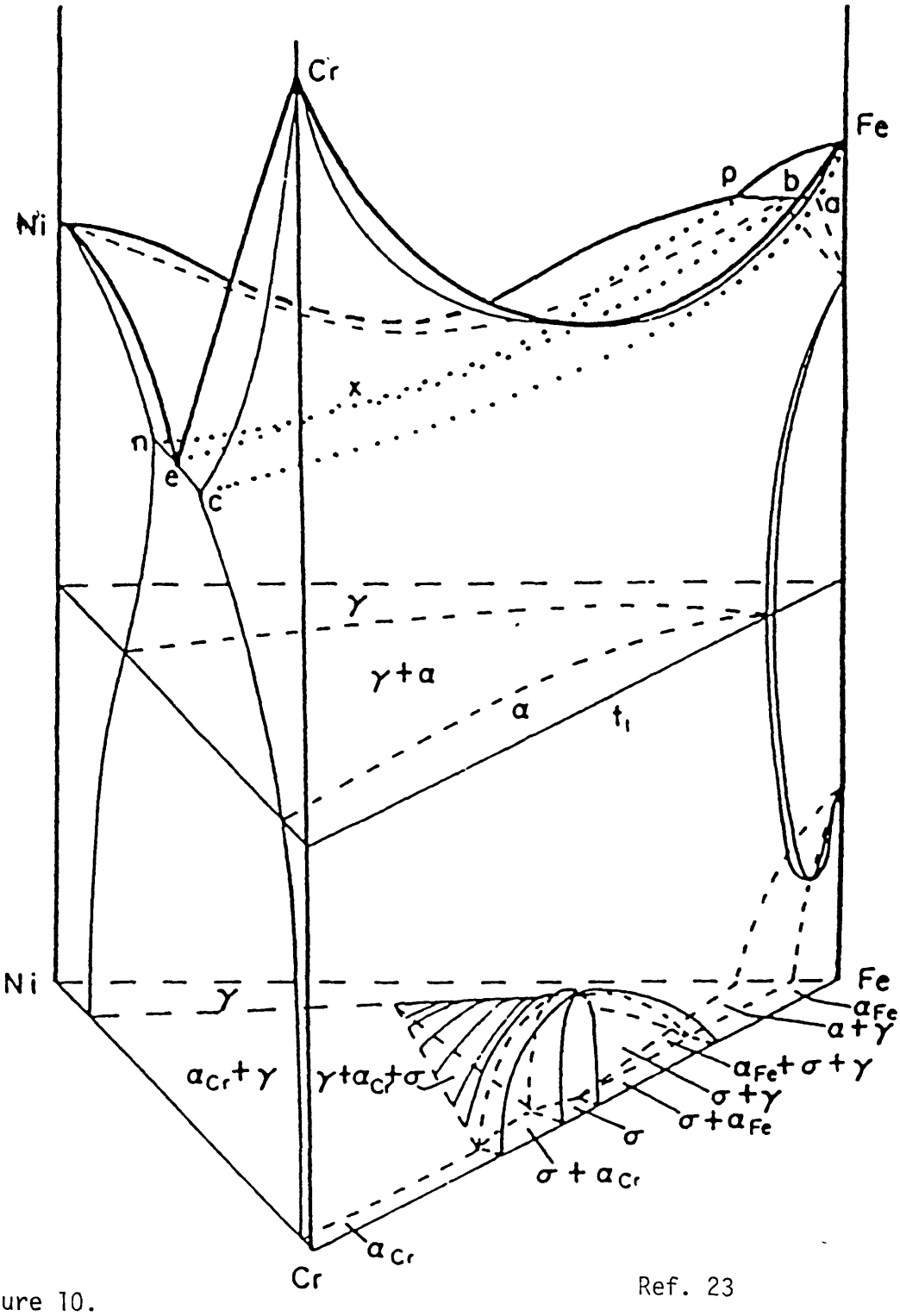

Figure 10. Ref. 23

Schematic representation of Fe-Cr-Ni system

2.1.3. Ternary System

The long standing importance of the Cr-Fe-Ni system in ferrous metallurgy (shown schematically in Figure 10), has resulted in the constitution being one of the most thoroughly investigated amongst ternary systems. Early work is summarized in a very comprehensive metallographic survey by Bain and Griffiths (30). More recently the system has been reviewed by Rivlin and Raynor (9). Using results and information which have been reliably corroborated, and noting discrepancies in the solid state diagrams, they have drawn a set of self-consistent projections in the temperature range 1300°C down to 550°C. Quantitative measurements of the isotherms from 1300 to 650°C and approximately at 550°C (31-39) are in general agreement on the identity of all phases (See Figure 11). The main techniques reviewed by Rivlin and Raynor (9) in determining liquidus, solidus and isothermal sections in Figures 8 and 9, include, thermal and dilatometric analysis, X-ray and microprobe analysis and metallographic examination.

In Figures 13 to 16 and 19 isotherms at 1300, 1200, 1100, 1000 and 650°C are shown. With respect to the fcc (γ) and bcc (α) phases, the diagrams are considered to be quite accurate; however, the precise limits of the σ phase regions are not clear at lower temperatures. The temperature range of σ stability is defined as being from $\sim$600°C to 950°C, but due to the sluggishness of the σ precipitation, the composition limits are poorly defined. Additionally, the purity of the ternary Fe-Cr-Ni alloy will often affect accurate prediction of tie-lines and boundary limits. Typically, element impurities are Si, P, and S. Rivlin and Raynor (9) additionally review literature based on thermodynamic considerations for isotherms 800 to 1400°C.

One of the most convenient ways of representing the effect of various elements on the basic structure of Cr-Ni stainless steels, is the Schaeffler (42) diagram (see Figure 12), often used in welding. It plots the compositional limits at room temperature of austenite, ferrite and martensite and has a wide application when the chromium and nickel equivalents of other alloying elements are used (24). The chromium equivalent has been empirically determined using the most common ferrite-forming elements:

$$\text{Cr. equiv.} = (\text{Cr}) + 2(\text{Si}) + 1.5(\text{Mo}) + 5(\text{V}) + 5.5(\text{Al}) + 1.75(\text{Nb}) + 1.5(\text{Ti}) + 0.75(\text{W}) : \text{wt.}\%$$

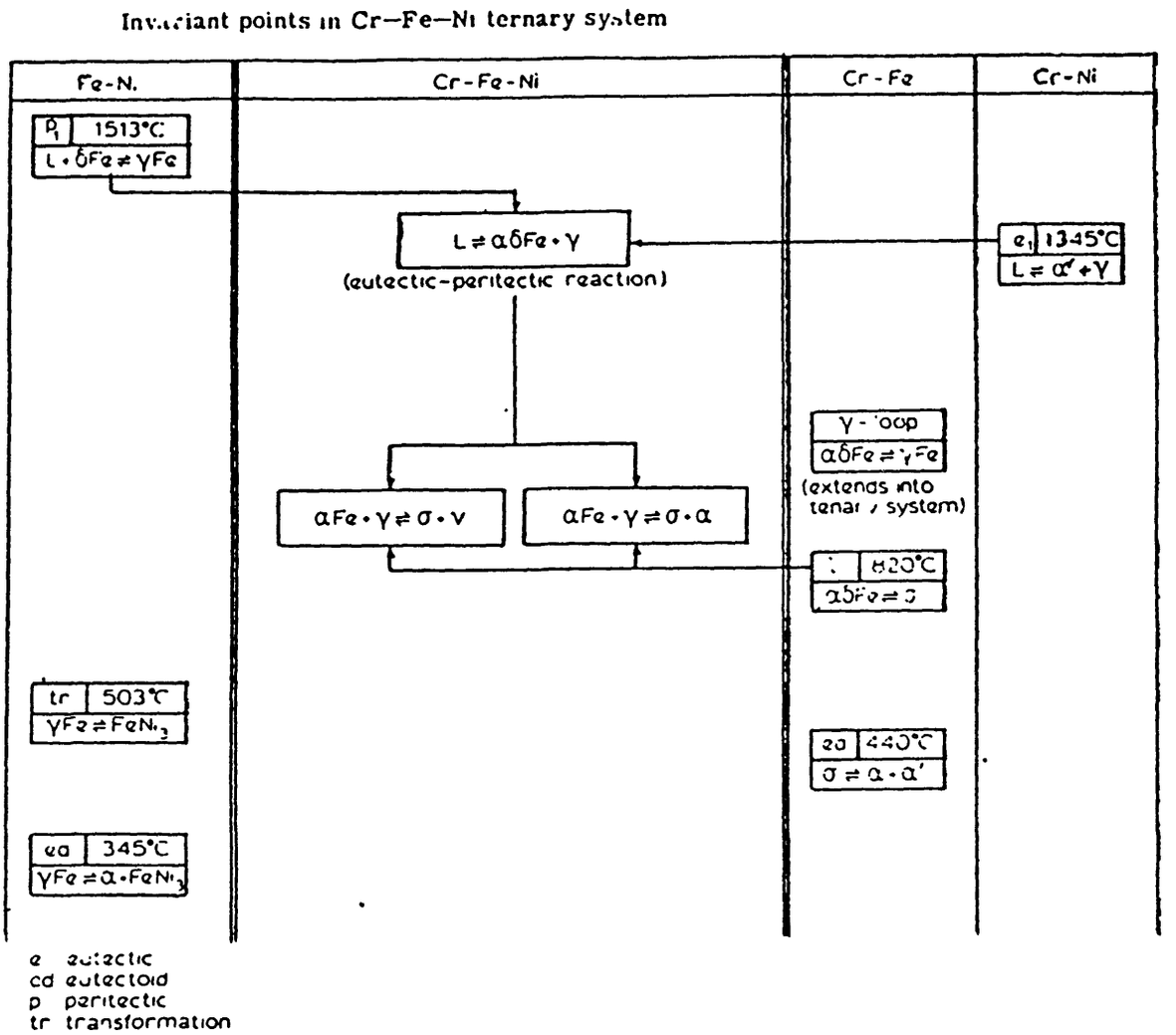

Figure 11.

Ref. 9.

Schaeffler diagram

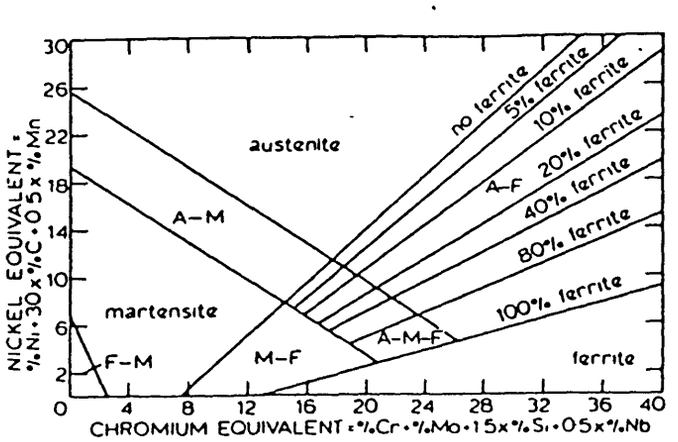

Figure 12.

Ref. 42

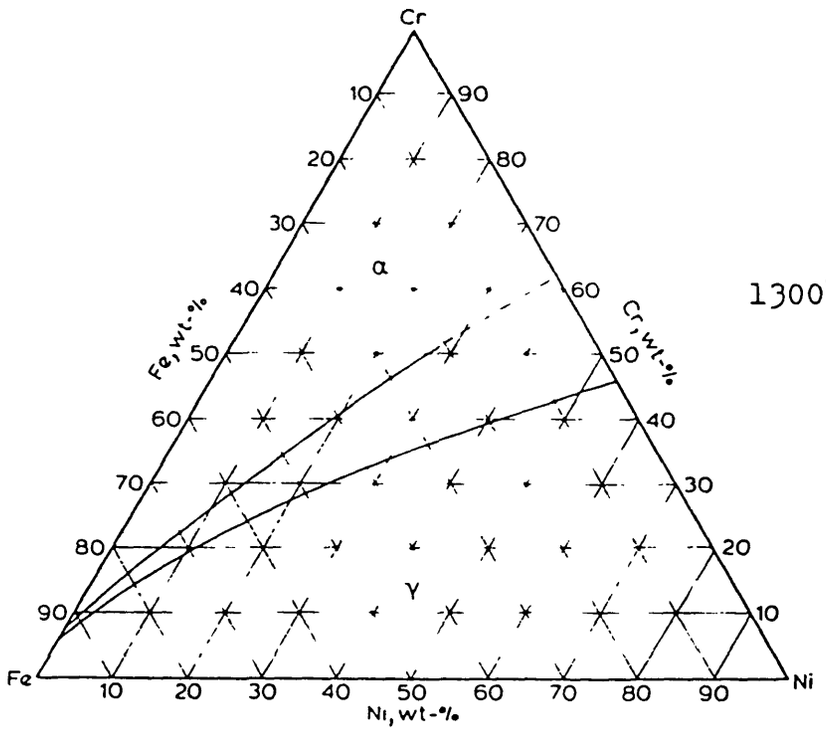

1300°C isotherm

Figure 13.

Ref. 43.

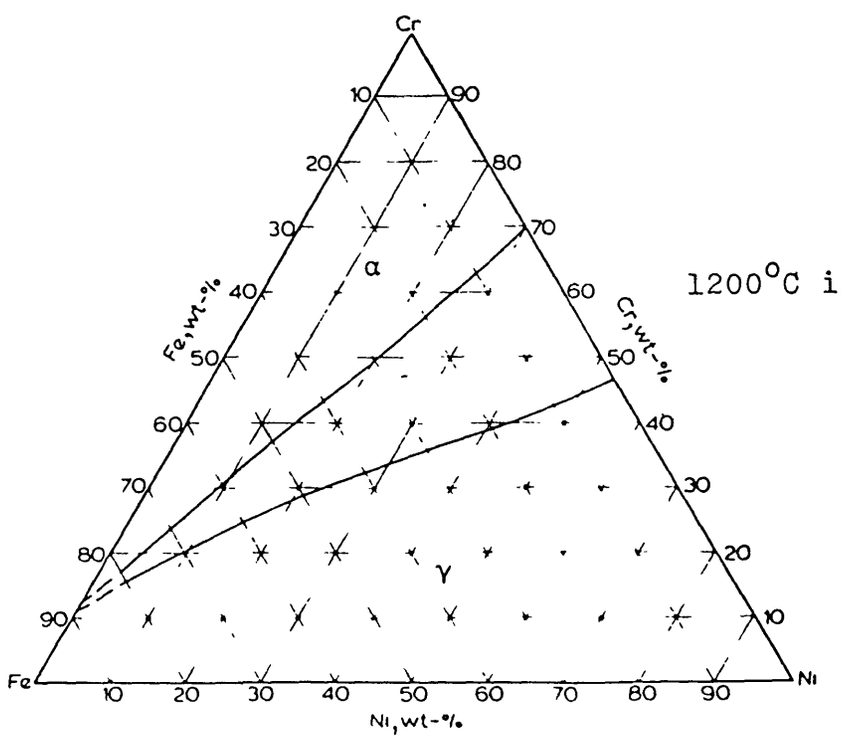

1200°C isotherm

Figure 14.

Ref. 44,45

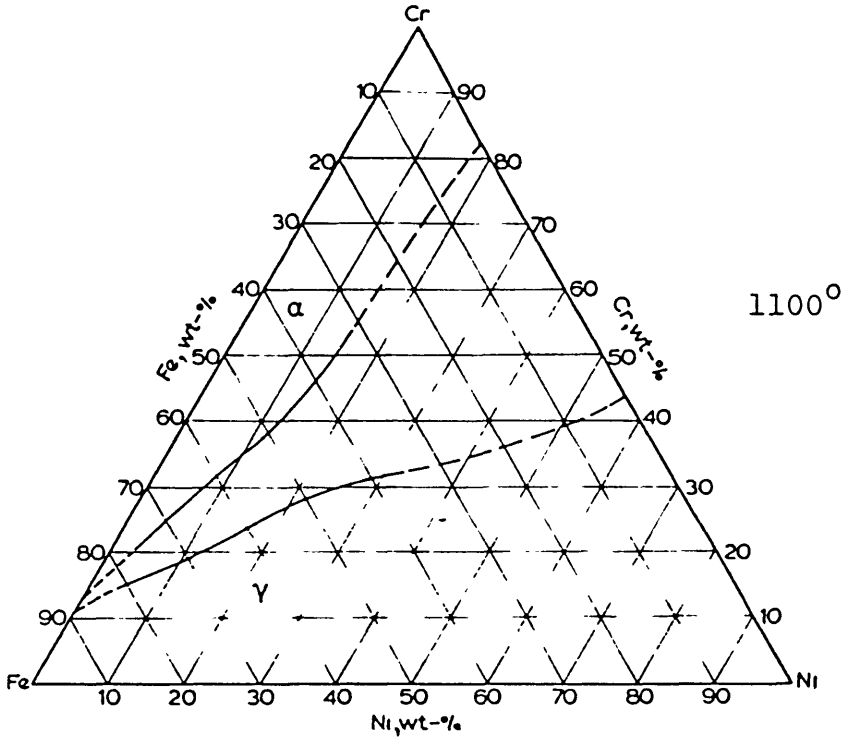

1100°C isotherm

Figure 15. Ref. 32

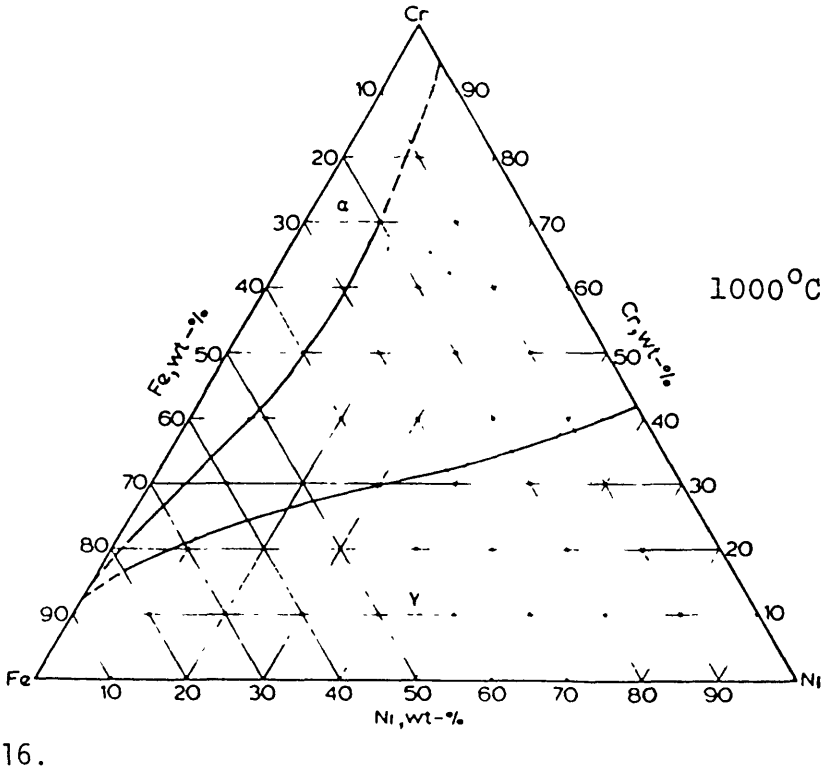

1000°C isotherm

Figure 16. Ref. 32

while the nickel equivalent has likewise been determined with the familiar austenite-forming elements:

Ni equiv. = (Ni) + (Co) + 0.5(Mn) + 0.3(Cu) + 25(N) + 30(C): wt%

All concentrations being expressed in weight percentages.

2.1.4. Austenite Stability

On quenching to room temperature (or deforming at) room or sub-zero temperature, austenite stability with respect to transformation to martensite is dependent on steel composition. Although there are different opinions as to the effect of individual elements on austenite, it is accepted that all elements except possibly Co (46,47) and Al (24) depress M_s (48-50).

Andrews (51) M_s (^oC) = 539 - 423(C) - 30.4 (Mn) - 17.7(Ni) - 12.1(Cr) - 7.5 (Mo).

Eichmann and Hull (49) M_s (^oC) = 1305 - 61.1(ni) - 41.7(Cr) - 33.5(Mn) -27.8(Si) - 1667.7(C + N)

Holmes et al (52) M_s (^oC) = 502 - 30(Ni) - 12(Cr) - 13(Mn) - 810(C) - 1230(N) - 54(Cu) - 46(Mo)

These relationships show that the interstitials solutes carbon and nitrogen have a much larger effect than the metallic solutes on M_s (24).

A more precise indication of γ stability can be gained from T_o (53,54), the temperature at which γ and α' have the same free energies (Figure 17). This is expressed as

$$\Delta G^{\alpha' \rightarrow \gamma} = (1-x)\Delta G_{Fe}^{\alpha \rightarrow \gamma} + x\Delta H_x^{\alpha' \rightarrow \gamma}$$

$\Delta H_x^{\alpha' \rightarrow \gamma}$ is the difference in enthalpy of element X in austenite (γ) and in martensite (α'). And x is the atomic fraction of alloying element.

Table (24)

X	C	N	Mn	Ni	Cu	Cr	W	Mo	V	Ti
$\Delta H_x^{\alpha' \rightarrow \gamma}$ ($kJmol^{-1}$)	-33.9	-22.4	-10.7	-8.4	-5.4	-5.0	+5.7	+5.7	+11.8	+37.7

Alloying elements either expand the γ-loop, i.e. stabilize γ, or contract the loop and encourage α-formation, and this will have different effects on $\Delta H_x^{\alpha' \rightarrow \gamma}$. Elements which expand the γ-loop will make this term negative and lower T_o, while elements which favour α formation will make the term positive and raise T_o.

Significant also is the M_d (temperature above which no martensite can form even by deformation).

T_o, M_s, M_{si} and T_{max} of Fe (17-18)% Cr-Ni alloy with varying Ni content

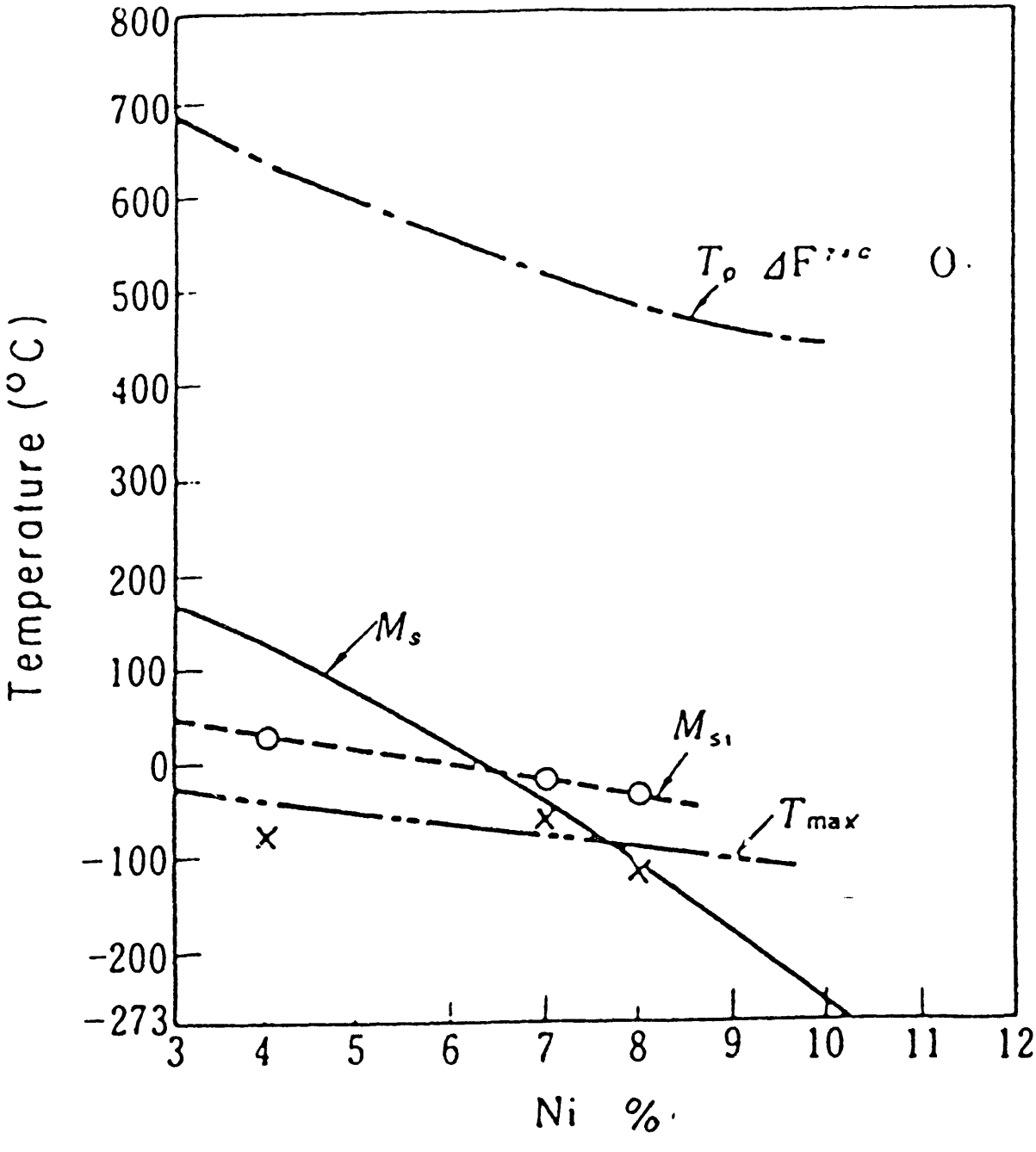

Figure 17.

Ref. 53

M_d (temperature at which no α' is formed at 45% true strain) = 0.23 M_s + 80°C/°C (55).

2.1.5. Intermetallic Compounds

The main compound that forms is sigma phase (see Figure 18). According to Honeycombe (24) and Pickering (46), the following characteristics are observed. Sigma is a tetragonal phase forming in the Fe-Cr binary system at about 25-60wt%Cr. Its formation is very slow requiring hours to form. Full development occurs at 750°C after 1500 hours (Figure 20). The presence of ferrite (rich in Cr) accelerates σ formation (because of higher diffusion rates), at α/γ boundaries below 600°C and then ferrite is known to dissolve preferentially as σ grows (56). Also ferrite forming elements, e.g. Cr and Mo, partition strongly to α-ferrite and accentuate sigma formation (57,58). The overall effect on properties is one of embrittlement involving a considerable lowering of ductility and toughness at room temperature. In a commercial duplex alloy Uranus 50, σ grows with time, Figure 20, and Mo stabilizes it, and allows it to form at temperatures in excess of 950°C (59). Sigma here is probably not a binary Fe-Cr, but a multicomponent phase containing molybdenum. Figure 18 shows the precipitation kinetics of σ and other intermetallics and carbide compounds. The deleterious effect of σ in such duplex steels has been reported by several investigators (60-63). Norstrom et al (60) have shown that in alloys containing 50-80 vol.% α, the transformation of only 1% of the α to σ reduced the room temperature toughness by 50%. A transformation of 10% of the α to σ reduced the toughness to only 5% of the value of the unembrittled structure.

There appears to be no relevant literature on the effect of PGMs on σ formation in Fe-based alloys. It remains in this study to establish any significant effects for alloys aged between 650-900°C. However, in nickel based alloys rich in Cr, it has been noted that PGMs do not increase the stability of sigma or other phases which are deleterious to mechanical properties (6).

Figure 18 also shows additional intermetallics in U50. Ageing at 600°C to 700°C for more than 6 to 10 hours results in the formation of chi (χ) phase. Chi phase, like σ, is brittle and is undesirable. It has an ordered cubic structure with a composition of $Fe_{36}Cr_{12}M_{10}$ (65). X-ray analysis has also revealed R phase (Fe_2Mo) which again is undesirable. Hochmann et al (66) only observed R phase in a study of U50.

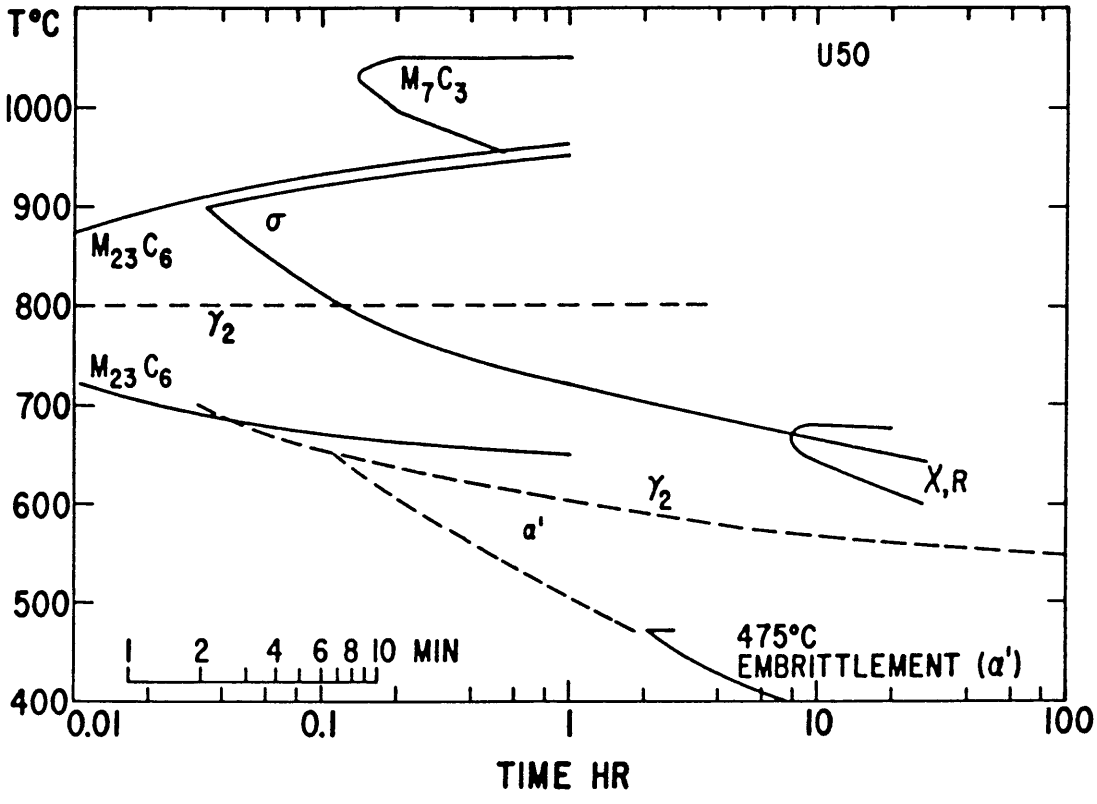

Temperature-time precipitation curves for various phases observed in alloy U50

Figure 18.

Ref. 59

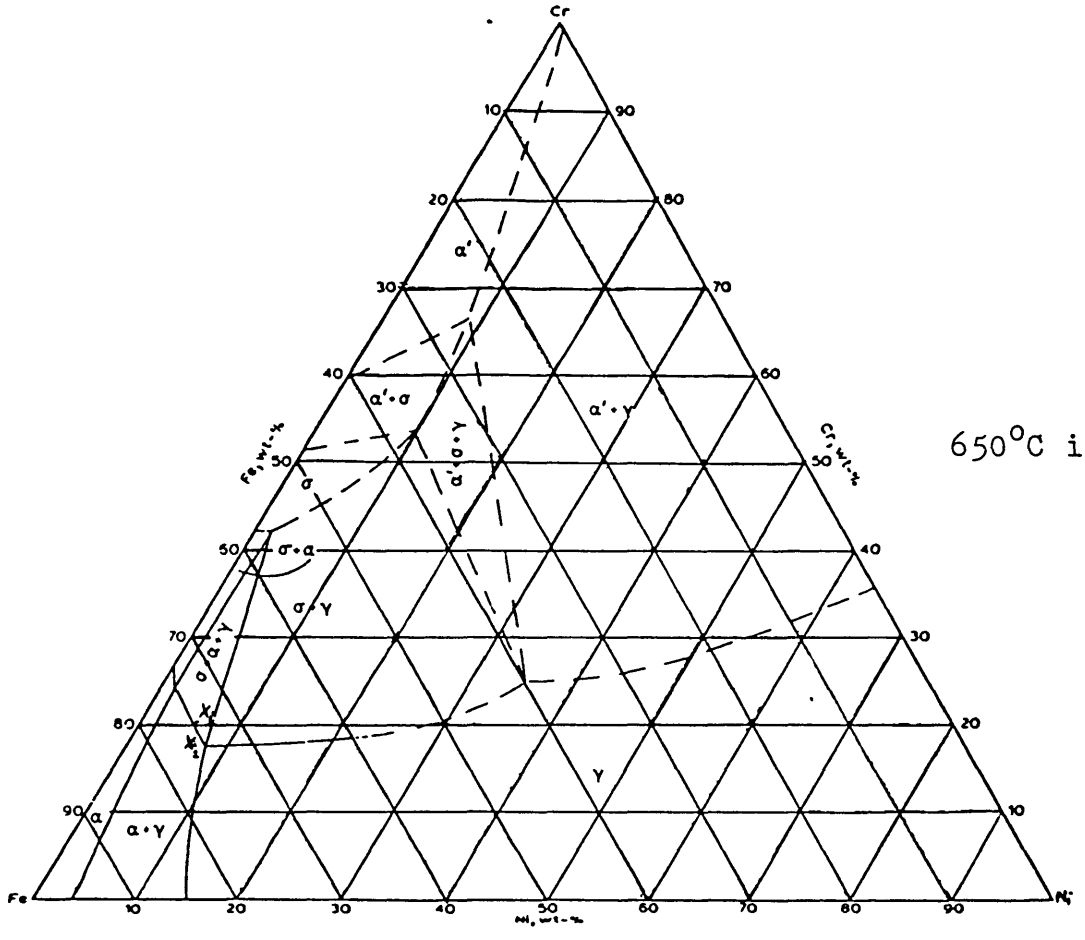

650°C isotherm

Ref. 9

Figure 19.

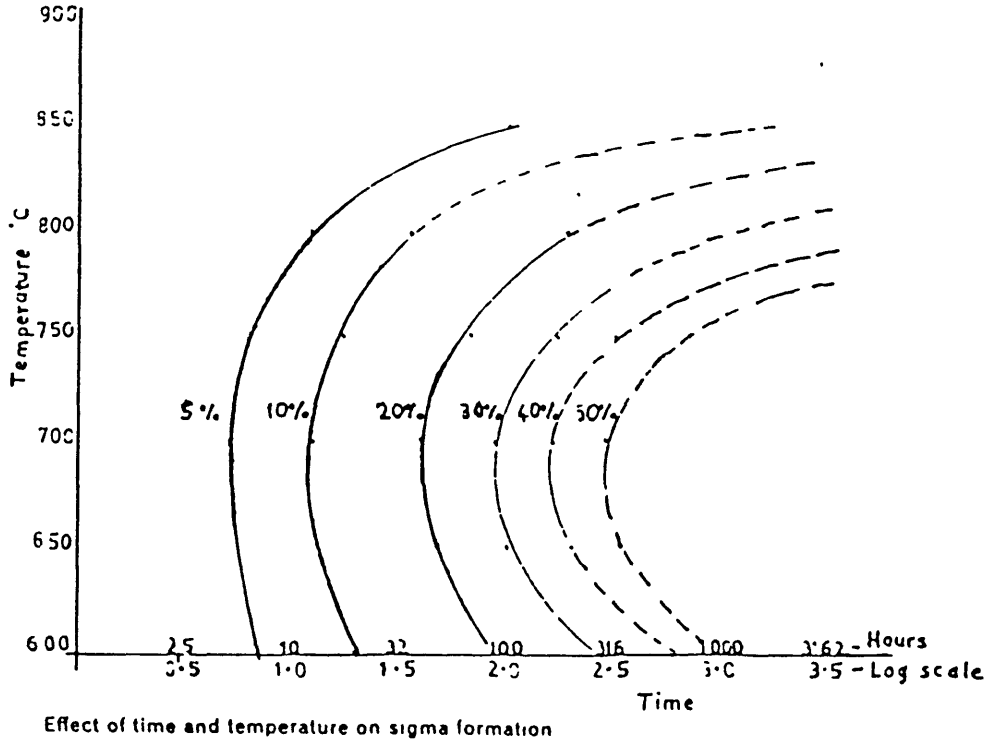

Effect of time and temperature on sigma formation

Ref. 64

Formation of sigma phase in a 26Cr:6Ni stainless steel

Figure 20.

The lowest temperature decomposition of the ferrite of a duplex stainless steel, is the transformation of $\alpha \rightarrow \alpha'$. The bcc α' precipitates are rich in Cr and give rise to the phenomenon of 475°C embrittlement in ferritic stainless steels (59). It has been shown (67) that in the α of the U50 alloy, a miscibility gap is present such that a spinodal decomposition at 475°C produces iron and chromium-rich regions, and that α' forms from these regions by 118 hours.

2.1.6. Carbide Formation

Carbon is inevitably present as an impurity even in nominally C-free alloys. Its high affinity for Cr makes carbide formation on extended ageing, highly probable.

Many studies have been carried out on carbide formation and precipitation in Fe-Ni-Cr stainless steels. For example, Hochmann et al (68) and Tedmon (69) report that on holding at temperatures below 1000°C, nucleation begins at the austenite-ferrite grain boundaries. As the temperature falls to 600°C, carbon solubility, which is low, reaches a value of approximately 0.005%C (70). This results in the formation of carbides on holding at temperatures of between 450-800°C, for carbon contents of up to 0.08% and 500-850°C for carbon contents of up to 0.03%C (70). If the concentration of stabilising elements such as Ti and Nb is low, then these carbides are always of the Cr-rich $M_{23}C_6$ type (71). They form preferentially at austenite grain boundaries and annealing twin boundaries. Occasionally nucleation may occur within the austenite grains (70,72). The morphology of these particles has been reported to be either polyhedral with $\{111\}_\gamma$ interfaces or cubic $\{110\}_\gamma$ interfaces, for those formed at grain boundaries (71).

Smith and West (71) observed $M_{23}C_6$ precipitation after annealing a solution treated semi-austenitic steel (14.9wt%Cr, 8.7wt%Ni, 0.09wt%C, 2.05wt%Mo), for 310 hours at 700°C. The occurrence of carbide precipitate in the 550°C-700°C range has been observed by Parshin and Vasil'kov (73) in Cr-Ni steels with 12-17%Cr and 2-6%Ni and about 0.05%C. A recent study by Beetge and Robinson (64) on a (25.27wt%Cr-6.20wt%Ni) duplex steel, did not reveal any carbide precipitation after annealing for times up to 258 hours in the temperature range 650°C to 850°C. This was probably due to the low carbon content of 0.026wt% used. Tedman and Vermilyea (74) noted that in specimens of 26.5Cr-6.6Ni duplex steel aged at 700°C, the carbide precipitation was confined to the austenite-ferrite boundaries. After a very short time the austenite-

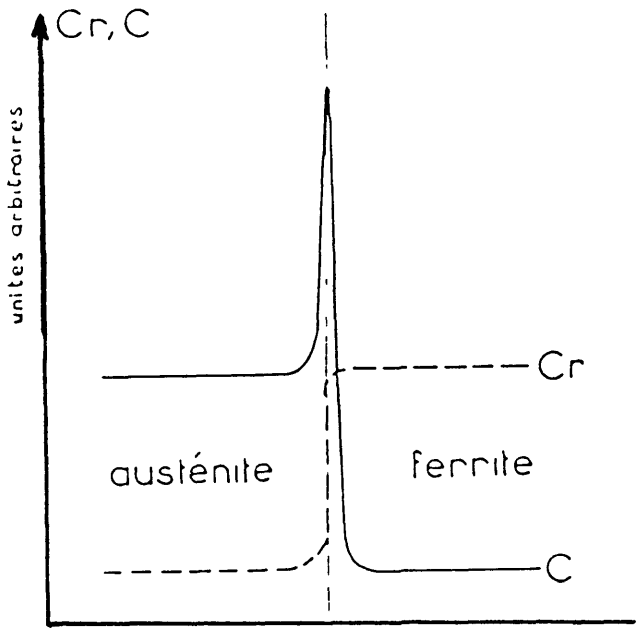

Figure 21. The partitioning of Cr and C across the γ/α boundary. Refs. 55,68

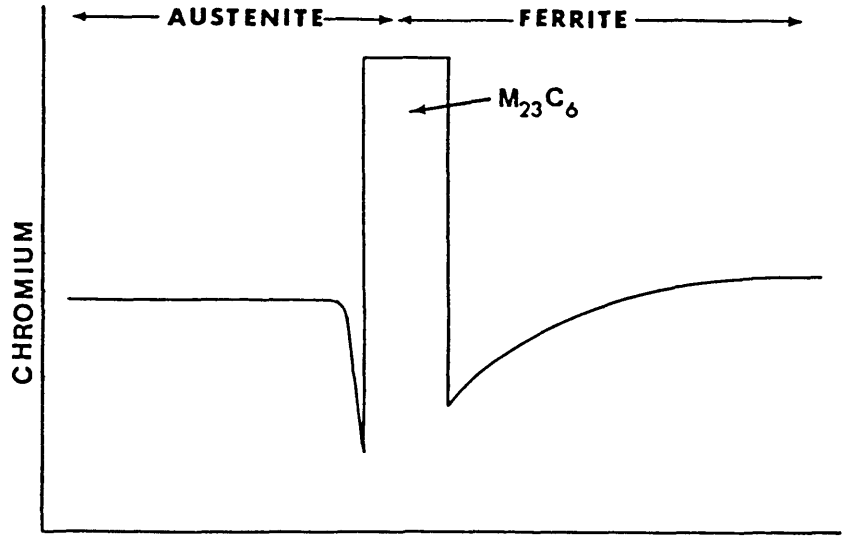

Schematic chromium concentration profile at an austenite-ferrite interface containing $M_{23}C_6$.

Figure 22. Ref. 59.

ferrite boundaries migrated towards the centre of the ferrite grains, effectively isolating the carbides from the boundaries. They suggested this separation of the carbides from the boundaries was the basis for the sensitization resistance of the duplex stainless steels. Devine (75) studied the carbide precipitation and sensitization of a heat of 308 duplex steel. Like Beckitt (76) Tedmon et al (74), Combrade et al (77) and Hockmann et al (78), Devine found that during isothermal treatments at 600°C the carbides first formed along austenite-ferrite boundaries. Also like Hochmann et al (78) he suggested that the chromium content of the carbides was largely supplied by the ferrite phase. He pointed out that because of the high activity coefficient of carbon in the ferrite phase, most of the carbon resides in the austenite phase. Consequently, after the initial amount of carbide precipitation the carbon content of the ferrite was exhausted. Continued growth of the carbides occurs by chromium from the ferrite phase reacting with carbon from the austenite phase. The result is a depletion of the carbon content of the austenite phase. Thus, before sufficient time has elapsed to permit carbide formation along austenite-austenite grain boundaries, the carbon content of the austenite phase is reduced to its limit of solubility. Figures 21 and 22 show these variations in chromium and carbon content across the austenite-ferrite interface. Figure 22 in particular refers to the model proposed by Devine (59). Most of the chromium in the carbide, is contributed by the ferrite phase. Consequently, a very wide chromium-depleted zone exists on the ferrite side of the interface. (Not identified by author in Figure 21). A very small amount of chromium is contributed by the austenite phase. This results in the formation of a very narrow but deep chromium-depleted zone on the austenite side of the interface. It is this narrow zone which is responsible for the sensitization of the duplex alloy. Because this zone is so narrow, it is quickly replenished by diffusion of chromium from the interior of the austenite grains, and is the reason for the rapid healing of duplex stainless steels (59).

2.2. Solidification Modes

In studying equilibrium phase structures it is pertinent to consider the as-cast structure of alloys, since equilibrium phase morphology and distribution are often dependent on the structure of the cast material prior to annealing. Further, the practical bearing of such phenomena in alloys, is that hot cracking or solidification cracking can occur in castings or weld metal, during solidification (59).

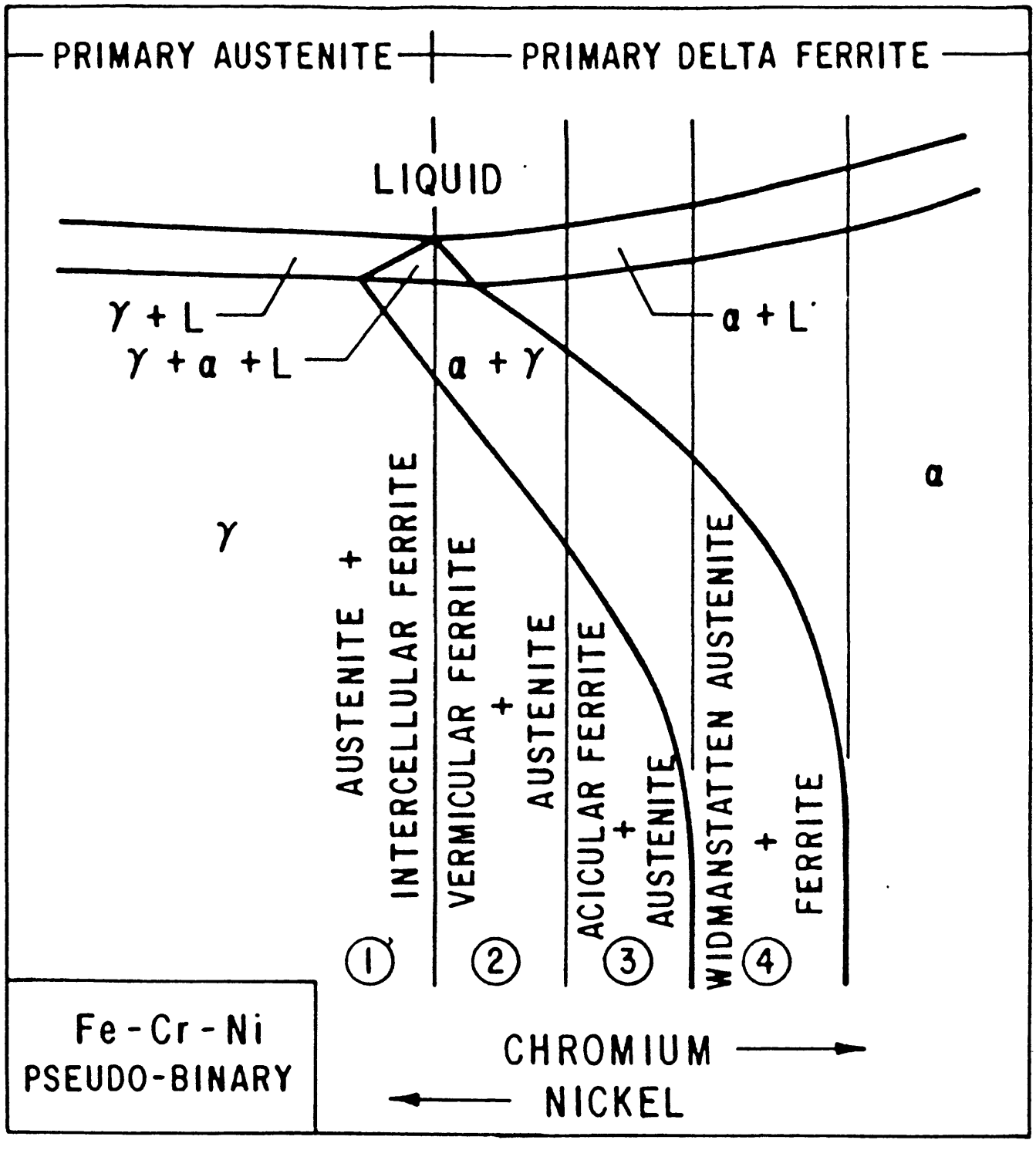

Schematic pseudobinary diagram for 70% Fe showing the structures developed in Fe-Cr-Ni alloys

Figure 23. Ref. 82

The presence of 5-10% ferrite in austenitic stainless steels is beneficial since it minimizes grain growth and reduces shrinkage stresses because of its smaller coefficient of thermal expansion, greater thermal conductivity and lower high temperature strength; all helping to reduce the tendency for hot-cracking (59). Notwithstanding this, recent studies (79-93) have established that it is the nature of solidification, which is important, not just the final ferrite produced, i.e. whether α or γ first precipitates from the liquid.

The influence of steel composition on solidification structures in Fe-Cr-Ni alloys has been studied by many authors (94-99), e.g. Hammer and Svensson (95), Suutala et al (98), Heriter (97) and Blanc (94). They report that when the effect of variables of composition and cooling rate on solidification mode are considered, it is alloy composition that is of primary importance. Figure 23 (from Lippold and Savage (82)) predicts the structure which will be developed for various Fe-Cr-Ni alloys. Since alloy composition is of primary importance, the Schaeffler Cr-equivalents and Ni-equivalents have been used as convenient parameters to predict solidification modes in these alloys. If the ratio of Cr-Eq/Ni-Eq < 1.5, solidification is as single phase γ, if > 2.0, it solidifies as a two phase α/γ , with single phase α predominating.

The different modes from Figure 23 may be described as follows:

1) Single phase austenitic solidification $L \rightarrow \gamma + L \rightarrow \gamma$
2) Austenitic-ferritic solidification $L \rightarrow \gamma + L \rightarrow L + \alpha + \gamma \rightarrow \alpha + \gamma$
3) Ferritic-austenitic solidification $L \rightarrow L + \alpha \rightarrow L + \gamma + \alpha \rightarrow \alpha + \gamma$
4) Single phase ferritic solidification $L \rightarrow L + \alpha \rightarrow \alpha \rightarrow \alpha + \gamma$

The term 'solidification mode' here, includes the solid-state changes since in (4), ferrite is the only phase formed during solidification but austenite nucleates after solidification preferentially at ferrite grain boundaries and grows into the ferrite as Widmanstatten plates.

In considering the effect of cooling rate on the mode of solidification, Pereira and Beech (96) report that in the 2 to 40°C s^{-1} cooling rate range, the changes in α-ferrite content were typically from 13 to 16% for a 19Cr/6-8Ni steel (Mode 4 solidification) and 5.5 to 8% for a 19Cr/10Ni steel (Mode 3 solidification). This emphasises that chemical composition has an over-riding effect and that cooling rate is of secondary importance with respect to solidification mode. Clearly, the addition of PGM's may have a significant effect on the mode of alloy solidification for

austenitic or duplex stainless steels. Whilst no literature exists on this, it is suggested that high levels of PGMs will favour an austenitic mode of freezing (modes 1 and 2), particularly Pt and Pd which are fcc, and thought to be strong austenite stabilizers (10-12).

2.3. Corrosion

2.3.1. General

The extremely low corrosion rate of stainless steels in many environments arises from their enhanced capacity for passivation. This is due to the formation of a protective oxide film formed on the metal surface insulating it from the corrosive medium. The function of chromium in these steels is to increase the probability of insoluble oxide formation and thus enhance stability of the film. Acid conditions tend to cause the destruction of the film while the presence of chloride can lead to local destruction with subsequent pitting (100,101).

2.3.2. Austenitic Stainless Steels

A great deal has been published on the general corrosion resistance of austenitic stainless steels (57, 101-104). These steels are very corrosion resistant in a wide range of corrosive media. Particularly, they have excellent atmospheric corrosion resistance, but chloride in marine environments causes a lowering of the corrosion resistance. Increasing the Ni content improves resistance to many organic acids and to H_2SO_4, while oxidizing media such as HNO_3 cause passivation. Mo is beneficial in improving the general and pitting corrosion resistance, and also improves the resistance to H_2SO_4 (104). In general, the higher the chromium content the better is the general corrosion resistance (46).

2.3.3. Duplex Steels

Where duplex stainless steels have replaced austenitic stainless steels, it is because of their superior corrosion and stress corrosion resistance (59). Figure 41 shows that these alloys are useful in highly oxidising environments, chloride environments and those containing H_2S. Duplex steels have therefore earned a place in chemical plants, in the pulp and paper industry, the oil and gas industry, in marine environments and in heat exchangers (59). The corrosion rate in such steels is established by the least resistant phase, but this could be either γ or α, depending upon the environment and composition.

In particular, if the Cr contents of the γ and α phases are significantly different and the aqueous environment is such that the corrosion potential of, e.g. the austenite phase is in its active region and that of the ferrite phase is within the passive region the alloy will corrode by either:-

1) Active dissolution of both phases
2) Passive dissolution of both phases
3) Active dissolution of γ and passive dissolution of α.

Which occurs depends on the precise nature of the polarization curves and the relative amounts of γ and α phases present in the duplex alloys (59).

Ageing treatments can have an adverse effect on corrosion resistance of a duplex alloy, which is thought to be due to α' (Cr rich bcc phase) formation (59) and σ (1) in the ferrite.

2.3.4. Pitting Attack

A comprehensive review detailing 270 papers is given by Shreir (105) on this subject. This form of attack being localised can be highly damaging and may result in the production of holes in some materials where local pitting is severe. Techniques for measuring pitting include electrochemical or ferric chloride immersion tests, where results are presented as either visible detection of pits or weight loss per unit area (1).

Both Cr and Ni alloying elements increase resistance to pitting. Additions of Mo also enhance pitting resistance (46, 106). Many duplex steels have considerable amounts of nitrogen included in the chemical composition, whose presence increases resistance to pitting although the mechanism by which this occurs is not clear (1). Investigations (107, 108) on commercial grades of γ and α stainless steels reveal that pit initiation occurs by the dissolution of soluble inclusion, e.g. MnS. In contrast, pits often initiate at the austenite-ferrite interface in duplex stainless steels (75, 109, 110). This is perhaps due to a high concentration of water-soluble sulfur compounds located at, or near the interface. Solomon and Devine (59) investigating Uranus 50 in 0.1 NHCl, illustrated that the low chromium and molybdenum containing γ_2 phase, which forms during the thermal decomposition of the ferrite phase (into $\alpha + \gamma_2 + \sigma$), also acts as sites for pit initiation.

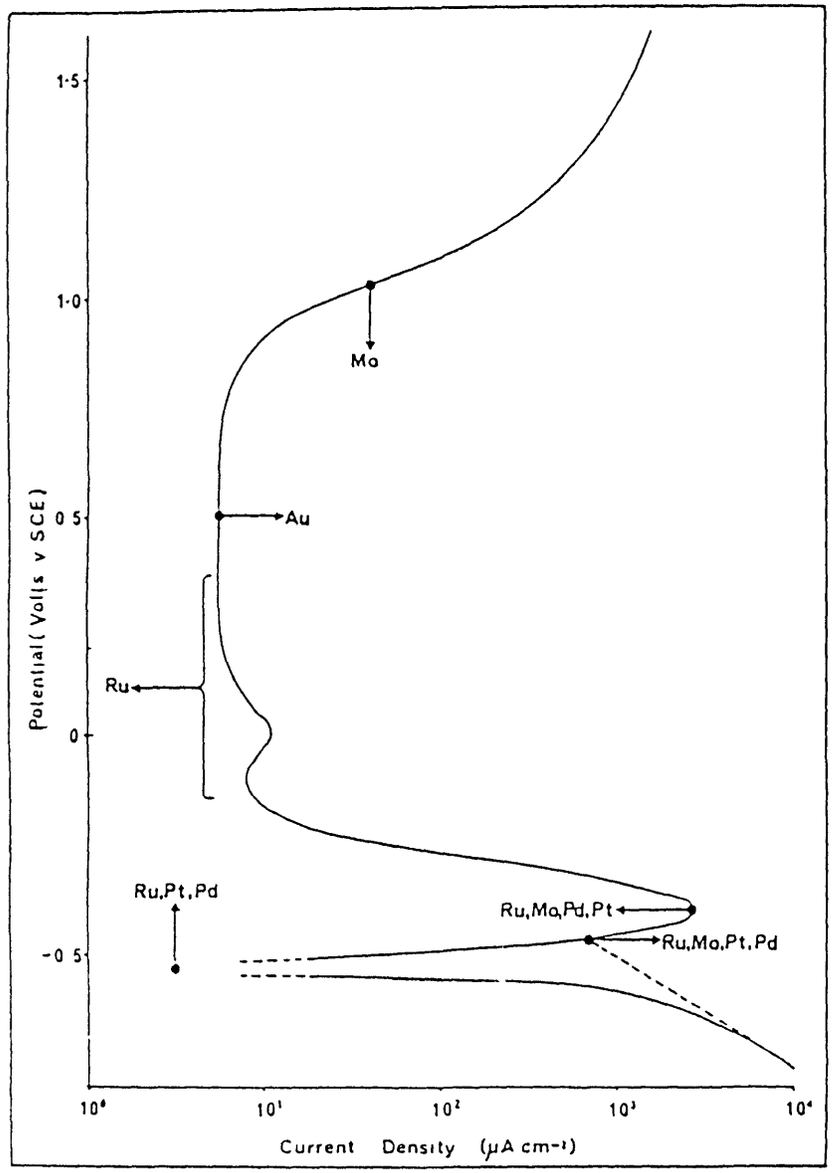

Summary of effects of alloy additions on polarisation characteristics of AISI 430 in N.H_2SO_4 at room temperature.

Figure 24. Ref.112

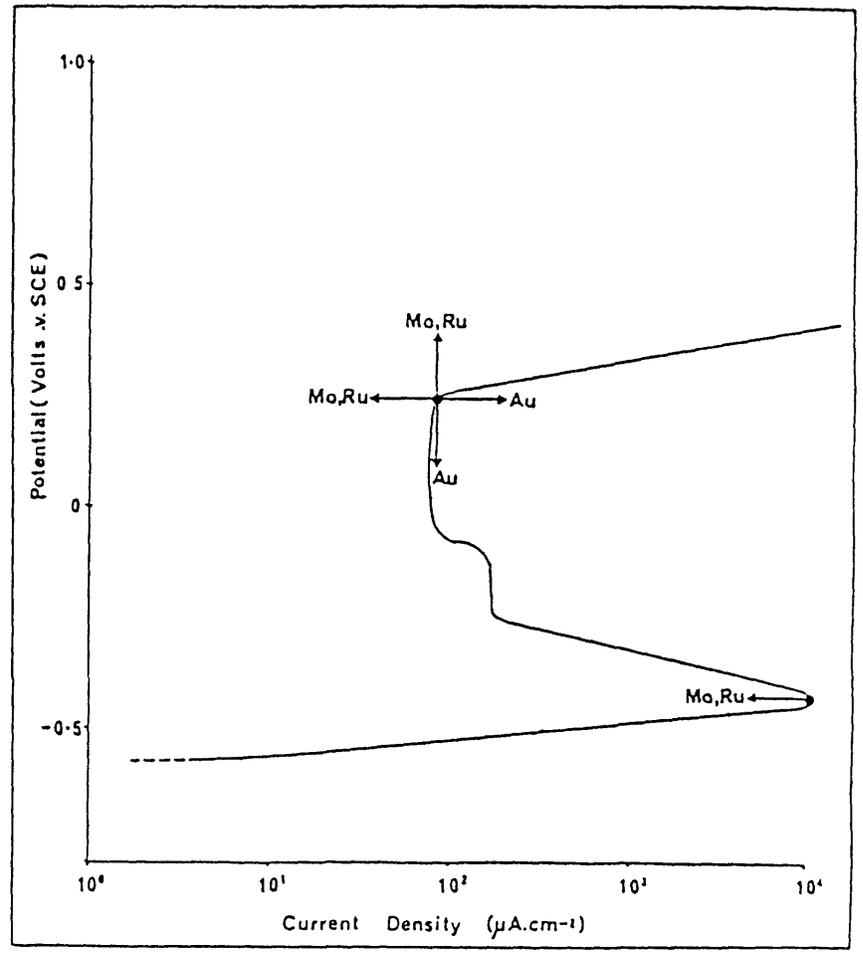

Summary of effects of alloy additions on the polarisation characteristics of AISI 430 in N.H_2SO_4 + 0.5N.NaCl at room temp.

Figure 25. Ref.112

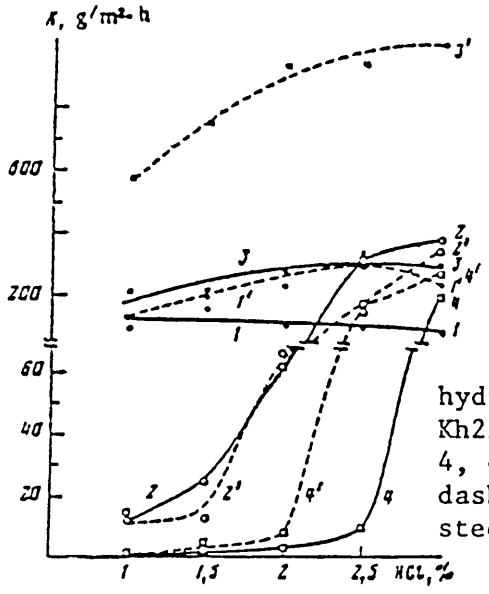

Corrosion rate g m^{-2} hr^{-1}

Figure 26.

Mean corrosion rates of steels in hydrochloric acid solutions at 80°C. 1, 1') Kh25; 2, 2') Kh25Pd 0.3; 3, 3') Kh25M2; 4, 4') Kh25MPd 0.3. Solid curves 1-4, 80°C; dashed curves 1'-4', 100°C. Test times: steels with Pd, 5 h; without Pd, 30 min.

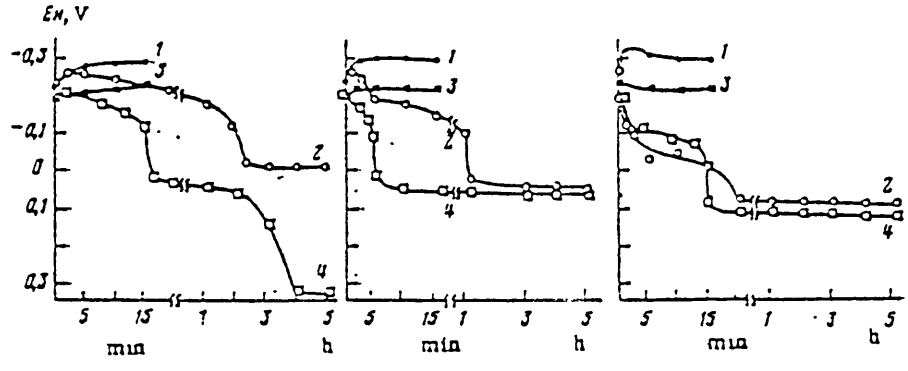

Potential—time curves in 3% HCl. 1) Steel Kh25; 2) Kh25-Pd 0.3; 3) Kh25M2; 4) Kh25M2Pd 0.3; a) 25°C; b) 50°C; c) 100°C.

Figure 27. Figure 28. Figure 29.

Ref.112

It should be remembered that the pitting potential is itself governed by the repassivation kinetics of the passive film, such that when the rate of hydrolysis is greater than the repassivation rate, pit initiation occurs.

The electrochemical corrosion behaviour of PGM modified steels has been exhaustively assessed by Gore (111, 112) (Figures 24 and 25 are typical). The effect of PGM's on pitting resistance has been determined by a number of Russian workers (113-125). Tests in HCl suggest that while palladium additions, for example, may increase the tendency of steels to pitting, they also broaden the range of acid concentration and temperature in which the steels are passive. Outside this range, however, palladium containing steels are found to have enhanced corrosion rates (112), Figures 26-29. The pitting potential is reduced with palladium additions, whilst corrosion potentials are increased, Figures 30 and 31. The rapid dissolution characteristics are obvious for the low palladium steels, while the increased passivation range for the 0.5%Pd steel is also apparent, with rapid depassivation occurring above 0.45NHCl, Figure 32. The passivity of the 0.5%Pd steel in 0.3NHCl is apparently maintained up to 100°C (125). Figure 30 further reveals that increased palladium additions decrease the time to passivation. This is also reflected in the corrosion rate diagrams, Figures 26-29.

2.3.5. General Effects of PGM Addition on Corrosion Properties

In 1911, Monartz (126) reported that the rapid corrosion of Fe-Cr alloys in certain acids can be supressed by adding Pt as an alloying element to the steel. Tomashov, Cherova et al, have studied effects over the past 30 years, of additions of Pt, and Pd, to chromium steels, (113-125), and report that with additions of typically 0.1-0.5%Pd to stainless steels, a substantial increase in corrosion resistance in acidic solutions is produced. This is due to the accumulation of Pd on the surface of the steel during its self-passivation (127).
In fact, to date, Pd has been the most frequently used PGM to produce passivity in steels (128). (These effects are supported by Biefer (129,130)). M.A. Streicher (128) reviews more recent work, and together with Tomashov et al (113-125) they report, with evidence from a Fe-28%Cr-4%Mo steel, that of the 6 PGM's, only indium, osmium and ruthenium can be used to produce passivity of stainless steels in sulphuric acid without lowering stress corrosion cracking resistance or impairing

Effect of Noble Metal Additions on the Corrosion of Fe28Cr4Mo(nominal)

Alloy Composition (wt.%)				Boiling 10% Sulphuric Acid		Pitting Corrosion		Stress Corrosion
Fe	Cr	Mo	Noble Metal	State	Corrosion Rate (mil/yr)	KMnO -NaCl[1]	$FeCl_3$[2]	Boiling $MgCl_2$[1](45%)
			PLATINUM					
bal	28	4	0.005	A	58000	R	R	-
			0.006	P	48	-	R	-
			0.008	P	39	-	R	-
			0.010	P	15	R	R	-
			0.030	P	6	R	R	R (NW)
			0.05	P	4	R	R	R (NW)
			0.10	P	2	R	R	-
			0.20	P	1	-	-	R (NW)
			0.30	P	2	R	R	-
			PALLADIUM					
bal	28	4	0.01	A	74000	-	F	-
			0.02	P	4	-	F	-
			0.05	P	2	F	F	-
			0.10	P	2	F	F	-
			0.20	P	1	F	F	R (NW)
			RUTHENIUM					
bal	28.5	4.5	0.015	A	62200	-	-	-
		4.0	0.017	A	-	-	R	-
			0.02	P	60	R	R	R (W)
			0.20	P	9	-	R	R (W)
			0.30	P	2	R	R	R (W)
		4.2	0.5	P[4]	3	-	R	F (17 hrs)
			0.75	P[4]	1	R	R	F
			1.50	P[4]	1	-	R	F
bal	26.0	1.0	0.02	A	-	F	F	-
		1.0	0.20	P	-	F	F	-
bal	27.0	3.0	0.02	A	-	-	-	-
bal	30.0	2.5	0.02	P	38	-	-	-
bal	28.5	4.0	0.01 +0.1 Ni	P	41	R	R	R (W)
			RHODIUM					
bal	28.5	4.2	0.005	P	14	R	F	-
		4.0	0.01	P	7	R	F	-
			0.1	P	1	R	F	R (NW)
			IRIDIUM					
bal	28	4.0	0.01	A	-	-	-	-
			0.01	P	112	R	R	-
			0.02	P	78	-	R	R (W)
			0.01	P	13	R	R	R
			OSMIUM					
bal	28.5	4.0	0.01	A	57800	-	-	-
		4.2	0.015	A	76600	R	R	-
		4.0	0.02	P	26	-	R	-
			0.1	P	65	R	R	R (W)
bal	28	4	NONE	A	52180	R	R	R

Notes: [1] 2% $KMnO_4$-2% NaCl 90°C R - no pitting, F - pitting

[2] 10% $FeCl_3.6H_2O$ 50°C with crevices R - no pitting, F - crevice corrosion

[3] R - resistant after 2400 hrs

[4] self-repassivating

Figure 30. Ref. 112

Alloy Type	HCl solutions/20°C			HCl solutions/50°C
	1%	2%	3%	1%
Cr-Mn-Ni-Mo	0·012	0·1	1·42	0·13
Cr-Mn-Ni-Mo-+0·2%Pd	0	0·26	0·15	0·11
Cr-Mn	41·4	70·3	97·0	163·9
Cr-Mn+0·2% Pd	4·4	212	282·3	15·4
Cr-Mn-Ni	4·6	8·06	10·22	24·3
Cr-Ni-Mn+ 0·2%Pd	0·035	4·3	36·9	0·35
Cr-Mn-Mo	13	16·3	17·9	90·9
Cr-Mn-Mo+ 0·2%Pd	0·073	2·0	12·9	0·38
Cr-Mn-Mo+ 0·2%Pd	0·036	1·6	7·0	0·68
Cr-Mn-Mo	5·6	12·5	12·0	64·4

Corrosion Rates (g m^{-2} hr^{-1}) of Various Steels in HCl Solutions

Figure 31.

Ref. 112

	0.3N HCl	0.45N HCl	0.6N HCl
0% Pd	Only passive 25°C	-	-
0.1% Pd	1 hr.	2-3 hrs.	Not
0.2% Pd	5 mins.	1 hr.	
0.5% Pd	< 1 min.	1 min.	Passive

Time to Passivation of Palladium-containing OKh25M3T Steel in Hydrochloric Acid Solutions at 100°C

Figure 32.

Ref. 112

resistance to pitting or crevice corrosion in oxidising chloride and bromide environments. Of these, ruthenium, because of its lower cost, offers the best combination of properties on a cost effective basis (106,131).

In contrast, it is known that platinum can considerably reduce the failure time of stainless steels in stressed corrosive environments (106). It increases the susceptibility to transgranular stress cracking in industrially pure steels (18%Cr-14Ni-0.2%N_2) already susceptible to this phenomenon (132). Also Pt additions, to this type of alloy, (typically 3wt%) have the effect of reducing the critical stress level, below which there is no danger of cracking, to essentially zero stress. Furthermore, it should be noted that the addition of PGM noble metals to stainless steels may result in the formation of microcathode sites on the surface stimulating cathodic reactions (hydrogen evolution) and thereby raising the anode potential of the metal (133). As suggested by Hoar (134) this is excellent if the addition gives an increase sufficient to cause passivation, but is highly deleterious if it does not, because then the rate of anodic dissolution is markedly increased by the potential rise.

2.3.6. Stress Corrosion Cracking

There have been many papers published on the subject of stress corrosion cracking (scc), (e.g. Tedmon (74) and Parkin (135)) which results in cracking in corrosive environments under a static load with little or no deformation (1,46). In austenitic stainless steels the effect is most pronounced in hot chloride solutions and takes the form of a brittle transgranular crack failure (46,136). Duplex stainless steels however, (e.g. FMN 0.06, 19.5Cr,8.7Ni, 2.8Mo) have a superior resistance to stress corrosion cracking than standard austenitic grades (1). Stress corrosion cracking is very substantially reduced by high contents of nitrogen and silicon at the expense of hot workability. In duplex steels though, superior resistance comes from a higher critical yield stress for cracking, even in severe environmental conditions such as boiling 42% $MgCl_2$ solution (1,59,100). Much of the stress corrosion behaviour of duplex stainless steels has been reviewed by Hochmann et al (137), Shimodaira et al (138) and Latanision et al (139). In summary, the duplex stainless steels appear to be fairly resistant to stress corrosion cracking in aqueous chloride ion media. The resistance to crack initiation may be due to a combination of two factors:

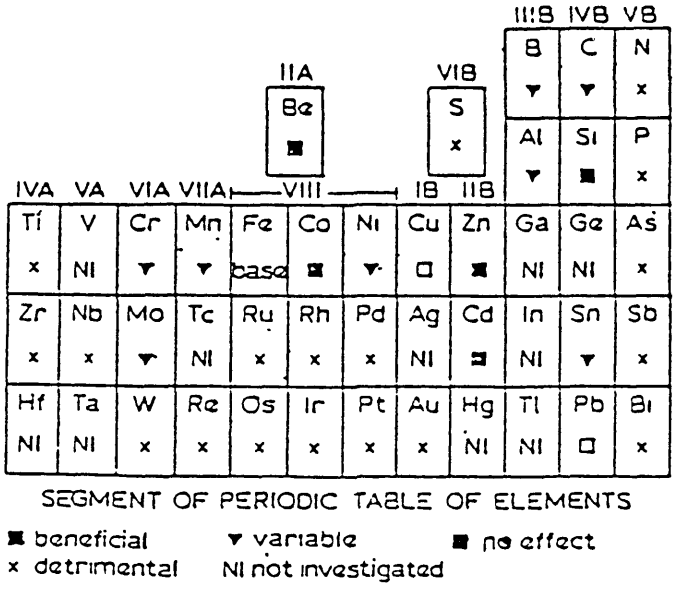

Effect of various alloying elements on resistance of austenitic stainless steels to SCC in chloride solutions

Figure 33. Ref.112

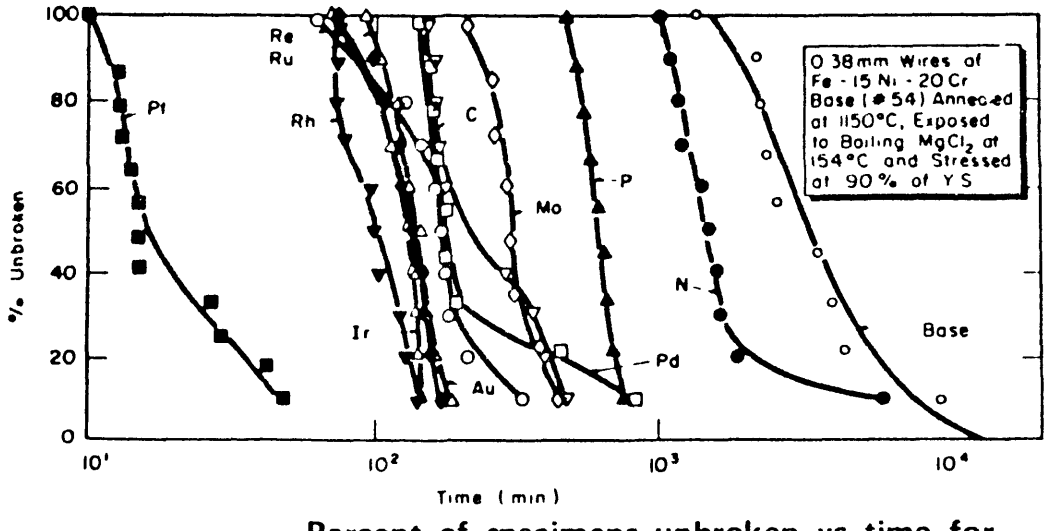

Percent of specimens unbroken vs time for fourth-component alloys in Group 2 having relatively rapid breaking times.

Figure 34. Ref.112

1) The region of severe chromium depletion is located at the γ/α interface, and
2) The ferrite phase is not heavily deformed until very high stresses are applied.

The resistance is reduced by high temperature, low pH, the presence of H_2S and high applied stresses (59).

2.3.7. Effect of PGMs on Stress Corrosion

Hannimen (140) has reviewed the effect of elemental additions on the SCC of austenitic steels. Figure 33 summarises these findings and indicates the detrimental effect of noble metal additions to such steels. These results, confirmed by Chaudron (141), show a progressive reduction in the life of an 18/10 steel in boiling $MgCl_2$ with increasing Pt additions.

%Pt	Life
0	6
0.1	3
1	1

Effect of Pt additions on the life of stressed 18/10 stainless steel in boiling $MgCl_2$ solution.

Streicher (142) however, tested a Fe28%Cr4%Mo steel with 0.5%Ru in NaCl solution up to 200°C and found no loss of resistance and recording lives up to 1400 hours without cracking. The NaCl test is claimed to be a better guide to service performance than the more often used $MgCl_2$ test in which the same alloy failed in less than 15 hours. The failure of the material is found to be due to transgranular cracking. Van Rooyan (131) suggests that platinum tends to induce this failure in industrial purity steels, though in very pure austenitic steels, the tendency is towards intergranular cracking, especially in high nickel steels. Staehle et al (143) investigated the SCC performance of an Fe-15Ni-20Cr alloy with 1.5% additions of Ir, Pd, Pt and Ru in boiling $MgCl_2$. Figure 34 clearly shows the detrimental effect of these elements. The mode of failure of these noble alloys was predominately intergranular.

Further electrochemical studies by Staehle (143) were made on the corroding/cracking sample wires. The open circuit potentials of the alloys during stressed exposure to boiling $MgCl_2$ solution were recorded for alloys containing noble metals. Just before fracture the potentials of the samples were found to rise rapidly and peak before failure.

The noble metal additions were found to accelerate the reduction kinetics in $MgCl_2$, Figure 34. Neilson (144) suggests this behaviour is due to hydrogen entry and its permeation kinetics. As PGMs increase the hydrogen exchange current, i_0, the extra hydrogen evolved would enter the stressed austenitic lattice, and increase the tendency to cracking. The tendency to intergranular cracking may be explained by the increased passivity of the bulk material restricting dissolution except at the grain boundaries at which there would be relatively little noble metal, and faster transport of hydrogen.

Montuelle et al (145) investigated high purity 18/8 steels with 0.1% platinum addition and again observed a dramatic reduction in life (1000 hrs to 50 hrs) when exposed to boiling $MgCl_2$. Similarly a 1% addition to an 18%Cr14%Ni alloy reduces the critical stress at which the alloy is susceptible to SCC to virtually zero. It has been generally assumed that the cold worked dislocation structure is related to the SCC phenomena, in that a planar dislocation structure leads to stress corrosion susceptibility, while a cellular structure is thought to be resistant. The addition of platinum, however, to the 18Cr-14Ni steel (which on working generates a cellular dislocation network and is resistant to stress corrosion) makes the steel susceptible but retains the cellular structure thought to be immune.

2.4. Oxidation

2.4.1. General

The large number of investigations of oxidation behaviour of ternary Fe-Cr-Ni alloys has been reviewed by Wood (146) and Yearian et al (147). Selection of this system in oxidising environments is based on the following propositions (147-149).

1) The external scale should consist of chromic oxide possibly containing some iron or nickel, or both.
2) Internal oxidation of the alloy should be absent as far as possible.

Wood and Hobby (150) have studied the oxidation of these Fe-Ni-Cr alloys at 800-1200°C. They are protected by a Cr_2O_3-healed scale, which thickens slower than on the corresponding binary Fe-Cr and Ni-Cr alloys. The scale adhesion as on Ni-Cr alloys is generally good after long times, at least partly due to the convoluted alloy-oxide interface, and in some cases to large intergranular Cr_2O_3-rich stringers.

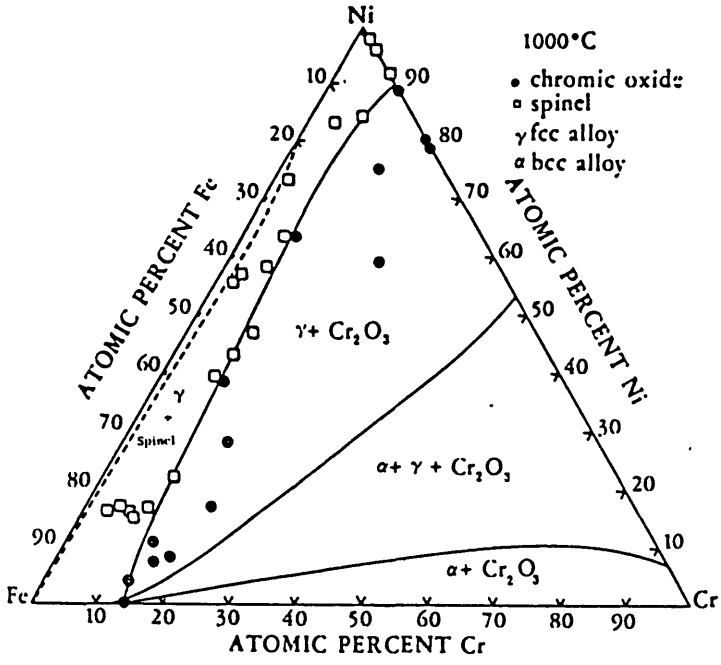

The section of the iron–nickel–chromium–oxygen phase diagram at 1000°C and a constant oxygen concentration approximating the limit of oxygen solubility in the alloy matrix, showing the oxides in equilibrium with the various alloy compositions.

Figure 35. Ref. 151

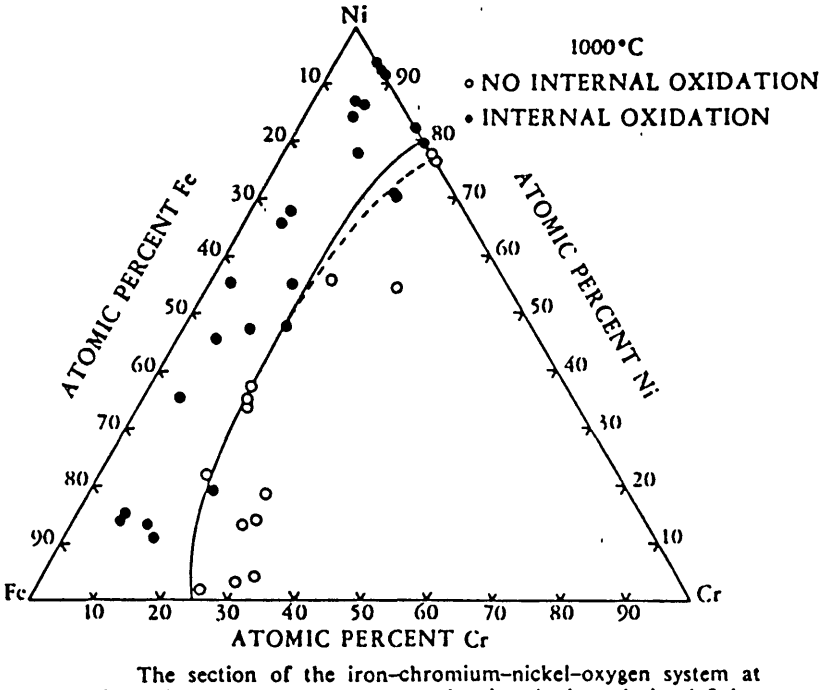

The section of the iron–chromium–nickel–oxygen system at 1000°C and constant oxygen content, showing the boundaries defining the limit of stability of chromic oxide (solid line) and the appearance of internal oxide in these alloys (broken line).

Figure.36. Ref. 151

The section of the iron-chromium-nickel-oxygen system at 1000°C, relevant to the present work, is shown in Figs. 35 and 36 from Croll and Wallwork (151). The important feature of this diagram is the critical chromium concentration required at the alloy-oxide interface in order to maintain chromic oxide as the stable oxide. This critical concentration reduces from 14at% in Fe-Cr alloys to about 7at% for an alloy whose interface composition is about 7at%Cr, 70at%Ni and 23at%Fe, and on further nickel addition, increases again until 10at%chromium is required for nickel-chromium alloys.

2.4.2. Effect of PGMs

Very little information is available on the oxidation of Fe-based alloys containing PGMs. However, Chaudron (141) tested an experimental 18Cr-12Ni alloy with 3% platinum in superheated steam at 500°C, 710 psi for 1000 hours and discovered a much reduced weight gain over the platinum free alloy (9 $mgdm^{-2}$ against 111 $mgdm^{-2}$). Similarly, a 1% platinum addition was found to improve the oxidation resistance of an 18Cr-10Ni steel by ≃20%, (in steam 600°C, 995 psi. for 6 days), while 0.1% addition had no effect. Saller et al (152) investigated platinum and palladium additions up to 20% to Fe25Cr5Al alloys, with a view to improve strength without loss of oxidation resistance. Both metals had a beneficial effect on stress rupture strength, but below 5%, they had little effect on oxidation resistance (1200°C). Above this, platinum increased the weight gain of the alloy substantially, palladium continuing to have only minor effects.

Assessment of the short term, cyclic oxidation of a 18Cr-15Ni steel with noble metal additions has been made by Truman and Pirt (153). Three alloys of interest containing 0.2% Ir, 1%Pd and 1%Pt showed that whilst Pd and Pt additions conferred limited oxidation resistance, the Ir alloy showed an improvement in oxidation over a commercial 18%Cr steel. However, the mechanism of this enhancement of oxidation resistance remained unexplained. A further study on cyclic oxidation by Htun (154) on an experimental duplex alloy, 18Cr-6Ni, showed a resistance to spalling with a 2%Pt addition, but negligible improvement of overall resistance to oxidation at 1000°C, was obtained.

2.5. Mechanical Properties of Duplex Steels

2.5.1. General

As previously mentioned, the useful combination of properties in these steels is derived from the two phase ($\alpha + \gamma$) structure. The mechanical properties of an ($\alpha + \gamma$) duplex steel reflects the mechanical properties of the individual ferrite and austenite phases, particularly the ferrite phase (59). The effect of ferrite content on yield strength, ductility and impact strength are shown in Figure 43 for a composition of 0.05C, 23Cr, 3Mo with varying nickel content (1). Material was rolled to small diameter bar form, so that the minor phase was elongated as stringers, and treated at 1120°C followed by water quenching. Similar behaviour is reported by Floreen and Hayden (155,156), and is shown in Figures 37-40, 42. Figure 37 in particular shows the strengthening due to the presence of 50-60% ferrite (Heat A) compared to austenitic and ferritic alloys with a similar composition as α and γ phases in Heat A. The yield strength is between that of austenite and ferrite but closer to the ferrite yield strength than a simple law of mixtures might predict. Strengthening is believed to be due to a finer grain size associated with the duplex alloy (156). However, the mechanism by which the increase in strength arises, has been debated. Irving et al (157) consider that a combination of four effects is involved: (1) solution hardening of the austenite due to enrichment in carbon and nitrogen. (2) Grain refinement due to a mixed structure. (3) A fibre strengthening effect of the ferrite stringers, and (4) dislocation generation because of differences in expansion coefficients of austenite and ferrite phases. While of possible relevance, these cannot provide the full explanation as strengthening continues up to 100% ferrite and a major feature would thus appear to be solid solution hardening of the ferrite phase by the substitutional elements. Notwithstanding this, Floreen and Hayden (155,156) established that the yield strength (and fatigue strength) of their duplex alloys followed a Petch (158) relationship, i.e.

$$\sigma_y = \sigma_o + k_y d^{-\frac{1}{2}}$$

where σ = yield strength, d = grain diameter and σ_o and k = constants. The Petch slope, K_y, for the yield strength was found to be greater for the duplex steel than for ferritic or austenitic alloys.

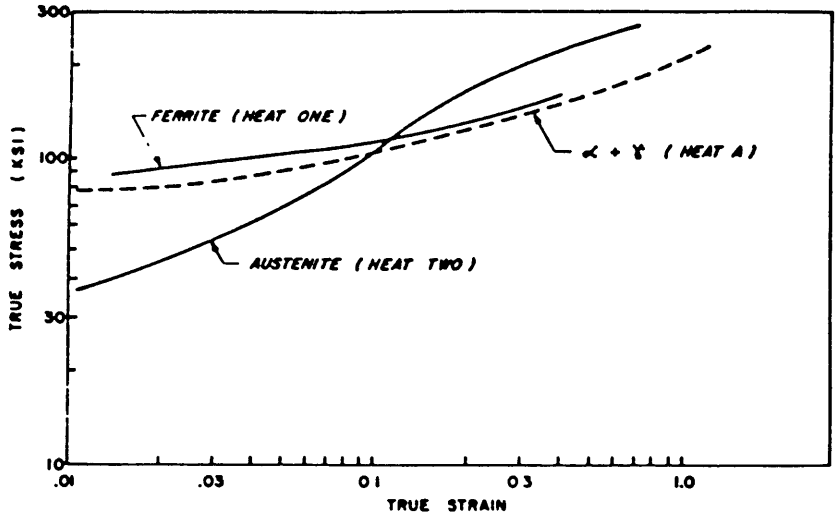

True stress-true strain behavior of a duplex alloy, containing 50-60 wt% α, compared to that of the α and γ phases of the alloy

Figure 37. Ref. 155

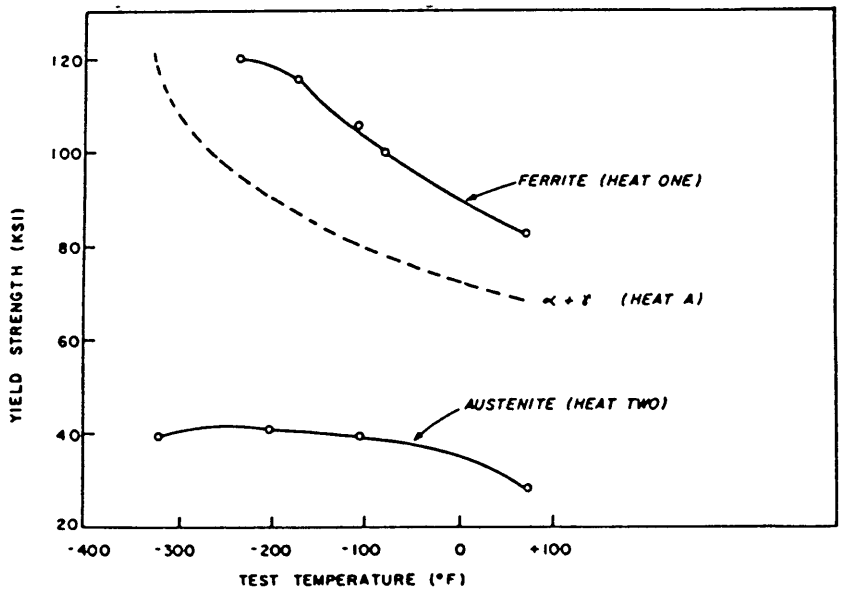

Comparison of the temperature dependence of the yield strength of a duplex alloy, containing 50-60 wt% α, compared to that of the α and γ phases of the alloy

Figure 38. Ref. 155

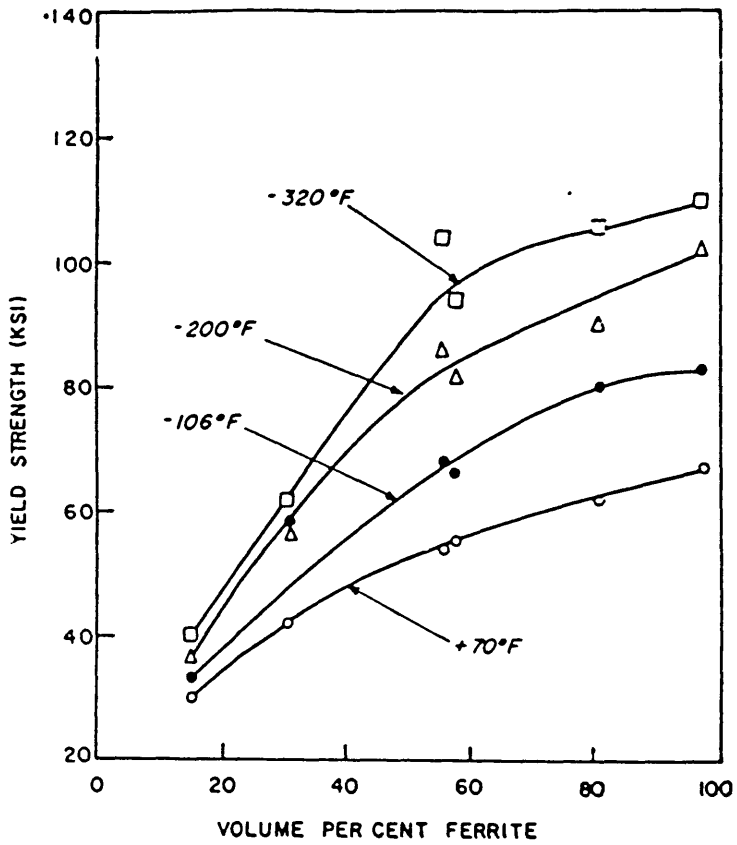

Ferrite dependence of the yield strength of duplex stainless steels

Figure 39. Ref. 155

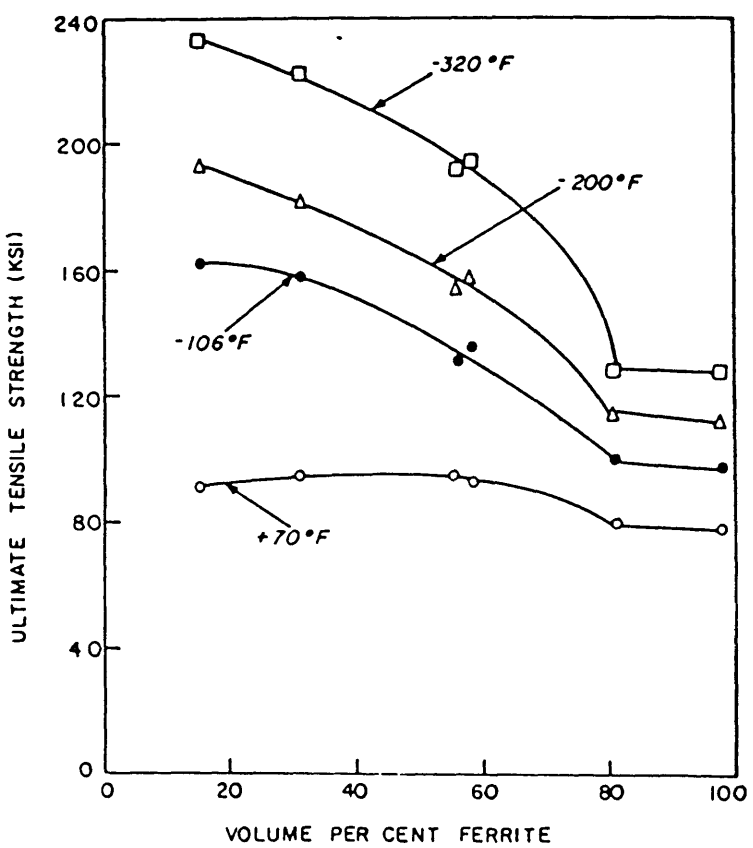

Ferrite dependence of the ultimate tensile strength of duplex stainless steels

Figure 40. Ref. 155

2.5.2. Temperature Dependence

The adverse effects of high ferrite content on toughness are readily understood being due to the brittle low temperature nature of the phase, Figures 43, 44. Figure 38 illustrates that the temperature dependence of the yield strength of the ferrite rich duplex steel parallels that of the pure ferrite heat. Figure 40 shows a decreasing UTS with increasing ferrite content and increasing temperature in these alloys. Floreen and Hayden (155) also found that the amount of martensite formation, which greatly influences the amount of work hardening, was decreased as the proportion of austenite in the duplex alloys decreased. In 80% ferrite alloys the constraint of the stronger α phase (particularly at low temperatures), prevented martensite formation in the austenite, thereby lessening the work hardening of γ and the σ_{UTS} of the duplex alloy. At room temperature, these factors reduce the σ_{UTS} of alloys with greater than 80% α to below the 304 type steel. The higher ferrite containing alloys also reveal a reduced ductility due to cleavage fractures. Alloys with increasing ferrite content and decreasing temperatures also had reduced ductilities.

2.5.3. Toughness and Fracture Behaviour

In the alloys studied by Floreen and Hayden (155,156) the development of cleavage fractures in the ferrite phase not only reduces the ductility it also greatly reduces the toughness, thus raising the ductile-brittle transition temperature shown in Figure 42. The orientation and morphology of the duplex structure is important in determining impact properties; not least because the austenite phase acts to prevent the propagation of cleavage cracks (155,156). Impact tests in Figure 42 were made with the crack propagation transverse to the banded structure of α and γ. The γ bands were therefore effective as crack stoppers, providing there was enough γ to ensure that long transverse α regions did not exist. Solomon and Devine further report a strong orientation dependence of toughness (59). The room temperature toughness of a duplex steel, Uranus 50, containing about 30-35% α, was 2.5 times greater for specimens where the crack growth was perpendicular to α and γ bands compared to specimens where the crack propagation was parallel to these bands.

2.5.4. Effect of PGMs

No systematic investigation of the effect of noble metals on the mechanical properties of Fe-based alloys appears to have been made,

TENSILE PROPERTIES, PRODUCT FORMS AND RECOMMENDED ENVIRONMENTS FOR SOME DUPLEX STEELS

Alloy*	R.T Tensile Properties** (Annealed Condition) σ_y (MPa) (.2%)	σ_{uts} (MPa)	ϵ_f %	Available Product Firms*** (Partial List)	Recommended by Manufacturers for Use in the Following Environments**** (Partial List)
Ferralium 225	480 (min)	740 (min)	20 (min)	Sheet, Strip, Plate, Bar, Wire, Tubing Pipe, Billet and Welding Wire	Sulfuric acid, phosphoric acid, nitric acid, organic acids, scrubbers/or SO_2 removal, feed water heaters for brakish water, marine applications, desalination, pulp and paper applications, oil and gas applications, surgical implants, copper smelting.
7 Mo	565	683	31	Pipe, Tubing	Nitric acid, polythionic acid, organic acids, pickling tanks, pulp and paper applications, heat exchangers.
U50	315-440	590-800	20-25	Plates, Sheets, Bars, Wire, Frogings, Castings (U50M)	Sulphuric acid, phosphoric acid, H_2S, dilute chlorides, heat exchangers, natural gas and nuclear applications, marine applications, pulp and paper applications.
3RE60	450	700-900	30	Pipe, Tubing (Seamless and Welded), Bar Strip, Plate	Heat exchangers, brakish water, pulp and paper applications, oil and gas applications, chemical plants, nuclear applications.
SAF 2205	410-450	680-900	25	Pipe, Tubing (Seamless and Welded) Plate, Sheet, Bar	Nitric acid, phosphoric acid, acetic acid, oil and gas applications, vinyl-chloride production, polyethylene production, chloride-bearing cooling water, desalination
DP3	390 (min)	585 (min)	18 (min)	Tube, Sheet	Fornic acid, acetic acid, H_2S, oil and gas applications, marine applications, heat exchangers.
44LN	450 (min)	700-900	25(min)	Plate, Pipe, Tubing	Sulfuric acid, phosphoric acid, nitric acid H_2S, oil and gas applications, desalination, hot brines, chemical plants.
UHB 119	620(min)	830(min)	15(min)	Plate, Bar, Castings	Water, steam and mildly corrosive environments, water turbines, chemical plants

* See Table I

** Not necessarily typical of commercial heats and should not be relied upon as representative for the purpose of applications. Actual values will depend upon the exact composition, heat treatment and processing schedule, product form and thickness

*** See manufacturers for a more complete and accurate list, including thickness and section size

**** Recommendations of the manufacturers not necessarily the authors. This is a partial list, see the manufacturers literature for a more complete list, including exact environments and temperatures.

Figure 41. Ref. 59

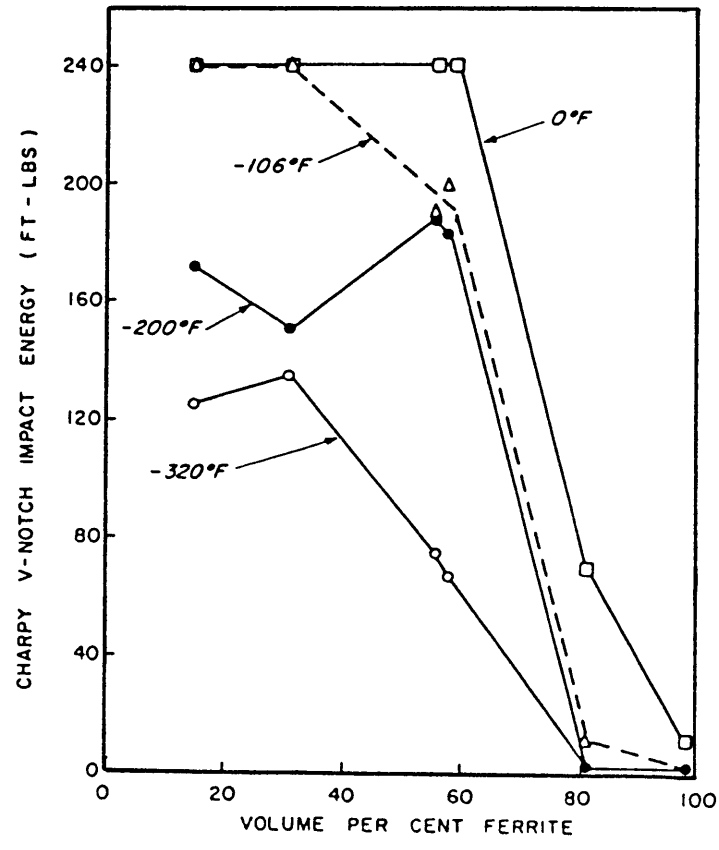

Ferrite dependence of the impact energy of duplex stainless steels

Figure 42. Ref. 155

Effect of ferrite content on Mechanical Properties.
Alloy Composition-0·05C,23Cr,3Mo,and varying Ni wt%.

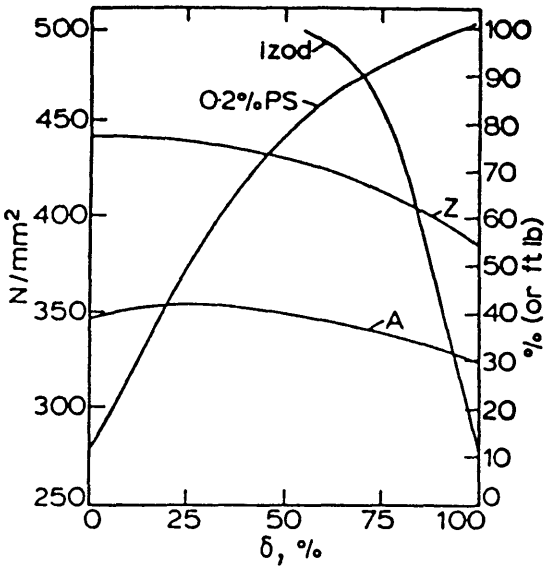

Figure 43. Ref.1

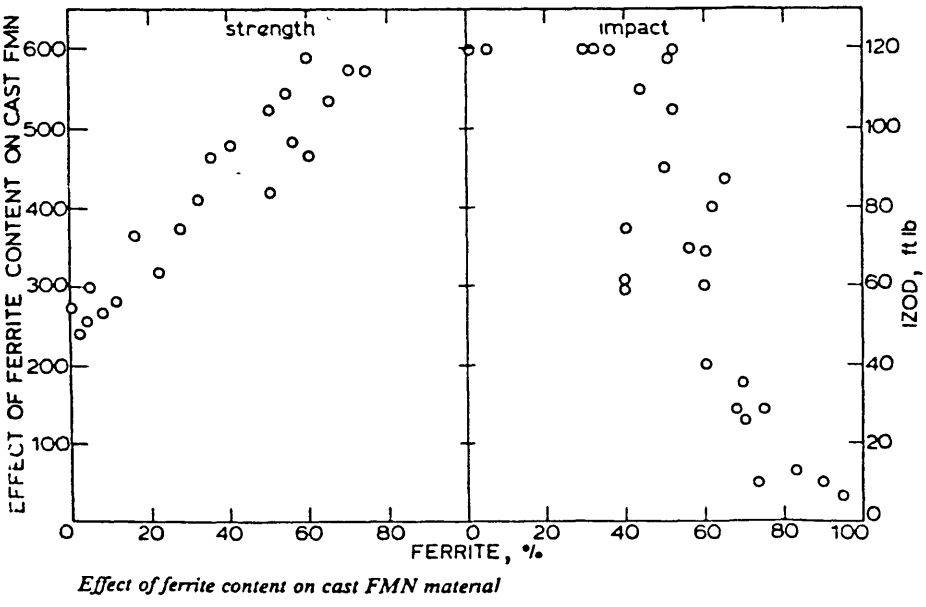

Effect of ferrite content on cast FMN material

Figure 44. Ref.1

Alloy Composition-0·04C,25Cr,5Ni,2Mo,0·2N_2wt%

though several workers have determined various mechanical properties of experimental alloys, often to assess required loading for subsequent stress corrosion testing. These properties are listed in Figure 45 (112). The additions of PGM to these alloys seems to generally increase the strength and hardness by small amounts with a concomitant decrease in ductility. Much of the data in Figure 45, however, is difficult to assess in this respect due to variations in other alloy constituents.

The effects of noble metals iridium, rhodium, ruthenium and platinum on the toughness of various iron-carbon alloys were determined by Floreen and Hayden (159). Each PGM alloying element significantly improved the toughness. The results support the general correlation that substitutional alloying elements are beneficial to toughness by lowering the ductile brittle transition temperature (160-162). However, the reasons for these improvements are not clear.

2.5.5. Hot Workability

Early studies suggest that two-phase stainless steel alloys exhibit poor hot workability (163) but Gibson et al (164) demonstrated that the difficulties are not inherent in the two-phase structure. Merrick et al (165) made a detailed study of the structural features affecting the hot workability of duplex steels; results show:

a) Edge cracking during hot rolling in the duplex range occurred at a C-content of about 0.03% and increased in severity as the C-content increased and also with increasing amounts of the austenite phase.

b) Cracks were observed at the α/γ interfaces: precipitation of $Cr_{23}C_6$ occurred in the same interfaces. The precipitation of $Cr_{27}C_6$ has been reported to result from the decomposition of high Cr ferrite into lower Cr (cellular) austenite and carbide.

c) Working in the single phase α-ferrite region and also in the duplex region of an alloy with a large amount of nickel to stabilise austenite, produced improved hot workability.

d) Increasing the titanium content of an alloy resulted in improved hot workability. The titanium was added to combine with carbon to form TiC, and reduce the carbon level available for the formation of $Cr_{23}C_6$ as well as reducing the volume fraction of the carbide.

The conclusions are that it is the precipitation of $Cr_{23}C_6$, not the duplex phase distribution which causes poor hot workability.

Mechanical Properties of Noble Metal Modified Alloys.

Steel	Noble Metal Addition	UTS (MPa)	0.2% Proof Stress (MPa)	Elongation %	Impact Strength $kg.m.cm^{-2}$	Vickers Hardness	Ductile/ Brittle Transition Temp.(°C)
Fe15Ni20Cr	-	344.75	99.98	14.0	-	-	-
	1.5% Pd	382.67	141.35	14.5	-	-	-
	1.5% Pt	355.09	153.76	14.5	-	-	-
	1.5% Ru	389.57	126.87	15.6	-	-	-
	1.5% Ir	439.90	168.93	17.8	-	-	-
Fe25Cr7Ni1.5Mn2MoN	-	-	970	57	-	-	-
	0.2%	-	1137	55	-	-	-
Fe22Cr8MnN	-	-	1108	56	-	-	-
	0.1%	-	902	50	-	-	-
	0.2%	-	931	48	-	-	-
	0.3%	-	1000	52	-	-	-
	0.4%	-	1010	55	-	-	-
	0.54%	-	1059	56	-	-	-
Fe26Cr5Ni8MnN	-	-	1029	59	-	-	-
	0.22%	-	1078	59	-	-	-
	0.27%	-	1059	56	-	-	-
	0.4%	-	1068	51	-	-	-
	0.49%	-	1010	38	-	-	-
Fe22Cr8Mn2MoN	-	-	1019	50	-	-	-
	0.1%	-	1137	56	-	-	-
	0.2%	-	980	34	-	-	-
	0.3%	-	1059	41	-	-	-
	0.4%	-	1078	49	-	-	-
	0.5%	-	1078	51	-	-	-
		-	1157	43	-	-	-
	0.2%	-	1137	51	-	-	-
Kh25N6M2G2A	-	-	970	57.4	-	-	-
	0.2% Pd	-	1137	54.6	-	-	-
Kh25N6M3G2A	-	-	784	56	-	-	-
	0.2% Pd	-	823	-	-	-	-
Kh25N6G2A	0.2% Pd	-	980	53.4	-	-	-
Kh25N6M3	-	-	676	25.6	-	-	-
	0.2% Pd	-	676	26.4	-	-	-
Kh25	-	402	304	63	10.5-30.7	156	20
	0.2%	460	372	55	8.7-13.2	170	0
Kh25M2	-	509	411	56	1.5-12.0	197	50
	0.2%	559	470	54	3.9	207	50

Figure 45. Ref. 112

Hot Ductility as a function of ferrite content for various forged Cr-Ni steels in the longitudinal direction.

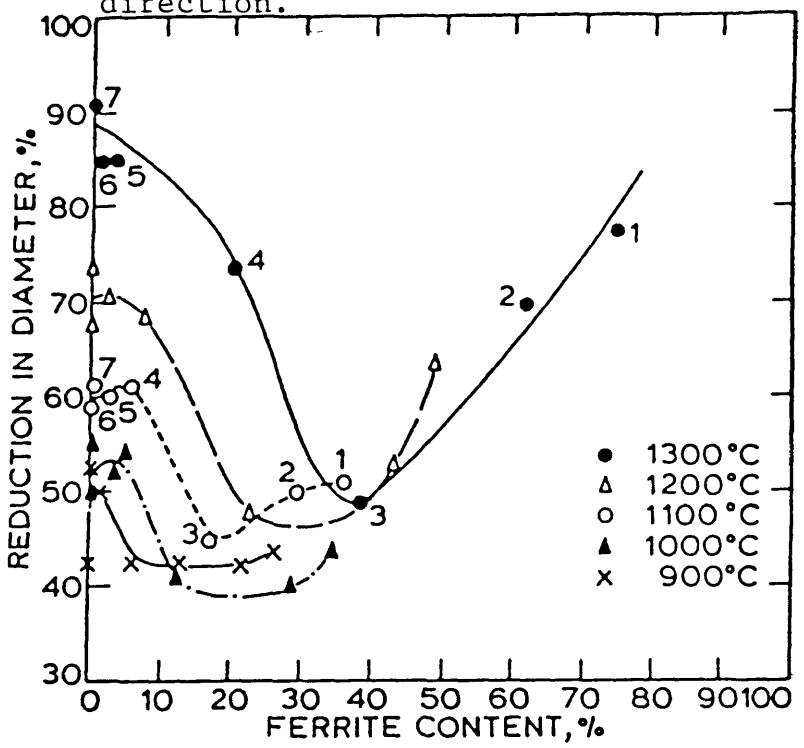

Figure 46.

Ref. 170

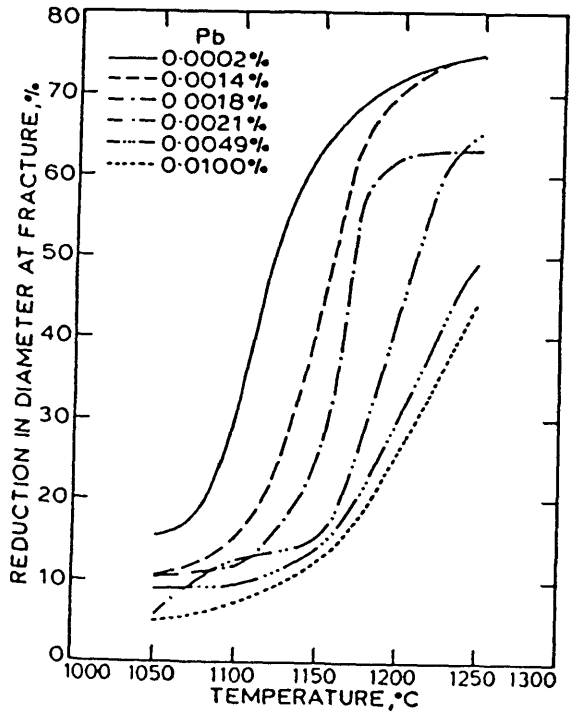

Influence of lead on hot ductility of 7Cr—13Ni—1Mo steel; as-cast material;

Figure 47.

Ref. 171

It is proposed that duplex alloys with 25-27%Cr and 6-7%Ni base composition will have good hot workability for carbon contents $\leq$0.03%. If the C-content increases then titanium should be added according to the relationship Ti = 4(C - 0.03) + N wt%.

The hot working of a duplex stainless steel involves several other variables, e.g. fraction and geometry of the ferrite, the relative strength and ductility of austenite and ferrite etc. (166). These are reviewed by Jarvinen (167) who suggests that ductility reached a minimum for a certain fraction of ferrite at about 0.15 - 0.35 in Figure 46. Although in general, a deleterious effect of δ-ferrite is found, a positive effect has been observed by Kane (168). Kane (168) associates the positive effect of δ-ferrite with the observed corrugation of γ/γ boundaries, in the presence of ferrite, which are resistant to crack propagation. In addition, Kane (168) found that the γ/δ boundaries acted as nucleation sites for recrystallisation and that cracks formed at the δ/γ boundaries were short and non-propagating. Further explanations of crack formation in duplex steels being hot worked, are those concerning the differences in softening processes and strengths of ferrite and austenite phases. Karling (169) suggests that soft areas of ferrite along austenite grain boundaries will increase the sliding along such boundaries. This seems to be relevant to rupture, as long as no precipitation occurs at δ/γ interfaces. Skuin et al (170) found that cracks in an ingot start in the columnar zone below the surface, and that the acceptable amount of δ-ferrite decreases with increasing tensile stress components in the working process (Figure 46). It was also noted that the ductility of duplex stainless steels is very sensitive to some trace elements during hot working, Figure 47. Gittins et al (172) claim that 50 ppm Pb, in a 71Cr-4Ni steel with some N, yields a virtually unworkable alloy material; Figure 47. They have also shown that the precipitation of carbonitrides in the ferrite has a strong influence. A uniform dispersion of the precipitates gives a high ductility, while a more non-uniform distribution, makes the steel less ductile.

The influence of the morphology of the ferrite-austenite mixture is especially important at low working temperatures (166). By forming a very fine mixed structure (microduplex), some Fe-Cr-Ni alloys, e.g. 36Cr-6Ni, 25Cr-7Ni - Mo-Nb and 26Cr-7Ni-7Ti steels, show a superplastic behaviour at low strain rates near 900°C (173,174). Such alloys also show good hot workability.

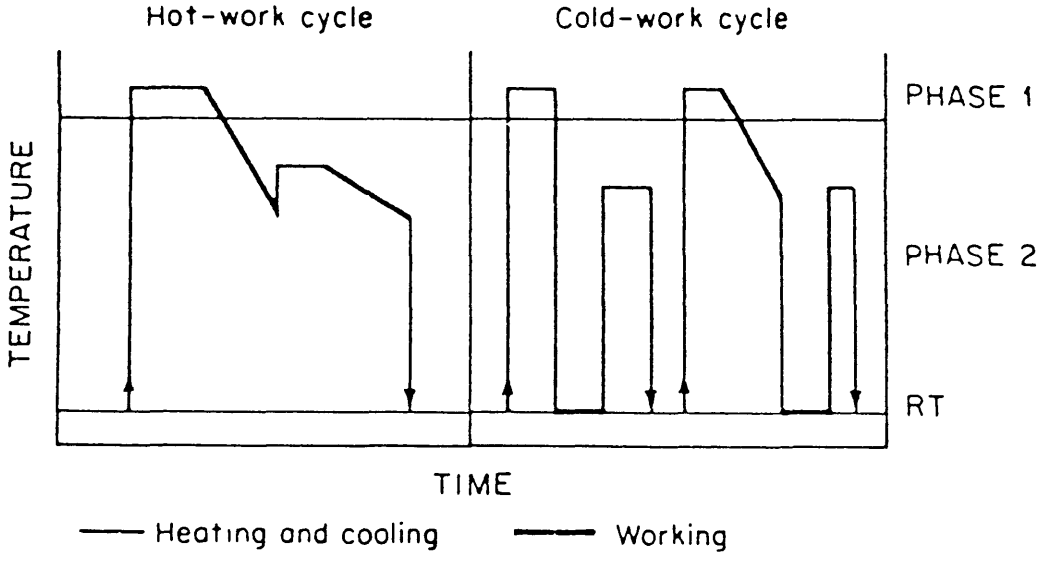

Thermomechanical treatments used to produce a microduplex, superplastic, stainless steel

Figure 48. Ref.59

The presence of α and γ phases is further significant since it can make the steel deform superplastically at the hot working temperature. This behaviour has been shown to exist in duplex steels, and is characterised by large amounts of neck free elongation provided there is no carbide induced cracking (175-178). Hot working is typically at 1000°C producing a microduplex structure (59): the γ aids the development of this structure by preventing α grain growth. Figure 48 illustrates some of the thermomechanical treatments that have been used to produce microduplex superplastic steels. Hot working in the $\alpha + \gamma$ region results in γ precipitation accompanying recrystallization (158,164,177,178). Cold working prior to ageing can also produce a microduplex structure. In this case the cold work results in γ precipitation in the $\alpha + \gamma$ region prior to recrystallization.

2.6. Deformation Induced Structures

Comprehensive studies into the structural inhomogeneities in deformed duplex steels have received limited attention - indeed there have been very few investigations concerning duplex alloys where both phases are deformed with strain (180). Blickarsk (181) however examined a two-phase ferrite-austenite steel (0.007C-25.5Cr-6.6Ni-0.27Mn-0.22Si) of coarse grain structure after 23, 43, 85% deformation induced by rolling at room temperature and the results are summarised as follows:

a) In ferrite after deformation <5%, Neumann bands form whereas at heavier reductions, the deformation takes place more homogeneously. Bands of increased dislocation density parallel to {110} planes, appear in the dislocation structure. With increasing deformation the dislocation density in the bands, increases, and the spacings between the bands, decreases.

b) The shear bands formed in ferrite differ considerably from those formed in single phase ferrite structures. Their formation is induced by the presence of austenite in the ferrite matrix.

c) The austenite deformation structure is formed in a similar way to the structures in fcc materials of low stacking fault energy. Initially austenite is deformed by slip only. For deformations in the range 20-40%, intensive twinning takes place, whereas for reductions above 40%, shear bands are formed.

d) Inhomogeneous deformation of austenite near the interphase boundaries is accommodated by ferrite, whereas inhomogeneous deformation of ferrite is accommodated by other ferrite regions adjacent to the interphase boundary.

e) In the course of plastic deformation, austenite hardens much more rapidly, and its hardness is always higher than that of ferrite, independent of the deformation level.

Martensite transformation within γ was not reported.

The deformation of these duplex steels also induces martensite formation within γ-austenite, of which there are 3 main morphologies, namely, lath, surface and plate (182). (Lath martensite is often associated with an hcp ε-martensite.) Surface martensite as its name implies is not formed in the bulk. The transformation morphology depends on the M_s temperature, the yield strength, the alloy composition, and the stacking fault energy (SFE) of the metastable austenite. The effect of composition was demonstrated by Breedis (182) for duplex alloys of decreasing Cr and increasing Ni contents. As chromium replaced nickel, the martensite morphology changed from lath to plate for quenched alloys. Similar morphologies are reported for strain-induced martensite (183). It is reported (184,185) that the effect of low stacking fault energy is to restrict slip to the stacking fault shear system which favours lath formation. The effect of SFE on the formation of the hcp ε-martensite as well as the sequence of transformation to α'-martensite has been widely investigated with conflicting reports (182,186-189). Breedis (182) suggests that the SFE must be zero for ε-martensite to form. Otte (186) and Cina (187) report that ε-martensite does not form in alloys quenched to -196°C or deformed at ambient temperatures if the (Ni + Cr) content of the alloy is less than 24-28%. More recently, Lecrosiey and Pineau (189) have reported on the martensitic transformation induced by plastic deformation in various alloys of three types: Fe-30Ni, Fe-20Ni-7Cr, and Fe-16Cr-13Ni with carbon contents up to 0.3%. The Fe-16Cr-13Ni alloy formed ε-martensite at low strains; the (Ni + Cr) content was not less than 28%, and in fact the SFE was found to be $22 J/m^2$. The investigation by Lecrosiey (189) also shows that the formation of ε-martensite is favoured at low temperatures and strains. At temperatures not favouring the formation of ε-martensite, deformation induced α'-martensite (lath morphology) can occur without the earlier occurrence of ε-martensite.

The early occurrence of ε-martensite has led to the proposal that it is a transition stage to the formation of α'-martensite. However, Breedis (182) has suggested that ε-martensite forms only as a result of shape changes that accompany the $\gamma \rightarrow \alpha'$ transformation by the introduction of intrinsic stacking faults on alternate $(111)_\gamma$ planes.

2.6.1. Deformation Induced Strength

Laptev and West (190) studied the deformation and annealing behaviour of some 300 series stainless steels. Alloy hardness increased progressively with increasing amounts of deformation at the same temperature or at a lower temperature (between M_d and M_s) at the same level of deformation. Similar results have been reported by Bowkett and Harries (188). The hardness dependence on α'-martensite formation decreases at increasing levels of deformation at the same temperature. The change in hardness is marked for the same level of deformation at different temperatures. Further increase is achieved by the work hardening of the austenite; this effect becomes greater at lower temperatures. A deleterious effect of α'-martensite formation is a decrease in ductility. This may be offset by high strength levels and the TRIP (transformation induced plasticity) effect (24), if the α'-martensitic content is optimised, such that there is a marked increase in uniform ductility prior to necking. The effect of strain-induced martensite for the development of TRIP steels has been illustrated by Wasaka (191,192) using two phase ($\gamma + \alpha$) alloys. The TRIP effect is characterised by a peak in plots of uniform elongation vs. testing temperature in tensile tests. Wasaka reports that α'-martensite serves to delay the onset of necking. An important feature of the TRIP effect is that it is associated with the formation of twin-related laths, and it is most significant when the tensile direction is parallel with the rolling direction. Maxwell et al (193) have shown that the effect occurs over a narrow range of temperature in steels in which plate-like α'-martensite occurs.

CHAPTER THREE

EXPERIMENTAL PROCEDURE

Thus I set pen to paper with delight,
And quickly had my thoughts in black and white,
For having now my method by the end,
Still as I pull'd, it came; and so I penn'd it down:
Until it came at last to be,
For length and breadth, the bigness which you see.

(J. Bunyan: Pilgrim's Progress)

3.1. Preparation of Materials

Two separate routes were used for the production of alloys. In route 1, 14 alloys were prepared by melting and casting ≈30g melts in an argon arc furnace. The compositions were determined by electron probe microanalysis, EPMA, using X-ray energy dispersive spectrometry, and are shown as follows in Figure 49:

Figure 49. Analysed Alloy Compositions - wt%.

S1	19.2Cr - 5.8Ni - Fe bal.
S2	18.6Cr - 5.9Ni - Fe bal.
S3	21.0Cr - 6.3Ni - 2.0Pt - Fe bal.
S4	21.2Cr - 6.2Ni - 7.9Pt - Fe bal.
S5	18.7Cr - 5.7Ni - 2.2Pt - Fe bal.
S6	18.3Cr - 6.1Ni - 8.1Pt - Fe bal.
S7	20.6Cr - 6.2Ni - 2.1Ru - Fe bal.
S8	21.5Cr - 5.8Ni - 8.2Ru - Fe bal.
S9	18.4Cr - 5.8Ni - 2.0Ru - Fe bal.
S10	18.5Cr - 6.0Ni - 8.0Ru - Fe bal.
S11	20.8Cr - 6.0Ni - 2.2Pd - Fe bal.
S12	21.0Cr - 5.9Ni - 7.8Pd - Fe bal.
S13	18.8Cr - 5.9Ni - 1.8Pd - Fe bal.
S14	18.9Cr - 6.0Ni - 8.1Pd - Fe bal.

Each value is an average of 3 separate area analyses, with an accuracy of ±0.4 wt%.

The purity of the elements used in this study are shown in Figures 50 and 51.

Figure 50. Fe, Ni and Cr Purity

Components	Composition/wt% (Purity)							
Fe (route 1)	C	Si	Mn	P	S			
	0.02	traces	0.08	0.02	0.015			
Fe (route 2)	C	Si	Mn	P	S	Cr	Mo	Ni
	0.016	<0.016	0.12	0.06	0.007	<0.01	<0.005	0.02
Uranus 50	C	Si	Mn	P	S	Cr	Mo	Ni
	0.026	0.46	1.6	0.031	0.088	20.60	2.45	6.62
Cr	electrolytic - 99.9							
Ni	carbonyl shot							

Figure 51. PGM Purity

Pt	Pd	Ru
99.98 ppm	99.7 + PGMs → 99.9 ppm	99.9 ppm
Fe - 5 max Zr - 1 max Pb - 1 max Sn - 1 max	Cu - 300 Ca - 100 Fe - 100 Al - 200 B - 50 Mn - 10 Si - 100 Ni - 50 Pb - 100 Ag - 300 Sn - 50	Pt - 20 Pd - 10 Ir - 10 Rh - 20 Os - 350 Al - 3 Cr - 2 Cu - 3 Fe - 70 Mg - 3 Mn - 1 Ni - 7 Si - 10 Ag - 1 Ca - 3

Before any experimental deformation or heat treatments were carried out, portions of alloys S1-14 were hot rolled at 700°C down to ≈1-2mm.

In route 2, three duplex alloys: 21Cr-6Ni, 21Cr-6Ni-2Ru, 21Cr-6Ni-2Pd, and an alloy with a composition equivalent to the commercial Uranus 50 were prepared by melting and casting 1 kg melts in an induction furnace. The ingots were subsequently soaked for 24 hours in argon at 1250°C, hot rolled at 1000°C to ≈6mm, and water quenched. Portions were cut from these lengths for the preparation of corrosion specimens. The remaining lengths of sheet were further hot rolled at 1000°C to ≈4mm. Final cold rolling produced sheet material of 0.5mm ± 0.04 thickness. All temperature measurements were made with a Pt-Rh thermocouple to give an accuracy of ±3°C within the furnace hot-zone.

3.2. Deformation and Heat Treatments

Alloy samples from route 1 were homogenised by annealing at 1250°C, being sealed in silica capsules containing high purity argon, and then rapidly quenched in water. Annealing times ranged from 24 to 70 hours. Slices of 1250°C solution treated material were further annealed at 1000°C and 1300°C. Alloy sheets hot rolled at 700°C were additionally treated for times and temperatures as above and air cooled. Sheet material, solution treated at 1250°C was then rolled at ambient and liquid nitrogen temperatures up to 80% by a series of small reductions; typically 5%. The percentage of γ-austenite transformed to α'-martensite was determined by measuring the percentage of ferromagnetic phase using a Sucksmith (194) magnetic balance and determining the volume fraction of γ-austenite and α-ferrite from a point counting method.

Alloy samples for ageing were prepared from cold-rolled material in route 2. These lengths were solution treated at 1250°C for 30 minutes in argon and 1 cm sq coupons were subsequently cut. These coupons were further sealed in argon in silica capsules, and aged between 650°C and 950°C for times of 5 minutes to 5 days, and water quenched. After metallographic preparation, the coupons were electrolytically etched at 6 volts in saturated KOH solution which satisfactorily stained the α-ferrite, σ-sigma, and γ-austenite phases, grey, black and white respectively, for phase identification. The volume fraction of α-ferrite transformed to σ-sigma was then determined by point counting.

Tensile deformation was carried out using an Instron tensile testing machine. Flat specimens were stamped out parallel to the rolling direction from sheet material in route 2. Dimensions were: Thickness = 0.5 mm ± 0.04; width = 6.19 mm; Gauge length = 22 mm. All tensile specimens were solution treated at 1250°C for 30 minutes in silica capsules containing high purity argon. Additional tensile specimens were either treated in liquid nitrogen or aged for selected times and temperatures. After these treatments, thermal oxide was removed from surfaces using a descaling solution of 15% HNO_3, 1%HF, and 84%H_2O, the samples being immersed for up to 15 minutes at 65°C. All tensile tests were performed at a strain rate of $3.79 \times 10^{-4} s^{-1}$.

For all solution treated and rolled material, samples were polished to 1 micron diamond paste and the hardness measured on a Vickers machine using a 10Kg load. Average values were obtained from at least two specimens using a minimum of six indentations.

3.3. Microscopy

Samples for light microscopy were polished down to 0.25 micron diamond paste. A variety of etching techniques were used:
1) A combination of Vilella's reagent and $FeCl_3$ in HCl and H_2O was used to reveal as-cast structures of alloys S1-14 by swab-etching.
2) Electrolytic etch; using a combination of 10% oxalic acid (for grain boundary delineation) and saturated NaOH solution (for grain contrast), at 6V for times of up to 1 minute.
3) Electrolytic etch using a combination of 10% oxalic acid and saturated KOH solution at 6 volts to highlight σ-sigma grains in aged specimens.
4) For alloys S4, 10 and 6 a semi-electrolytic polish was necessary to produce a satisfactory etch.

Conditions were: Electrolyte - 20% perchloric acid in methanol
Temperature - 20°C
Voltage - 5 to 10 volts
Time - 30 secs.

Bulk phase analysis on solution treated and aged material was carried out by X-ray energy dispersive analysis (EDS) on a JSM 35 CF scanning electron microscope operating at 20 kV. Analysis was made using a LINK system with a ZAF-4 correction procedure and elemental standards. That is, all spectra intensities were measured relative to standards containing the elements required in known concentrations, measured under identical conditions. Allowances were then made since the measured intensity is not simply proportional to mass concentration, but is affected by the composition at the analysed point. These matrix corrections (dependent on composition)are known as ZAF corrections, where Z (atomic no.) - the efficiency of X-ray generation (including the effect of the loss of electrons due to backscattering) is a function of atomic number, Z, of the specimen.

A (absorption) the generated X-rays are subject to absorption on emerging from the specimen, by an amount strongly dependent on composition.

F (Fluorescence) the intensity of peaks may be enhanced due to excitation by other X-rays of higher energy in the specimen.

Since the correction factors depend on the composition and this is not known until the correction factors are known, an iterative computation procedure is adopted, and the corrected concentrations converge on the true values in a few cycles (usually).

Figure 52. Electro polishing Conditions for an alloy, 21Cr-6Ni-8Ru(annealed at 1250°C),1cm.sq.in a 10% perchloric acid/methanol solution at -40°C.

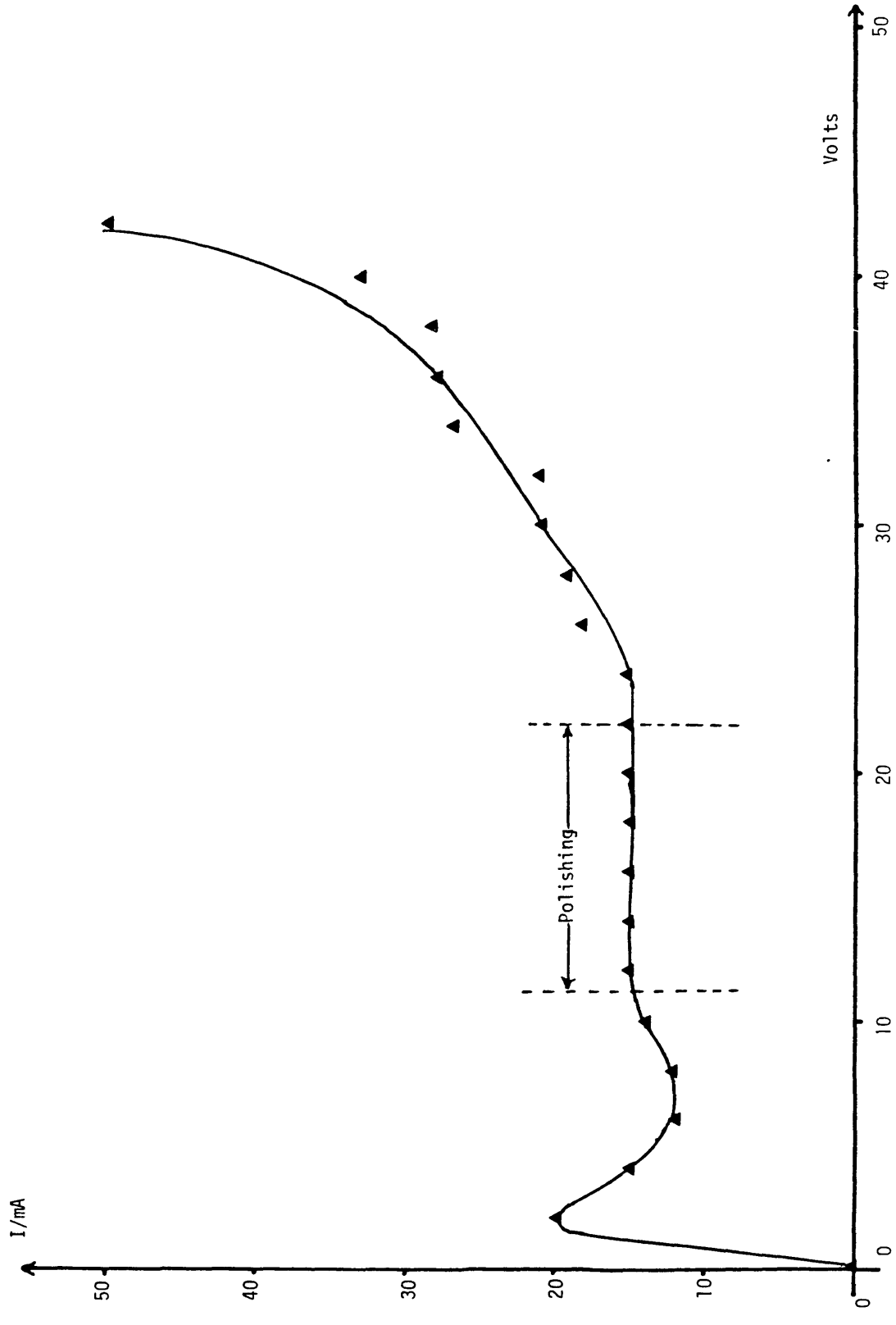

Characterisation was further performed using a transmission electron microscope (TEM); a Philips EM301 microscope operating at 100 kV. Since both ferrite and α-martensite are ferromagnetic, it was found advantageous to have the material surrounding the electron transparent regions, as thin as possible to reduce the deflection of the electron beam. An initial disc thickness of 0.2 mm was always used. To prepare the discs, samples were first ground on 220 grade SiC paper to approximately 0.2 mm thickness. They were then glued on to small steel sheets using Durafix glue containing graphite powder. 3 mm discs were spark cut using a brass tube cutting tool, and removed from the sheet by soaking in acetone. The discs were jet-thinned using a Tenupol jet polisher manufactured by Struers containing a solution of 10% perchloric acid/methanol, and operated at 17-20 volts at -40°C. After perforation the discs were thoroughly washed in methanol. (The polishing characteristics of a typical PGM containing alloy are shown in Figure 52.)

3.4. Magnetic Balance Measurements

Of the phases present within these materials, only the α'-martensite and α-ferrite are ferromagnetic. (Since the carbon content of the steels in this study was $\leq$ 0.02wt% the volume fraction of ferromagnetic carbides was found to be small.) A Sucksmith magnetic balance, constructed by H. Smith (194) (Ph.D. Thesis, London University, 1968), was used to measure the α'-martensite content. The method of determining the ferromagnetic content from the magnetic balance readings is given in Appendix 1.

A schematic representation of the balance is given in Figures 53, 54 and 55. The samples to be measured are held within a brass box held by a brass rod. The sample is then positioned centrally between two pole pieces. A downward force and deflection is then experienced by the sample, the value of which is dependent upon its mass and specific saturation magnetic intensity. This deflection is then measured by a transducer.

To determine the (α + α') content, it must be assumed that the field gradient is constant. The pole pieces are designed so that this is maintained within a particular region, as shown in Figure 54. Readings are then taken from the specimens, using a constant supply current, and also from a standard iron sample.

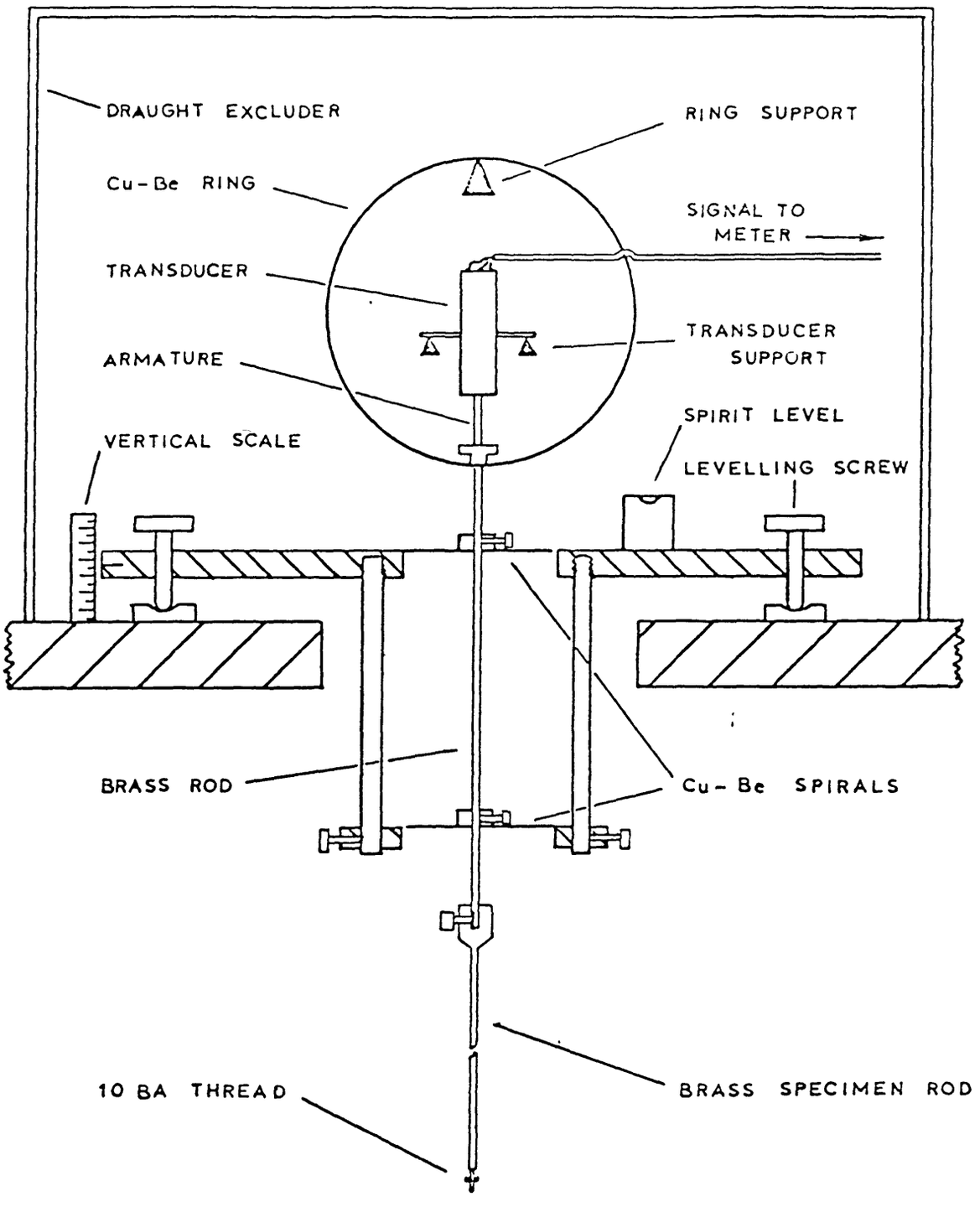

THE RING BALANCE.

Figure 53. Ref. 194

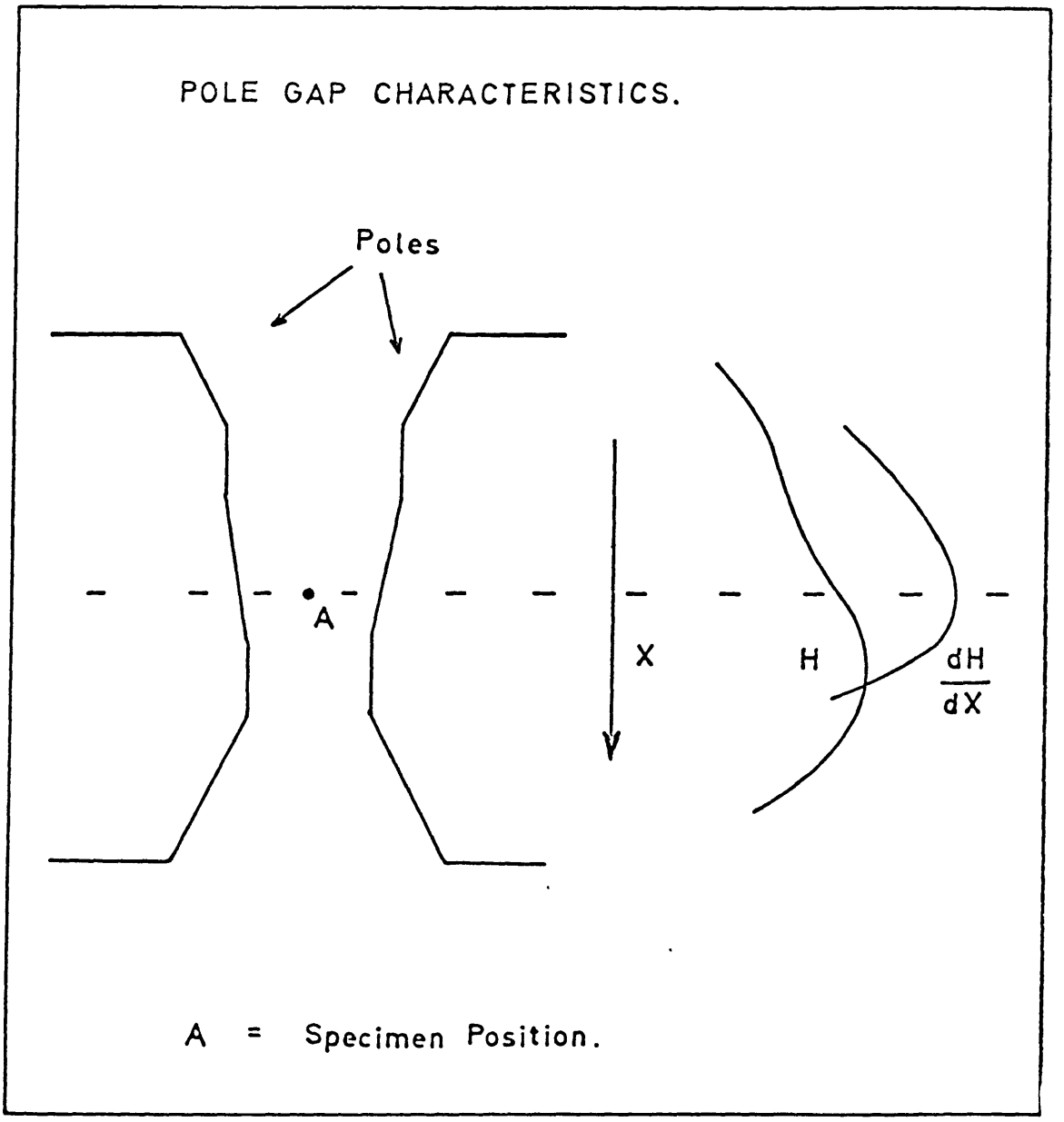

Pole Gap Characteristics

Figure 54.

Ref. 194

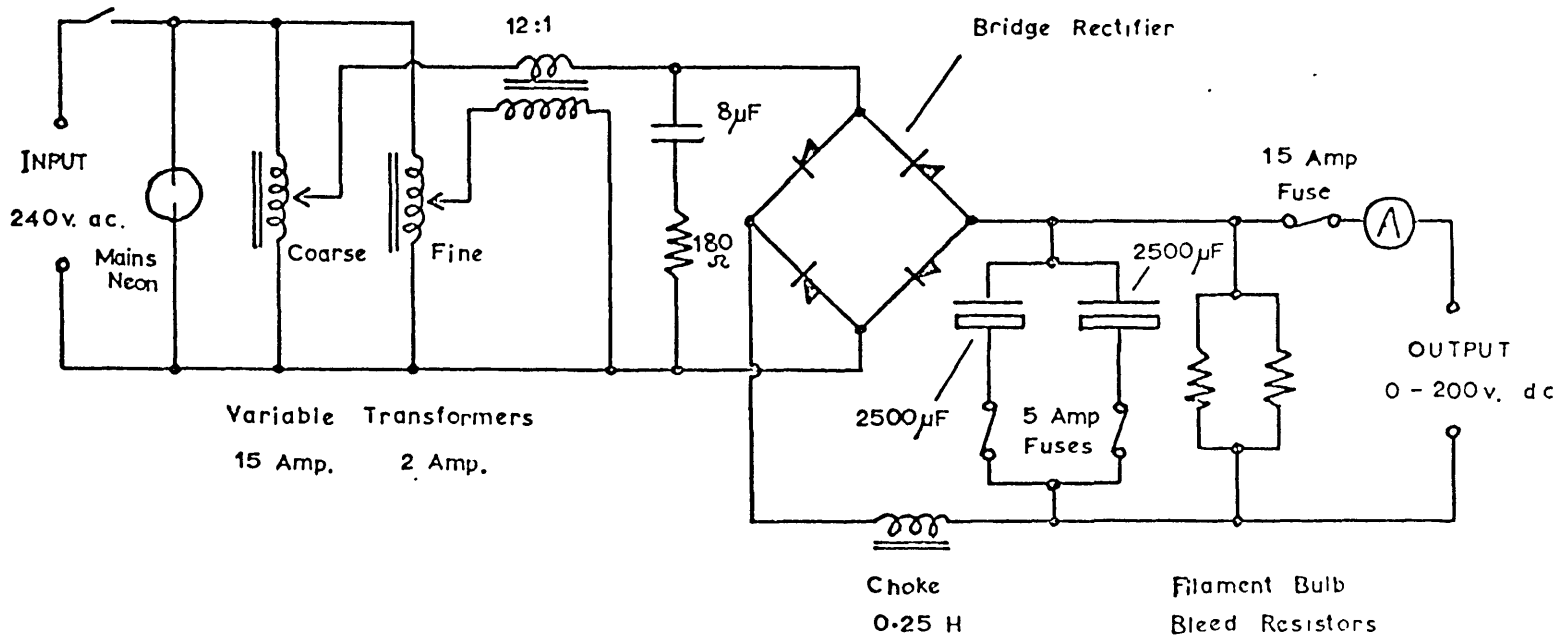

POWER SUPPLY FOR MAGNETIC BALANCE.

Figure 55. Ref. 194

Smith (194) calculated the value of the magnetic field gradient down a vertical axis through the pole pieces. From these results, it is possible to determine that a sample of 18Cr-8Ni steel containing 100% α'-martensite, will deflect by an amount to give a 1% change in the field gradient if it weighs 0.8g. The samples used in these experiments always contained less than 100% (α + α') and weighed less than 0.37g. Because of this, and because the deflections are maintained in the vertical axis by springs, then, from the distance that these specimens will move, the field gradient can be considered to be constant.

Smith (194) suggested that ideally elliptical or cylindrical samples should be used. For the present work however, only square shaped samples could be conveniently used. As temperature fluctuations and slight changes in the positioning of the specimen may lead to errors, a reading of a standard iron sample was taken after each test, and this was used in the calculation. These errors can be assessed and determined qualitatively by measuring the ratio of the saturation magnetic intensities of iron and nickel. This was given by Weiss and Forrer (195). Guy (196) obtained a ratio of 3.890 for this value, indicating an error of 2.4% for a sample containing 20% α'-martensite, i.e. ± 0.24%.

3.5. Dilatometry Studies

The M_s temperatures for the alloys 21Cr-6Ni, 21Cr-6Ni-2Pd and 21Cr-6Ni-2Ru, prepared from route 1, were measured by means of a commercial dilatometer (Theta Dilatronic III dilatometer). Specimens were machined to produce 6 mm long, hollow tubes, of 0.5 mm thickness and were positioned as shown in Figure 56a. Figure 56b shows the heating cycle imposed on the alloy specimens. Helium was used as the quenching gas to effect a fast efficient quench. An accuracy of $\pm 10^{o}C$ was achieved on M_s temperature measurements.

3.6. Potentiodynamic Polarisation Measurements

Polarisation data were obtained by the use of a modified Wenking ST72 potentiostat and linear voltage sweep generator. The potentiostat was modified to allow for computer control of voltage sweep and corrosion current density logging. The incorporation of suitable differential amplifiers and filters allowed the system to cope with a rapid throughput of samples with automatic logging and plotting of polarisation data. The equipment and arrangement of the polarisation cell are shown in Figures 57, 58 and schematically presented in Figure 59.

Figure 56a. Quenching Dilatometer Head and Specimen Position.

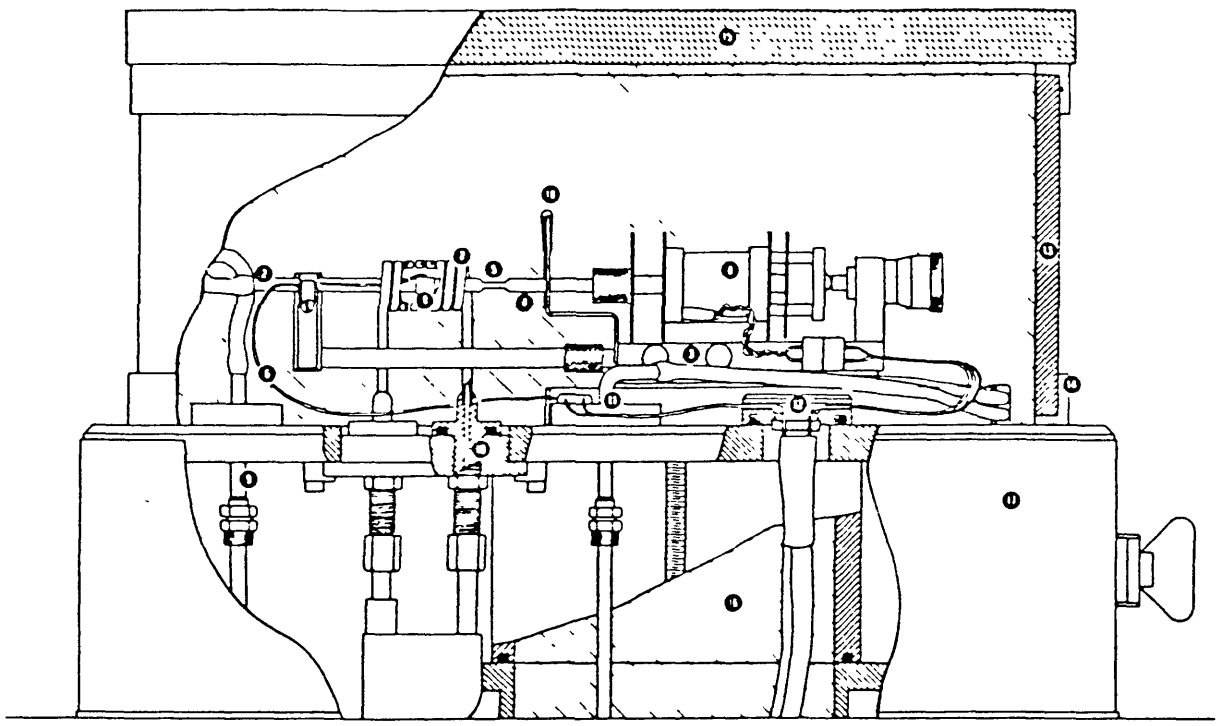

The specimen (1) rests between the tips of the fixed rod (2) and sensing rod (4) in the center of the RF furnace(7). The phase change signal is transfered through the frictionless mounted rod(4) into the transducer (8). The thermocouple (6) senses the temperature. Quenching gas passes through the hollow specimen and escapes through openings.

PRINCIPLE OF OPERATION

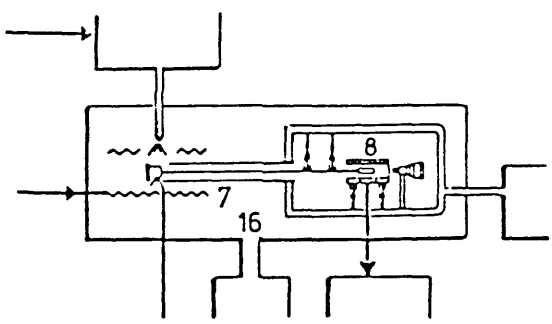

SPECIMEN HOLDER ASSEMBLY

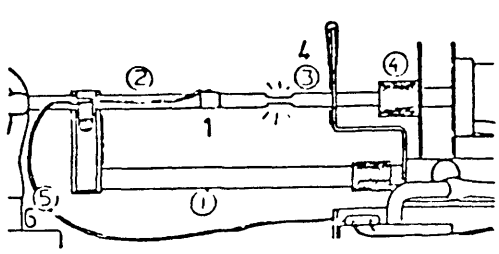

LEGEND

1. Sample
2. Fixed Rod
3. Fixed Rod Adjustment Screws
4. Pushrod (Sensing Rod)
5. Quenching Gas Escape
6. Thermocouple
7. HF Water-Cooled Furnace
8. Transducer
9. Quenching Gas Feedthrough
10. HF Feedthrough
11. 40°C Stabilization and TC Reference
12. TC and LVDT Feedthrough
13. Vacuum Collar
14. Sealing Boot
15. Vacuum Glass Cover
16. Vacuum Port
17. Service Collar
18. Radiation Shield

Figure 56(b). Schematic Diagram of Specimen Heating Cycle during Dilatometry Measurements. The quenching gas used was helium.

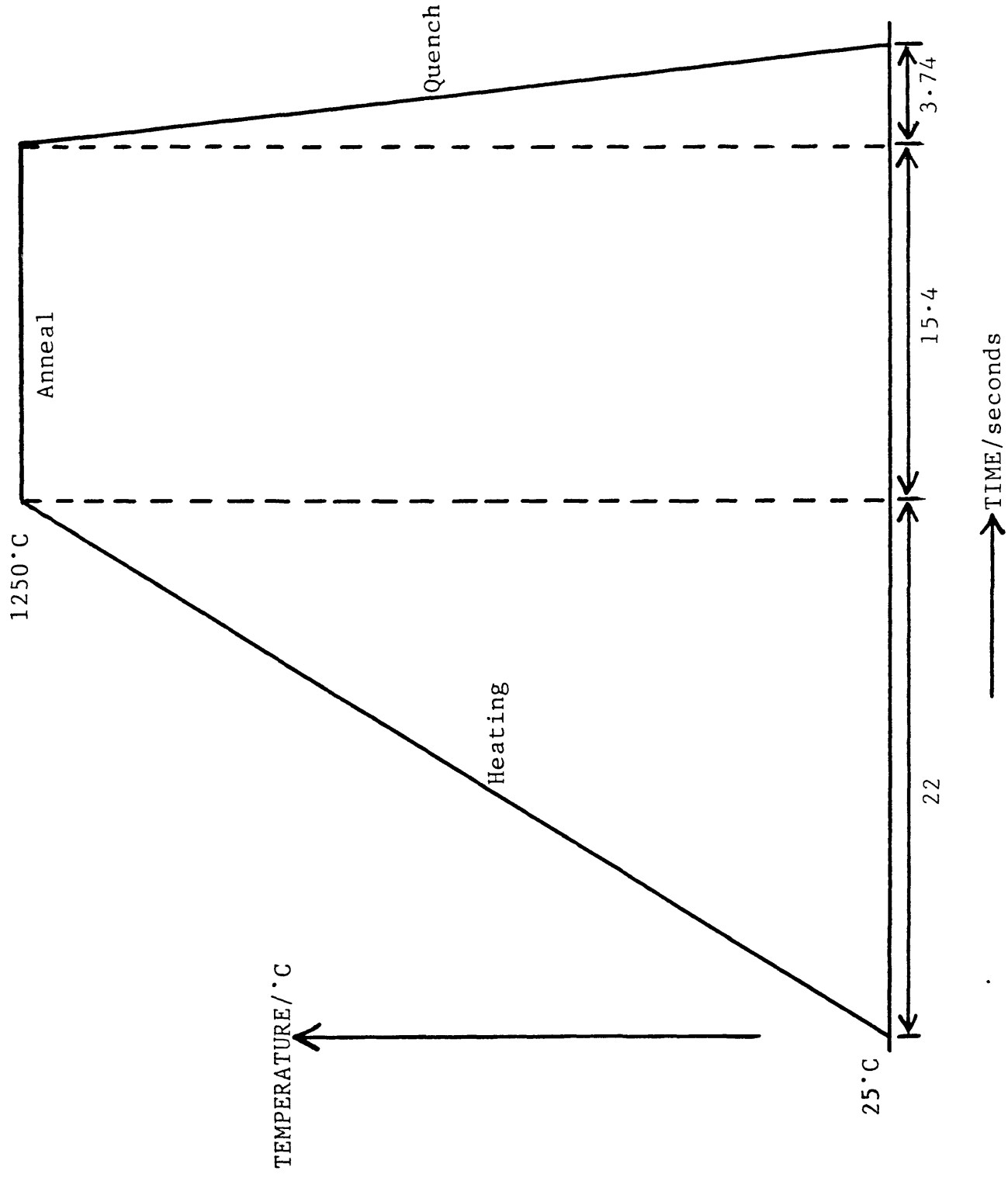

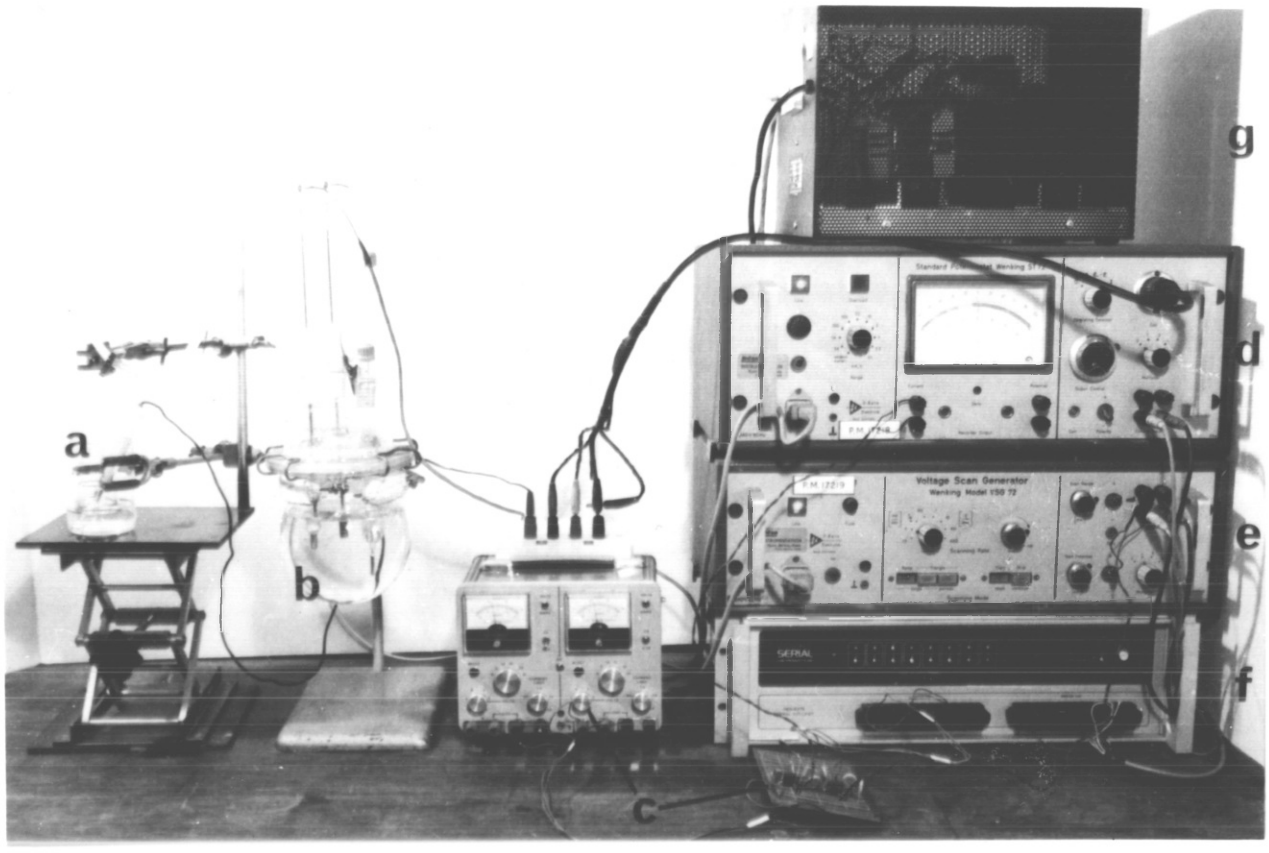

FIG. 57 Apparatus for Polarisation Curve Determination

a) Reference Electrode Assembly
b) Polarisation Cell
c) Differential Amplifiers/Filters
d) Potentiostat
e) Voltage Scan Generator
f) Analogue/Digital Converter
g) In-line Mains Filter



FIG.58 Close-up of Polarisation Cell

a) Platinum Counter Electrode
b) Working Electrode (Test piece)
c) Luggin-Haber Probe (to reference electrode)
d) Gas Sparger

Figure 59 SCHEMATIC DIAGRAM OF APPARATUS FOR POLARISATION CURVE DETERMINATION.

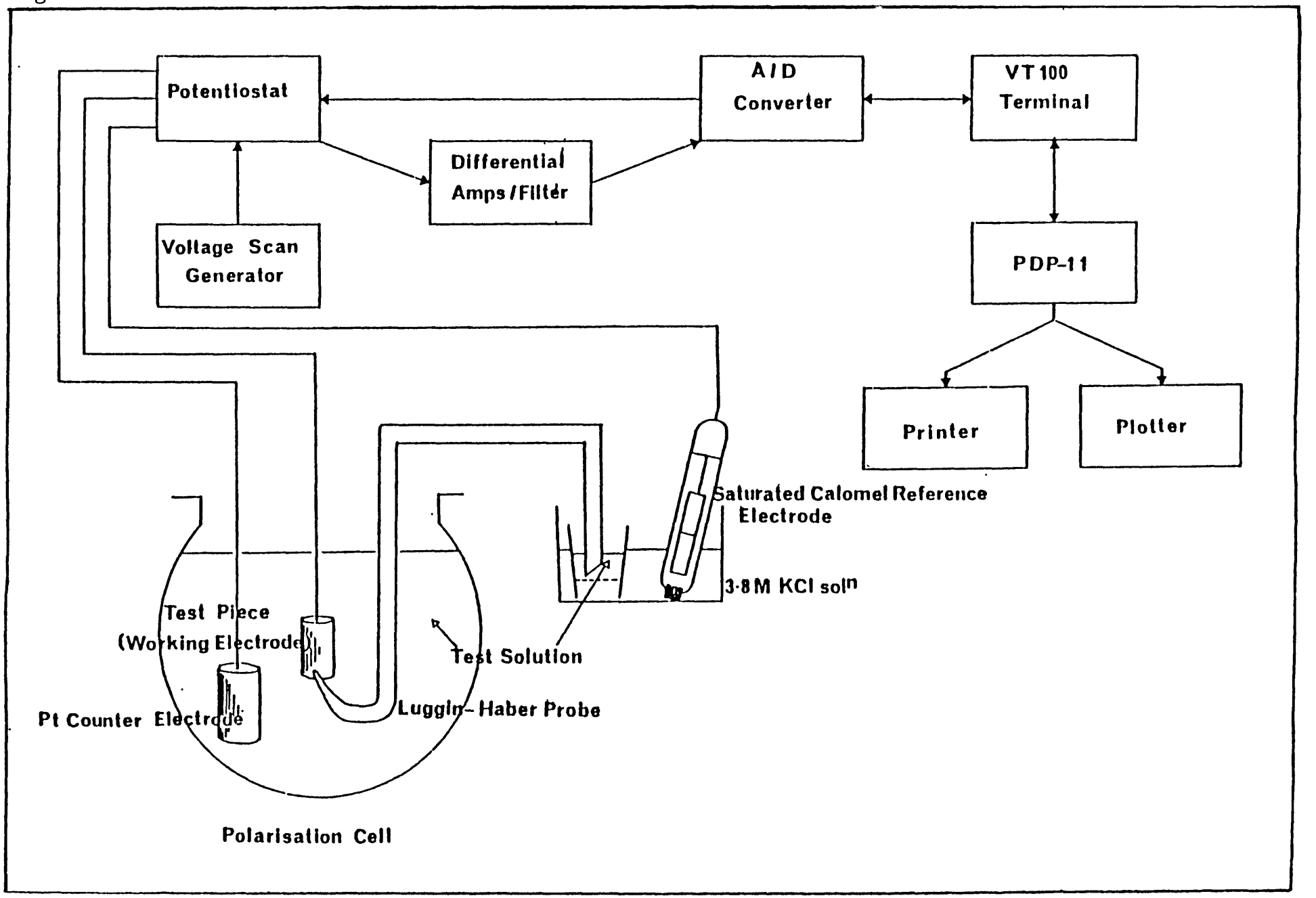

The polarisation cell incorporates a platinum secondary electrode, Luggin-Haber capillary salt bridge system leading to a standard calomel reference electrode and gas and temperature monitoring ports. The specimens which form the working electrode, were cylindrical in shape; 6 mm diameter and 12 mm long, being machined directly from rolled material and then solution treated in argon at 1250°C for 1 hour.

The polarisation test procedure was based upon the recommended practice of the ASTM G5-72 specification for polarisation measurements. All tests carried out on alloy specimens were conducted in 1N.H_2SO_4 at 25°C. Polarisation samples were ground to a 600 gmt SiC finish, degreased in acetone, washed in distilled water and immersed in the test solution. Prior to commencement of a polarisation run, the solution was completely deaerated by continuous purging with nitrogen. After a short period of equilibration the samples were polarised at a voltage scanning rate of 16mVmin^{-1}. This scan rate is somewhat faster than the recommended 6mVmin^{-1} according to ASTM G5-72 but is within the range of rates used by other workers investigating similar corrosion behaviour. However, it should be noted that increasing the voltage scan rate does decrease the time for equilibrium to be attained by the specimen during a polarisation scan.

3.7. Thermogravimetric Studies

The alloys 21Cr-6Ni,21Cr-6Ni-2Ru, and 21Cr-6Ni-2Pd were prepared from material in route 2 of alloy production, having been hot rolled at 700°C to 1-2 mm and solution treated at 1250°C for 30 minutes. The alloy sheets were subsequently cold sheared to approximately 1 sq.cm. x 1.5 mm and the burred edges removed. A 2 mm hole was drilled at one end and the surfaces given a shiny finish on 600 gmt SiC paper. Immediately prior to oxidation, specimens were individually electro-polished for 5-10 minutes at 20 volts in 1:20 (vol) perchloric and glacial acetic acids at 15-20°C, washed in ethanol and dried in cold air and weighed. Specimens were then located in the hot zone of an open ended furnace at 1000°C for 100 hrs, suspended by a silica glass hook rod connected to a spring thermogravimetric balance, Figure 60. Weight readings were taken every minute with a sensitivity of ±100 mg being achieved. Subsequent to the 100 hours of oxidation specimens were studied by conventional metallographic techniques.

Schematic Diagram of Thermogravimetric Balance.

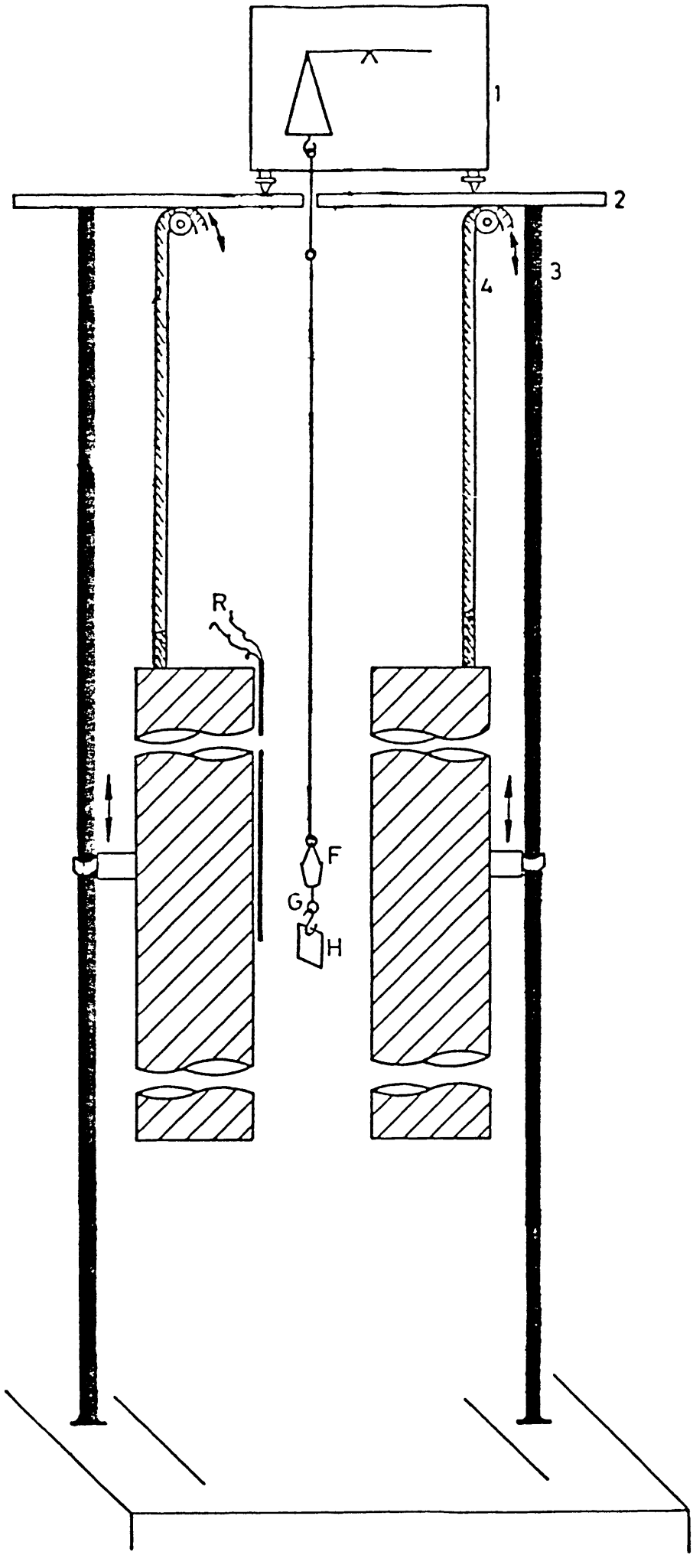

1. Recording Thermobalance.
2. Aluminium Plate (71 x 56 x 1.3 cm.) su-ported on angle iron stand.
3. Steel guide rods (dia. 1.3 cm.) to lift and lower furnace.
4. Steel ropes over pulleys connected to furnace from a worm drive assembly.
F. Platinum micro-crucible (cap 1.1 ml.)
G. Silica hook.
H. Test Specimen.
R. Pt/Pt-Rh Thermocouple connected to eurotherm for furnace temperature control.

Figure 60.

CHAPTER FOUR

SOLIDIFICATION MODES

Heavens fire doth melt all her impurities
Such liquid and gaseous, solid beauties
And now free from all her sublimed dross
She doth freeze them, purged,
And counts the cost.

(S. McKenzie)

Figure 61. Planar section through the primary pipe of a 21Cr-6Ni-8Ru wt% alloy showing the radial projection of dendrites.

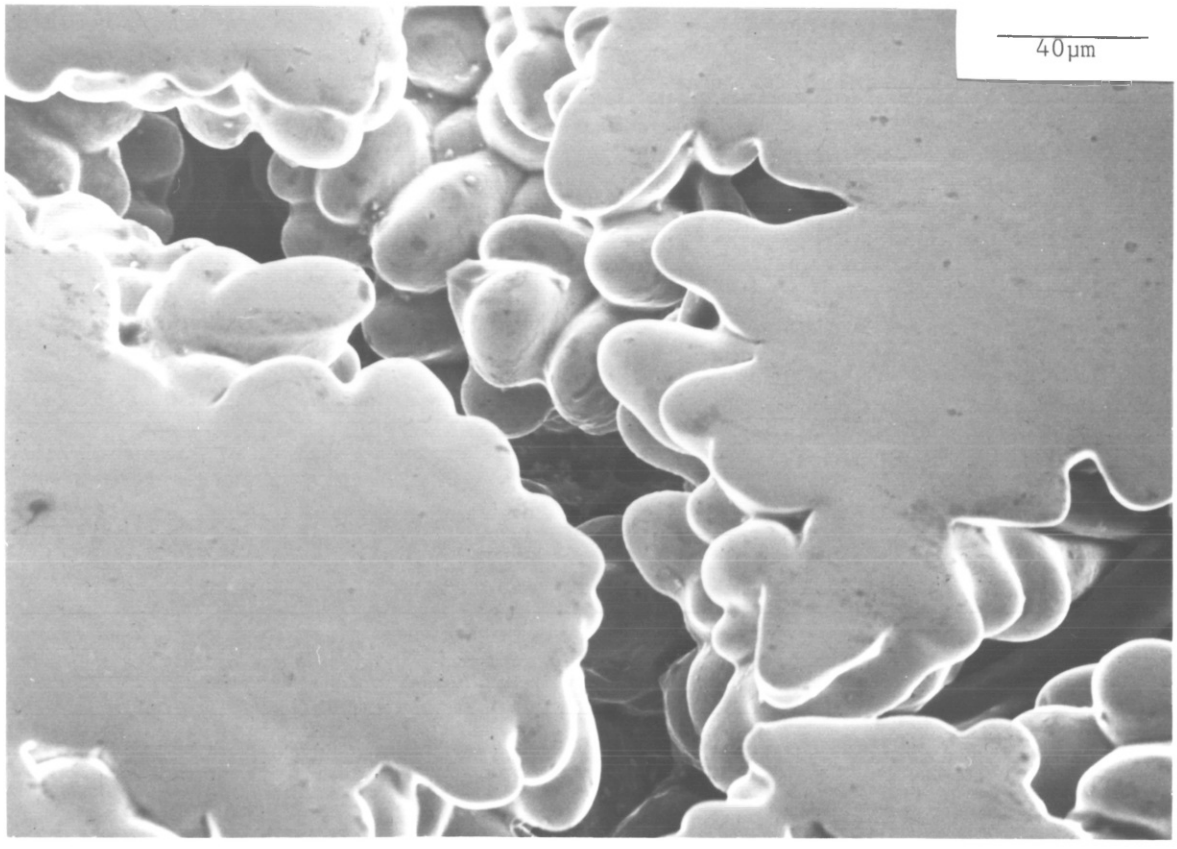
40µm

4.1. Results

4.1.1. Solidification Modes

The effects of Pt, Pd and Ru additions on the mode of solidification (and solid state transformations), and subsequent partitioning of elements in selected Fe-Ni-Cr alloys, Figure 63, have been investigated using electron-probe microanalysis and light microscopy.

All of the alloys were cast in a water-cooled copper hearth, the cooling rate being of the order of $100^{o}C/sec$. This relatively fast cooling prevents equilibrium from being attained and produces coring effects, e.g. Figure 69, similar in principle to those occurring in binary systems. These coring effects are associated with dendrites whose presence is readily observable in these alloys, e.g. Figure 61.

All duplex stainless steels contain alloying elements such as C, N, Mn, Si, etc., which influence the amount of α and γ which forms (59). The relative effectiveness of elements in stabilizing α is compared to the effectiveness of Cr and expressed in terms of their Cr equivalents. A Cr equivalent of 1 means that an element (on a wt% basis) is as strong as Cr in stabilizing α. Elements which stabilize γ are similarly expressed in terms of their Ni equivalent. In this study the platinum group elements, Pt, Pd and Ru have been assigned a nickel equivalent of 1. This is on the basis that PGM's (Pt and Pd in particular) have a similar effect to nickel in opening up the γ-austenite field of the Fe-Cr binary system (24). (Although this is rather an arbitrary premise, results confirm that it works well for Pt and Pd.) So the Cr and Ni-Equivalents used in this study are:

$$\text{Ni-Eq.} = \text{Ni} + (\text{Pt, Pd or Ru}) + \text{Co} + 0.5(\text{Mn}) + 25(\text{N}) + 30(\text{C}) \text{ wt\%} \quad (24)$$

$$\text{Cr-Eq.} = \text{Cr} + 2(\text{Si}) + 1.5(\text{Mo}) \text{ wt\%} \quad (24)$$

On the above basis then, the ratio of Cr-Equivalent/Ni-Equivalent has been determined and used to predict the mode of solidification for the range of alloy composition referred to in Figure 63. The effect of alloying additions on the mode of solidification can therefore be conveniently treated on the basis of such equivalents both in small laboratory melts and in weld metal, as described in the literature review (82-99), and graphically in Figure 62. Figure 64 graphically represents four possible solidification modes in a 70%Fe pseudobinary section of the Fe-Cr-Ni system (82).

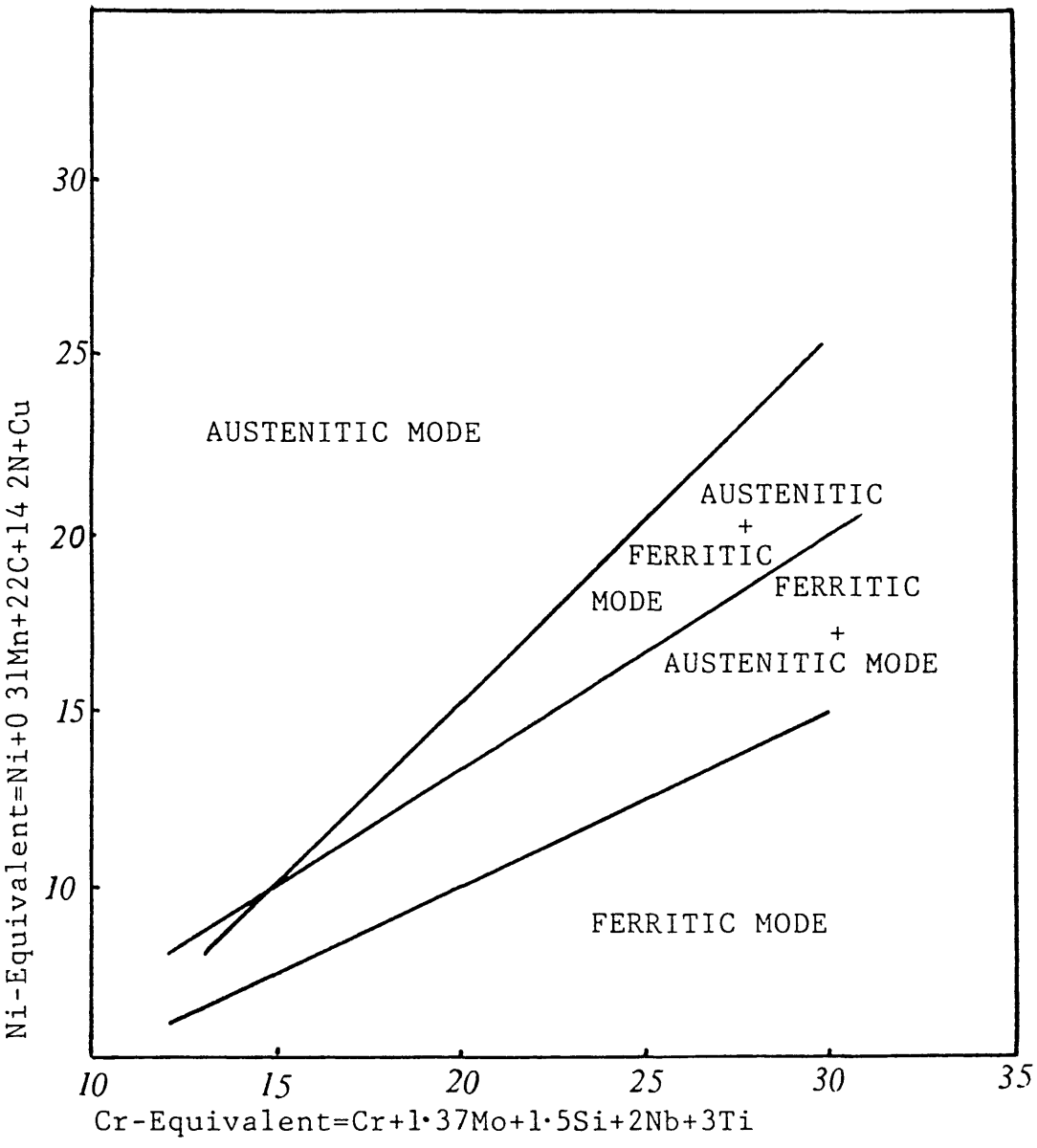

EFFECT OF ALLOY COMPOSITION ON SOLIDIFICATION MODE.

Figure 62. Ref.98

Compositions (Base-Alloy) wt%	Additions wt%	Cr-Eq./Ni-Eq.	Predicted Mode of Solidification (Primary Phase)
S1 - 6Ni + 21Cr + Fe bal.	-	>2.0	α-ferrite
S2 - 6Ni + 18Cr + Fe bal.	-	>2.0	"
S3 - 6Ni + 21Cr + Fe bal.	2Pt	>2.0	"
S4 - 6Ni + 21Cr + Fe bal.	8Pt	<1.5	γ or γ-α
S5 - 6Ni + 18Cr + Fe bal.	2Pt	>2.0	α-ferrite
S6 - 6Ni + 18Cr + Fe bal.	8Pt	<1.5	α or γ-α
S7 - 6Ni + 21Cr + Fe bal.	2Ru	>2.0	α-ferrite
S8 - 6Ni + 21Cr + Fe bal.	8Ru	<1.5	γ or γ-α
S9 - 6Ni + 18Cr + Fe bal.	2Ru	>2.0	α-ferrite
S10- 6Ni + 18Cr + Fe bal.	8Ru	<1.5	γ or γ-α
S11- 6Ni + 21Cr + Fe bal.	2Pd	>2.0	α-ferrite
S12- 6Ni + 21Cr + Fe bal.	8Pd	<1.5	γ or γ-α
S13- 6Ni + 18Cr + Fe bal.	2Pd	>2.0	α-ferrite
S14- 6Ni + 18Cr + Fe bal.	8Pd	<1.5	γ or γ-α

Figure 63. Predicted Mode of Solidification for experimental alloys.

4.1.2. α-Ferrite Solidification Route

Figures 65a,b,d,f,g and 66a,b,d,f show duplex alloys each having compositions where ferrite stabilizing elements dominate, and where the Cr-Eq/Ni-Eq ratio is >2.0. The predicted solidification reaction is consequently:

$L \rightarrow L + \alpha \rightarrow \alpha \rightarrow \alpha + \gamma$ (see Figure 64)

This is in fact observed in the present alloys where the microstructure is typified most clearly by Figure 66d, 21/6/2Pd, where large columnar grains of α-ferrite have formed from the liquid out from the mould wall. Ferrite is the only phase formed during solidification. After solidification, γ-austenite is seen to precipitate preferentially at α-ferrite grain boundaries as feathery needles, but is additionally able to nucleate independently within ferrite grains as the grain boundaries become saturated. Ferrite and austenite phases were identified by etching techniques described in 3.3. In the main, α remained light in contrast relative to γ. Alloy 18wt%Cr-6wt%Ni, Figure 65a again typifies the above features showing most clearly this solid state Widmanstatten precipitation of austenite within a central α-ferrite columnar grain. The addition of 2wt%Pt, Pd and Ru (Figures 65b,d and f) to this base alloy serves only to increase the volume fraction of this Widmanstatten austenite whilst the α-ferrite grains themselves are effectively unaltered.

Increased Cr content in the 21wt%Cr-6wt%Ni alloys shows an effective reduction in the amount of γ-austenite able to precipitate in the solid state, but essentially the same α-ferrite columnar grain structure observed for the 18wt%Cr-6wt%Ni alloys. Additions of 2wt%Pt, Pd and Ru to the base 21/6 base alloy (Figures 66b,d and f) show no significant increase in the volume of austenite precipitated.

The transformation of α-ferrite to γ-austenite at grain boundaries is observed to occur initially by the formation of an almost continuous layer of austenite along the original ferrite boundaries (Figure 65a). Figure 67b further shows the effect of cooling rate on these alloys. During solidification the liquid in contact with the mould wall is rapidly cooled below the liquidus effectively supressing the $L \rightarrow L + \alpha$ reaction. Figure 67c shows the increased volume fraction of γ-austenite precipitation that results from this higher cooling rate and consequent undercooling associated with the mould wall as compared

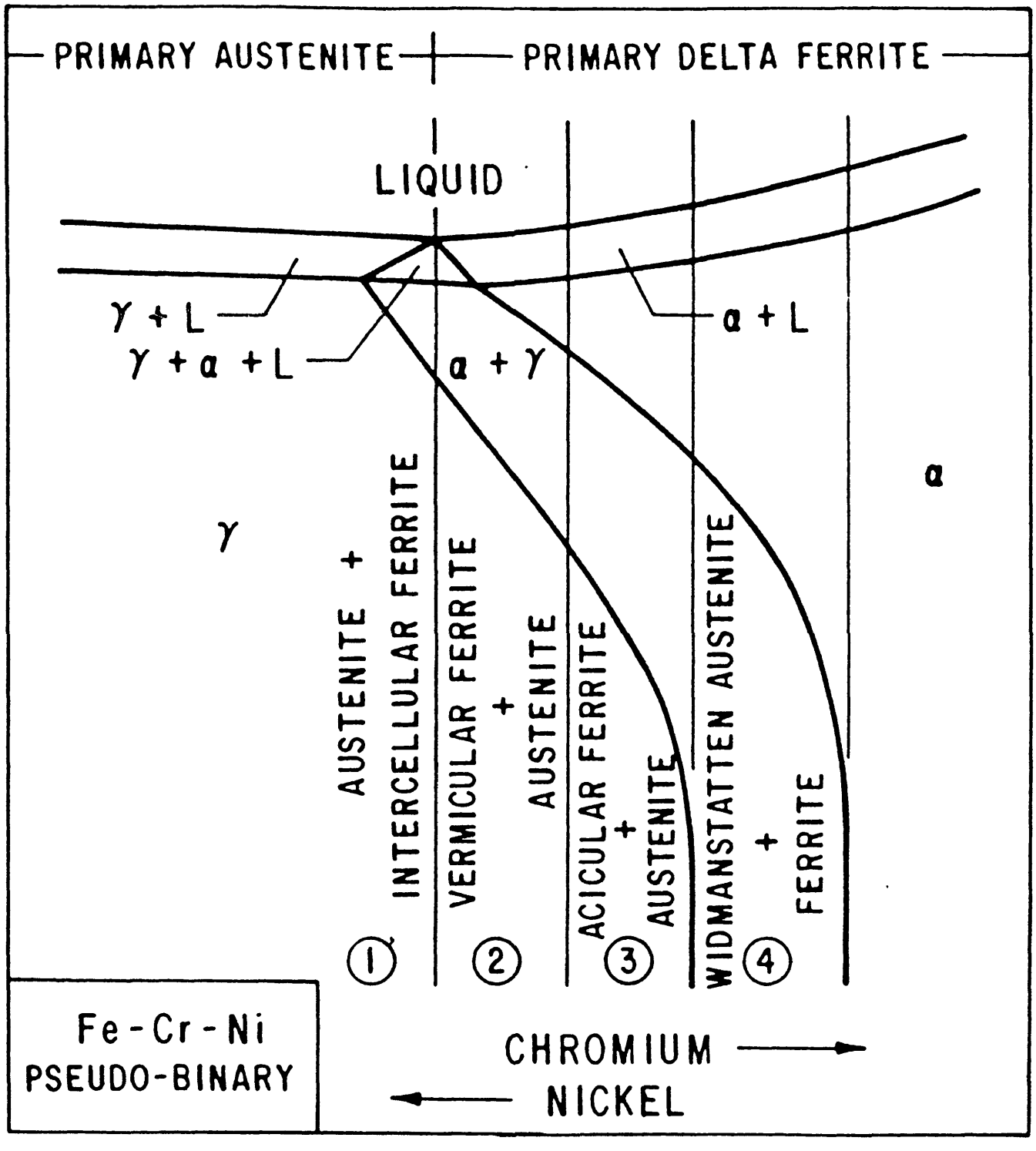

Schematic pseudobinary diagram for 70% Fe showing the structures developed in Fe-Cr-Ni alloys

Figure 64. Ref. 82

Figure 65. 18Cr-6Ni Alloy Series

Light micrographs of the 18/6 alloy series resulting from casting in a water-cooled argon-arc furnace. Alloys were etched via a combination of Vilella's reagent, and $FeCl_3$ in HCl and H_2O, etchant.

(a) The structure reveals primary columnar grains of ferrite with Widmanstatten austenite nucleating at grain boundaries on cooling to room temperature.

(b) Primary grains of ferrite with Widmanstatten austenite at grain boundaries having grown to fill whole ferrite grains in some cases.

(c) Primary dendrite arms of austenite separated by a eutectic mixture of α and γ phases (dark in contrast)

(d) Primary grains of ferrite with Widmanstatten austenite infilling.

(e) Primary dendrite arms (light) of austenite separated by cored interdendritic regions of ferrite (dark). Additional dark regions (running from top to bottom) highlight the effect of non-equilibrium associated with fast cooling rates and dendritic freezing in these alloys, constituting a 'divorced eutectic' of $\alpha + \gamma$ phases.

(f) Primary grains of ferrite with dense Widmanstatten austenite infilling.

(g) Large grains of primary ferrite with Widmanstatten austenite infilling.

18wt%Cr-6wt%Ni-Fe bal.

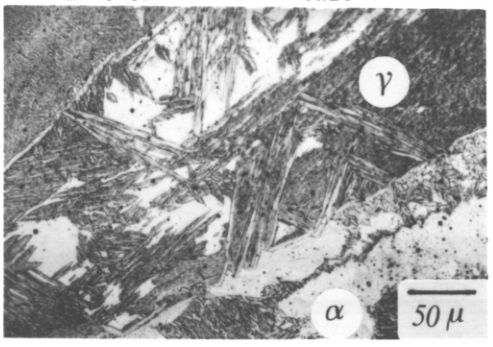

(a)

18wt%Cr-6wt%Ni-2wt%Pt-Fe bal.

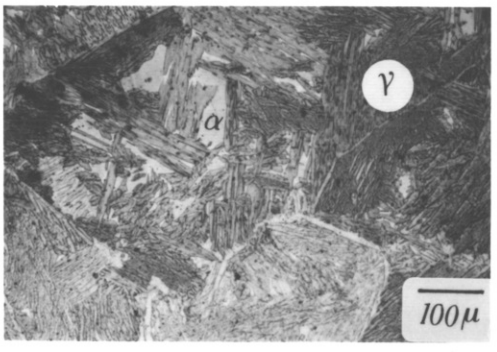

(b)

18wt%Cr-6wt%Ni-8wt%Pt-Fe bal.

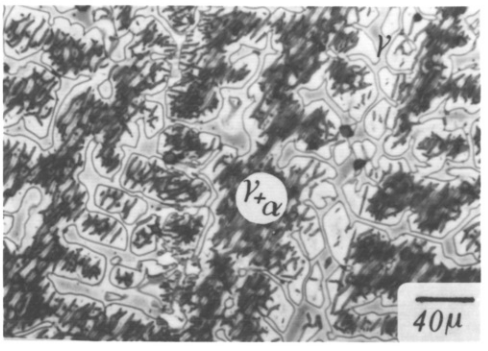

(c)

18wt%Cr-6wt%Ni-2wt%Pd-Fe bal.

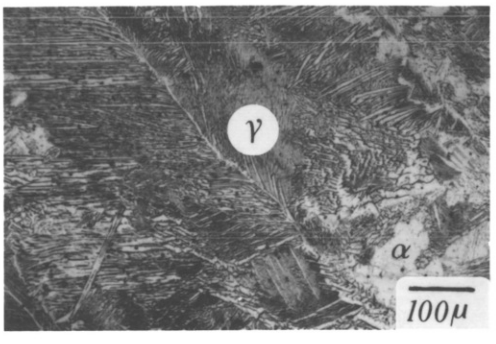

(d)

18wt%Cr-6wt%Ni-8wt%Pd-Fe bal.

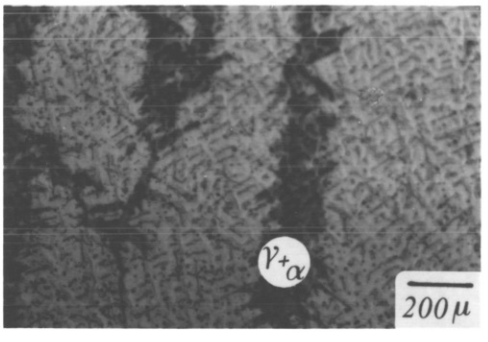

(e)

18wt%Cr-6wt%Ni-2wt%Ru-Fe bal.

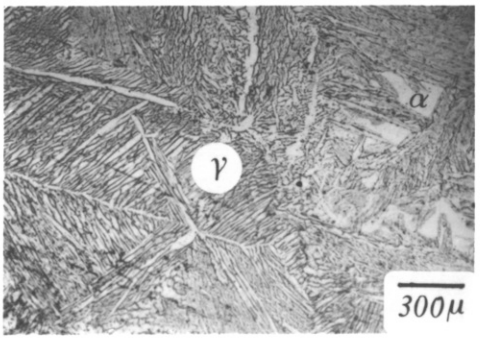

(f)

18wt%Cr-6wt%Ni-8wt%Ru-Fe bal.

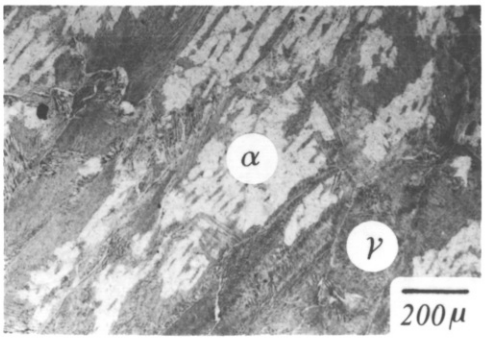

(g)

Figure 66. 21Cr-6Ni Alloy Series

Light and scanning electron microscope micrographs of the 21/6 alloy series, resulting from casting in a water-cooled argon-arc furnace. Alloys in a, b, d, e and f were etched via a combination of Vilella's reagent and $FeCl_3$ in HCl and H_2O, etchants. Alloys c and g were polished and imaged via SEM using backscattered electrons in (c) and a combination of backscattered and secondary electrons in (g).

(a) Actual alloy composition is 19Cr-6Niwt% shows primary grains of ferrite with Widmanstatten austenite growing from α grain boundaries which are almost 100% coated in γ-austenite.

(b) Primary grains of ferrite with austenite nucleated (as Widmanstatten particles) both within, and at α grain boundaries.

(c) Duplex structure of ferrite grains (dark) in an austenitic matrix (light)

(d) Large columnar grains of ferrite with Widmanstatten austenite at α grain boundaries.

(e) Primary dendrite arms (light), of austenite separated by cored interdendtiric regions of ferrite (dark).

(f) Large columnar grains of ferrite with Widmanstatten austenite at α grain boundaries.

(g) Duplex structure of grains of austenite (light) in a ferrite matrix (dark).

21wt%Cr-6wt%Ni-Fe bal.

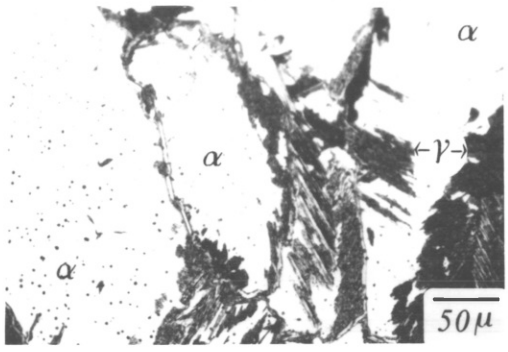

(a)

21wt%Cr-6wt%Ni-2wt%Pt-Fe bal.

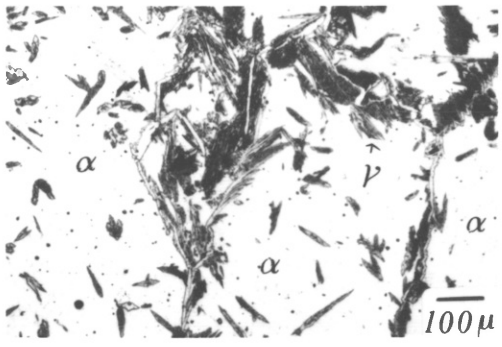

(b)

21wt%Cr-6wt%Ni-8wt%Pt-Fe bal.

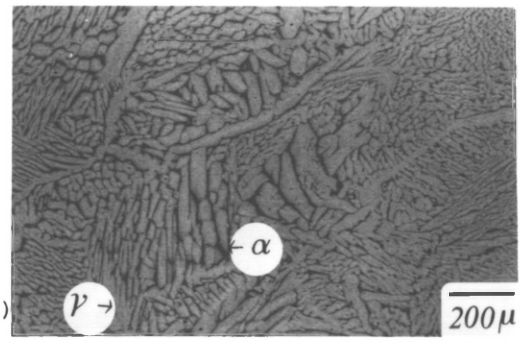

(c)

21wt%Cr-6wt%Ni-2wt%Pd-Fe bal.

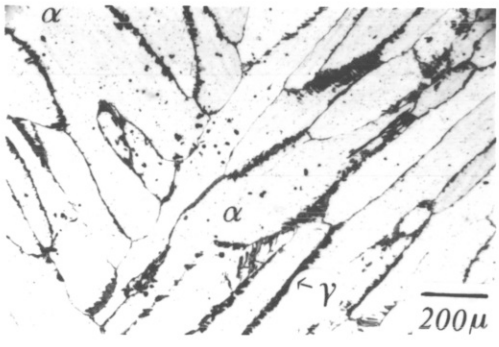

(d)

21wt%Cr-6wt%Ni-8wt%Pd-Fe bal.

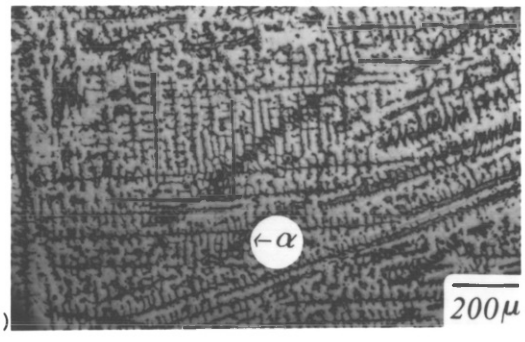

(e)

21wt%Cr-6wt%Ni-2wt%Ru-Fe bal.

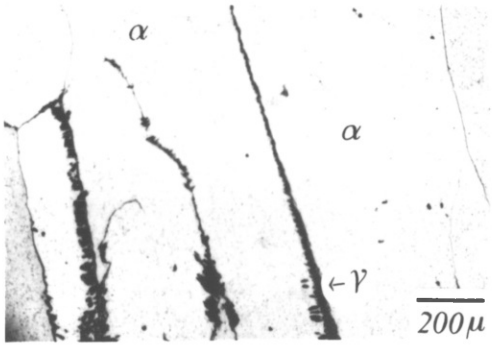

(f)

21wt%Cr-6wt%Ni-8wt%Ru-Fe bal.

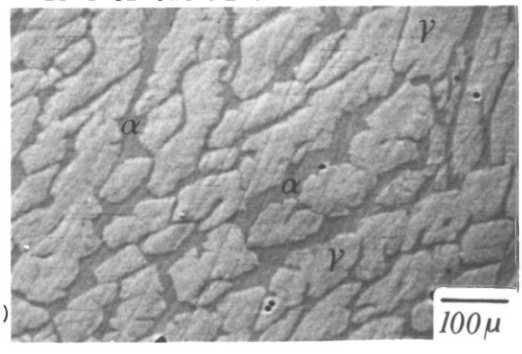

(g)

Figure 67. The effect of cooling rate on the precipitation of austenite.

(a) Light micrograph of an as-cast structure as observed in alloy 21Cr-6Ni-2Pt, shows Widmanstatten grains of austenite in a ferrite matrix (light).

(b) This diagram shows that for a given alloy composition, a faster cooling rate, typically associated with weld material, significantly increases the volume fraction of γ-austenite that may be present on cooling to room temperature. The thermal analysis specimens show slower cooling rates and favour a larger fraction of primary ferrite on freezing.

(c) The light micrograph of the same alloy as in 67(a) above, (taken near the edge of the sectioned specimen), shows the increased precipitation of Widmanstatten γ-austenite in ferrite, due to a depressed solidus associated with a faster cooling rate of alloy material immediately adjacent to the water-cooled copper hearth.


α
α
γ
50μ

a

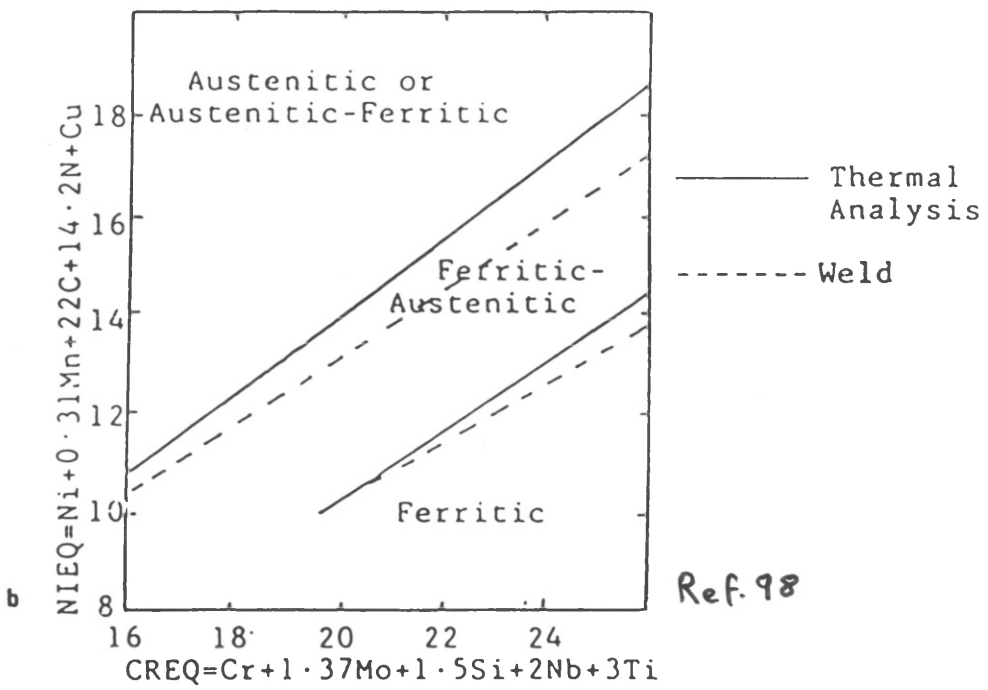
Austenitic or
Austenitic-Ferritic
Ferritic-
Austenitic
Ferritic
Thermal
Analysis
Weld
NIEQ=Ni+0·31Mn+22C+14·2N+Cu
CREQ=Cr+1·37Mo+1·5Si+2Nb+3Ti
8
10
12
14
16
18
16
18
20
22
24

b Ref. 98

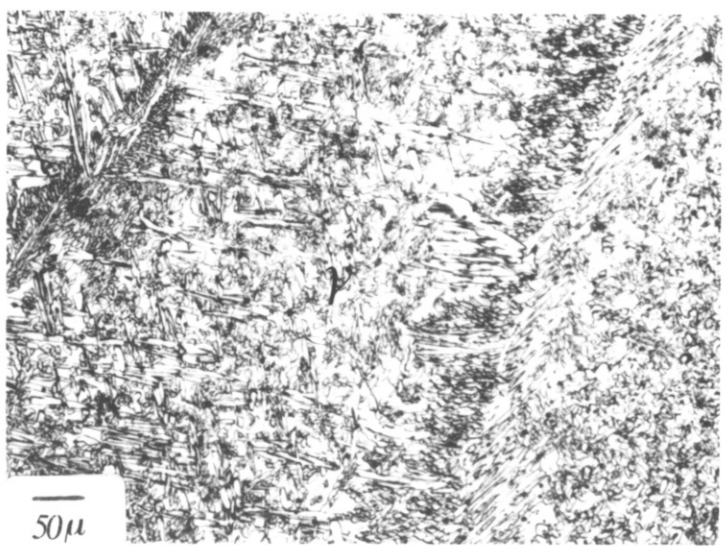
γ
50μ

c

with the centre of the melt in Figure 67a. This is largely due to the depressed solidus, but may also involve microchemical segregation of nickel, due to coring, to the ingot walls.

4.1.3. γ-austenite Solidification Route

Figures 65e and 66e show duplex alloys each having compositions where the Ni-forming elements dominate and where the Cr-Eq/Ni-Eq ratio is <1.5. The predicted and observed solidification reaction is consequently:

$$L \rightarrow L + \gamma \rightarrow L + \alpha + \gamma \rightarrow \alpha + \gamma \quad \text{(Figure 64)}$$

Here the morphology of the microstructure is typified most clearly by Figure 56e, which shows ferrite located in between primary austenite dendrites. γ-austenite forms from the melt first whilst the ferrite is the last liquid to solidify via the ternary eutectic reaction. There is no evidence of any solid state transformations. Alloys 21/6/8Pd, 21/6/8Pt and 18/6/8Pd (Figures 65e, 66c,e) show microstructures which have solidified austenitically, following route 2 in Figure 64. Hence at the 8wt% level of PGM, Pd and Pt in Figures 68, 69 and 71 have been effective in promoting γ-austenitic freezing, verifying the assumption of giving them a nickel eq. of 1. Figure 65c shows this austenitic mode of freezing for alloy 18/6/8t with a divorced eutectic of α + γ phases. A peritectic reaction of $L + \gamma \rightarrow \alpha$ has occurred with $L \rightarrow \gamma + L \rightarrow L + \alpha + \gamma \rightarrow \alpha + \gamma$ being the complete reaction. The morphology of the ferrite here, 65c, is known as intercellular or eutectic ferrite (Mode 1) and is unlike the vermicular ferrite found in α-ferrite freezing.

In Figures 65 and 66g the addition of 8wt% Ru to both 18/6 and 21/6 duplex alloys has resulted in microstructures where α-ferrite is the primary phase. X-ray EDS analysis of alloy 21/6/8Ru in particular in Figure 70 shows the austenitic grains to be rich in Ru and Ni, and the ferrite phase , the matrix (dark in contrast), is rich in Cr. Clearly then Ru is not effective (compared to Pd or Pt) in promoting a primary γ-austenite mode of freezing in either the 18/6 or 21/6 alloy series, and therefore appears to have an Ni-equivalent of less than 1.

Figure 68. EDS analysis of alloy 21Cr-6Ni-8Pd wt%.

(a) Light micrograph of the as-cast alloy structure. Austenite is the matrix and ferrite is formed from the last liquid to solidify to produce cored interdendritic regions (dark).

(b) This SEM back scattered electron image has allowed chemical inspection of ferrite and austenite grains in the above alloy. The black horizontal line represents the path traversed by the electron beam during its qualitative analysis of elements Cr, Ni and Pd.

(c) Qualitative analytical information obtained by the linescan in (b), is quantified by carrying out additional microprobe point analyses of ferrite and austenite regions, along the path traversed initially by the electron beam.



a

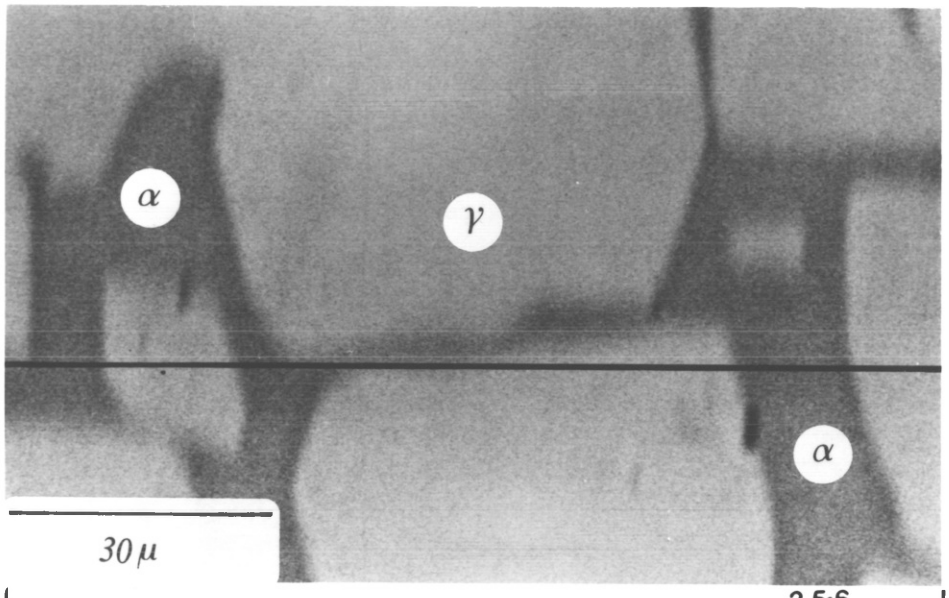

b

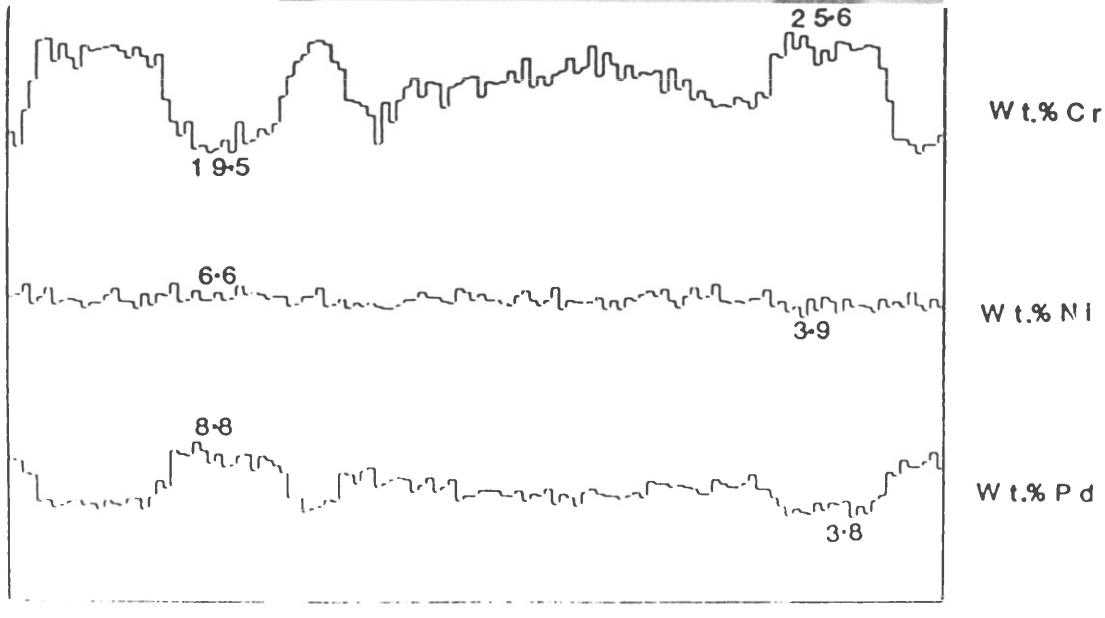

c

Figure 69. EDS analysis of alloy 18Cr-6Ni-8Pd wt%.

(a) Light micrograph of the as-cast alloy structure, reveals heavy coring with primary dendrites arms of austenite (light) separated by interdendritic regions of ferrite (dark).

(b) Imaging the back scattered electrons in this SEM micrograph allows phase identification. It also highlights cored regions of ferrite. The horizontal line represents the path of the electron beam during qualitative analyses of elements Cr, Ni and Pd.

(c) Additional microprobe point analysis has enabled quantification of elements. This is indicated by the numbered values of minimum and maximum observed for Cr, Ni and Pd elements along the linescan path.

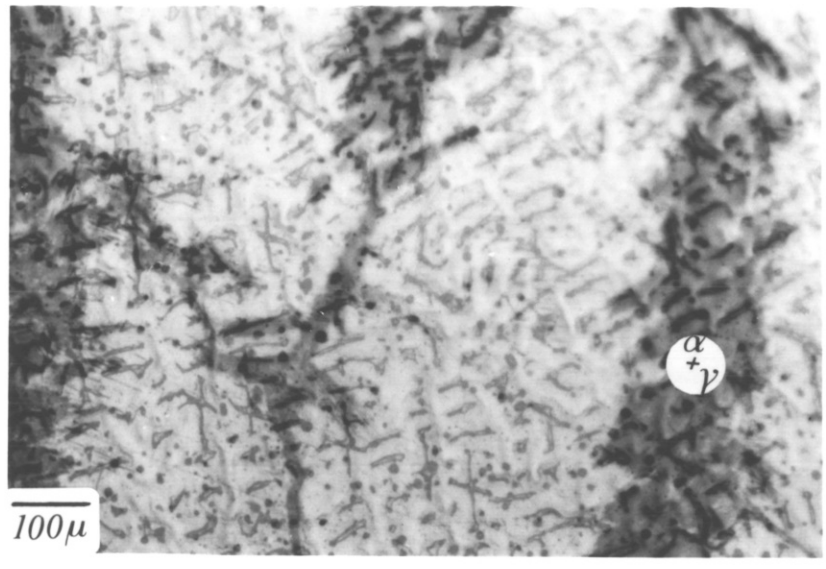

a

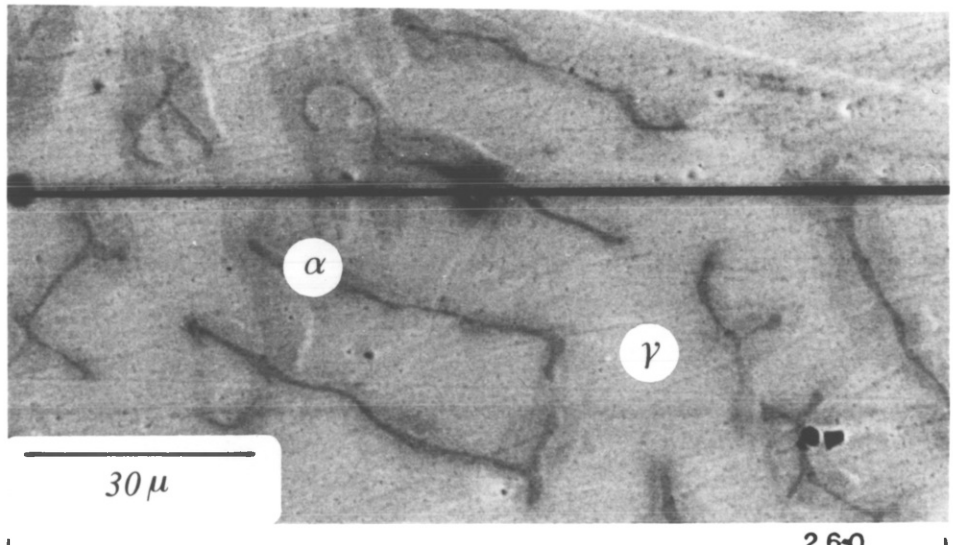

b

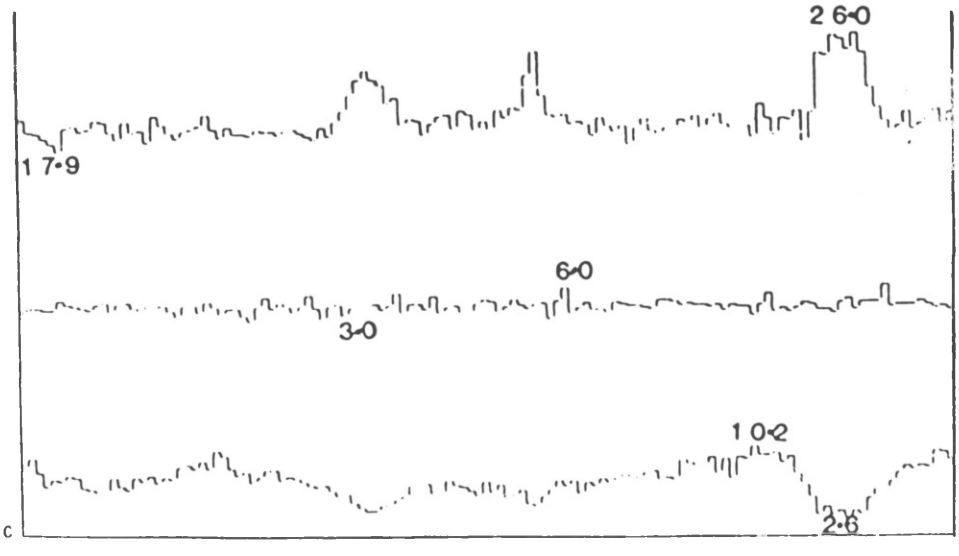

c

Figure 70. EDS analysis of alloy 21Cr-6Ni-8Ru wt%.

(a) This SEM micrograph, imaging both back scattered and secondary electrons reveals grains of austenite (light in contrast) in a ferrite matrix.

(b) Imaging the back scattered electrons in this SEM micrograph allows phase identification via chemical analysis. The horizontal line represents the path of the electron beam, during qualitative analysis of elements Cr, Ni and Ru.

(c) Additional microprobe point analysis has enabled quantification of elemental concentrations. This is indicated by the numbered values of min. and max. observed for Cr, Ni and Ru elements, along the initial linescan path.

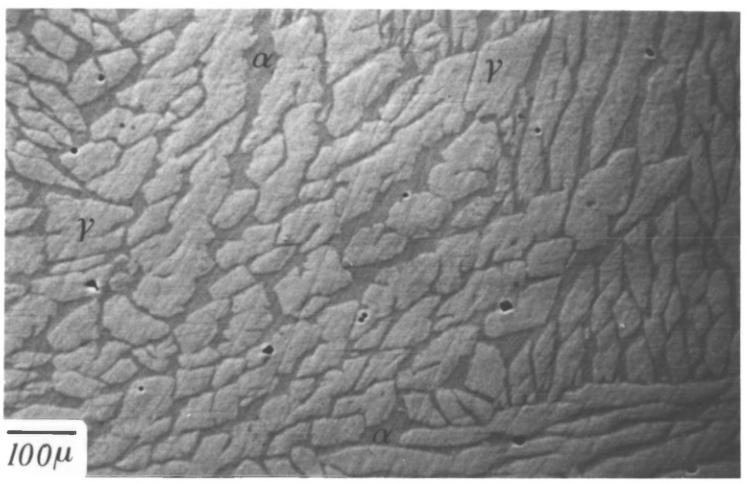

a

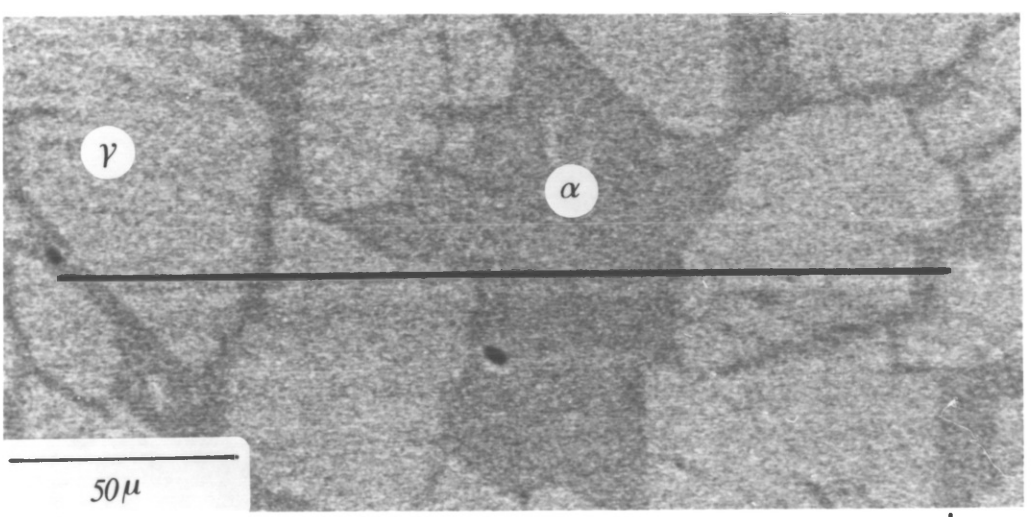

b

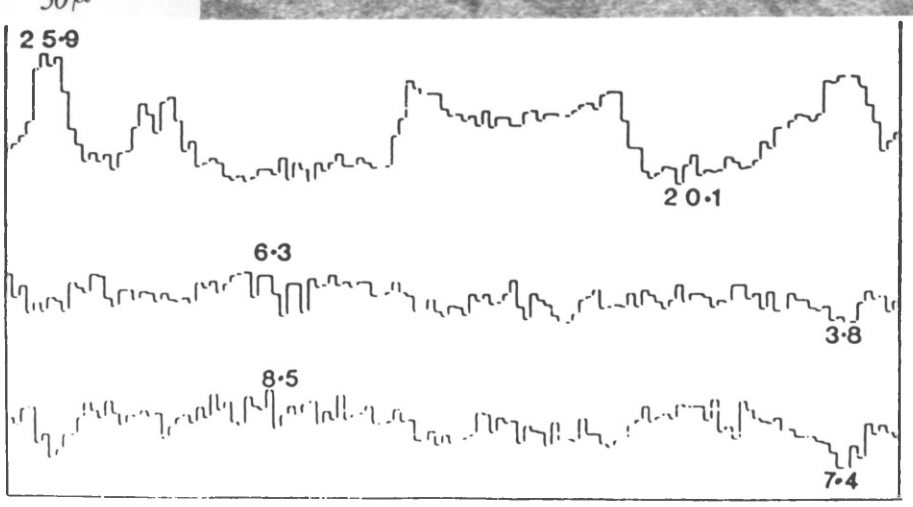

c

Figure 71. EDS analysis of alloy 18Cr-6Ni-8Pt wt%.

(a) Light micrograph of the as-cast alloy structure reveals a three phase structure resulting from the solidification of a divorced eutectic of $\alpha + \gamma$ and primary austenite.

(b) This SEM back scattered electron image has permitted chemical inspection of ferrite regions in the above alloy. The black and grey areas are the respective α and γ eutectic whilst the light areas delineate primary austenite dendrite arms. The black horizontal line represents the path traversed by the electron beam during its qualitative analysis of elements Cr, Ni and Pt.

(c) Qualitative analytical information obtained by the linescan in (b), is quantified by carrying out additional microprobe point analyses of ferrite and austenite regions, along the path traversed initially by the electron beam.

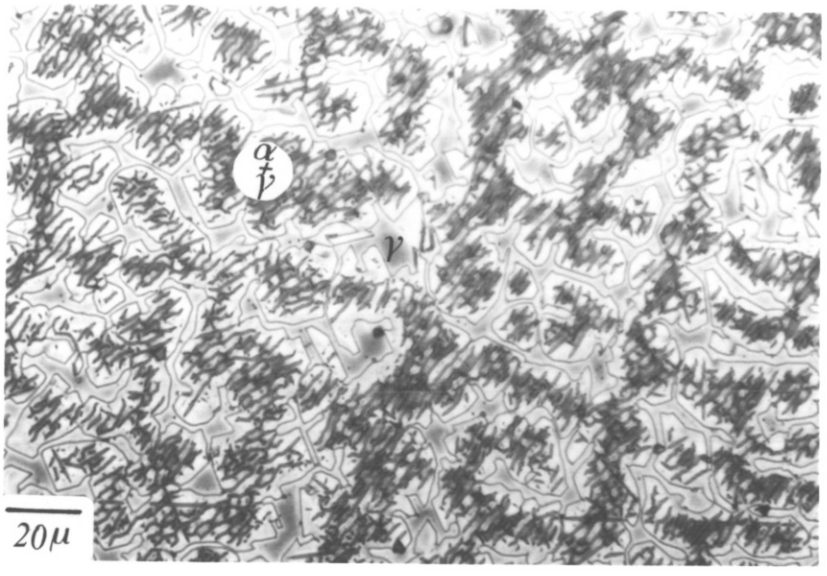

a

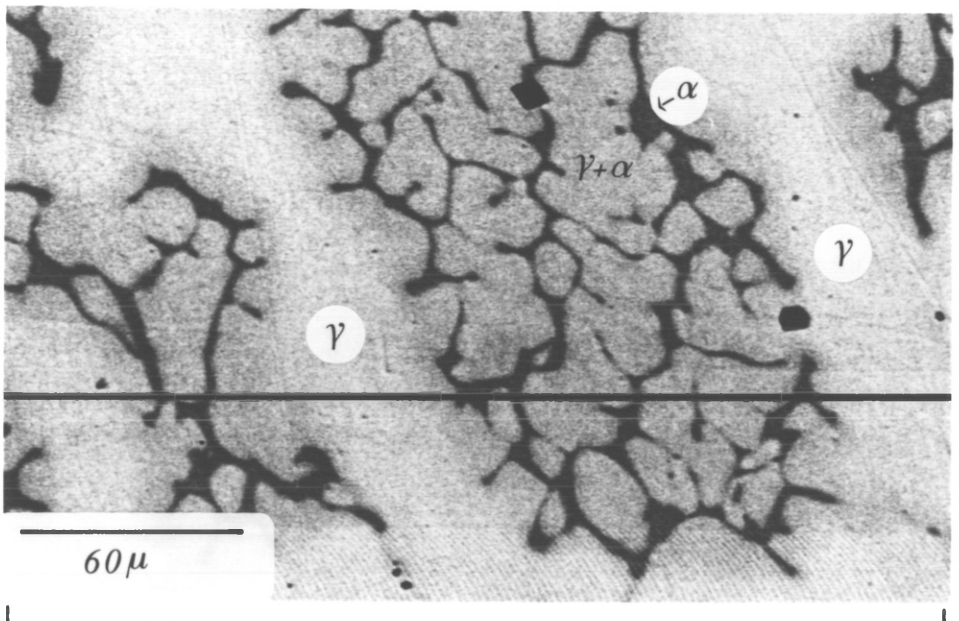

b

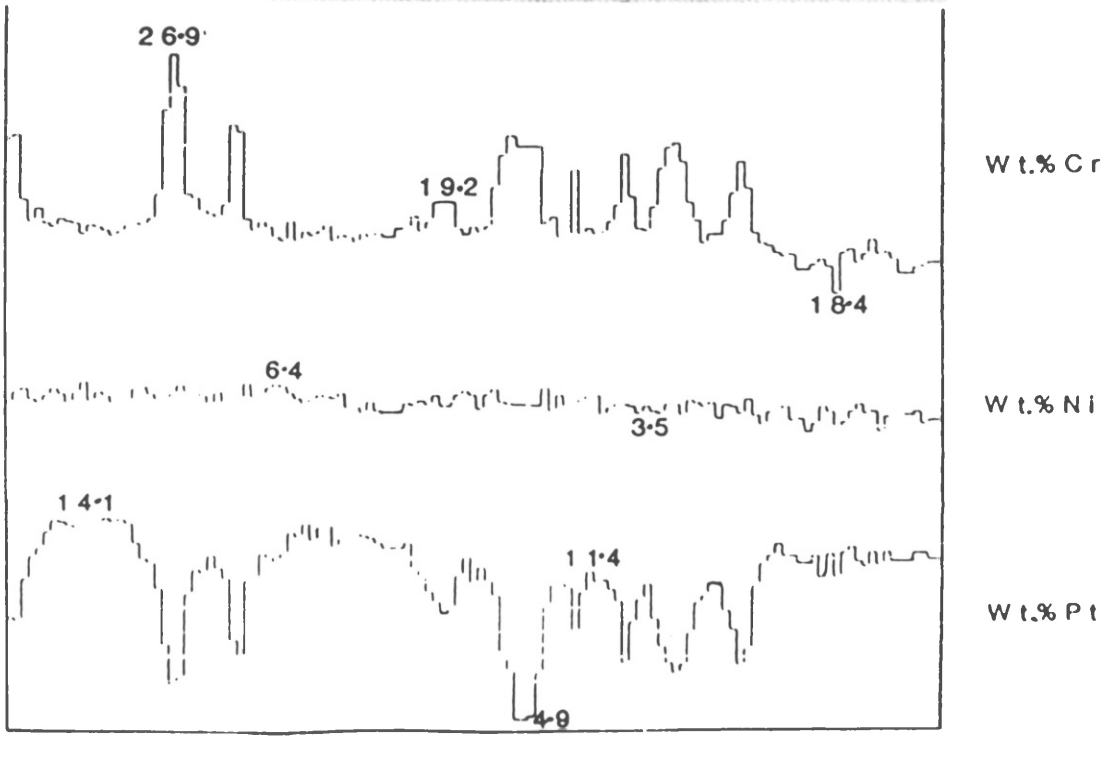

c

4.1.4. SEM Chemical Analysis

Here the use of elemental linescan analysis and additional quantitative point analyses along the line traversed by the electron beam have provided valuable microchemical information. Importantly it has characterised the partitioning of platinum group elements and their possible synergistic effects with Cr and Ni. Four alloys microstructurally described earlier, have been studied. Alloys 21/6/8Pd (Figure 68), 18/6/8Pd (Figure 69) and 18/6/8Pt (Figure 71) illustrate γ-austenite freezing whilst alloy 21/6/8Ru (Figure 70) illustrates a ferritic mode of freezing. For alloy 18/6/8Pt in Figure 71 the SEM micrograph shows the intercellular ferrite regions (dark) to separate the γ dendrite arms which is an intermetallic phase (light) rich in Pt and Ni. In many of the micrographs, black precipitates were seen and identified as being SiC particles originating from mechanical polishing. An understanding of the as-cast structures in Figures 68-71 can be made via the liquidus projection of the Fe-Ni-Cr system in Figures 72 and 73. The series of alloys in this study containing 6wt%Ni, 21 and 18wt%Cr, place them close to the eutectic region of this projection on the α-ferrite side as indicated.

4.2. Discussion

4.2.1. Significance of Solidification Mode and Alloy Composition

The practical significance of this study lies in the fact that where different solidification modes are possible in stainless steels, a change from primary delta-ferrite solidification to primary austenite, results in an increase in hot-cracking susceptibility (197,198) in weld material. Further, hot workability (99,199) and the formation of non-metallic inclusions (200) are dependent to a greater or lesser extent on whether the alloy solidifies primarily as austenite or ferrite. The effect of PGM's on these different modes of solidification might therefore be significant for commercial duplex alloys.

Alloy composition exercises the primary effect on solidification mode. There are two critical values for the ratio of Cr-Eq/Ni-Eq: 1.5 and 2.0. If the Cr-Eq/Ni-Eq < 1.5 solidification is as single phase austenite and if > 2.0, single phase ferrite predominates (94-99). (See Figures 62 and 64). These two values in fact correspond to compositions lying on either side of primary solidification path observed in the Fe-Ni-Cr ternary liquidus projection, Figures 72 and 73 (9). A section through the Fe-Ni-Cr system at 70%Fe (Figure 64) shows

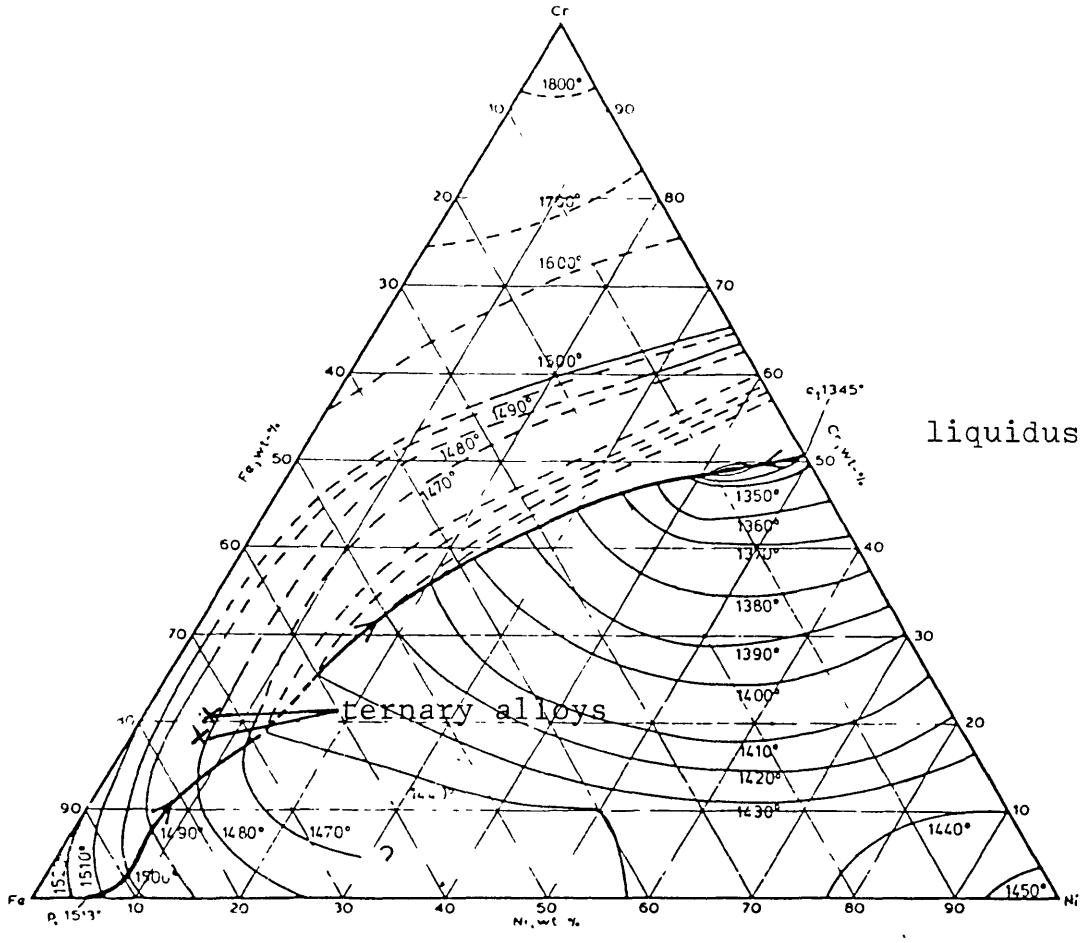

liquidus projection

Figure 72.

Refs. 22, 40, 41.

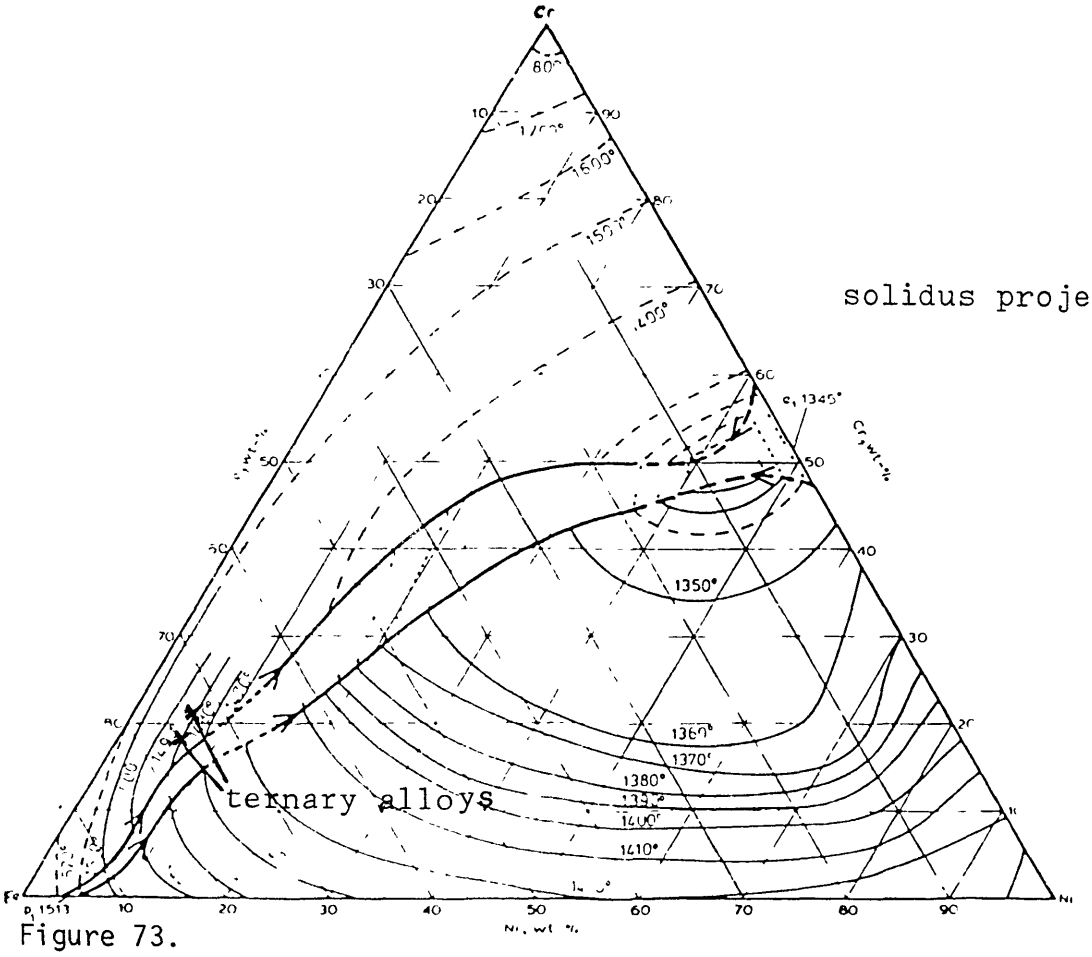

solidus projection

Figure 73.

Ref. 22.

that a number of solidification modes are possible.

1) Single phase austenitic solidification $L \rightarrow \gamma + L \rightarrow \gamma$

2) Austenitic-ferritic solidification $L \rightarrow \gamma + L \rightarrow L + \alpha + \gamma \rightarrow \alpha + \gamma$

3) Ferritic-austenitic solidification $L \rightarrow L + \alpha \rightarrow L + \alpha + \gamma \rightarrow \alpha + \gamma$

4) Single phase ferritic solidification $L \rightarrow L + \alpha \rightarrow \alpha \rightarrow \alpha + \gamma$

The Cr-Eq/Ni-Eq has therefore been used to predict the modes of solidification in this study and is referred to in Figure 63.

4.2.2. Microstructural Features

Alloys which have shown a ferritic solidification mode have been characterised via light and scanning electron microscopy and are shown in Figures 65 and 66a,b,c,f. These microstructures show that when a ferrite stabilizer, i.e. Cr, dominates the composition of an alloy, e.g. 21/6/ 2Pd and 21/6/2Pt (Figures 66b,d), α-ferrite is the first to crystallize from the liquid. It grows to form the conventionally shaped columnar grains. On cooling to room temperature, this α-ferrite is seen to become metastable, and to partially transform to austenite. The austenite is seen as an acicular phase both at grain boundaries, Figures 65 and 66a, and proceeding into ferrite grains. Leon and Kerr (201) propose that this solid state ferrite to austenite transformation occurs by a diffusion controlled process in which nickel diffuses towards and chromium away from the advancing austenite/ferrite interface. Detection of this was not possible by microprobe analysis. Further studies by Lippold (82,83) suggest that primary α-ferrite can transform to austenite (in zones 2 and 3 of Figure 64) by a massive transformation in the solid state, which produces a polymorphic phase change and can occur during rapid cooling. The transformation is characterised by the fact that the parent (α-ferrite) and product (austenite) phases have the same chemical composition but differ in crystal structure. The formation of this particular microstructure has not been observed in the alloys investigated in this study. It is clear that whilst Figures 65 and 66 show alloys solidified by the reaction $L \rightarrow L + \alpha \rightarrow \alpha \rightarrow \alpha + \gamma$, no evidence of a massive transformation (typically characterised by new large irregularly shaped grains) is seen. In fact other authors (89,201) report that this massive transformation is unlikely to occur except when very high cooling rates are observed with high energy processes like electron beam or laser welding. The feature of $\alpha \rightarrow \gamma$ solid state transformation is however increased by the additions of Pt, Pd, Ru in Figures 65b,d and f; indeed they have served

to lower the Cr-Eq/Ni-Eq ratio allowing austenite to nucleate at high temperatures.

Alloys which show an γ-austenitic mode of solidification have also been characterised via light and scanning electron microscopy. They are typified by a morphology of primary dendrites separated by ferrite regions, e.g. Figure 71. This morphology has been further characterised by several authors (82-84,99,201) using STEM and TEM and reveals the interdendritic eutectic-ferrite (found in hot-cracked sensitive welds) to have sharp or stepped facets with its γ-austenite interface.

4.2.3. Microchemical Features

Compositions on the nickel-rich side of the eutectic liquidus, Figure 72, will solidify as primary austenite. If the composition is sufficiently far from the eutectic composition, solidification will occur completely as austenite. The first solid, rich in nickel and depleted in Cr, will form as cells or as dendrites advancing into the liquid, rejecting Cr and absorbing Ni. This drives the liquid composition to the eutectic composition as solidification proceeds. As the amount of liquid is small, it forms a divorced eutectic of ferrite + austenite phases. This eutectic or intercellular ferrite is confined to the interdendritic γ solidification cell boundaries (59) and is typified by the structures seen in Figure 71. Although the nominal compositions for these alloys lies on the Cr-rich side of the eutectic liquidus, the expected primary ferrite solidification is not evident. Instead the additions of 8wt%Pd (Figures 68 and 69) and Pt have modified the thermodynamics and phase diagram so as to follow a solidification path close to, but to the right of the liquidus eutectic trough on the liquidus projection in Figure 72 (and to the left in the pseudo-binary section in Figure 64). This corresponds to mode 1 freezing, where the solidification reaction is:

$$L \rightarrow \gamma + L \rightarrow L + \alpha + \gamma \rightarrow \alpha + \gamma$$

The result is the formation of primary austenite dendrites rich in Pd or Pt and Ni, separated by Cr-rich ferritic regions.

Compositions on the Cr-rich side of the eutectic liquidus of the liquidus projection will conversely solidify as primary ferrite. α-ferrite forms first and is rich in Cr and depleted in Ni relative to the bulk composition and even more so, relative to the eutectic composition.

Again the liquid composition will be driven towards the eutectic. The final liquid to solidify will again do so as a divorced $\gamma + \alpha$ eutectic. The primary α phase which forms at the cell or dendrite core will be stable at room temperature because of its high Cr content. Subsequent α which forms will be less stable and most will transform to γ. This corresponds to mode 2 solidification, Figure 64. The ferrite that forms is known as vermicular (87-92) and is distinguished from eutectic ferrite (59) in mode 1 by a higher Cr content and forming at the core of dendrites. No evidence of vermicular was observed in this present study. As the Cr-equivalent is increased, ferrite predominates, and the alloy moves into the mode 4 solidification region in Figure 64, far from the pseudobinary eutectic region. The majority of the alloys in this study follow this solidification path, i.e. the base alloys and those containing 2wt% PGM and 8wt%Ru. The reaction that predominates is $L \rightarrow \alpha + L \rightarrow \alpha \rightharpoonup \alpha + \gamma$. No chemical analysis of the Widmanstatten austenite colonies and ferrite matrix was made since back scattered image contrast did not permit phase identification for X-ray EDS analysis, i.e. there was little local chemical difference between the solid state γ and α phases.

The general observations from these microchemical measurements are as follows:

1) From linescan analysis of PGM modified duplex alloys in Figures 68-71.

(a) Pd and Pt have partitioned to the dendritic regions of γ which is the first to solidify from the melt and promote an austenitic mode of freezing.

(b) Ru partitions less strongly to the austenite phase which solidifies as the secondary phase in a ferrite matrix. Ru does not strongly promote austenitic solidification.

(c) Cr partitions to the interdendritic regions very strongly with Pt or Pd modified alloys in a synergistic manner. In this case, the ferrite phase is last to solidify.

(d) No significant variations in Ni content were detected in the linescan analysis. However, from point analysis, Ni is found in the main to be associated with Pd and Pt in the austenite phase.

2) Alloys which solidify in mode 4 by ferritic freezing develop negligible chemical variations across Widmanstatten γ and α grains as detectable by X-ray EDS analysis.

Partitioning coefficients, (below) , of selected alloys in this study show that Pt and Pd in particular partition heavily to austenite such that interdendritic regions are additionally enriched in Cr.

Analysed Partitioning Coeff. $K = \frac{\text{wt\% element in } \gamma}{\text{wt\% element in } \alpha}$

Alloy	Cr	Ni	Pt	Pd	Ru
18/6/8Pt	0.84	1.38	1.87	-	-
21/6/8Ru	0.78	1.64	-	-	1.14
21/6/8Pd	0.75	1.70	-	2.30	-
18/6/8Pd	0.69	1.96	-	3.97	-

Rapid quenching of molten drops by Arata et al (80) and Lippold (82,83) on fully austenitic and duplex stainless steels indicate that both chromium and nickel are rejected to the liquid during primary γ-austenitic solidification. The dendrite cores were thus depleted in chromium and nickel. It is also noted that chromium partitions more heavily than nickel and that diffusion processes are more sluggish in austenite than in ferrite (80).

Another reported (201) feature of the eutectic or intercellular ferrite (59) formed here, is the increased tendency for small precipitates to form at the austenite/eutectic ferrite interface. TEM investigations by Leon and Kerr (201) revealed that precipitates, occurring at the stepped interfaces, were enriched in Cr and Mo. Clearly this is caused by the rejection of elements ahead of the moving austenite/liquid interface. Alloys 21/6/8Pd (Figure 68), 18/6/8Pd (Figure 69) and 18/6/8Pt (Figure 71) therefore typify γ-austenitic solidification where the ferrite (dark in contrast) is located at dendrite interstices supporting the hypothesis that it forms from the liquid as a divorced-eutectic phase during the terminal stages of solidification (59). Figure 70 shows the microstructure of alloy 21/6/8Ru, and in contrast this alloy typifies compositions that lie on the Cr-rich side of the eutectic liquidus where the primary phase to form is ferrite. Clearly then in this instance, Ru has not been able to promote austenitic freezing.

The use of the liquidus projection in this study to understand solidification paths, has serious shortcomings. The main one is, that where significant solid solubility occurs, accurate determination of compositions of solid and liquid phases co-existing is not possible and necessitates data on solidus tielines (202).

However, in practice this is not practical. If thermal analysis is used, the best that can be done is to cool the alloy very slowly with vigorous stirring until the temperature at which the first solid freezes, and then to maintain the alloy slightly below the temperature until equilibrium is obtained. Thus the main problems are to (1) ensure the liquid is completely mixed during freezing, (2) that the freezing is slow enough that only a slight departure from kinetic equilibrium exist at the solid/liquid interface, and (3) diffusion in the solid occurs at a negligible rate compared to the rate of freezing (203).

However, the use of the Cr-Eq/Ni-Eq ratio with X-ray EDS analysis and metallographic examination of microstructures, is thought to give a reasonable indication of solidification reactions occurring during alloy freezing (99).

4.2.4. Implications of PGM Additions

Since these studies show that additions of PGMs, Pd and Pt in particular, to selected duplex alloys result in primary austenitic solidification, poor weld stability, e.g. hot-cracking and workability, would result. This clearly would constitute a major problem for commercial duplex alloys, since it is the alloys in region 1 of Figure 64 which are prone to hot-cracking (59). They have a residual ferrite content (less than 5%). The ferrite which is present, is the last material to solidify and is enriched in impurities, particularly S and P, which expands the freezing temperature range and promotes hot cracking (204-209).

The composition of austenitic stainless steel filler metal is generally chosen so that the weld metal will contain 5-10% ferrite. Type 308 stainless steel (20Cr-10Ni wt%) is an example of a weld metal which is clearly hyper-eutectic (regions 2-4 in Figure64).
In general the more residual ferrite the more hyper-eutectic the alloy and the more P and S that can be tolerated without cracking (59).

CHAPTER FIVE

PHASE CONSTITUTION

The things that we see to be hard and
dense must needs consist of particles more
mutually hooked and must be deeply held
compact by branch-like elements

(Lucretius, De rerum natura)

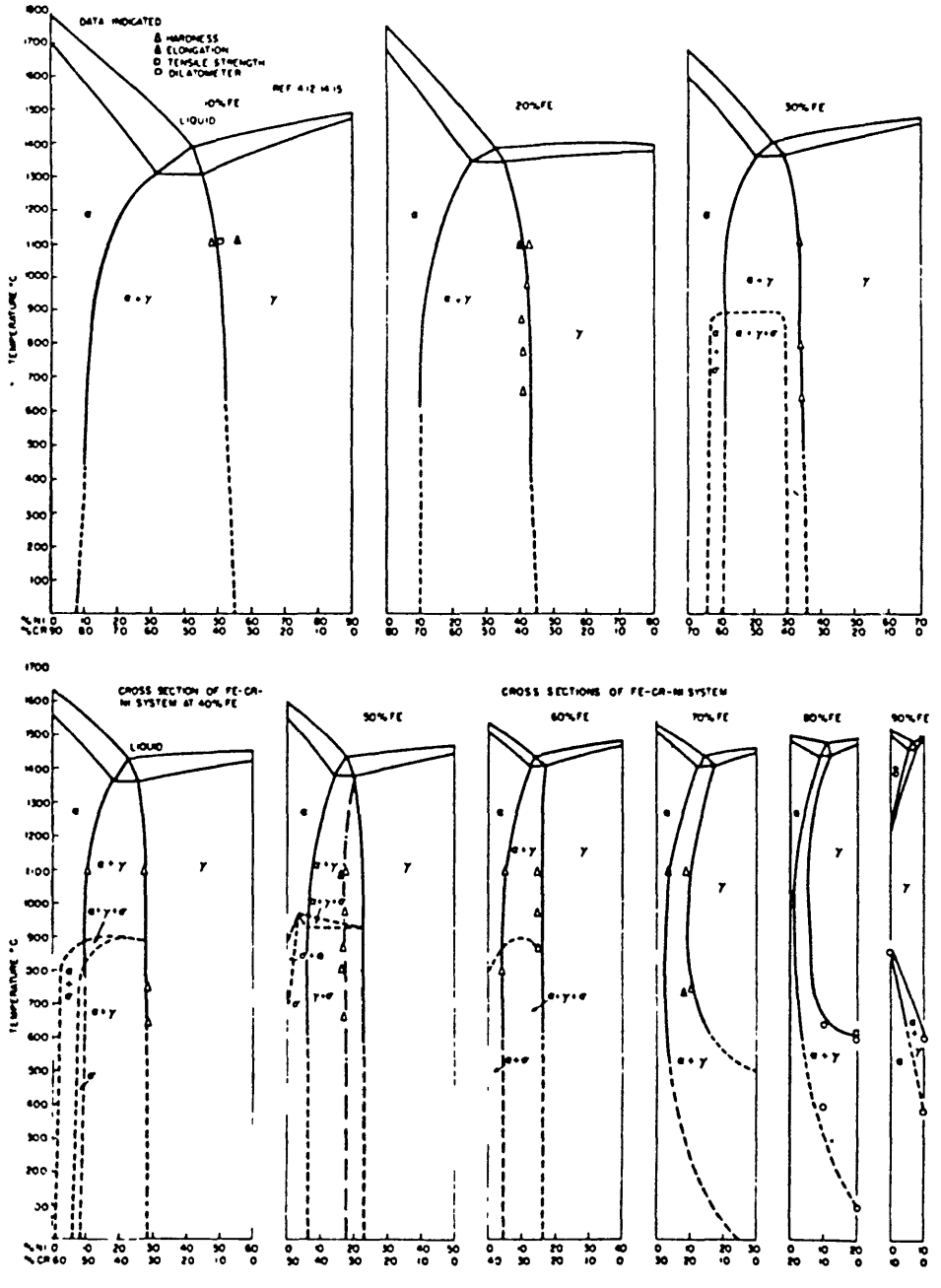

Cross sections of the Fe-Cr-Ni system

Figure 74. Ref. 38.

5.1. Introduction

Duplex stainless steels are those whose compositions place them in the $\alpha + \gamma$ phase field of the Fe-Ni-Cr system (59). Since as Figure 74 shows, the $\alpha/(\alpha + \gamma)$ and $\gamma/(\alpha + \gamma)$ phase boundaries for 70% Fe, are far from vertical; whether or not an alloy resides in the $\alpha + \gamma$ field depends upon what temperature is considered. The structure is often developed by hot working at an elevated temperature (typically 1000-1200°C) to produce a wrought steel with a structure that can be characterised as bands of α and γ which are elongated in the working direction. The ferrite bands are often polycrystalline (59).

In this present study, the alloys have been placed in two series of base compositions 18wt%Cr-6wt%Ni (Figure 81) and 21wt%Cr-6wt%Ni (Figure 79). These compositions give Cr an Ni-equivalents which are placed on the Schaeffler (42) diagram (Figure 75) and on the modified diagram (Figure 76), from Pryce and Andrews (210) for wrought alloys. The Schaeffler (42) diagram developed for weld metal, is only strictly applicable to rapidly cast and cooled alloys. The modified diagram (210) was developed for steels working at 1150°C. Nonetheless, together, they give an idea of the amount of ferrite expected in these alloys. The effects of platinum group metals (PGMs), Pt, Pd and Ru on the constitution of these selected duplex alloys have been investigated and effectively characterised using light, scanning and transmission electron microscopy. In particular, the effect of 2 and 8wt% Pt, Pd and Ru PGMs on microstructure and chemistry has been studied. Solution treatments of 1300°C, 1250°C and 1000°C, and ageing between 650°C and 950°C have been used. A wide range of microstructure are observed and are characterised in Figures 79 and 81, highlighting the effect of temperature on ferrite volume fraction via light microscopy. Additional studies on σ and more particularly γ_2 have been made via light microscopy and TEM.

5.2. Results

5.2.1. Microstructural Characterisation

5.2.2. 21/6 Alloy Series

Volume Fraction

Referring to Figure 78a analysis of alloy S1, 21/6, revealed the composition to be nearer 19Cr-6Ni which accounts for the low volume

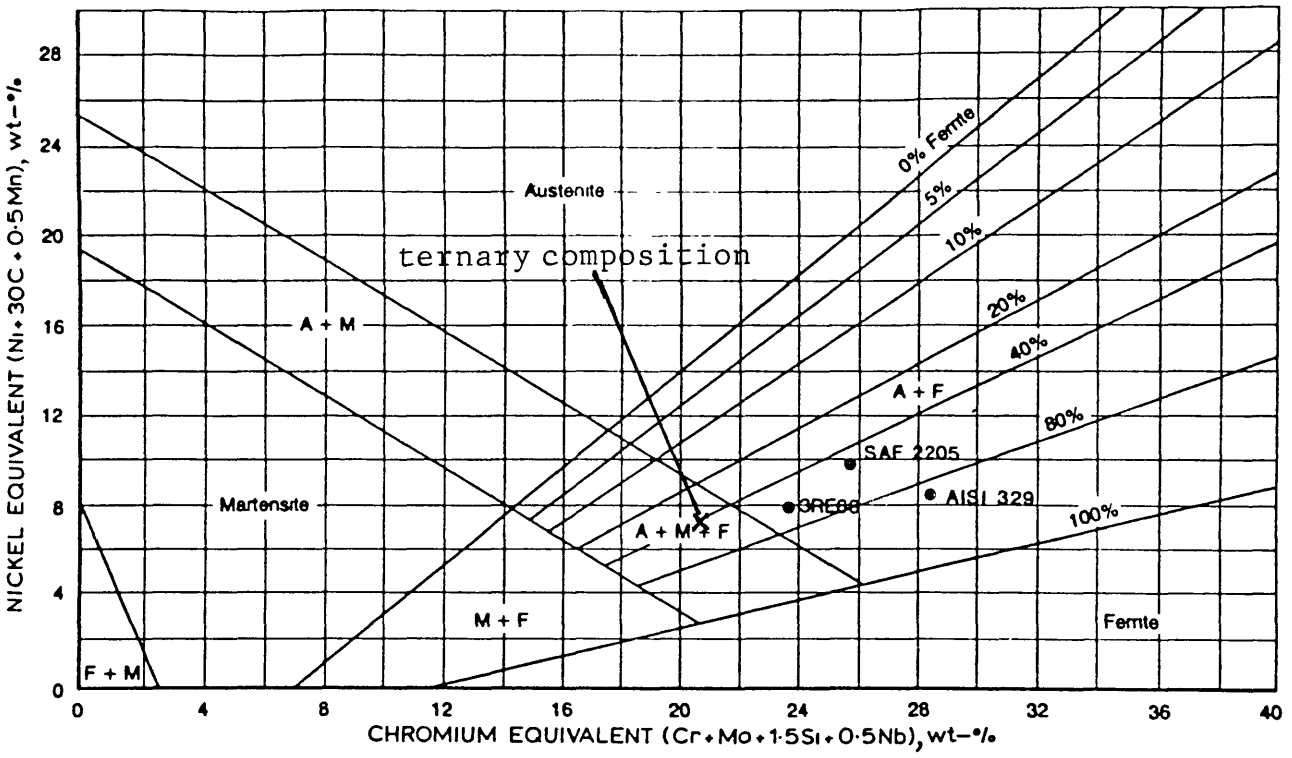

Modified Schaeffler diagram giving microstructural compositions as function of steel Cr and Ni equivalents

Figure 75. Ref. 9.

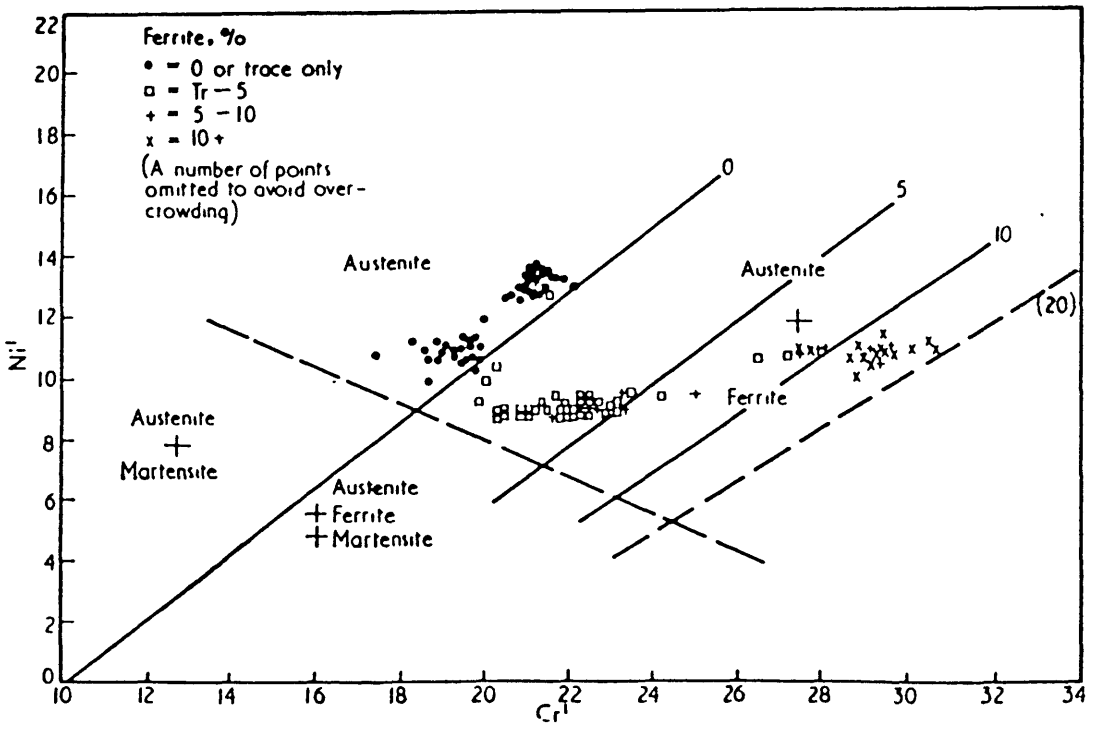

Schaeffler type diagram for wrought alloys, hot worked at 1150 °C

Figure 76. Ref. 210.

Figure 77.

TYPICAL OF A SOLID STATE TRANSFORMATION, IS THE MORPHOLOGY OF A WIDMANSTATTEN PRECIPITATION OF ϵ-MARTENSITE IN γ-AUSTENITE IN ALLOYS, 18/6/8Pt & 21/6/8/Pt, WATER QUENCHED FROM A 1250°c SOLUTION TEMPERATURE.

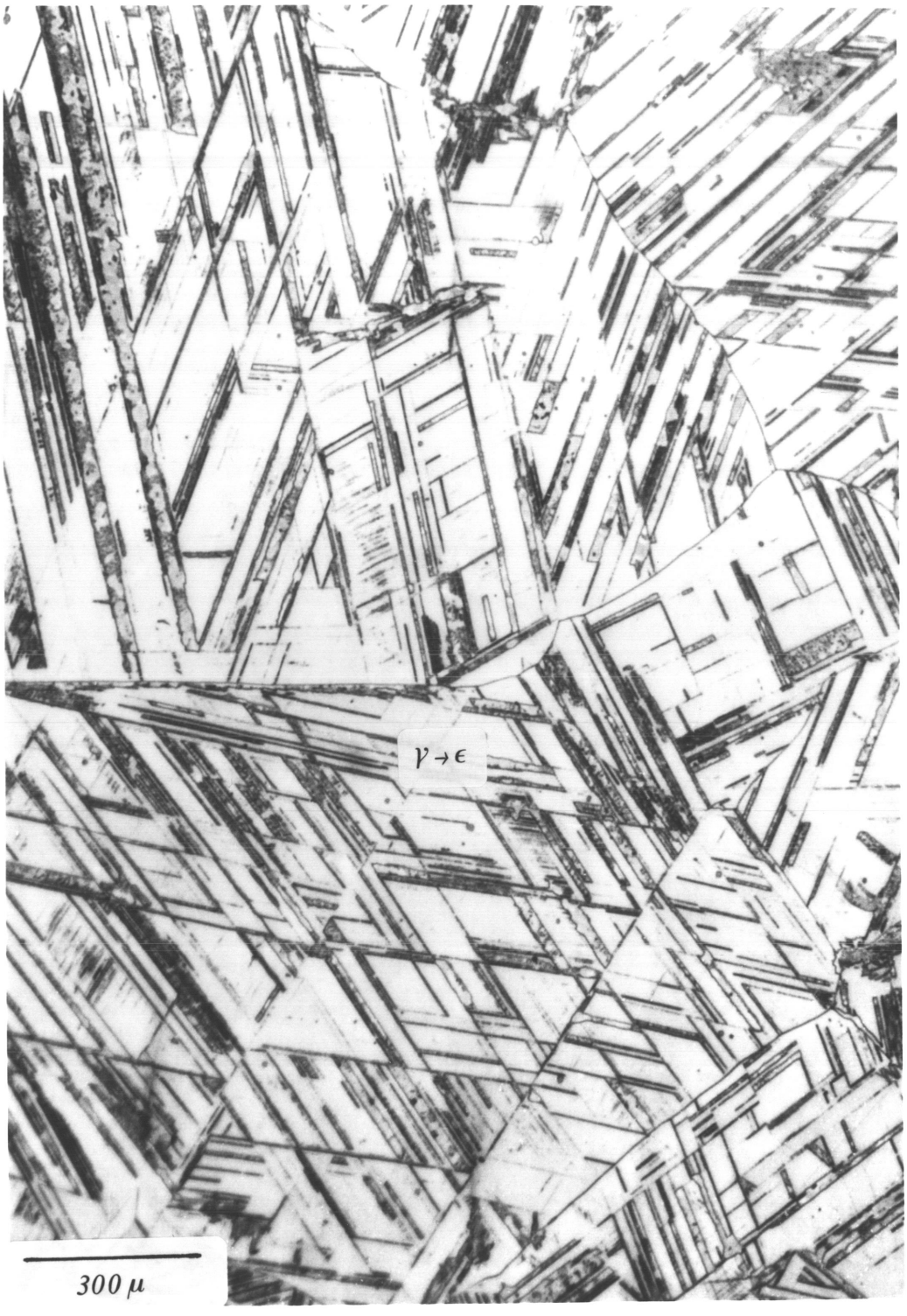
γ → ε
300 μ

Figure 78.

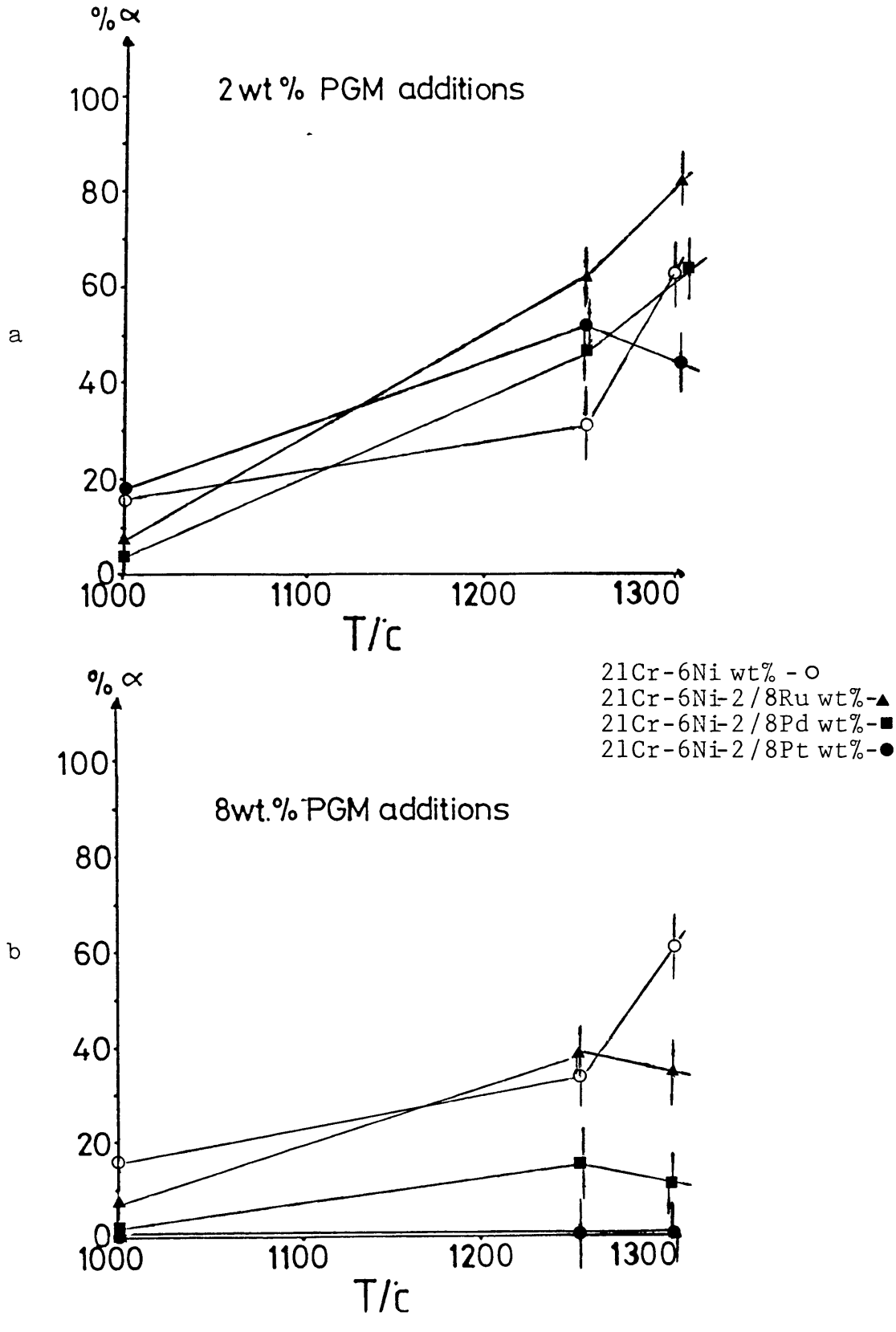

21/6 alloy series

Ferrite volume fraction determined by point counting as a function of annealing temperature.
Annealing times ranged from 24 to 70 hours.

Figure 79. Light micrographs of the 21Cr-6Ni alloy series, solution treated at 1250°C for times of up to 70 hours. All alloys were etched electrolytically in a solution of 10% oxalic acid.

(a) Actual alloy composition is 19Cr-6Ni shows a duplex structure of ferrite angular grains with austenite grains.

(b) The duplex structure shows austenite particles in a ferrite matrix (light), and nucleated at α grain boundaries.

(c) The austenitic structure shows partial transformation to martensite on cooling to room temperature.

(d) The duplex structure shows austenite at α grain boundaries and within α grains.

(e) The duplex structure shows isolated pools and stringers of ferrite in an austenite matrix.

(f) The duplex structure shows austenite nucleated as a continuous film at α grain boundaries and within the ferrite matrix.

(g) The duplex structure shows angular particles of ferrite in an austenite matrix (light in contrast).

21/6 ALLOY SERIES

21wt%Cr-6wt%Ni-Fe bal.

(a)

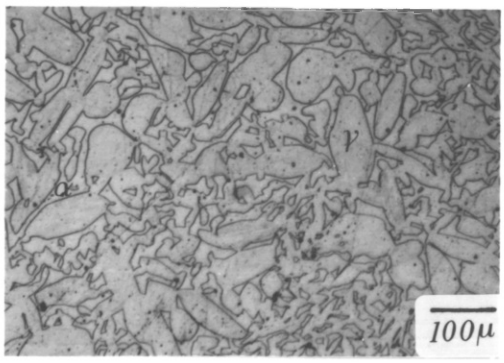

21wt%Cr-6wt%Ni-2wt%Pt-Fe bal.

(b)

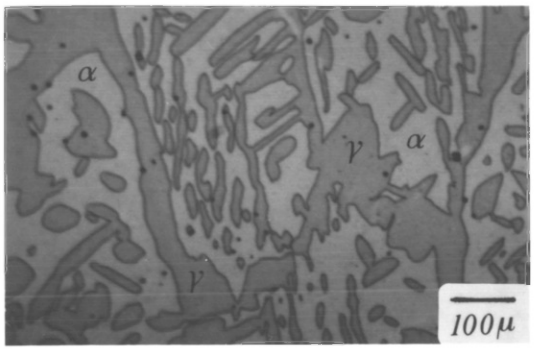

21wt%Cr-6wt%Ni-8wt%Pt-Fe bal.

(c)

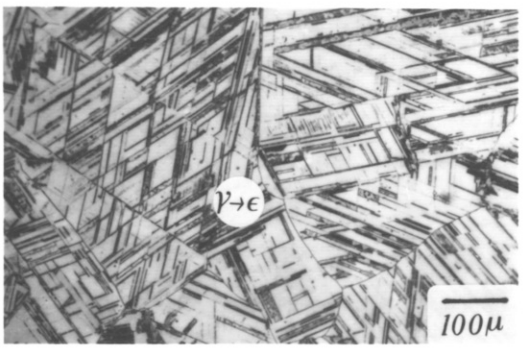

21wt%Cr-6wt%Ni-2wt%Pd-Fe bal.

(d)

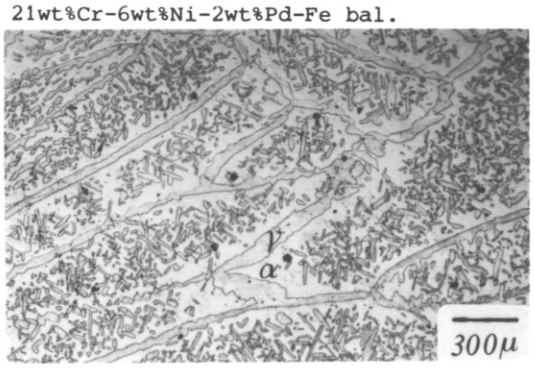

21wt%Cr-6wt%Ni-8wt%Pd-Fe bal.

(e)



21wt%Cr-6wt%Ni-2wt%Ru-Fe bal.

(f)

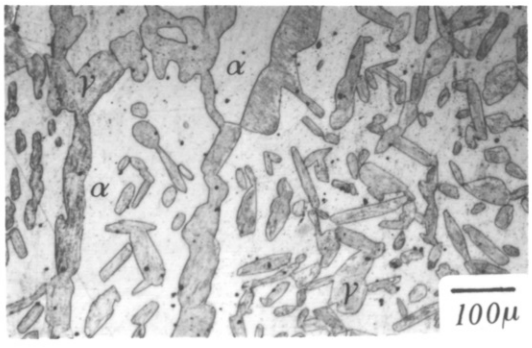

21wt%Cr-6wt%Ni-8wt%Ru-Fe bal.

(g)

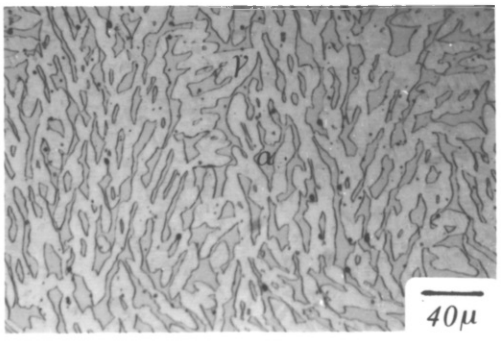

fraction of ferrite. Considering Figure 78b it is noted that even at the 8%PGM level, both Pd and Ru containing alloys have significant amounts of ferrite present in contrast to the 18/6 series (Figure 80b). Only Pt is able to produce a fully austenitic structure at the 8wt% level.

Microstructure

The base alloy solution treated at 1250°C (Figure 79a) shows a duplex structure of angular particles of ferrite and austenite. 2wt% additions of Pt, Pd and Ru to this alloy in Figures 79b,d and f show essentially similar structures of austenite occupying original α-ferrite grain boundaries and precipitated as elongated grains within the ferrite matrix.

The addition of 8wt% PGMs (Figures 79c,e and g) to this series causes austenite to be the primary matrix phase typically in alloys 21/6/8Ru (Figure 79g) and 21/6/8Pd (Figure 79e), ferrite existing as isolated angular or rounded grains. The 21/6/8Pt alloy (Figure 79c) however is fully austenitic. Each large grain shows Widmanstatten precipitation of extremely parallel sided plates which has occurred on cooling to room temperature: this morphology is consistent with a martensitic transformation of the ε-martensite type.

5.2.3. 18/6 Alloy Series

Volume Fraction

At the 2% PGM level, increasing the temperature from 1000°C to 1300°C causes the volume fraction of ferrite to increase for Pt, Pd and Ru additions (Figure 80a) whilst at the 8% PGM level, austenite is the phase which predominates, excluding any ferrite over the temperature range 1000 to 1300°C (Figure 80b).

Microstructures

The microstructure of the base alloy (Figure 81a) is very similar to the 21/6 alloy with a mixture of angular particles of ferrite and austenite co-existing. The addition of 2wt% PGMs to this base alloy causes austenite to dominate as the primary phase. Ferrite exists as isolated grains (Figures 81b,d and f).

The additions of 8wt% PGMs to this base alloy in Figures 81c,e and g results in a fully austenitic structure in each case. Large grains

Figure 80.

a

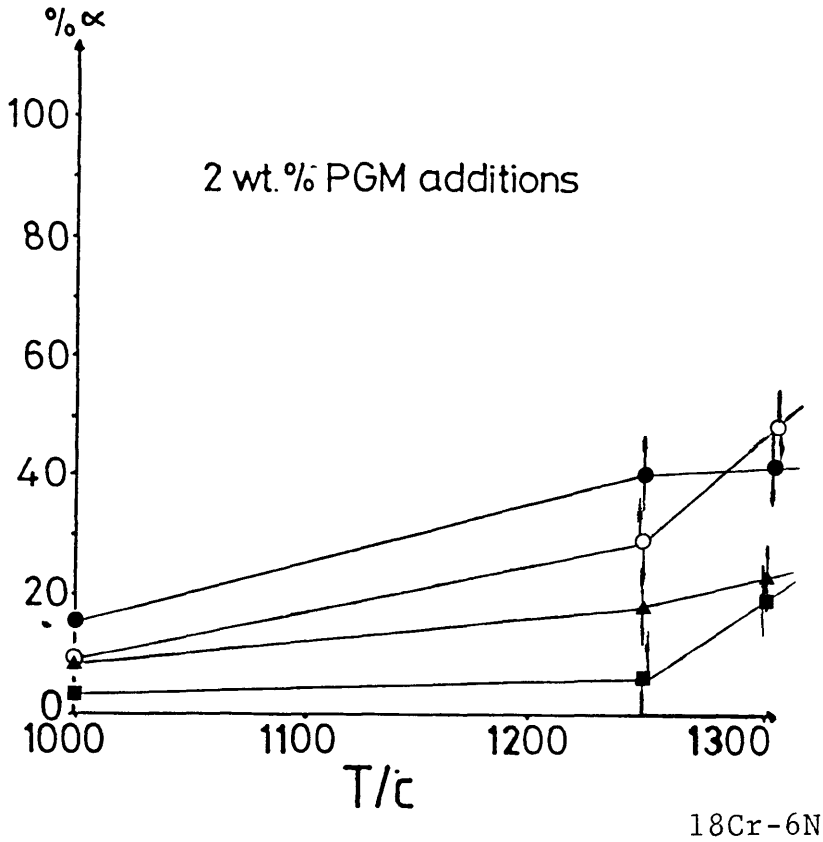

18Cr-6Niwt%-o
18Cr-6Ni-2/8Ru wt%-▲
18Cr-6Ni-2/8Pd wt%-■
18Cr-6Ni-2/8Pt wt%-●

b

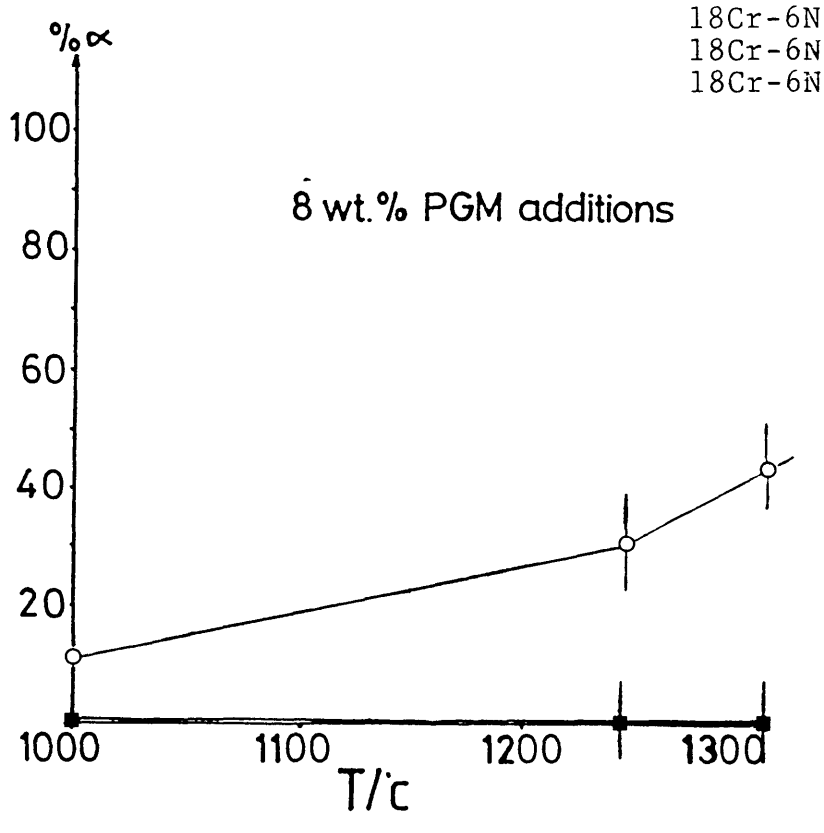

18/6 alloy series

Ferrite volume fraction determined by point counting as a function of annealing temperature.
Annealing times ranged from 24 to 70 hours.

Figure 81 Light micrographs of the 18Cr-6Ni alloy series, solution treated at 1250°C for times of up to 70 hours. All alloys were etched electrolytically in a solution of 10% oxalic acid.

(a) The duplex structure shows angular grains of ferrite and rounded grains of austenite (shows partial transformation).

(b) Duplex structure of ferrite and austenite phases.

(c) The austenitic structure shows partial transformation to martensite on cooling to room temperature.

(d) Angular grains of ferrite (6% volume fraction), in an austenite matrix which shows partial transformation to martensite.

(e) Large grains of austenite contain needle-like features indicating a shear transformation on cooling to room temperature.

(f) The duplex structure shows angular particles of ferrite within an austenite matrix.

(g) Large polyhedral grains of single phase austenite, show partial transformation on cooling to room temperature.

18wt%Cr-6wt%Ni-Fe bal.

(a)

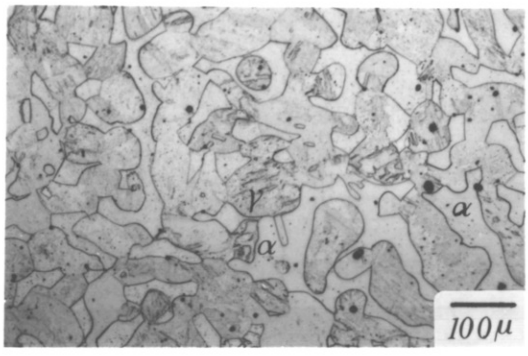

18wt%Cr-6wt%Ni-2wt%Pt-Fe bal.

(b)

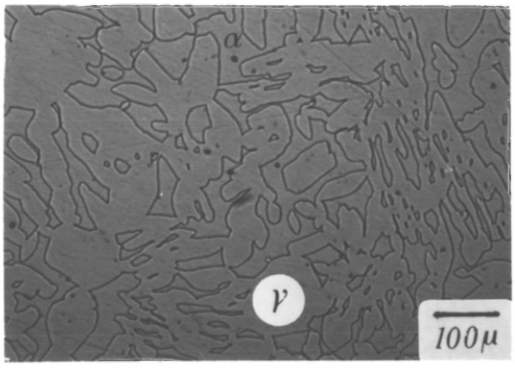

18wt%Cr-6wt%Ni-8wt%Pt-Fe bal.

(c)

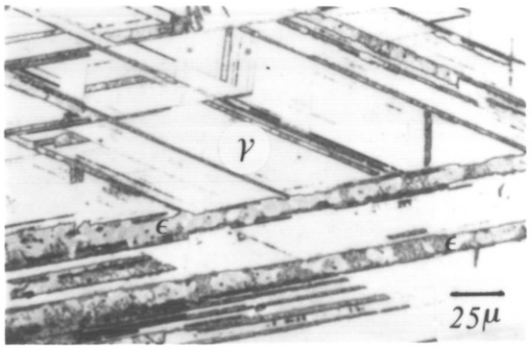

18wt%Cr-6wt%Ni-2wt%Pd-Fe bal.

(d)

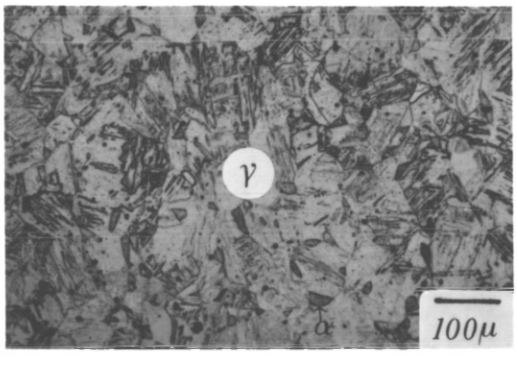

18wt%Cr-6wt%Ni-8wt%Pd-Fe bal.

(e)

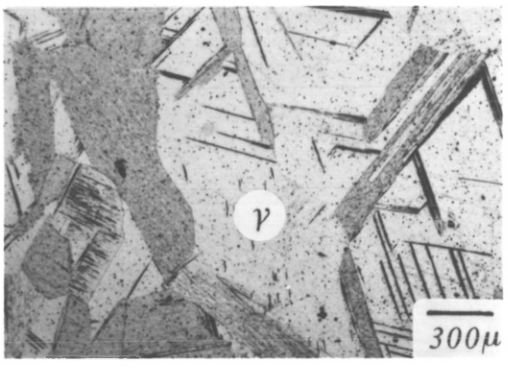

18wt%Cr-6wt%Ni-2wt%Ru-Fe bal.

(f)

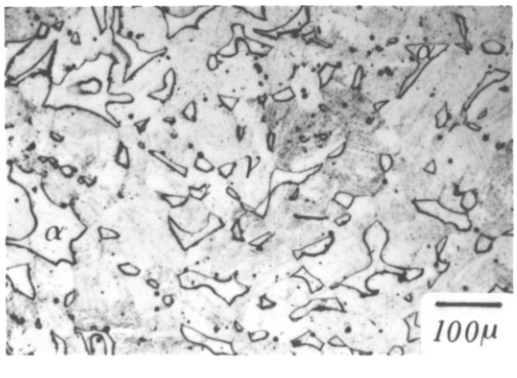

18wt%Cr-6wt%Ni-8wt%Ru-Fe bal.

(g)

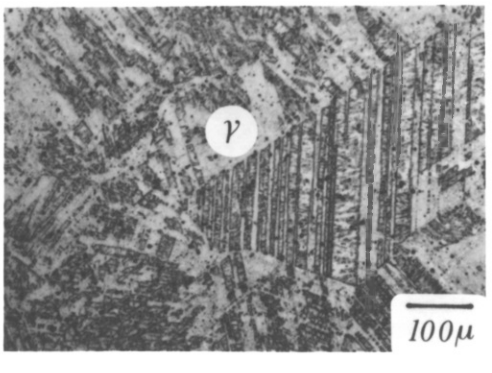

of γ-austenite exist in alloy 18/6/8Pd, Figure 81e. Solution treatment and water quenching has resulted in 'needle' like features within the γ -austenite grains. These 'burst' plates indicate the occurrence of a diffusionless shear transformation on cooling to room temperature. The 18/6/8Ru alloy, Figure 81g, shows larger polyhedral grains of austenite which again show evidence of a diffusionless shear transformation on water quenching.

Two additional characteristic phases have been noted and studied in the constitution of these duplex alloys:-

5.2.4. Sigma - σ precipitation

The first, the intermetallic sigma phase, will be discussed in detail in a further chapter, but its presence is readily observable in many of the alloys in this present study. This is typified in alloy 21/6/8Ru aged at 650°C for 168 hours (Figure 84); the sigma phase grows by consuming the Cr-rich ferrite phase.

5.2.5. γ_2- austenite precipitation

The origins of γ_2 in duplex steels is described previously in the literature review. Special reference is made to Figure 95 since γ_2 has approximately the same composition as γ (59) and forms from reannealing (ageing) in the temperature range 900 - 600°C, where re-equilibration of α content occurs via a $\alpha \rightarrow \gamma$ transformation. Figure 82 shows the typical distribution and morphology of γ_2-austenite, as acicular grains that grow from and within ferrite grains. These acicular precipitates grow together eventually forming new regions of γ-austenite within ferrite. Ageing of duplex alloys shows γ_2-austenite to form before sigma in Figures 83a, and 83b,c. Additionally TEM studies show the γ_2-austenite which forms at low temperatures (<650°C) to precipitate as laths with a midrib separating faulted regions (Figure 83e).

5.2.6. Microchemical Characterisation

The microchemical characterisation of these selected alloys has been made via electron probe microanalysis using X-ray energy dispersive analysis. This has enabled tie-lines and phase boundaries to be established for the series of 'model' duplex alloys solution treated at 1300°C, 1250°C and 1000°C. These results are presented most

Figure 82. Alloy: 21Cr-6Ni.
Condition: hot rolled at 1000°C and annealed for 30 mins. at 1250°C. Electrolytically etched in concentrated NaOH solution.

(a) The light micrograph shows the precipitation of γ_2 in ferrite for the alloy described above having subsequently been aged at 900°C for 5 minutes.

(b) Alloy: 21Cr-6Ni-8Ru.
Condition: Solution treated at 1250°C for 24 hours and subsequently aged at 650°C for 168 hours.
The transmission electron micrograph shows the precipitation of γ_2 as a lenticular grain separated by a midrib. This ageing treatment also results in σ precipitation shown in the micrograph.

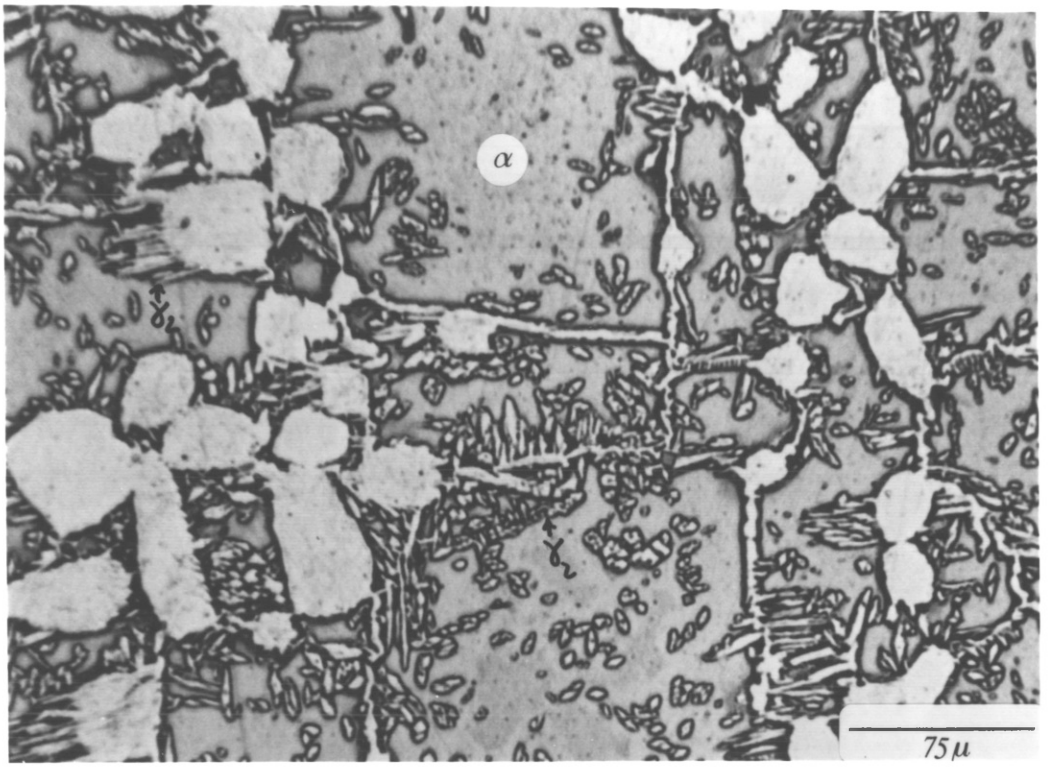

a

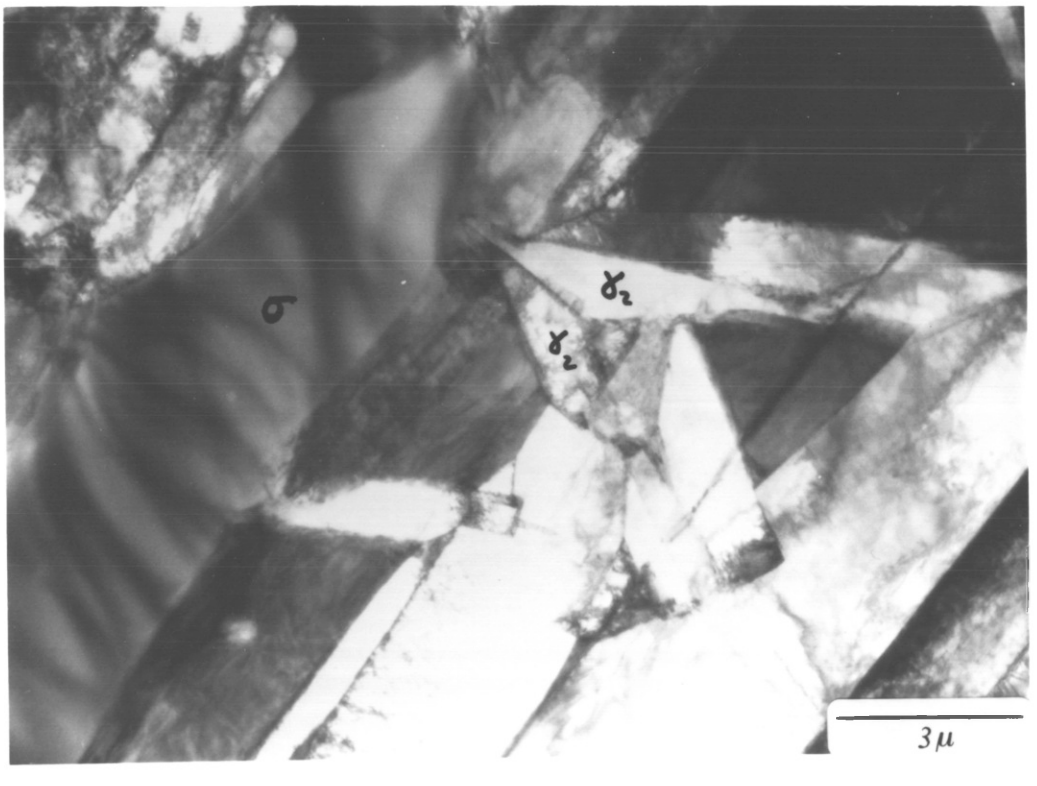

b

Figure 83.

(a) Alloy: 21Cr-6Ni-2Pd
Condition: Hot rolling of ingot at 1000°C is followed by a 30 minute anneal at 1250°C.
The microstructure shows bands of austenite and ferrite phases, electrolytically etched in 10% oxalic acid.

(b) Subsequent ageing of alloy in (a), at 950°C for 5 minutes shows γ_2 precipitation within α-ferrite grains.

(c) Ageing of alloy in (a), at 900°C for 5 minutes shows γ_2 precipitation prior to σ (black in contrast).

(d) Ageing of alloy in (b), at 800°C for 5 minutes shows no evidence of γ_2-austenite precipitation.

(e) Alloy 21Cr-6Ni-8Ru
Condition: Annealed at 24 hours at 1250°C.
The TEM micrograph shows that a low ageing temperature of 650°C (168 hours), results in γ_2-austenite precipitation which takes the appearance of a mid-rib separating faulted regions.

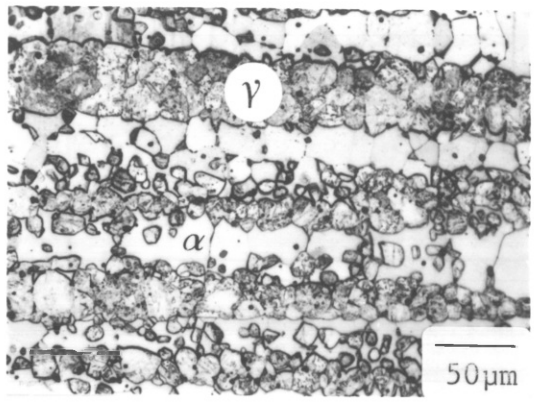

a

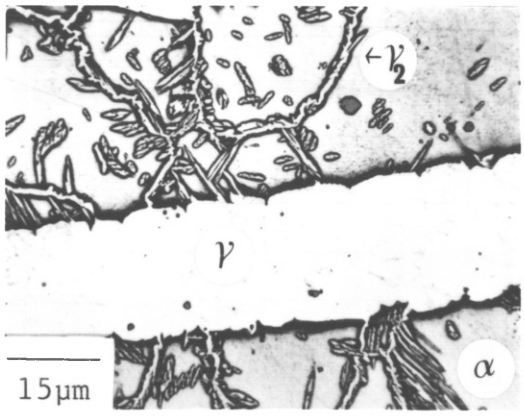

b

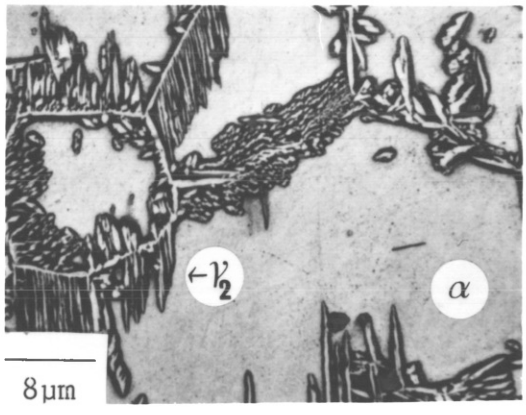

c

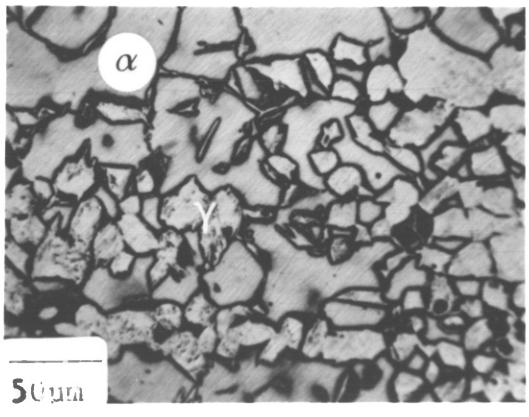

d

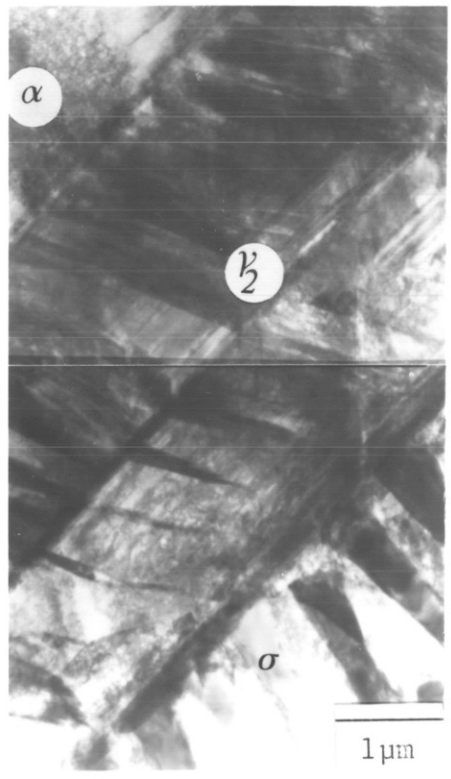

e

Figure 84.

Alloy: 21Cr-6Ni-8Ru

Condition: The thin foil TEM micrograph shows the structures developed in the above alloy, annealed at 1250°C and subsequently aged at 650°C for 168 hours.

(a) In this duplex alloy the α-ferrite has decomposed to σ.

(b) Selected area diffraction pattern from arrowed region in Fig. 84(a) with diagram of analysed pattern. $2\lambda L = 5.29$ Å cm

(c) The TEM micrograph shows areas in this alloy where α-ferrite has decomposed to a lamellar mixture of σ and γ phases.

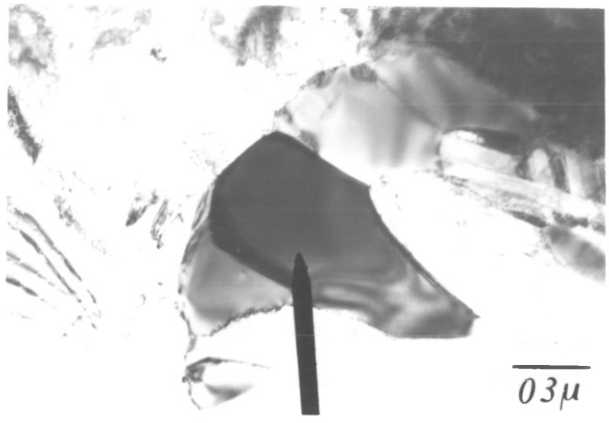

a

σ

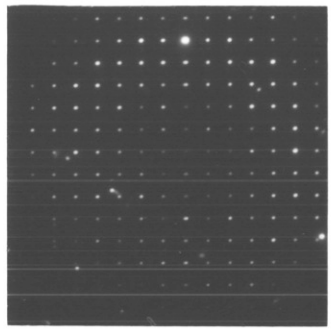

b



[0 0 1]σ

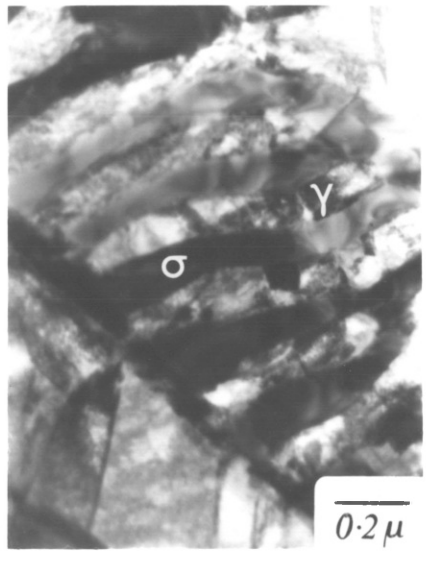

c

EDS Analysis of Alloy Compositions

Each value is an average of 3 separate point analyses, with an accuracy of ± 0.4 wt%

Figure 85. 1000°C Solution treatment

	Nominal Composition wt%				Austenite			Ferrite		
	Fe	Cr	Ni	PGM	Cr	Ni	PGM	Cr	Ni	PGM
S 1	Bal	21	6	-			-			-
S 2	"	18	6	-	18.05	6.50	-	24.21	3.18	-
S 3	"	21	6	2 Pt	19.38	7.40	2.44	25.76	3.73	0.93
S 5	"	18	6	2 Pt	17.65	5.35	2.51	20.41	4.30	1.50
S 7	"	21	6	2 Ru	19.35	7.24	2.53	23.35	4.69	2.22
S 8	"	21	6	8 Ru	20.36	6.32	7.99	27.89	3.43	7.18
S 9	"	18	6	2 Ru	18.30	6.51	2.10	20.03	5.27	2.30
S10	"	18	6	8 Ru	18.53	5.97	8.54		- - - -	
S11	"	21	6	2 Pd	19.68	6.2	2.50	25.31	3.86	1.48
S12	"	21	6	8 Pd	20.69	5.81	7.96	29.29	2.92	2.82
S13	"	18	6	2 Pd	18.40	6.04	2.22	21.63	4.69	1.49
S14	"	18	6	8 Pd	18.70	6.00	8.08		- - - -	

Figure 86. 1250°C Solution treatment

	Nominal Composition wt%				Austenite			Ferrite		
	Fe	Cr	Ni	PGM	Cr	Ni	PGM	Cr	Ni	PGM
S 1	Bal	21	6	-	17.29	6.35	-	20.2	4.78	-
S 2	"	18	6	-	17.78	6.46	-	21.1	4.67	-
S 3	"	21	6	2 Pt	19.28	7.04	2.73	23.51	5.02	1.53
S 5	"	18	6	2 Pt	17.00	5.89	2.65	20.33	3.81	1.69
S 7	"	21	6	2 Ru	19.17	7.11	2.47	23.2	5.13	2.14
S 8	"	21	6	8 Ru	20.08	6.64	8.59	24.62	4.84	7.89
S 9	"	18	6	2 Ru	18.33	6.28	2.26	22.1	1.43	2.01
S10	"	18	6	8 Ru	18.53	5.97	8.54	-	-	-
S11	"	21	6	2 Pd	19.45	7.30	2.67	23.58	5.03	1.64
S12	"	21	6	8Pd	20.49	4.11	8.24	25.84	5.93	4.87
S13	"	18	6	2 Pd	18.49	5.98	2.26	22.84	4.17	1.36
S14	"	18	6	8 Pd	18.70	6.00	8.08	-	-	-

Figure 87. 1300°C Solution Treatment

	Nominal Composition wt%				Austenite			Ferrite		
	Fe	Cr	Ni	PGM	Cr	Ni	PGM	Cr	Ni	PGM
S 1	Bal	21	6	-	17.61	6.26	-	20.33	4.49	-
S 2	"	18	6	-	17.52	6.36	-	20.31	5.01	-
S 3	"	21	6	2 Pt	19.25	7.24	2.16	22.68	5.31	1.86
S 5	"	18	6	2 Pt	17.32	5.36	2.70	20.08	4.16	1.74
S 7	"	21	6	2 Ru	18.81	7.09	2.14	22.24	5.40	2.08
S 8	"	21	6	8 Ru	19.84	6.57	8.60	23.30	4.86	7.88
S 9	"	18	6	2 Ru	17.66	6.29	2.30	20.06	4.82	1.65
S10	"	18	6	8 Ru	18.53	5.97	8.54	-	-	-
S11	"	21	6	2 Pd	19.15	6.38	2.67	22.46	5.21	1.88
S12	"	21	6	8 Pd	20.61	5.98	8.61	24.36	4.42	5.53
S13	"	18	6	2 Pd	18.02	6.18	2.01	20.92	4.75	1.54
S14	"	18	6	8 Pd	18.70	6.00	8.08	-	-	-

Figure 88. PGM Partitioning Coefficients.

$$P_{\gamma/\alpha} = \frac{\text{wt\% PGM in Austenite}}{\text{wt\% PGM in Ferrite}}$$

21/6 Alloy series

(a)

2 wt%	1300°C	1250°C	1000°C
Pt	1.42	1.78	2.62
Pd	1.16	1.63	1.69
Ru	1.03	1.15	1.14

18/6 Alloy Series

(b)

2 wt%	1300°C	1250°C	1000°C
Pt	1.50	1.57	1.67
Pd	1.31	1.66	1.49
Ru	1.39	1.12	0.91

Figure 89. Cr and Ni Partitioning Coefficients for 2 wt% PGM additions - $P_{\gamma/\alpha}$ at 1250°C.

PGM addition	Element	$P_{\gamma/\alpha}$	
		21/6	18/6
-	Cr	0.86	0.84
-	Ni	1.33	0.82
Pt	Cr	0.82	0.82
Pd	Cr	0.82	0.81
Ru	Cr	0.83	0.83
Pt	Ni	1.40	1.55
Pd	Ni	1.45	1.43
Ru	Ni	1.39	1.55

$$P_{\gamma/\alpha} = \frac{\text{wt\% Cr or Ni in Austenite}}{\text{wt\% Cr or Ni in Ferrite}}$$

Figure 90.

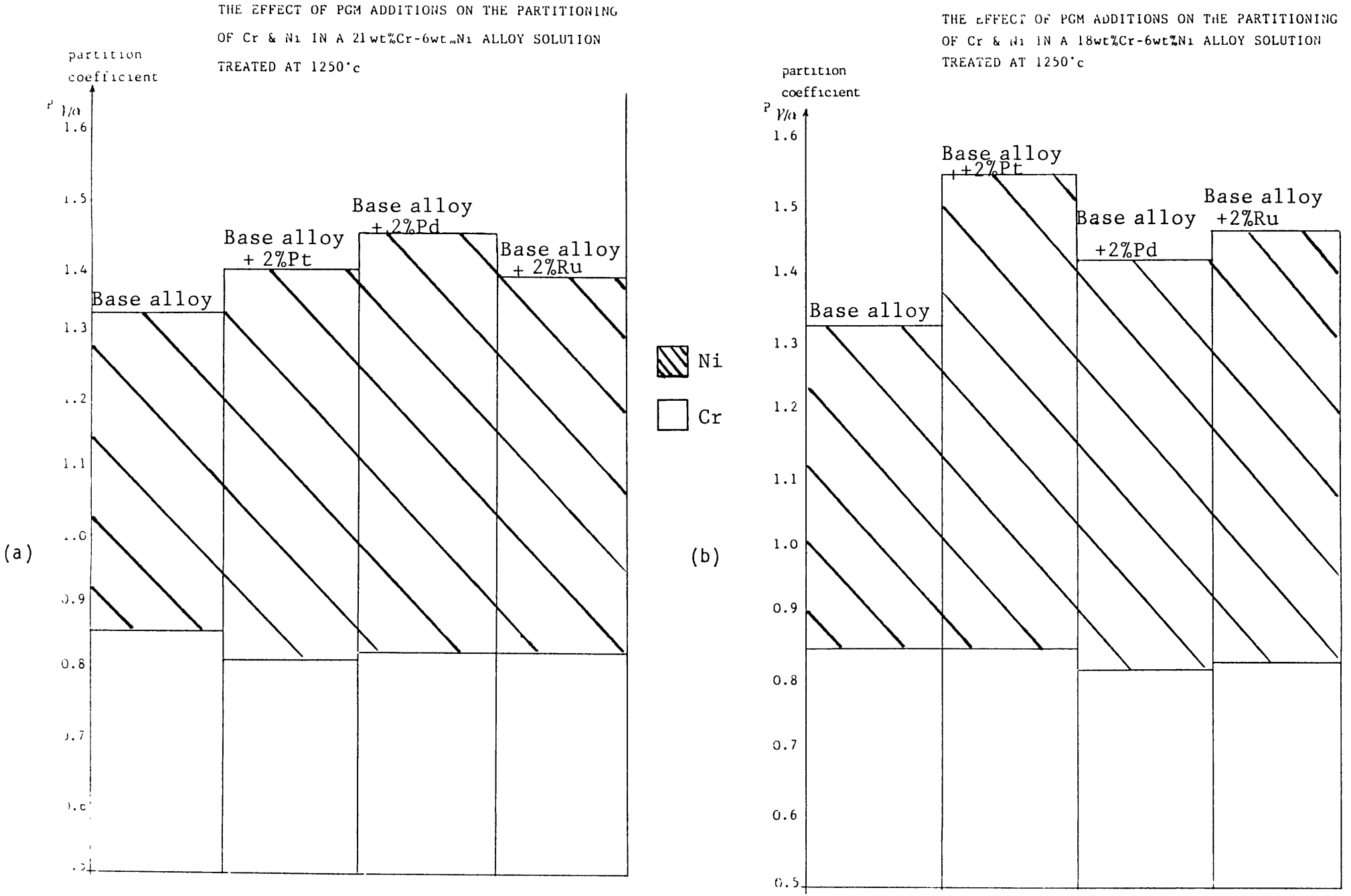
THE EFFECT OF PGM ADDITIONS ON THE PARTITIONING OF Cr & Ni IN A 21wt%Cr-6wt%Ni ALLOY SOLUTION TREATED AT 1250°c
partition coefficient
$P^{\gamma/\alpha}$
1.6
1.5
1.4
1.3
1.2
1.1
1.0
0.9
0.8
0.7
0.6
0.5
Base alloy
Base alloy + 2%Pt
Base alloy +2%Pd
Base alloy + 2%Ru
Ni
Cr
(a)
(b)
THE EFFECT OF PGM ADDITIONS ON THE PARTITIONING OF Cr & Ni IN A 18wt%Cr-6wt%Ni ALLOY SOLUTION TREATED AT 1250°c
partition coefficient
$P^{\gamma/\alpha}$
Base alloy
Base alloy +2%Pt
Base alloy +2%Pd
Base alloy +2%Ru

Figure 91. The Effect of 2 wt% PGMs on Tie-Lines in the 1300°C Isotherm of the Fe-Ni-Cr System.
Ternary Data Ref.9

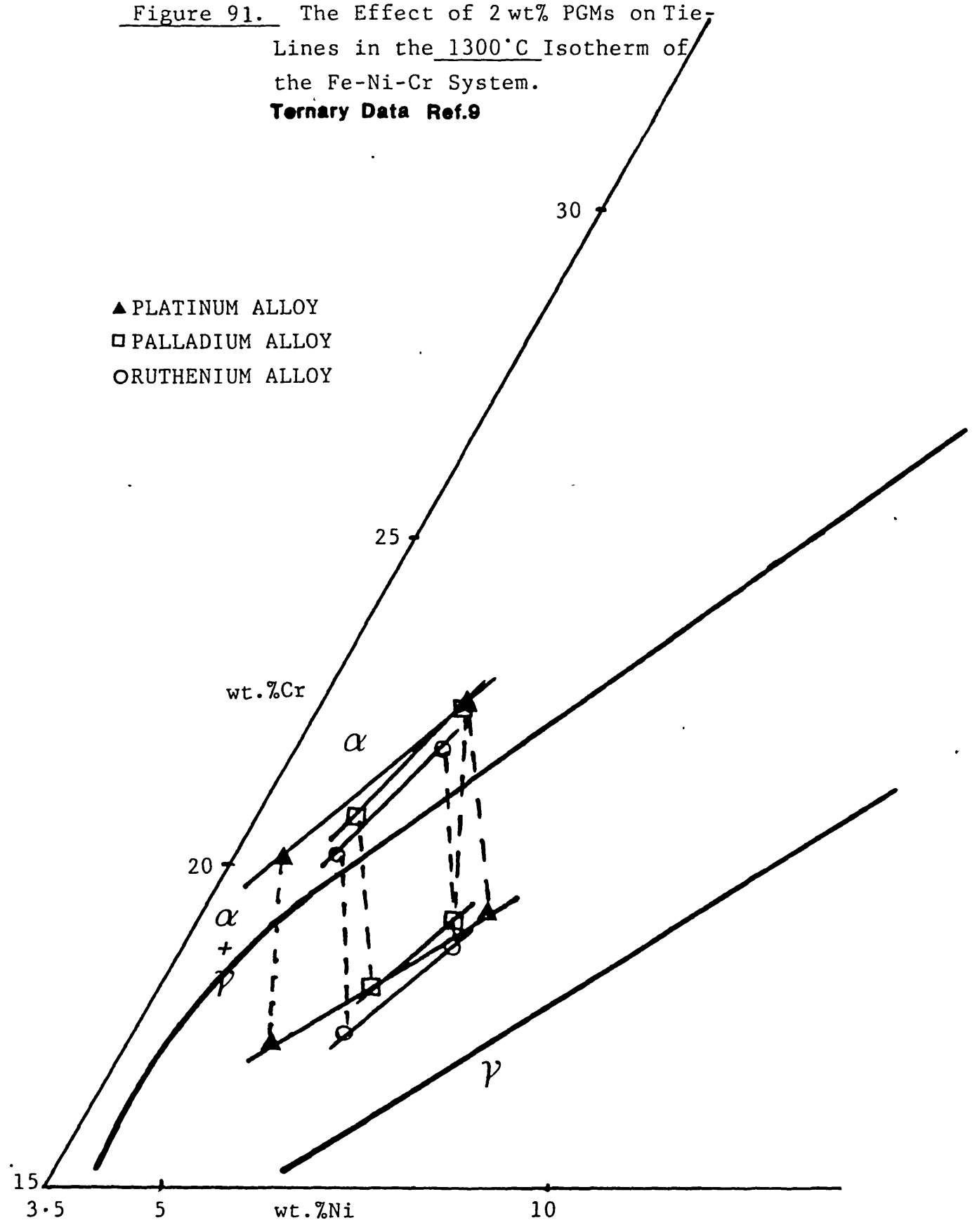

Figure 91. The Effect of 2 wt% PGMs on Tie-Lines in the 1300°C Isotherm of the Fe-Ni-Cr System.

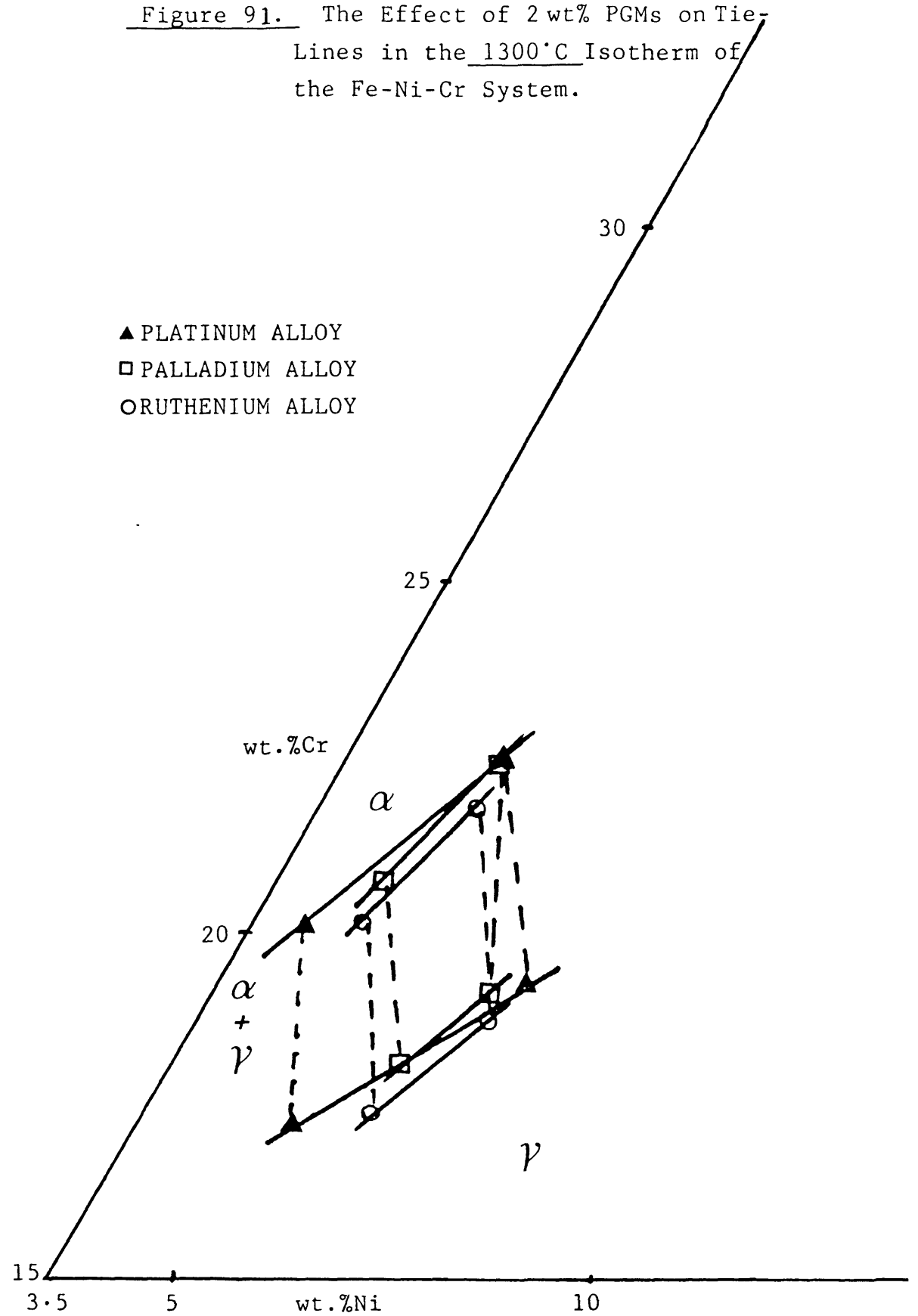

Figure 92. The Effect of 2 wt% PGMs on Tie-Lines in the 1250°C Isotherm of the Fe-Ni-Cr System.

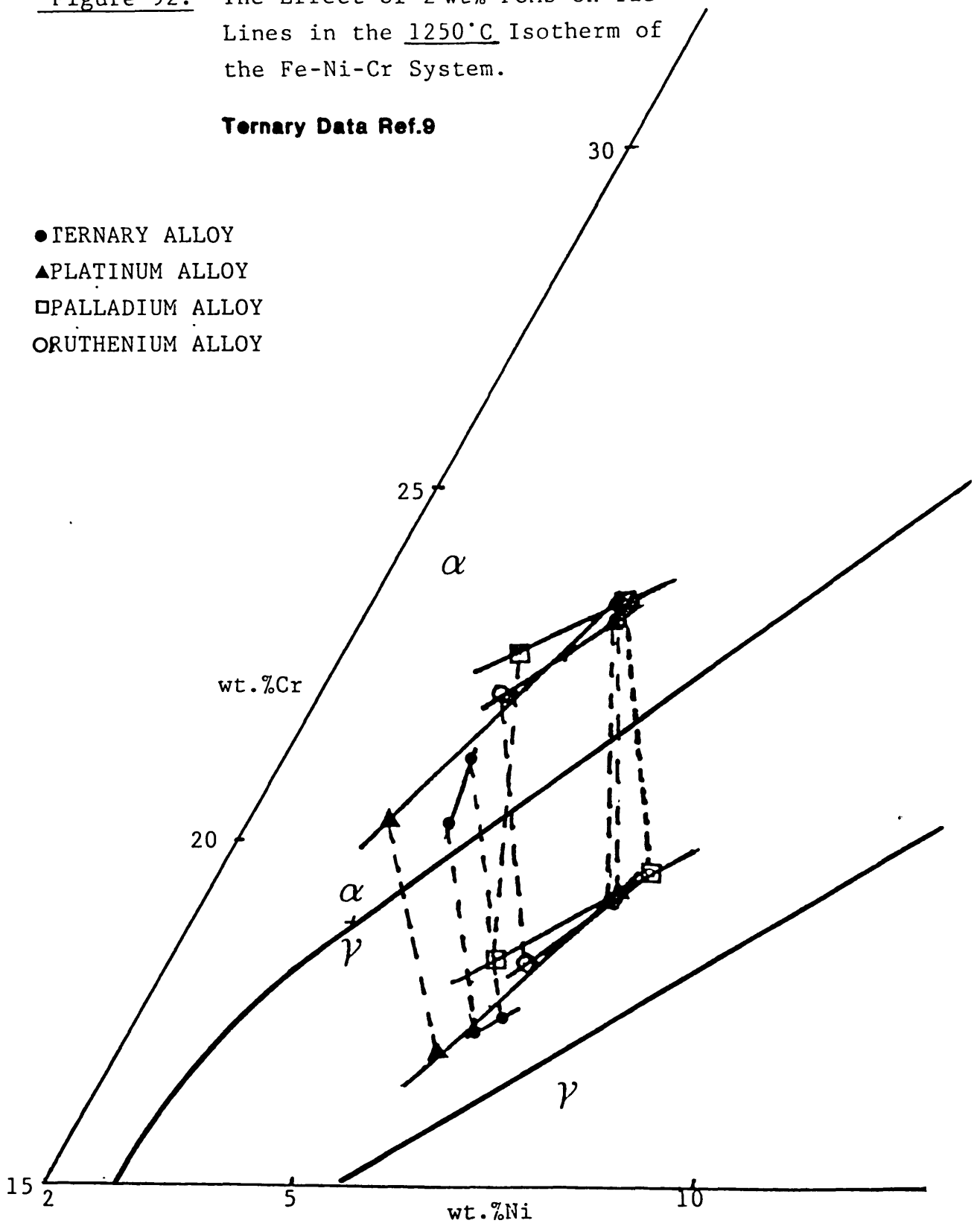

Figure 92. The Effect of 2 wt% PGMs on Tie-Lines in the 1250°C Isotherm of the Fe-Ni-Cr System.

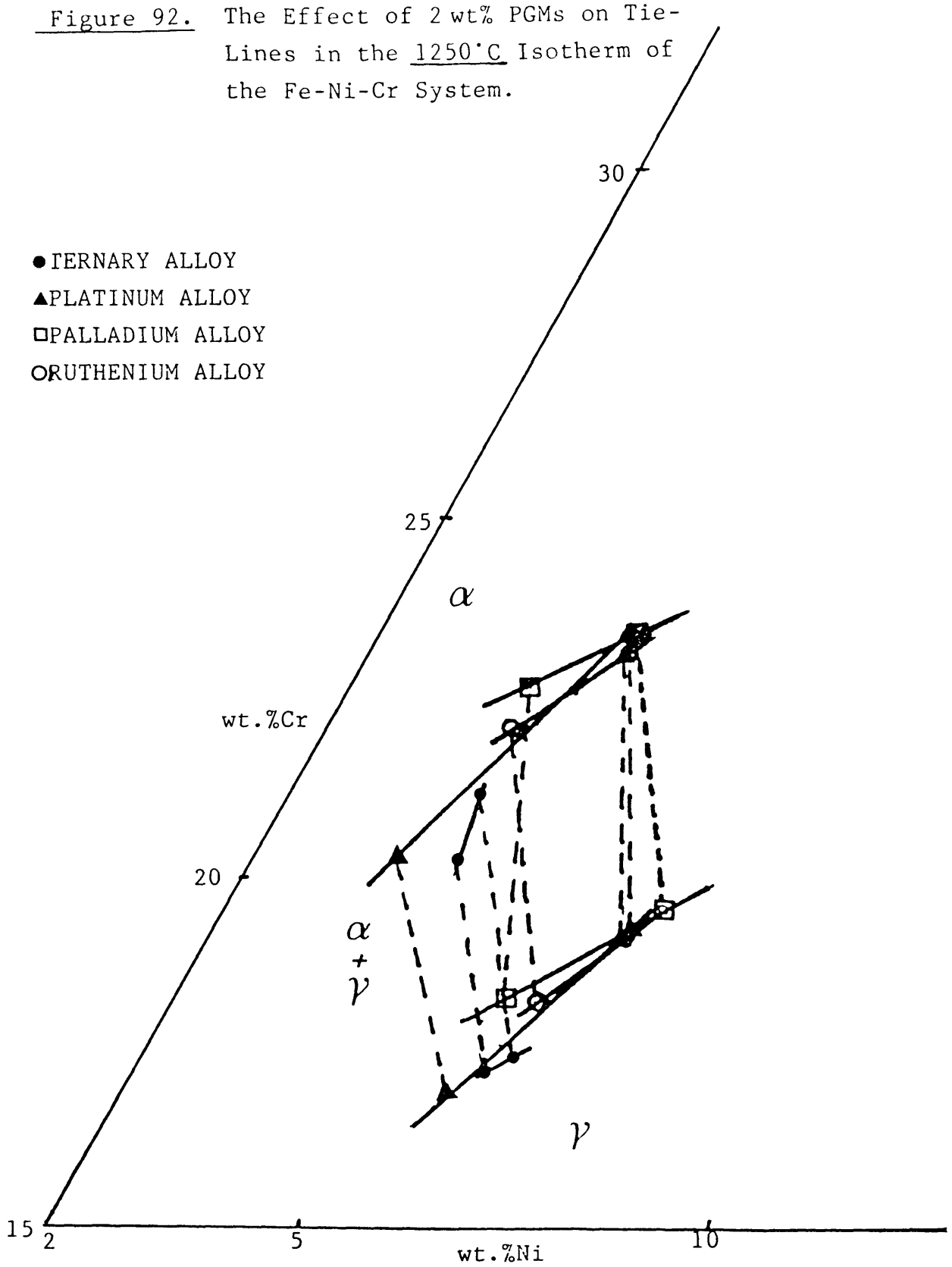

Figure 93. The Effect of 2 wt% PGMs on Tie-Lines in the 1000°C Isotherm of the Fe-Ni-Cr System.

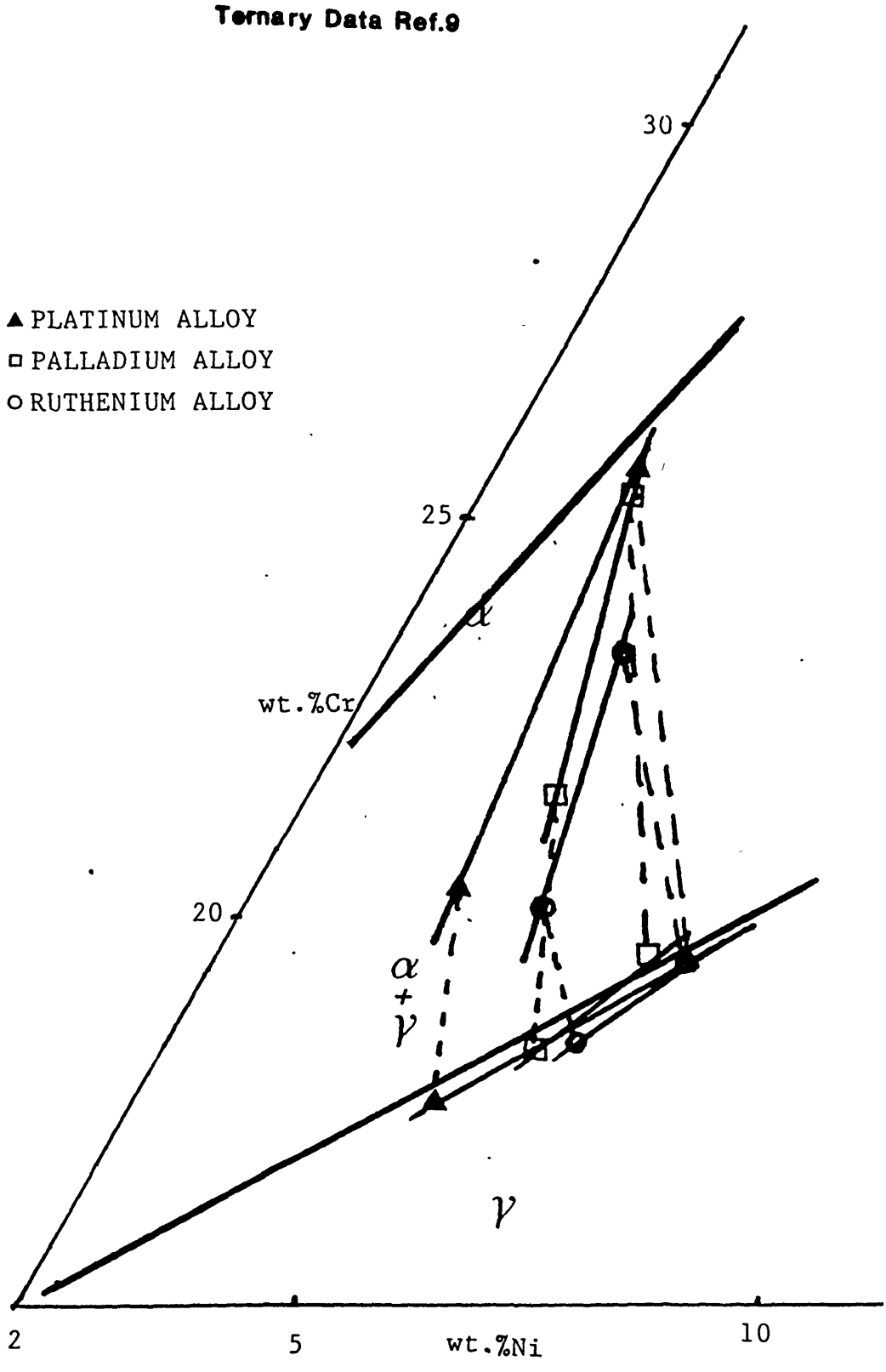

Figure 93. The Effect of 2 wt% PGMs on Tie-Lines in the 1000°C Isotherm of the Fe-Ni-Cr System.

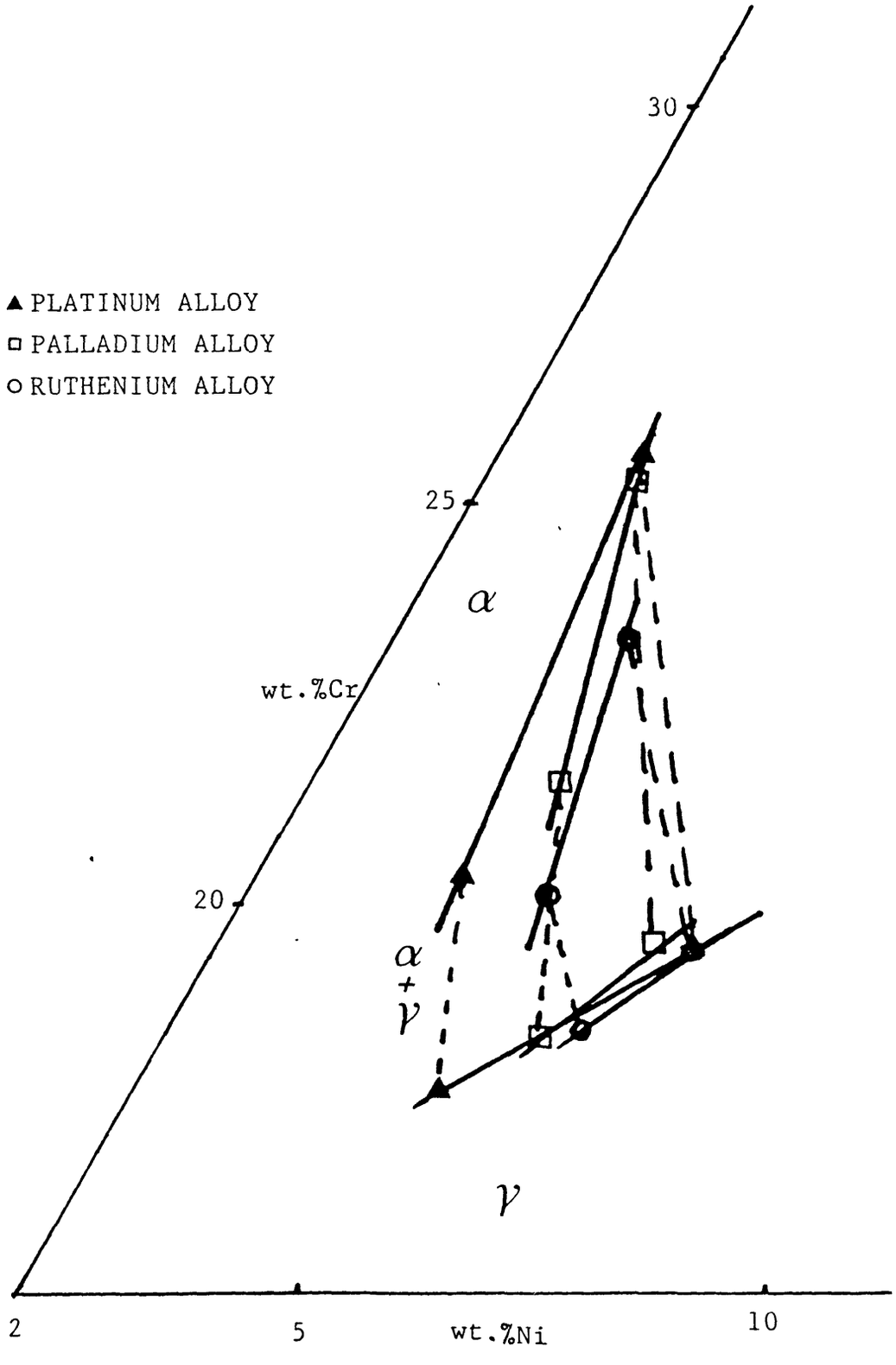

informatively in the form of isothermal sections (Figures 91-93). The data showing the compositions of ferrite and austenite phases co-existing in equilibria at 1300, 1250 and 1000°C are shown in Figures 85-87. Each value is an average of 3 separate point analyses, with an accuracy of ±0.4wt%. Tie-lines for the ternary alloys are only presented reliably for the 1250°C condition (Figure 92). This is because the local difference in chemical composition between ferrite and austenite phases was too small to permit reliable analyses and hence presentation of tie-lines at 1000°C and 1300°C. The positions of the tie-lines are also not shown for the 8wt% PGM alloys on any isotherm since they are too inclined in the plane of the isothermal section to permit reliable positioning. Indeed, even if the tie-lines were drawn, no confidence in the position of γ/α and α/γ boundaries, could be obtained.

5.3. Discussion

5.3.1. Microstructural Characterisation

A duplex stainless steel is one that contains two phases, generally austenite and ferrite (as seen in this study). The co-existence of such phases creates a wide variety of possible microstructures, as seen in Figures 79 and 81. Further, neither the austenite or ferrite may be completely stable, either water quenched from the solution treatment temperature, e.g. 1250°C, or aged between 650 and 950°C, resulting in further microstructural and chemical changes. It has therefore, been intended only to highlight important features and trends in the characterisation of alloy series 21/6 and 18/6.

5.3.2. 21/6 Alloy Series

Figures 79a-g illustrate the wide range of structures observed for the Fe-21wt%Cr-6wt%Ni series. Two features stand clear. Firstly, the additions of 2 wt% Pt, Pd and Ru to the base alloy have only a marginal effect on the shape, distribution, and volume fraction of austenite. For each, ferrite remains as the matrix phase for the solution treatment temperature of 1250°C. Microprobe analysis of these individual laboratory prepared alloys, revealed the composition of the 21/6 base alloy, to be 19/6, hence there is a perhaps misleading impression from Figure 78a, of an increase in α-ferrite volume fraction by the additions of Pt, Pd and Ru PGMs. Secondly, at the 8wt% PGM level γ-austenite exists as the matrix phase in Figures 79c,e and g,

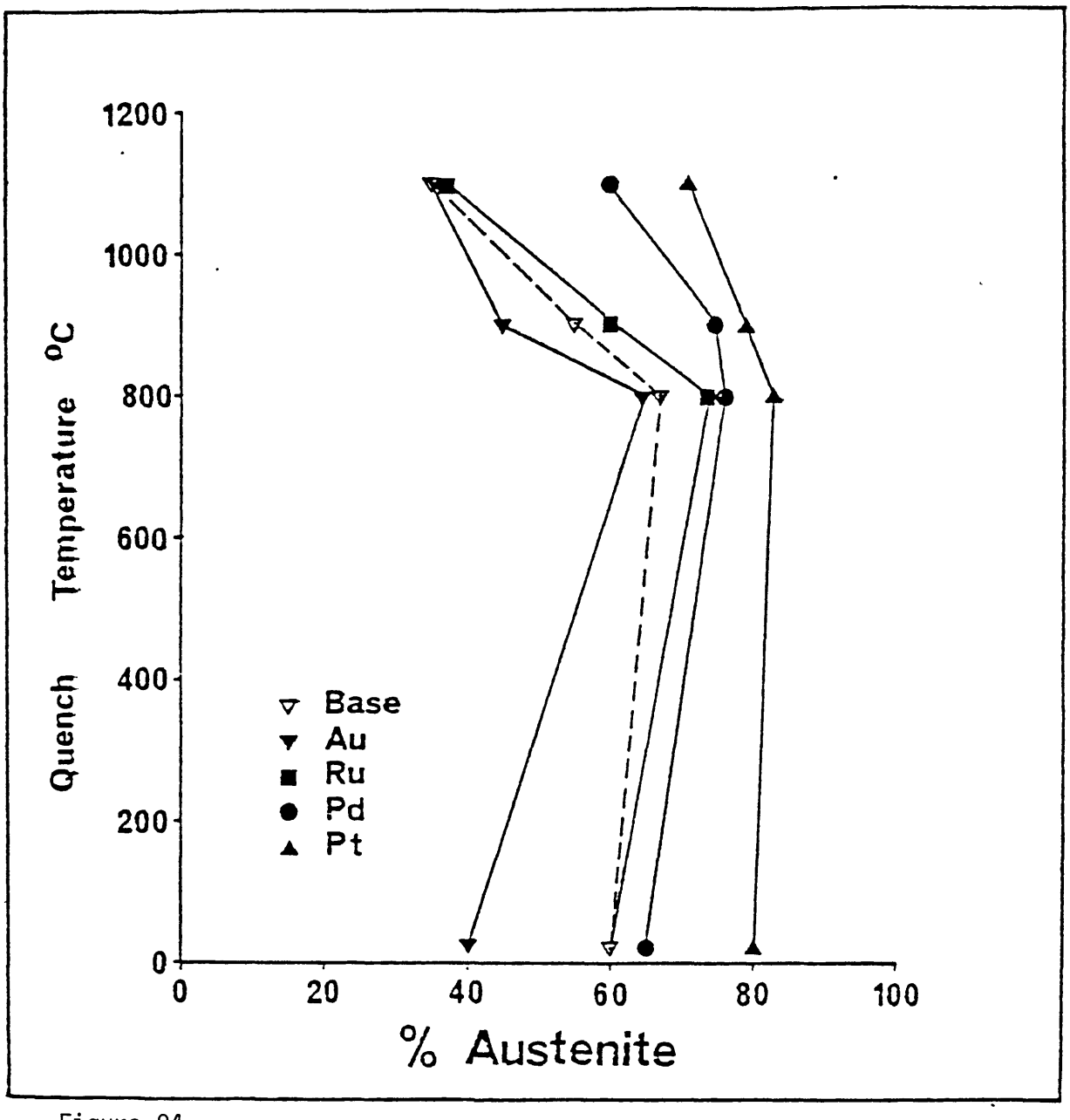

Figure 94.

Ref. 111.

Effect of 2wt% noble metal addition on the constitution of an experimental Fe - 26%Cr- 8% Ni Alloy

but only alloy 21/6/8Pt is fully austenitic at the solution treatment temperature of 1250°C.

At both the 2 and 8wt% PGM addition levels to this series, Ru is seen to be the least effective in retarding the dissolution of γ-austenite with increasing temperature (e.g. 1300°C). Although Pt is seen clearly from Figure 78a to have an increased α-ferrite volume fraction (with increasing annealing temperature, 1000 - 1250°C). Pd has an intermediate effect to Pt and Ru at the 8wt% PGM level with only alloy 21Cr-6Ni-8Pt being fully austenitic (78b).

5.3.3. 18/6 Alloy Series

Figures 81a-g illustrate the range of structures observed for the Fe-18wt%Cr-6wt%Ni series. The chromium equivalent in this series is less than the 21/6 series, consequently austenite is seen to exist as the matrix phase at the 2wt% PGM level. Whilst Pd and Ru follow this trend at the 2wt% level, the 18/6/2Pt presents the anomaly of a marginal increase in ferrite volume fraction, greater than the base alloy at 1250°C, but levelling off at 1300°C (Figure 80a). The effect is similar to behaviour in the 21/6/2Pt alloy. Clearly in both alloy series, Pt, at the 2wt% level does not increase the volume fraction of austenite between 1000 and 1250°C. This is somewhat surprising as the Fe-Pt binary diagram implies that much increased stability is conferred by Pt, to open up the γ field. The platinum containing alloy behaviour in this study is additionally contradicted by results from P. Gore, Figure 94 (111). In a duplex alloy 21Cr-8Ni; 2wt%Pt is very effective in increasing the content of austenite over the ternary alloy over the temperature range 800°C - 1100°C.

The addition of 8wt%Pt, Pd and Ru PGMs to the 18Cr-6Ni alloy series produces in each case a fully austenitic structure over the temperature range 1000°C - 1300°C (Figure 80b), seen in Figures 81c,e and g.

The stability of the γ-austenite on cooling at room temperature (and subsequent deformation), will be discussed in detail in a later chapter, but it is noted here that e.g. solid state transformations do and have occurred for alloys in both 21/6 and 18/6 series, e.g. Figure 77.

5.3.4. Microchemical Characterisation

No single publication can claim a definitive phase diagram for the Fe-Ni-Cr system in the solid state. However, the critical review

by Rivlin and Raynor (9) has drawn together a reliable set of self-consistent isotherms. The 1000°C, 1250°C and 1300°C isotherms in Figures 13-16 are used as a comparison of microchemical results in this chapter. Figures 85-90 show results obtained from X-ray EDS analysis of laboratory prepared alloys, solution treated at 1000°C, 1250°C and 1300°C. These results are graphically represented in Figures 91-93 as isothermal and quasi-isothermal sections revealing the effects of:

1) Increasing temperature on the movement of tie-lines.
2) The relative effects of 2wt%Pd, Pt and Ru on tie-lines.
3) The effect of a PGM on the partitioning of both Cr and Ni elements between austenite and ferrite.

From these sections and tables, the effect of these PGMs is seen to be significant in moving both the ferrite and austenite boundaries. Figures 88a and b show the partitioning coefficients of 2wt%Pt, Pd and Ru in austenite for both 21/6 and 18/6 alloy series solution treated at 1000°C, 1250°C and 1300°C. They show that Pt, Pd and Ru partition strongly to the austenite phase. In the 21/6 alloy series, the partitioning coefficients decrease in the sequence Pt > Pd > Ru at the temperatures studied, whereas the sequence is only followed in the 18/6 alloy series at 1000°C. The significance of these coefficients are that they conclusively establish that Pt and Pd PGMs partition strongly to γ-austenite in a duplex steel, whereas Ru is seen generally to partition less strongly to γ-austenite, equilibrating itself more homogeneously between austenite and ferrite phases and may indeed partition more to ferrite, as seen at 1000°C. No explanation is made of Ru partitioning more than Pd at 1300°C in the 18/6 alloy series, as this is seen as an anomalous result. The possible synergistic effects of Pt, Pd and Ru on the partitioning of Cr and Ni is seen readily from the bar charts in Figures 90a and b for duplex alloys solution treated at 1250°C and in Figure 89. The partitioning of Pt, Pd and Ru to the austenite phase is seen to be accompanied by:

a) an increase in the level of nickel partitioning to the γ-austenite phase and
b) an increase in the level of chromium partitioning to the α-ferrite phase.

Accompanying this enrichment of Cr and Ni elements in the respective ferrite and austenite phases it is relevant to remember that there are changes in the relative amounts of α and γ, represented in Figures

78 and 80. Figure 94 shows the percentage of γ-austenite present in a 26Cr-8Ni quenched from annealing temperatures 1000°C to 800°C. The effect of 2wt%Pt, Pd and Ru in this duplex alloy is seen as an increase in the austenite fraction with a sequence of Pt > Pd > Ru and Ru having the least effect in increasing the proportion of austenite.

A detailed consideration of Figures 91-93 will now be made. Over the temperature 1000°C to 1300°C the $\alpha + \gamma$ phase field widens as the temperature falls. The quasi-isotherm sections in Figures 91-93 show this trend to be altered by the presence of 2wt%Pt, Pd and Ru which cause a restriction of the duplex phase field with decreasing temperature. This is perhaps not surprising, as Pt, Pd and Ru elements increase the stability of γ in preference to α and have complete solubility in χ phase over the temperature range considered. These isotherms are quasi in the sense that because of the preferred partitioning of PGMs to γ-austenite, the tie-lines do not lie precisely in the plane of the section. However, the sections do indicate the movements of both $\alpha/(\gamma + \alpha)$ and $\gamma/(\gamma + \alpha)$ boundaries together, and are therefore considered to be of importance. For PGM modified alloys at 1300°C (Figure 91), the $\gamma/(\alpha + \gamma)$ boundary is altered such that Cr levels are increased and nickel levels decreased. The result is an expanded γ-austenite field compared with the boundary data from Rivlin and Raynor (9). The $\alpha/(\alpha + \gamma)$ solvus boundary, is likewise altered, with increasing levels of Cr and decreasing Ni. However, the $\gamma/(\alpha + \gamma)$ boundary has altered more than the $\alpha/(\alpha + \gamma)$ boundary such that the $\alpha + \gamma$ is marginally restricted for Pt, Pd and Ru containing alloys. This trend is continued down to 1250°C in Figure 92, where the γ field is expanded, however there is no restriction of the duplex $(\alpha + \gamma)$ field with PGM containing alloys as compared to data from Rivlin and Raynor (9). In Figure 93 the effect of Pt, Pd and Ru on the 1000°C isotherm are seen to be more dramatic; particularly in moving the $\alpha/(\alpha + \gamma)$ boundary. There is a considerable swing of the boundary causing significant restriction of the duplex $\alpha + \gamma$ field at the lower Cr levels. The effect is greatest for the Ru containing alloy, with increased nickel and decreased Cr contents compared to the ternary data. Pt and Pd have similar effects on the $\alpha/(\alpha + \gamma)$ boundary, with Pd being intermediate to Ru and Pt. The $\gamma/(\alpha + \gamma)$ boundary for the PGM containing alloys is not significantly changed from the ternary boundary data. The significance of these quasi-isotherm sections is that they undoubtedly reveal a general expansion of the γ-austenite field

compared to the ternary, Fe-Cr-Ni data: the implcation being an increased stability of austenite conferred by Pt, Pd and Ru elements. A cautionary comment is made on these experimental duplex alloys, since the ternary results in this study differ markedly from the ternary boundaries reported from Rivlin and Raynor (9) at 1250°C in Figure 92. This implies that absolute direct comparison of PGM modified alloys, with ternary data from Rivlin and Raynor (9), to be unwise.

5.3.5. γ_2-Austenite Precipitation

Austenite, designated γ_2 can precipitate at lower temperatures due to:

(1) A change in the compositions of the $\alpha/\alpha + \gamma$ and $\gamma/\gamma + \alpha$ boundaries with decreasing temperature.

(2) A depletion in Cr-content of the ferrite, resulting from carbide formation.

Figure 83 shows the precipitation of γ_2 austenite within a band of ferrite. The alloy 21/6/2Pd had been hot rolled at 1000°C and solution treated at 1250°C for 30 mins. and subsequently aged at 900°C for 100 mins. This γ_2 precipitation results from changes in the positions of the $\alpha/\alpha + \gamma$ and $\gamma/\gamma + \alpha$ boundaries, and can occur below an annealing temperature of 1250°C (211). This is illustrated in Figure 74. From these constructed sections (Figure 74) it is apparent that the boundaries are not vertical below about 1200°C; and an increasing volume fraction of γ-austenite, denoted γ_2 is suggested at temperatures down to about 900°C (59). Below 900°C the boundaries are not reliably known because the limits of the σ phase are uncertain (9). However, γ_2 proportions in excess of the higher temperature values may be possible at lower temperatures. The results presented in Figures 83a-e are derived from TTT studies of σ-sigma precipitation (described in a subsequent chapter). For the three alloys studied; 21/6, 21/6/2Pd and 21/6/2Ru, Figures 83a-e are typical, in that they show how quickly and readily γ_2 precipitates after 5 mins. ageing at 900 and 950°C in the ferrite, but is not evident at the lower ageing temperature of 800°C for the same time. Clearly at these relatively high temperatures (e.g. 900°C) the mechanism for γ_2 precipitation is, and has been identified as being diffusion controlled nucleation and growth (211,212). The effect of 2wt%Pd and Ru on γ_2 precipitation on this base alloy 21/6, has been too small for any conclusions to be drawn concerning their role at this level of alloying addition. However, whilst their effect on γ_2 precipitation

STEM ANALYSIS OF PRECIPITATES OBSERVED AFTER AGING AT 700 °C AND 600 °C

Aging	Area Analyzed	wt % Fe	Cr	Ni	Mo	Cu
700 °C/10 min	γ_2	63.6±0.3	18.1±0.9	13.7±1.0	2.8±0.4	1.7±0.7
700 °C/10 min	Small Ppts	56.8±0.3	18.6±0.1	7.2±0.2	3.0±0.1	14.5±0.2
700 °C/10 min	Matrix	65.2±0.9	22.4±0.2	7.6±0.3	4.6±0.3	0.4±0.2
600 °C/30 min	Small Ppts	57.2±0.6	27.3±1.3	9.6±0.4	3.8±0.3	1.9±0.7
600 °C/30 min	Matrix	65.0±0.4	21.7±0.2	10.9±0.2	2.4±0.1	0.2±0.2
600 °C/2 hr	γ_2	61.2±0.9	18.1±1.0	17.7±2.4	2.0±0.4	1.1±0.7
600 °C/2 hr	Matrix	66.0±0.2	21.7±0.5	7.6±1.0	3.8±1.6	0.9±0.5
600 °C/8 hr	γ_2	63.4±2.3	16.6±1.2	16.0±1.3	2.2±1.1	1.9±2.0
600 °C/8 hr	Matrix	67.9±0.2	25.5±0.4	3.2±0.3	0	3.4±0.3

Alloy Composition-21·1Cr,7·4Ni,2·4Mo,0·62Mn,0·032C, 1·3Cu,Fe bal. wt%

Figure 95. Ref. 212.

kinetics is not certain, it is likely that Pd, being a stronger γ-austenite former, accelerates γ_2 precipitation more than Ru in this instance. This is further borne out in the studies on σ precipitation, where Pd is found to accelerate the nucleation and growth of σ ahead of the Ru containing alloy, by initially providing new nucleating sites at the γ_2/α interfaces. Southwick and Honeycomb (211) studied the precipitation of γ_2 in a duplex (26Cr-5Ni + other alloying elements) stainless steel. The alloy was heated to the single phase α region and subsequently held isothermally at lower temperatures down to 600°C. They identified a diffusion controlled mechanism for γ_2 precipitation at high temperatures (650-1250°C) with growth kinetics intermediate between volume diffusion control and growth by a ledge mechanism. But at lower temperatures, e.g. 300-650°C, the precipitation of γ_2 followed an athermal diffusionless shear mechanism of growth. Solomon and Devine (59) have defined the characteristic structure of this lower γ_2 precipitation to be lath-like in shape with a midrib separating twinned regions, for a duplex commercial alloy, Uranus 50 (see Figure 50 for composition), aged between 600°C and 800°C for up to 100 hours. (See Figure 18 for precipitation kinetics.) This morphology can be clearly seen in an alloy 21Cr-6Ni-8Ru solution treated at 1250°C and subsequently aged at 650°C for 168 hours in Figures 82b and 83e. The γ_2 lath in Figure 83e runs diagonally across the TEM micrograph, with faulted regions separated by a midrib.

5.3.6. σ-Sigma Precipitation

Figures 84a-c represent the formation of σ phase in a 21Cr-6Ni-8Ru alloy, aged at 650°C for 168 hours. In this duplex alloy, ferrite has been totally consumed by σ-sigma. This would clearly be expected to produce a substantial reduction in alloy toughness. The kinetics of sigma precipitation will be discussed in a subsequent chapter. It is of interest to note however, that in some cases, at the interface between austenite and ferrite grains, the ferrite decomposes to give a lamellar mixture of sigma and austenite phases through the reaction $\alpha \rightarrow \gamma + \sigma$, in Figure 84c. This morphology has been noted by T. Thorvaldsson et al (213), Lu shi Ying (214) and G.W. Lorimer et al (215). Maehara et al (63,216,217) also observes in a duplex alloy, 25Cr-7Ni-3Mo, that sigma phase nucleates at α/γ interfaces and grows into α grains by the eutectoid reaction; $\alpha \rightarrow \sigma + \gamma$.

CHAPTER SIX

SIGMA PRECIPITATION

All beauteous things for which we live
By laws of time and space decay.

(W.J. Cory)

6.1. Results

6.1.1. Microchemical Features

This chapter details the precipitation of sigma phase in laboratory prepared duplex alloys: 21Cr-6Ni, 21Cr-6Ni-2Pd and 21Cr-6Ni-2Ru. Microchemical results are presented in Figure 97 from X-ray EDS analysis of bulk polished samples to obtain elemental concentrations in γ and σ phases. An accuracy of ±0.3wt% was achieved for Cr, Ni, Pd and Ru elements. The size of sigma particles analysed was typically 1μm. X-ray EDS analysis of samples showed the PGM concentration in sigma to be generally lower than that in γ-austenite. For both 800°C and 950°C ageing temperatures, the concentration of Cr in sigma increases with time and is, in general, greater in the presence of either Ru or Pd. Ageing for 5 minutes at 950°C and 800°C shows Ru concentrations in γ and σ to be unchanged, i.e. negligable partitioning has taken place. Pd, however, partitions more quickly, and in particular values of 2.9 and 0.9wt% are observed in γ and σ phases, respectively for 5 mins. ageing at 950°C.

6.1.2. Microstructural Features

Microstructural characterisation of these alloys has been via light, transmission and scanning electron microscopy. Figure 96 illustrates the typical structures developed in these alloys, with the original solution treated structure composed of bands of ferrite and austenite phases ≈40μm apart (Figure 96a). Subsequent ageing at the elevated temperature of 950°C for 5 mins. promotes sigma and γ_2-austenite precipitation (Figure 96b). At the longer time of 250 mins. both sigma and γ_2-austenite are well developed within the ferrite phase (Figure 96c).

Figure 98 serves to illustrate the effect of temperature on sigma precipitation for each alloy. Temperatures of 700°C and 900°C are compared for an ageing time of 5 mins. Sigma is selectively stained black and is seen to grow by consuming ferrite grains which are stained grey. An accelerated growth of sigma is clearly established for alloys aged at 900°C over those aged at 700°C. Inspection of the sigma/ferrite interface in these optical micrographs, show it to be often highly irregular and jagged, whilst in contrast, the sigma/austenite interfaces are more rounded and smooth. Figure 99 illustrates the effect of ageing time at a given temperature. Times of 5 and 250 mins. are

Figure 96. Alloy: 21Cr-6Ni-2Pd
Condition: Hot rolled at 1000°C followed by a 30 mins. anneal at 1250°C. Electrolytically etched in saturated NaOH solution.

(a) Annealed at 1250°C shows a banded structure of ferrite and austenite phases.

(b) Ageing the above alloy at 950°C for 5 mins. shows the precipitation of γ_2-austenite. σ subsequently precipitates at γ_2/α boundaries.

(c) Ageing the alloy in (a) for 250 mins. at 950°C shows that σ (dark) competes strongly with γ_2 to consume ferrite grains ahead of growing γ_2 (white in contrast) grains.

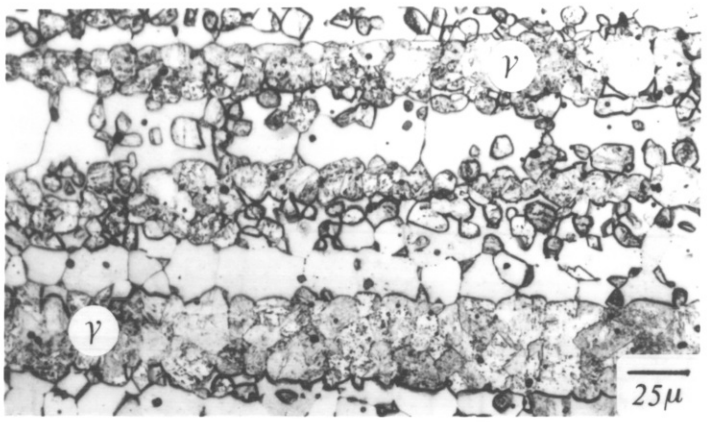

a

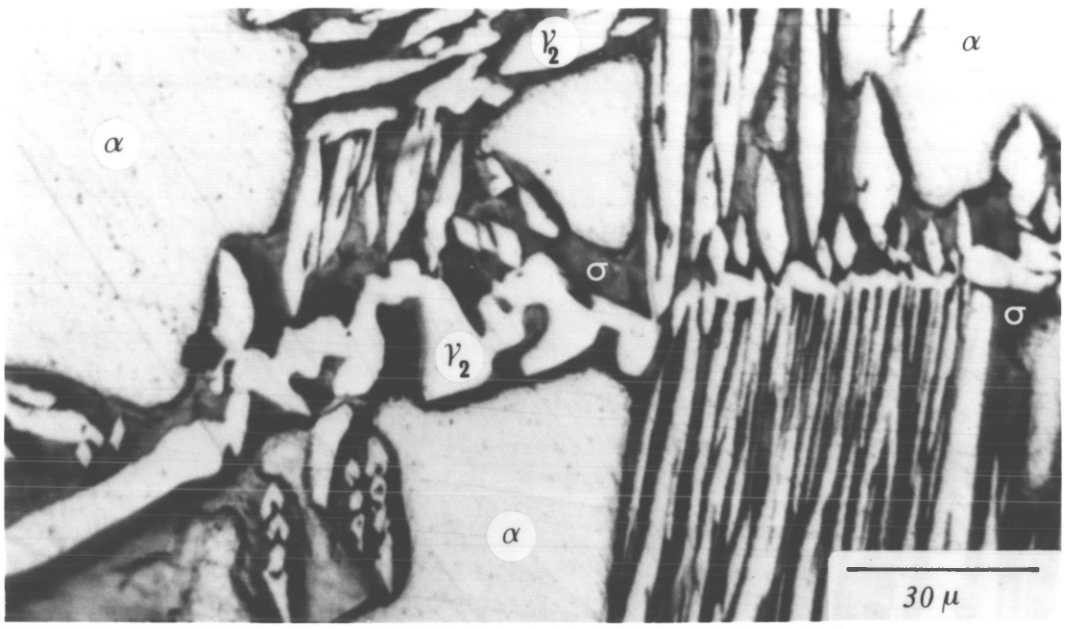

b

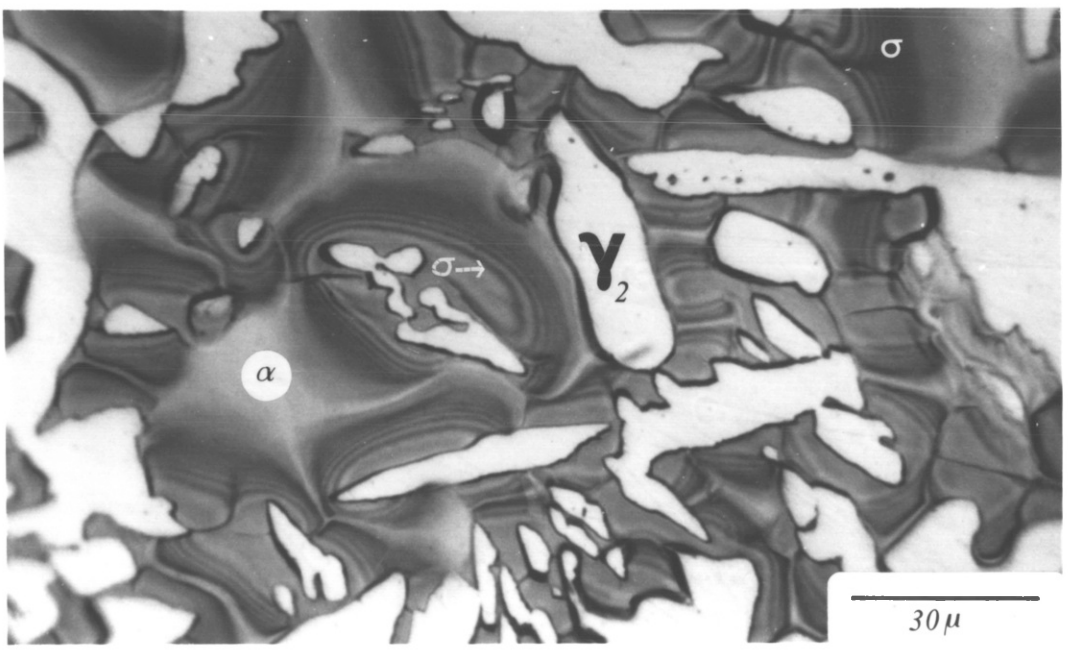

c

Figure 97. EDS Microchemical Analysis of Bulk Aged Specimens
Values in wt% have an accuracy of ± 0.3 wt%

800°C/5 mins.

Alloy	Cr	γ Ni	PGM	Cr	σ Ni	PGM
21/6	18.0	8.4	-	21.5	5.9	-
21/6/2Pd	18.0	6.9	2.2	21.1	5.1	1.7
21/6/2Ru	17.8	7.7	1.9	22.4	4.8	1.9

(a)

800°C/60 mins.

Alloy	Cr	γ Ni	PGM	Cr	σ Ni	PGM
21/6	18.8	8.3	-	22.2	5.4	-
21/6/2Pd	19.0	6.7	2.8	23.0	4.0	1.4
21/6/2Ru	18.1	6.6	1.9	23.1	4.8	1.7

(b)

800°C/250 mins.

Alloy	Cr	γ Ni	PGM	Cr	σ Ni	PGM
21/6	19.0	7.6	-	24.2	4.3	-
21/6/2Pd	18.9	6.7	2.5	23.8	4.2	1.5
21/6/2Ru	18.8	7.1	2.1	25.3	3.3	1.6

(c)

800°C/5 mins.

Alloy	Cr	γ Ni	PGM	Cr	σ Ni	PGM
21/6	19.0	6.7	-	22.1	4.0	-
21/6/2Pd	18.0	7.2	2.9	23.1	4.1	0.9
21/6/2Ru	18.1	7.1	2.0	22.3	4.8	2.0

(d)

Figure 97 (contd.)

950°C/60 mins.

Alloy	Cr	γ Ni	PGM	Cr	σ Ni	PGM
21/6	18.3	7.2	-	23.0	6.1	-
21/6/2Pd	20.3	6.1	2.4	24.9	2.5	1.5
21/6/2Ru	18.2	7.3	2.2	23.8	4.6	1.8

(e)

950°C/250 mins.

Alloy	Cr	γ Ni	PGM	Cr	σ Ni	PGM
21/6	17.7	8.1	-	24.8	5.2	-
21/6/2Pd	17.8	7.2	2.3	26.9	3.7	1.6
21/6/2Ru	18.0	7.8	2.2	25.2	3.2	1.6

(f)

Figure 98. Sigma precipitation in alloys annealed at 1250°C followed by subsequent ageing for 5 minutes at 700°C and 900°C.

(a) 21Cr-6Ni alloy aged at 700°C shows σ precipitation as discrete grains at γ/α grain boundaries.

(b) 21Cr-6Ni alloy aged at 900°C shows precipitation of γ_2-austenite with σ at γ/α interfaces.

(c) 21Cr-6Ni-2Pd alloy aged at 700°C shows σ precipitation at γ/α grain boundaries.

(d) 21Cr-6Ni-2Pd alloy aged at 900°C shows extensive growth of σ at γ/α interfaces.

(e) 21Cr-6Ni-2Ru alloy aged at 700°C shows γ/α grain boundaries to be saturated with transformation to σ.

(f) 21Cr-6Ni-2Ru alloy aged at 900°C shows substantial growth of σ from γ/α boundaries into ferrite.

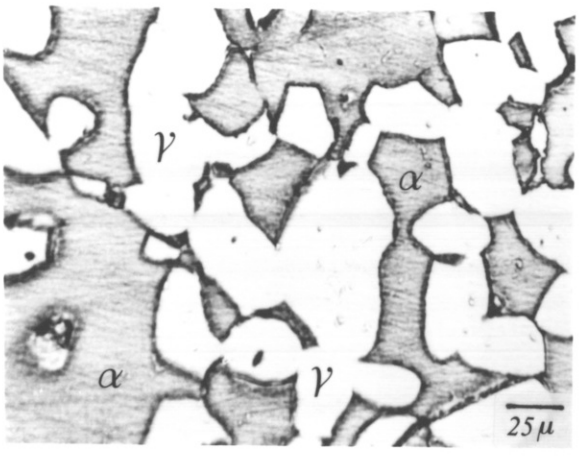

a

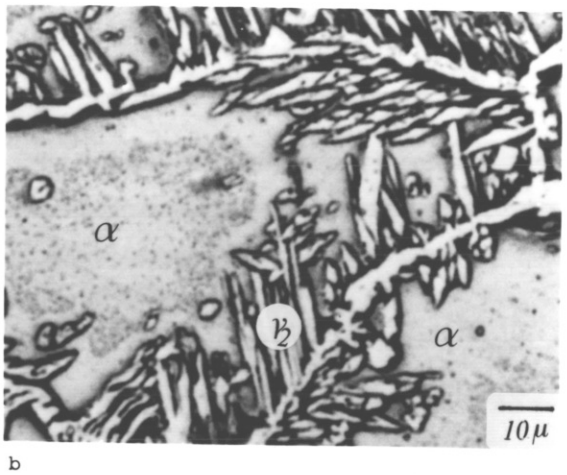

b

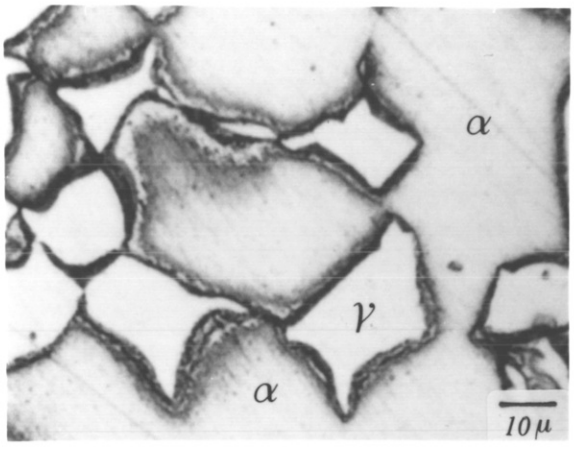

c

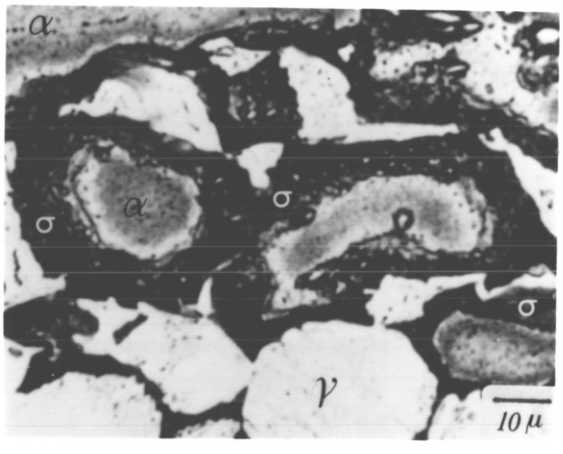

d

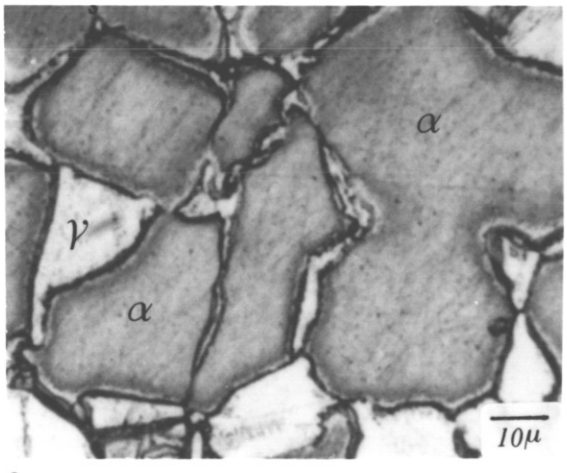

e

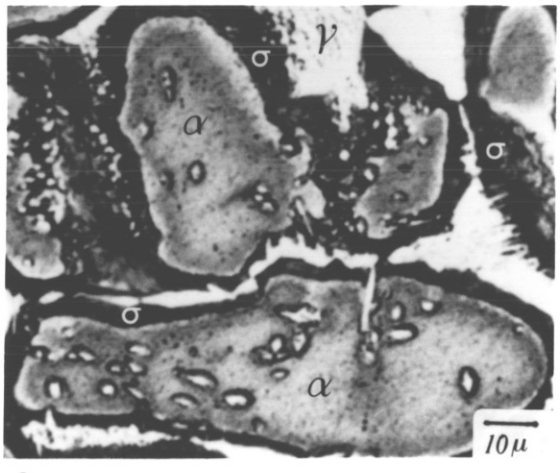

f

Figure 99. Sigma precipitation in alloys annealed at 1250°C followed by subsequent ageing at 950°C for 5 and 250 minutes.

(a) 21Cr-6Ni alloy aged for 5 mins. shows σ and γ_2 precipitation.

(b) 21Cr-6Ni alloy aged for 250 mins. shows extensive precipitation of σ.

(c) 21Cr-6Ni-2Pd alloy aged for 5 mins. shows σ precipitation at γ_2/α interfaces.

(d) 21Cr-6Ni-2Pd alloy aged for 250 mins; σ develops a lamellar morphology as it precipitates within ferrite.

(e) 21Cr-6Ni-2Ru alloy aged for 5 mins: sigma precipitation occurs readily at γ/α interfaces.

(f) 21Cr-6Ni-2Ru alloy aged for 250 mins. Extensive σ precipitation has occurred within ferrite resulting in a lamellar morphology.

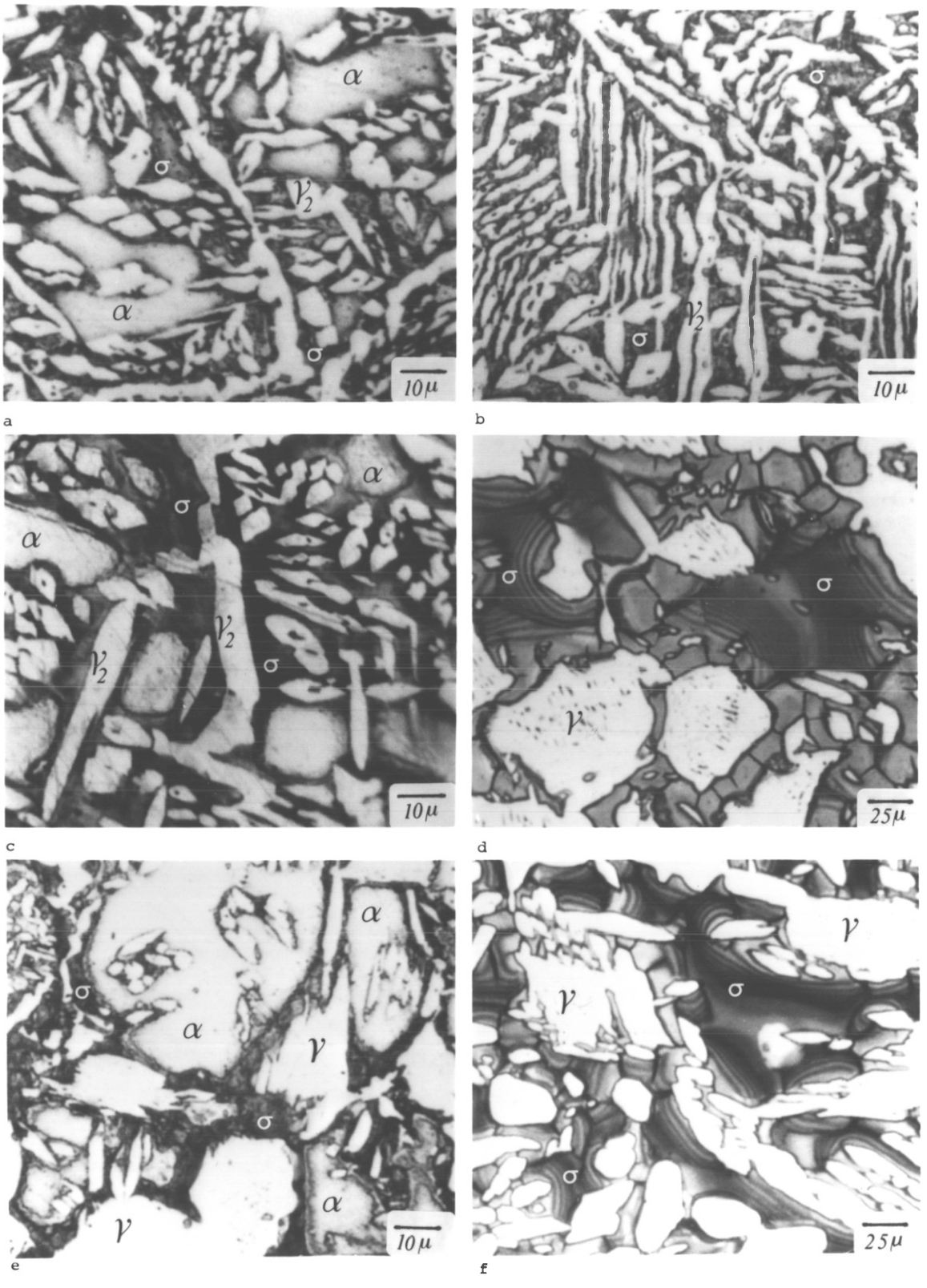
α
σ
γ2
α
σ
10μ
a
σ
γ2
σ
10μ
b
α
α
σ
γ2
γ2
σ
10μ
c
σ
σ
γ
25μ
d
α
σ
α
γ
σ
α
γ
10μ
e
γ
γ
σ
σ
25μ
f

compared at an ageing temperature of 950°C. The volume fraction of sigma is increased for the longer ageing temperature for each alloy; this effect being greatest for the PGM containing alloys. An interesting feature observed in the PGM containing alloys aged for 250 minutes, was the pattern of 'stripes' developed in the advancing sigma fronts as it consumed ferrite regions. As the selective etch of KOH produces a stain which highlights the phases via contrast differences, these features cannot be considered to be mere artefacts, but representative of local chemical differences. This unusual morphology was commonly observed in the Pd and Ru containing alloys aged for >250 mins. at 900 or 950°C, and is not too unlike morphologies obtained from eutectoid transformations producing lamellar structures (24).

6.1.3. Sigma Precipitation Kinetics

The values of sigma fraction, determined by the method of point counting provide the data for plotting the kinetic curves in Figure 100. They describe the quantity of sigma precipitated as a function of isothermal annealing time, from 5 minutes to 5 days. The data from these curves was subsequently used to construct the time-temperature-transformation (TTT) curves for alloys 21Cr-6Ni, 21Cr-6Ni-2Pd and 21Cr-6Ni-2Ru (Figure 101). The peak transformation of sigma precipitation (as shown by the nose of the C-curve) occurs at ≈925°C for Pd and Ru alloys, and at ≈900°C for the 21Cr-6Ni ternary alloy. From these curves in Figure 101, additions of 2wt%Pd and Ru to the base alloy are shown to result in an acceleration of sigma precipitation. Further, concerning the kinetics of sigma precipitation, evaluation of the results in Figures 100 and 101 has been made via the Johnson-Mehl equation (218,219) and results are presented in Figure 102. The 21Cr-6Ni alloy is compared with the 21Cr-6Ni-2Ru alloy.

At 900°C sigma precipitation is relatively fast consistent with relatively steep slopes of 2.1 (21/6 at 900°C) and 3.6 (21/6/2Ru at 900°C). For relatively lower ageing temperatures, sigma precipitation slows down and reaches a saturation plateau. Analysis of these graphs enables a reaction constant, K (with arbitrary units), to be determined and values are presented in Figure 103. In the ternary alloy, the reaction constant, K, is 5 times greater at 950°C than 800°C whereas in the Ru containing alloy it is 2.3 times greater at 900°C than 800°C.

Figure 100 The Effect of Ageing Time and Temperature On Sigma Precipitation.

(a)

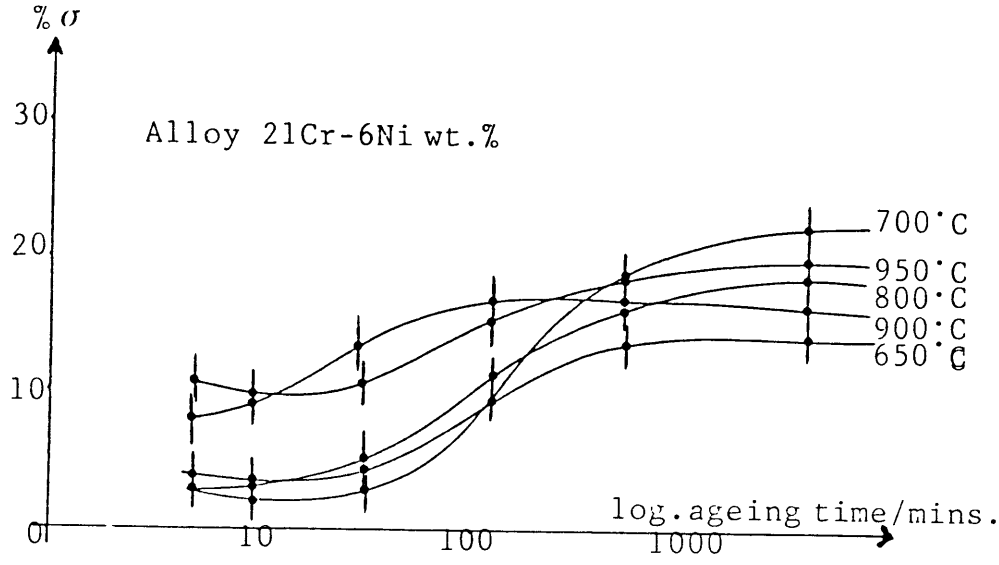

(b)

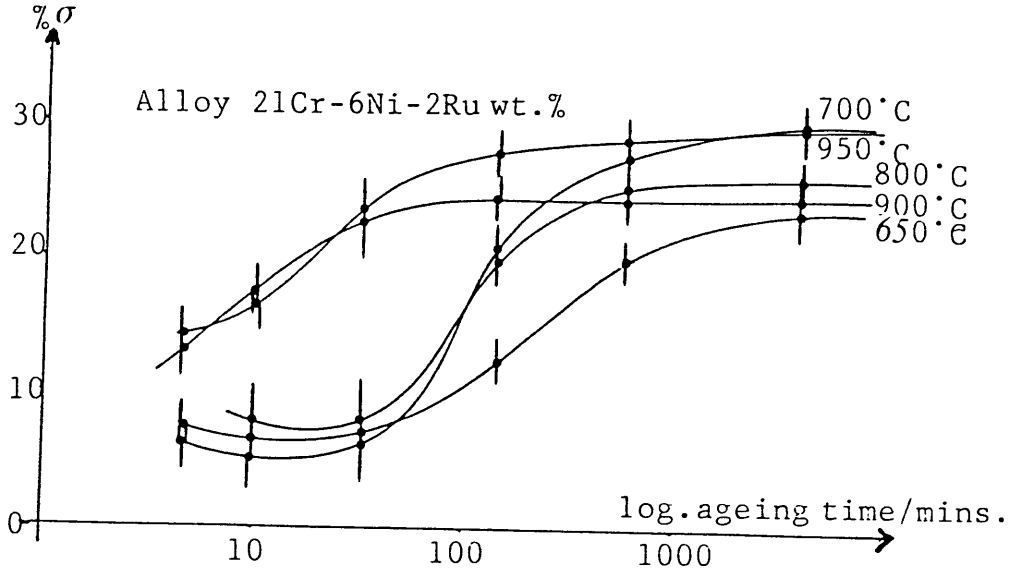

(c)

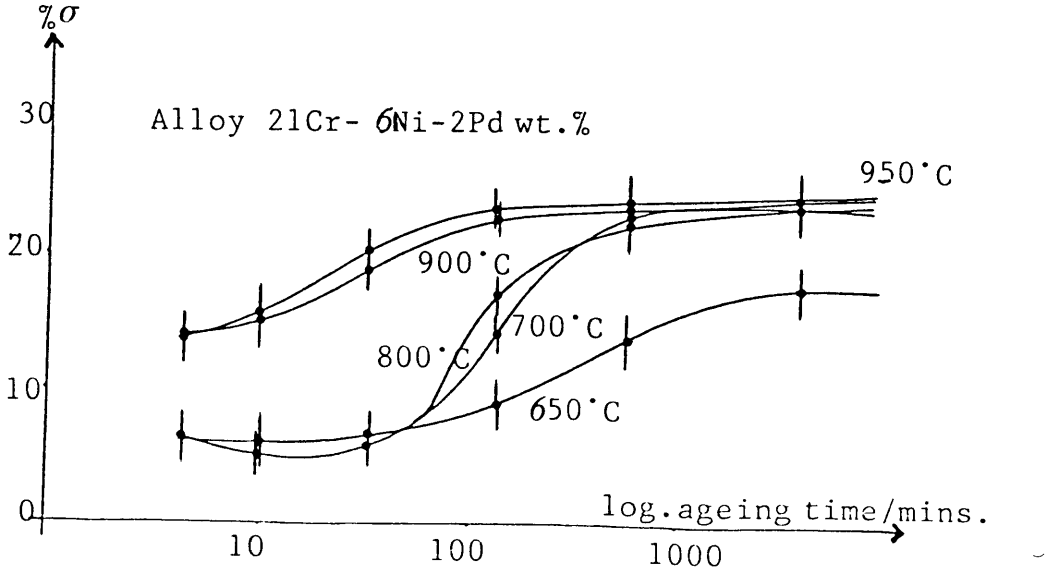

Figure 101. Time-Temperature-Transformation Curves For Sigma Precipitation in Duplex Alloys.

(a)

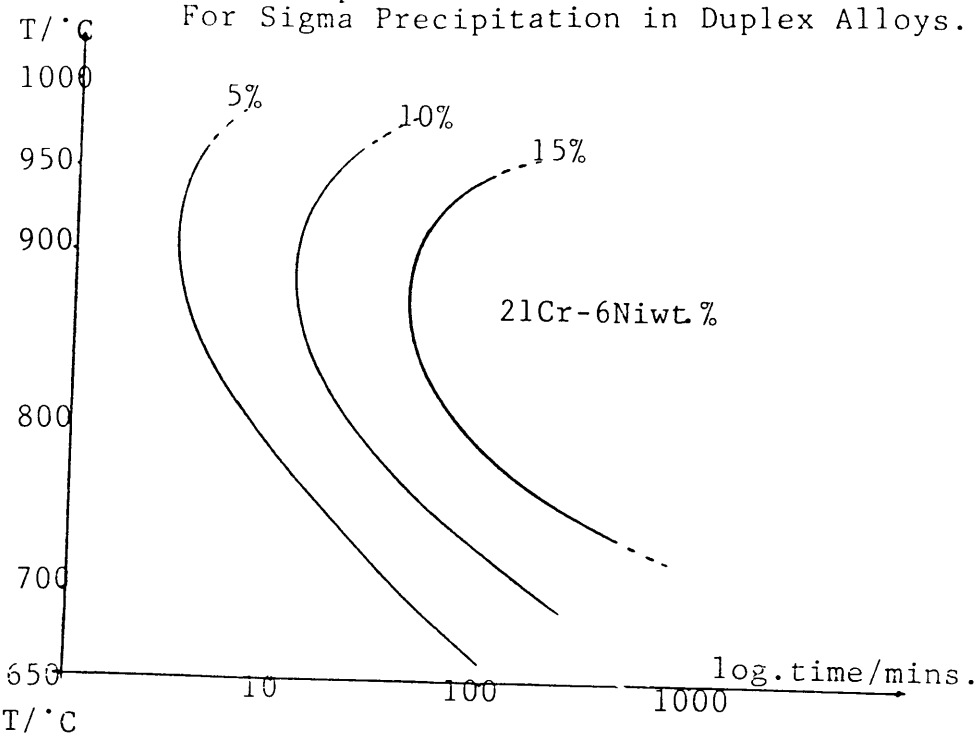

(b)

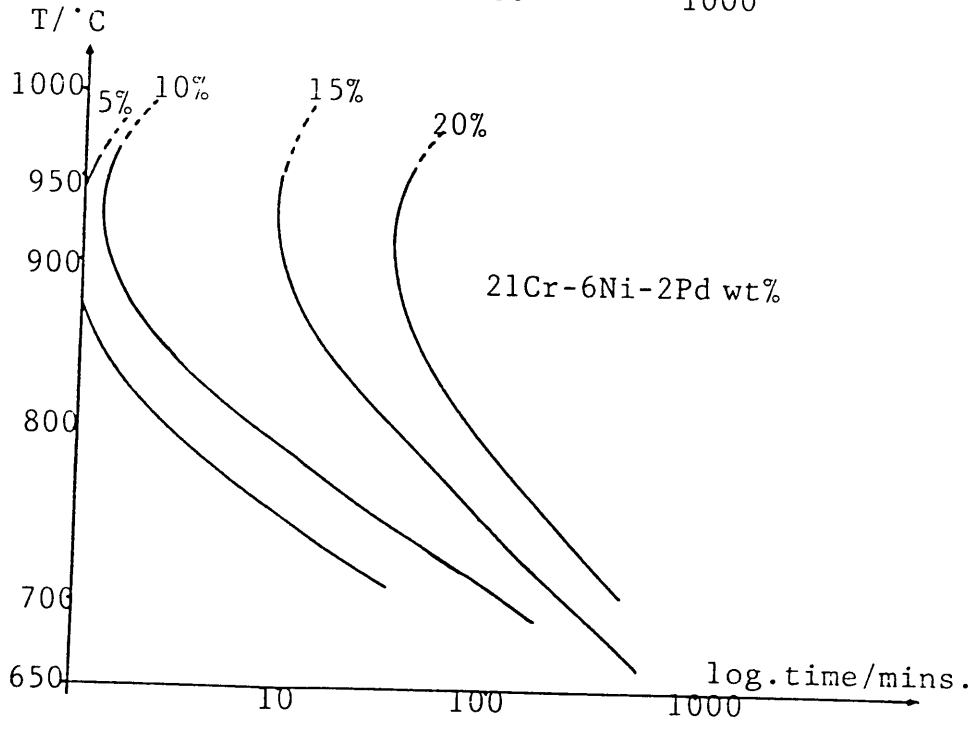

(c)

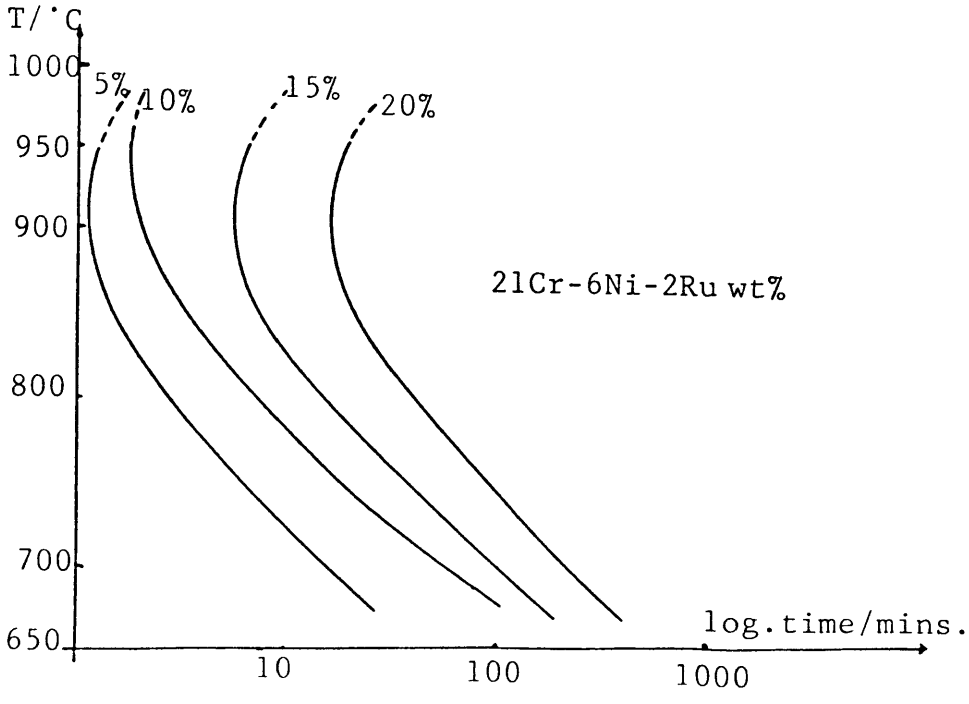

Figure 102 Plot of the Kinetic Law, $X=1-e^{(Kt)^n}$
At Various Temperatures.
X=the fraction of ferrite transformed to sigma

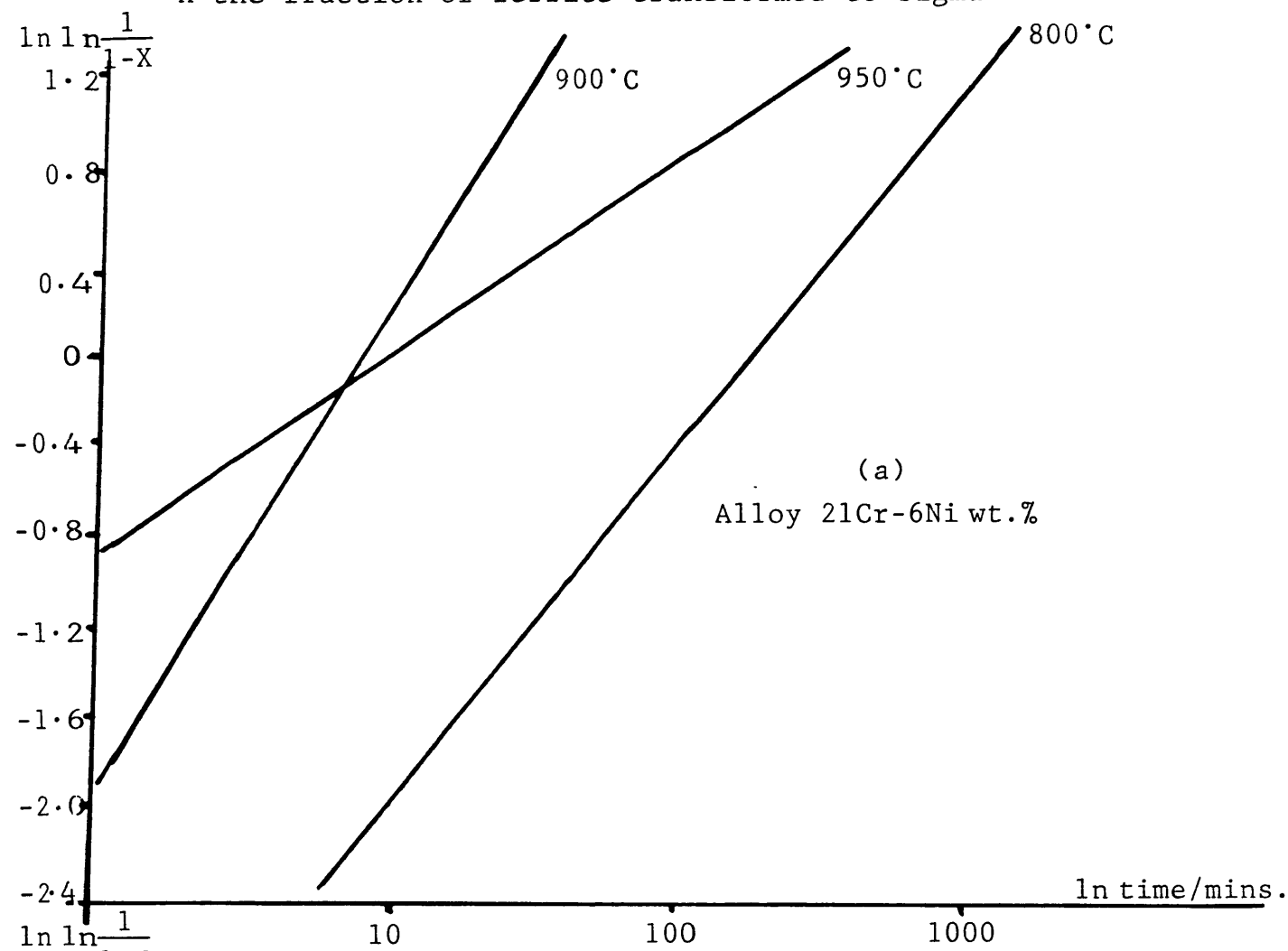

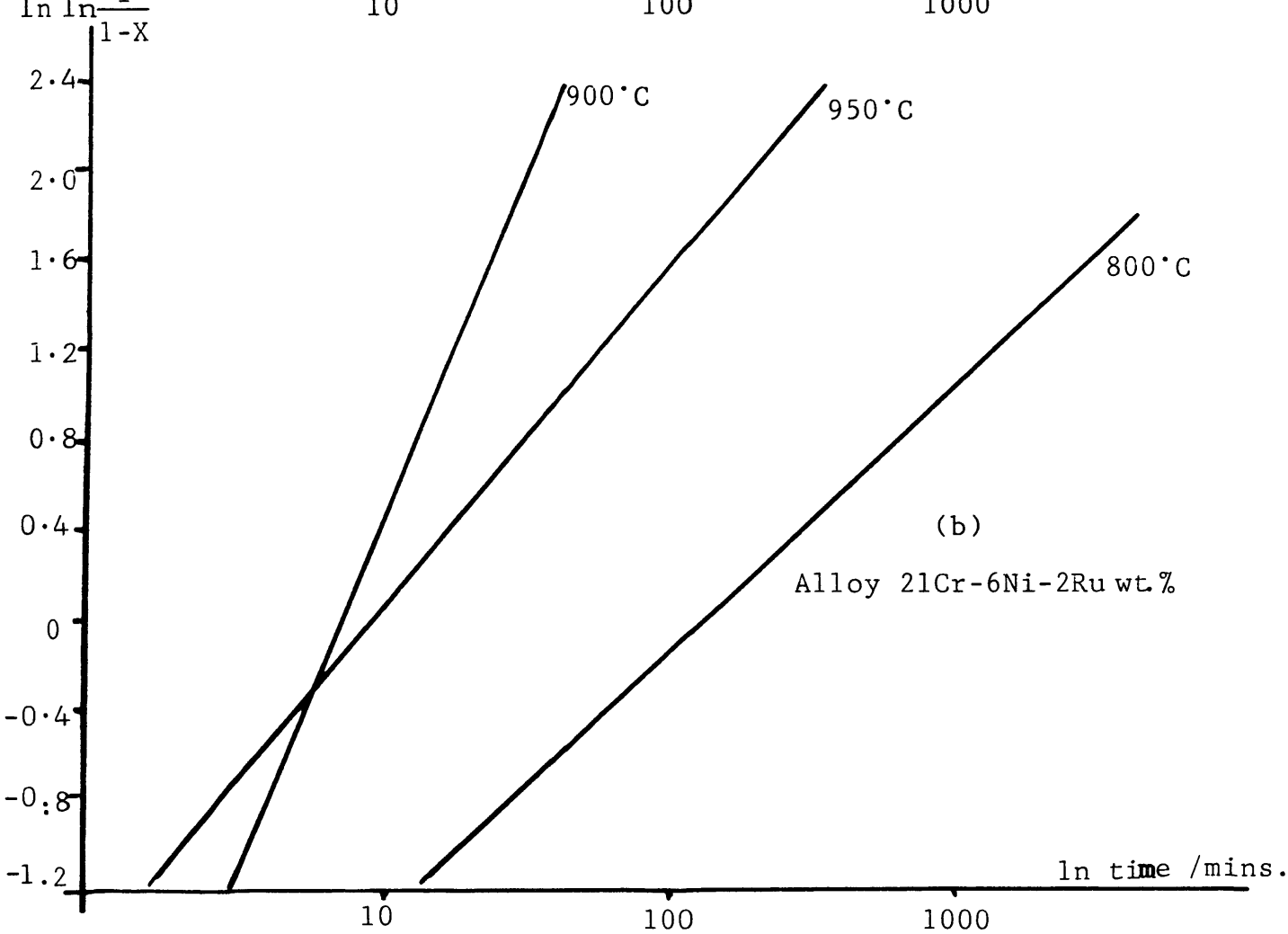

Figure 102 Plot of the Kinetic Law, $X=1-e^{(Kt)^n}$
At Various Temperatures.
X=the fraction of ferrite transformed to sigma

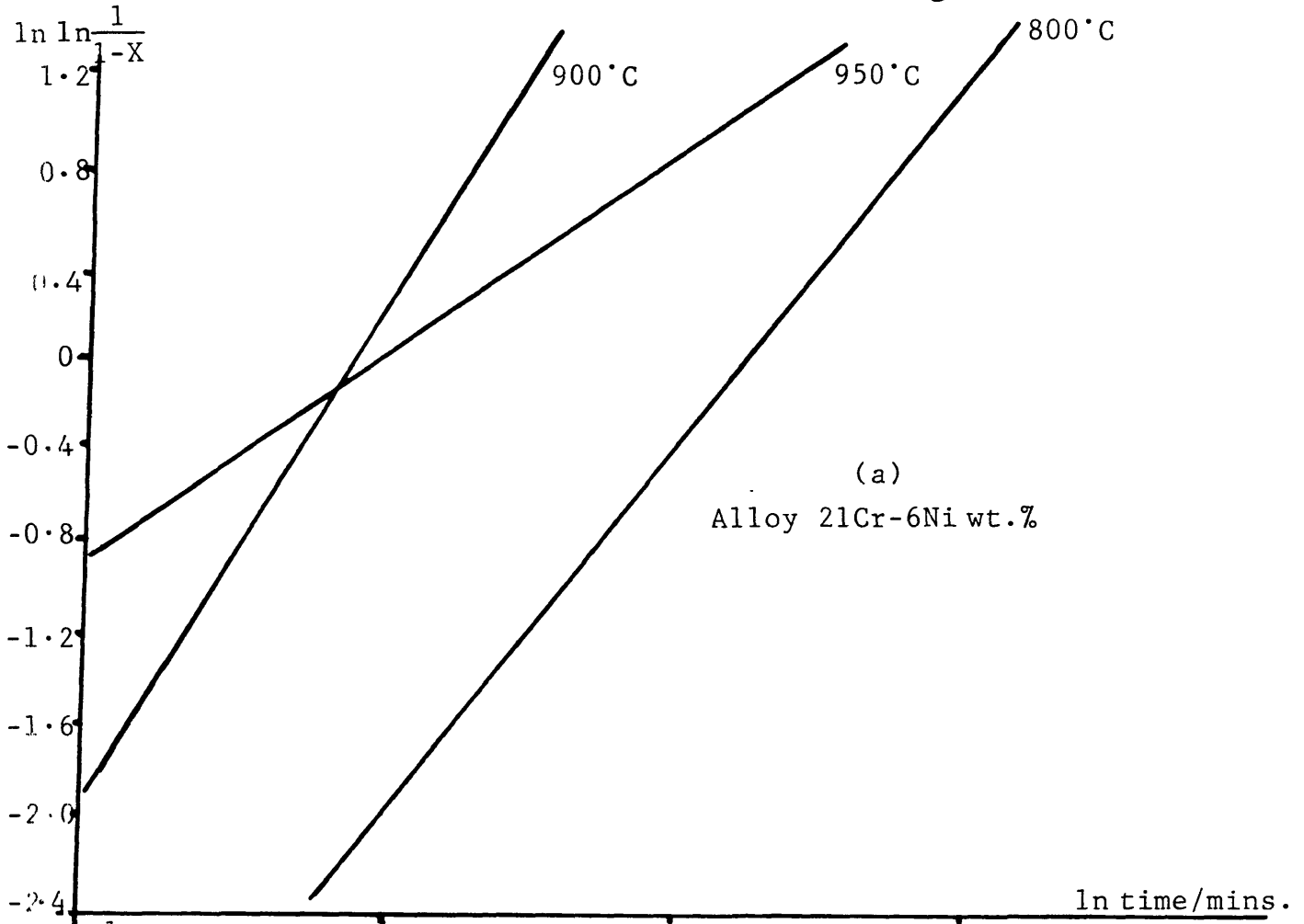

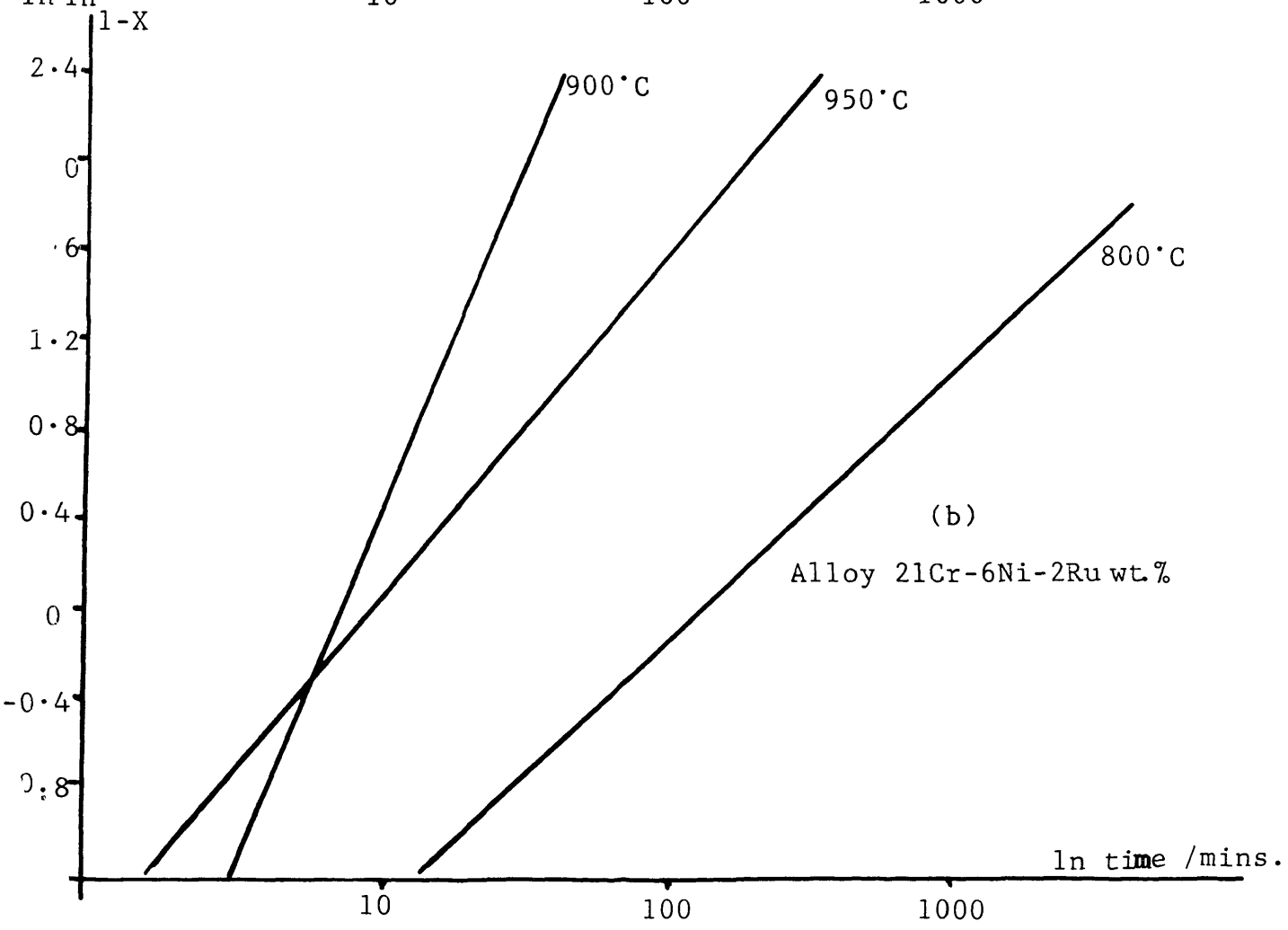

Figure 103. n & K values for sigma precipitation in the Johnson-Mehl equation.

Alloy 21Cr-6Ni wt% (a)

Temp./°C	Slope n	K arbitary unit
950	1·3	100
900	2·1	63
800	1·4	21

Alloy 21Cr-6Ni-2Ru wt% (b)

Temp./°C	Slope n	K arbitary unit
900	3·6	100
950	1·4	83
800	1·3	43

6.1.4. TEM Studies

Transmission electron microscopy results concerning sigma precipitation are shown in Figures 104-112. Figure 104 reveals extensive sigma precipitation in an alloy 21Cr-6Ni-8Ru aged at 650°C for 168 hours. Figures 105 and 106 show sigma to be a well faceted phase. The ferrite instability is further shown in Figures 107 and 108 where α has decomposed in places to a lamellar mixture of γ-austenite and sigma phases. The SADP, (Figure 109) from this area shows the σ phase to be $[0\bar{1}1]_{\sigma}$. Figures 110 and 111 show sigma precipitation in the alloy 21/6/2Pd aged at 650°C for 168 hours. Extensive mismatch is accommodated by interfacial dislocations at the sigma/ferrite interface.

An additional feature in these aged alloys, concerns the partial transformation of austenite to martensite. On ageing the martensite is able to revert back to austenite; $\alpha' \rightarrow \gamma$. Figure 112 shows this partial decomposition of γ-austenite to ε-martensite on rapid cooling to room temperature from the ageing temperature of 650°C. Two variants of the hcp ε-martensite phase are present and give rise to extra reflections. These reflections are streaked because the hcp phase is present as very thin overlapping plates shown in the HRDF micrographs in Figures 112c,d, and e.

6.1.5. Hardness Variations

Figure 113 shows the relation of hardness variations with ageing time and temperature. Hardness in general increases continuously with ageing time, reaching a plateau after 100 mins. However, an initial softening at short times is observed for alloys 21Cr-6Ni and 21Cr-6Ni-2Pd, associated with the re-equilibration of α and γ phases and the reversion of $\alpha' \rightarrow \gamma$. A peak hardness is also observed for the 21Cr-6Ni alloy after ≈40 mins. ageing. This is attributed to a change in σ morphology precipitating as a continuous film at α/γ grain boundaries (Figure 114). After 40 mins. ageing, the hardness of this alloy falls rapidly. The reasons for this behaviour are not evident from microstructural examination, but it seems likely that a phase instability is occurring. The Ru-containing alloy exhibits a softening for the 650°C condition at ≈100 hours: no explanation may be given for this. The Vickers hardness values show a peak of approximately 289 for the base alloy, whilst the Pd and Ru containing alloys do not exceed 280. The changes in hardness in Figure 113 can be generally related to and explained in terms of sigma precipitation, since the Vickers hardness of the sigma,

Alloy: 21Cr-6Ni-8Ru.
Condition: Solution treated at 1250°C produces a duplex structure of α grains in an γ matrix. Subsequent ageing at 650°C for 168 hours produces the following structures shown in the TEM micrographs.

Figure 104. Ageing the above alloy reveals extensive precipitation of sigma phase surrounded by grains of γ.

Figure 105. Sigma precipitate identified by the SADP in Figure 106.

Figure 106. SADP of sigma phase shows $[001]_{\sigma}$.
$2\lambda L = 5.29 \text{Å cm}$

Figure 107. In places α-ferrite has transformed to sigma via the reaction $\alpha \rightarrow \sigma + \gamma$ with a resultant lamellar morphology.

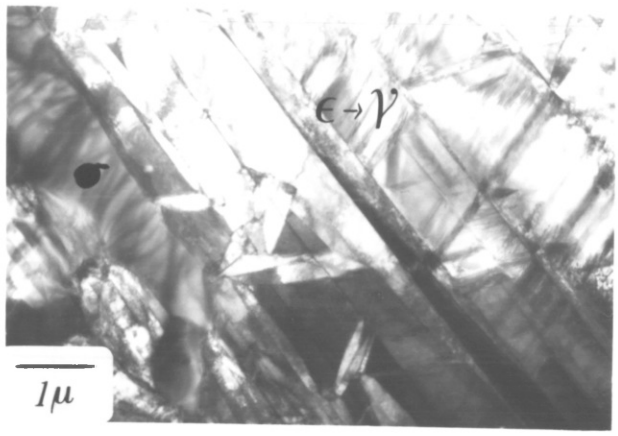

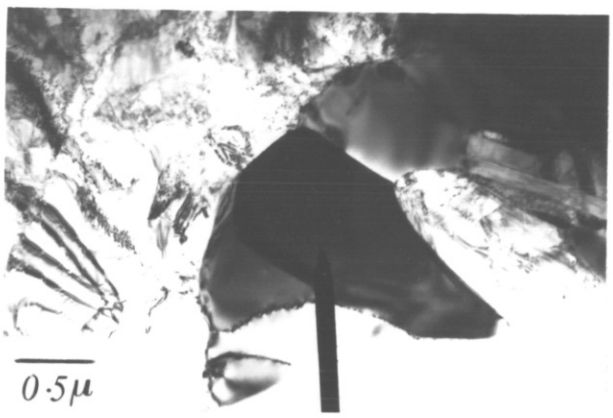

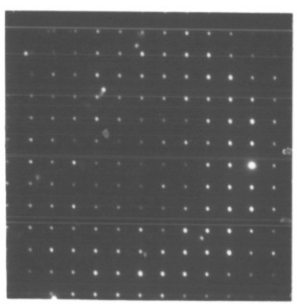
[001]σ

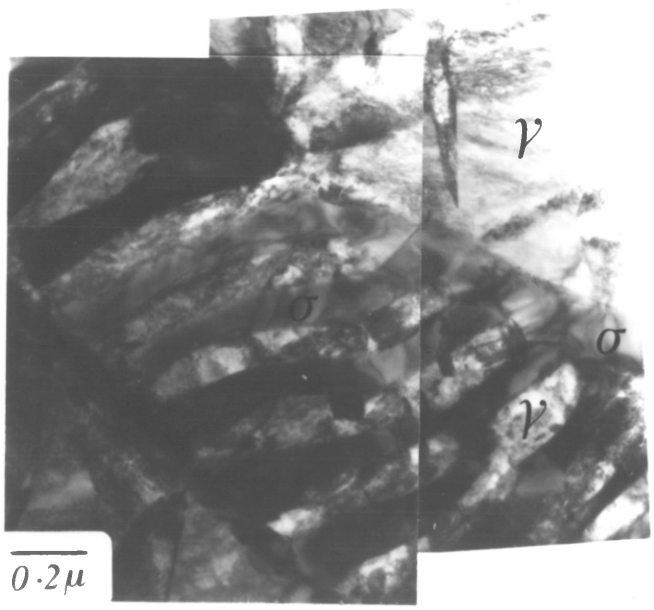

Figure 108. Alloy 21Cr-6Ni-8Ru aged at 650°C for 168 hours. The TEM shows σ and γ phases co-existing together as a lamellar mixture.

Figure 109. SADP of sigma phase above shows $[0\bar{1}1]_{\sigma}$. Extra odd reflections originate from the austenite phase.

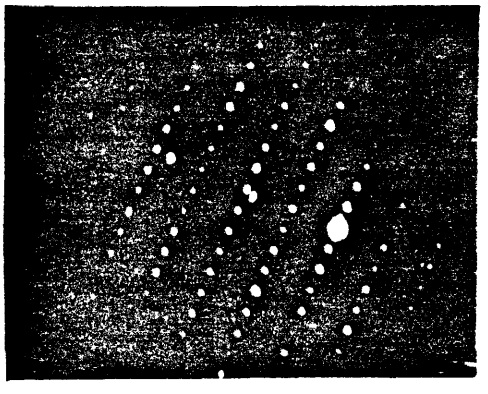

Figure 110. The TEM micrograph of the above alloy shows grains of σ and α. $2\lambda L = 5.29 \text{ Å cm}$

Figure 111. The TEM micrograph of the above alloy shows σ phase growing into and consuming α.

γ
σ
0·1μ

α
α
σ
σ
σ
0·1μ

σ
α
α
σ
α
σ
0·1μ

Figure 112. Alloy: 21Cr-6Ni-8Ru.
Condition: The structure annealed at 1250°C contained α grains in a γ matrix.
The structures in the TEM micrographs below result from ageing at 650°C for 168 hours.

The TEM micrographs show an austenite grain which has partially decomposed into an hcp phase, ε-martensite, of near ideal c/a ratio. Two variants of the hcp phase are present and give rise to the extra reflections in the SADP. These reflections are streaked because the hcp phase is present as very thin (and overlapping) plates seen in (d) and (e) HRDFs. The HRDF in (c) originates from a $\{\bar{1}3\bar{1}\}_\gamma$ reflection.
The SADP in (b) shows $[310]_\gamma // [\bar{1}2\bar{1}3]_\varepsilon$ with $[\bar{1}2\bar{1}3]$ having a mirror image which is $\{10\bar{1}1\}$ twin related. $2\lambda L = 5.29$ Å cm

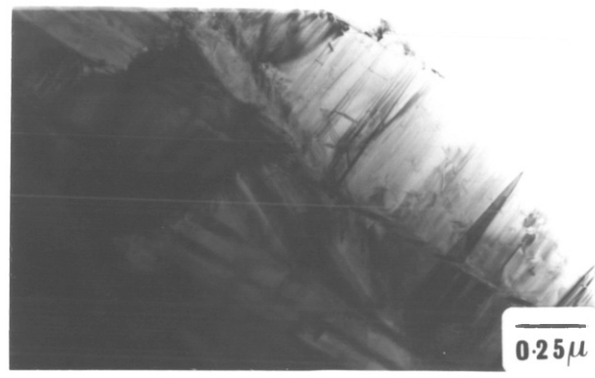

a

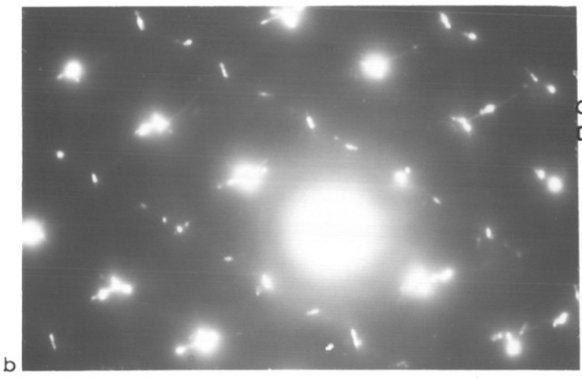

b

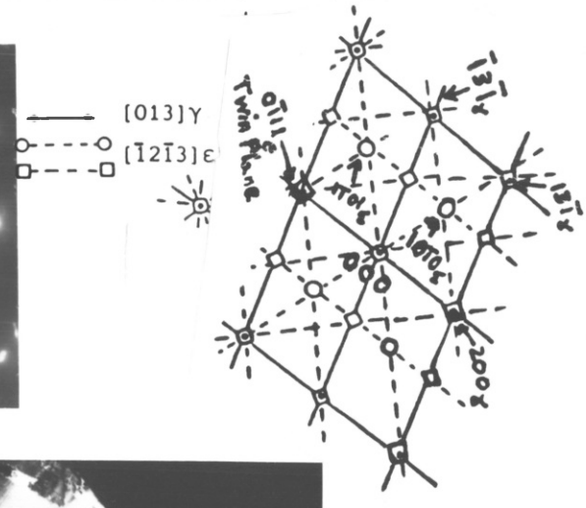

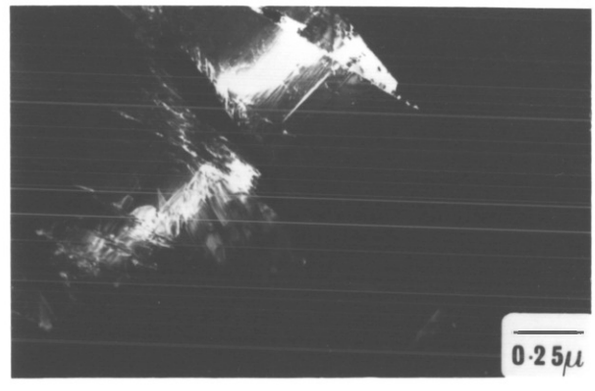

c

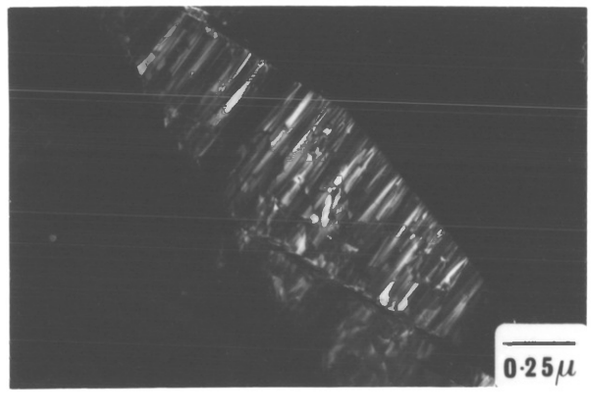

d

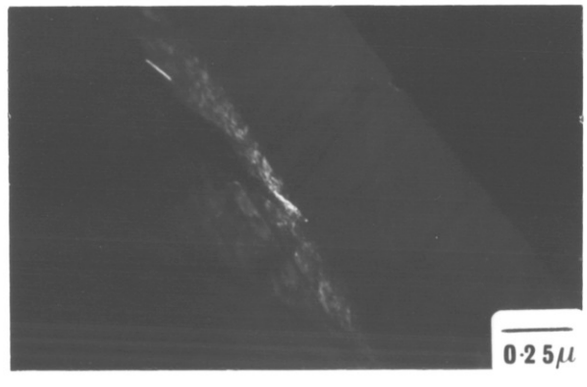

e

Figure 113. Hardness Variations with Ageing Time And Temperature.

(a)

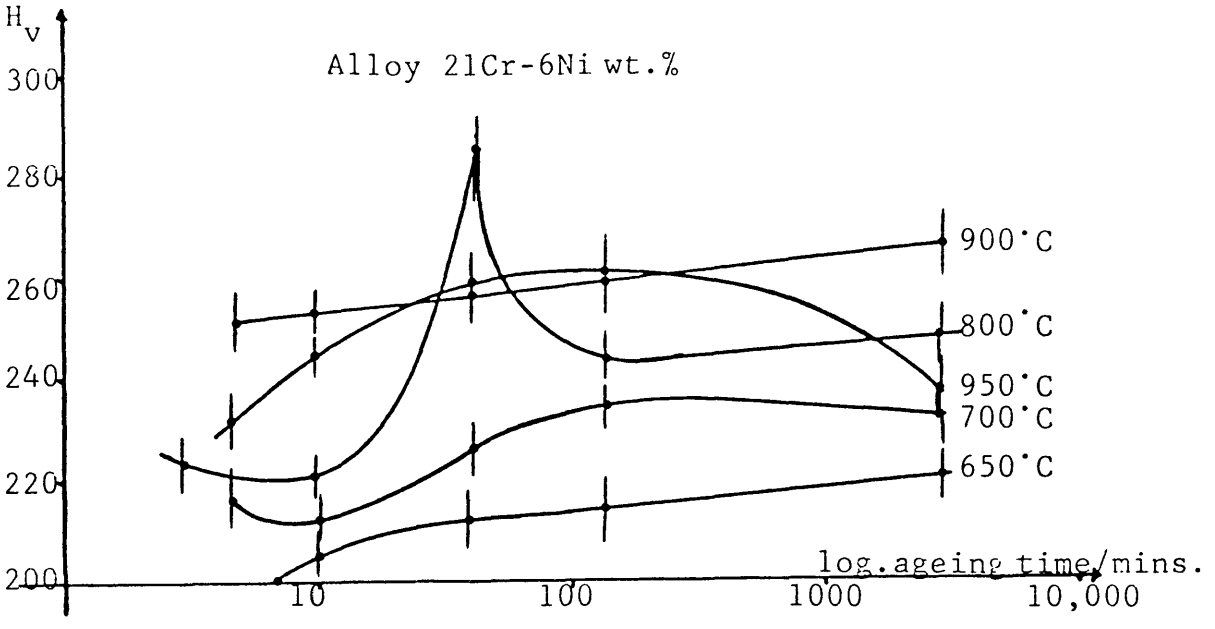

(b)

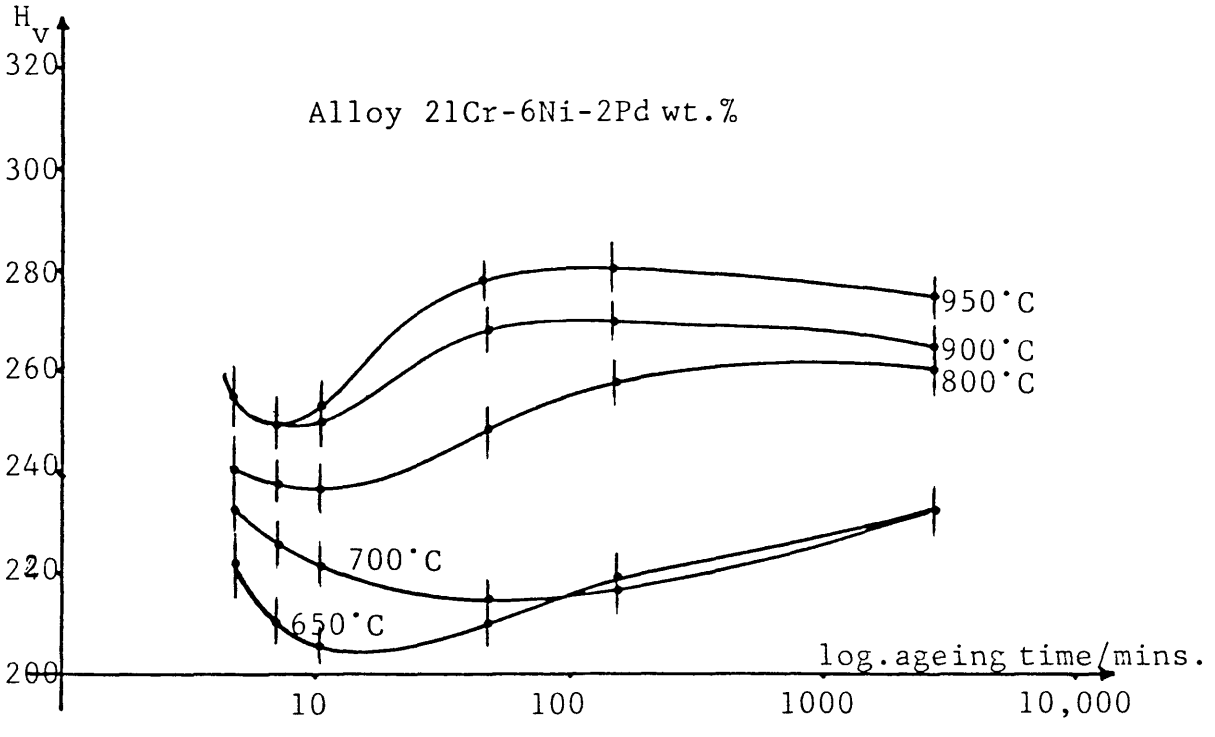

(c)

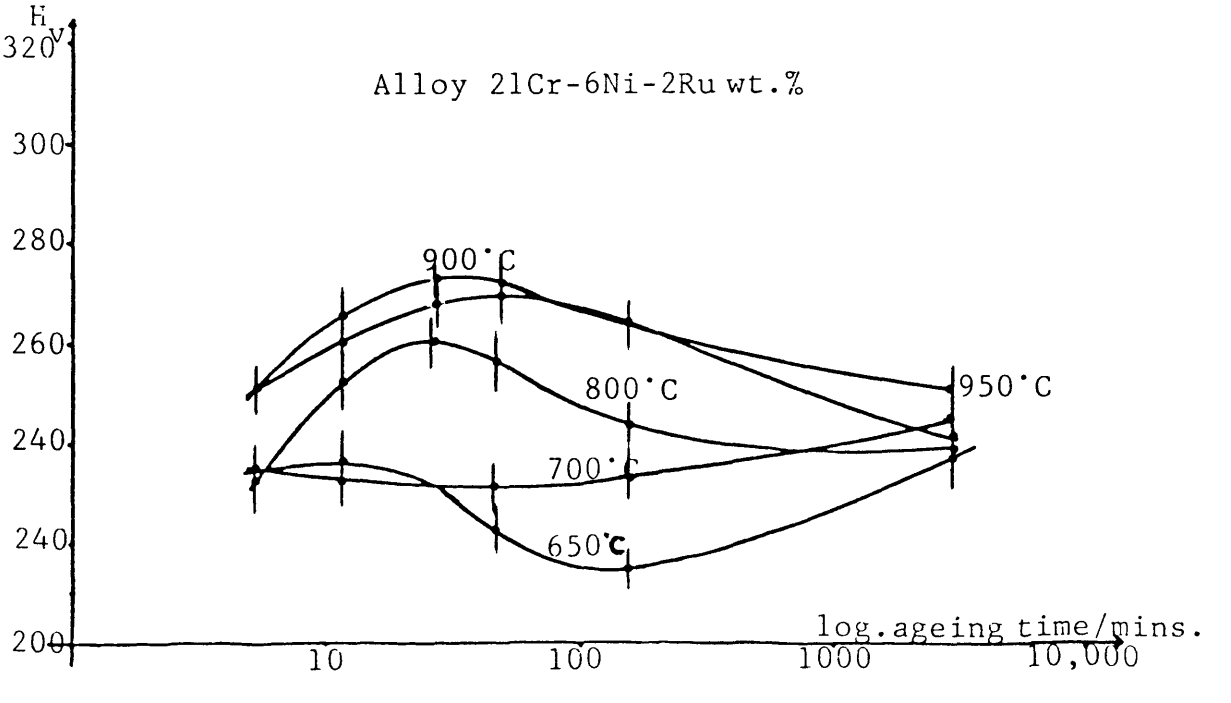

Figure 114. Variations in σ-Sigma morphology
Alloy: 21Cr-6Ni-2Pd wt%

(a) Aged at 950°C for 40 minutes, the above alloy precipitates σ phase as fine discrete grains at α/γ grain boundaries.

(b) Aged at 900°C for 40 mins., the above alloy precipitates σ phase as a continuous coalesced structure at ferrite grain boundaries.

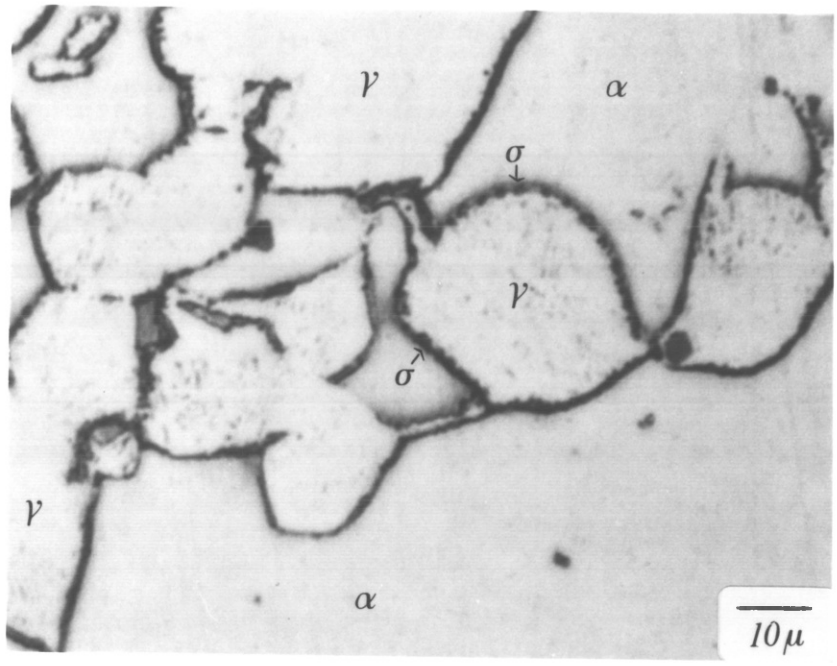

a

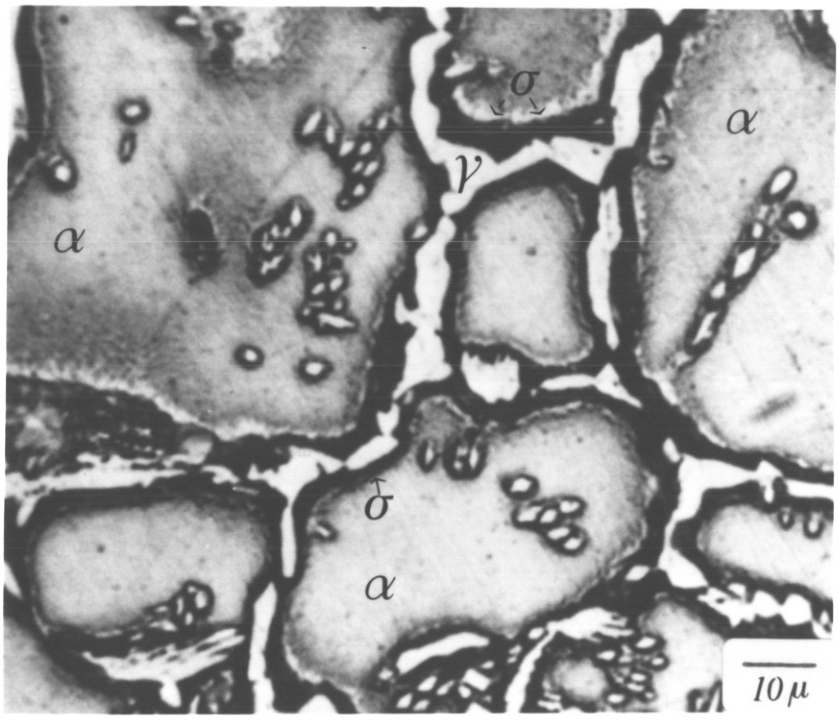

b

ferrite, and austenite phases are 900-1000, ≈260 and ≈230 respectively (216).

6.2. Discussion

6.2.1. Phase Constitution

Sigma phase in the Fe-Ni-Cr ternary system has an upper limit of ≈950-960°C (from Pugh and Nisbet (38)), for a section of constant 50%Fe. However, the precise limits in the ternary system are still uncertain. A narrow range is proposed at 900°C below 10%Ni (Figure 74). At lower temperatures of 800 and 650°C, this range expands to include the Cr-Fe edge (9).

The ternary alloy in this present work is 21Cr-6Ni. With an increasing ageing temperature of 650°C to 800°C (Figures 116 and 117), this composition moves from the $\sigma + \alpha + \gamma$ triangular phase field, to the two phase $\alpha + \gamma$ phase field; the $(\alpha + \gamma)/(\sigma + \alpha + \gamma)$ boundary moving to higher Cr and Ni levels with increasing temperature. The results in this chapter are then at variance with respect to the phases expected at temperatures greater than 700°C, from isotherms in Figures 117 and 118, since Figure 101 shows that α does in fact develop an instability with time, and transform to sigma. Indeed, comparing the results for peak precipitation of sigma at ≈900°C for the ternary alloy in this study, to the 900°C isotherm in Figure 118, highlights the anomaly, where σ precipitation occurs quickly, but its presence is not readily predicted by the phase diagram. Such results are not uncommon, since the 25Cr-6Niwt% duplex alloy, studied by Beetge and Robinson (64) does not lie within a sigma containing phase field at 800°C or 900°C, yet their C-curves, similar to those in Figure 101, show that precipitation of σ would occur readily with time. It has been suggested that the effect of impurities such as Si, Mn, Ti, Nb, Ta and Mo are important in explaining these anomalies (59). Machlin and Shao (220) proposed a model for such effects for steel compositions at 600°C and 650°C applicable to multicomponent steels. Osuoji (221) also suggests that such a model may be a realistic modification of the isothermal sections with quaternary (or impurity) additions at temperatures higher than 700°C. The model was based on the observed change in free energy of bcc, fcc and sigma phases in the Fe-Cr-Ni system by the addition of an element X, deduced on the basis of pair potentials for element components. At temperatures >700°C, L Pryce et al (222) and A. Talbot et al (223) also report that impurities, particularly silicon, accelerate σ proportions

Figure 115.

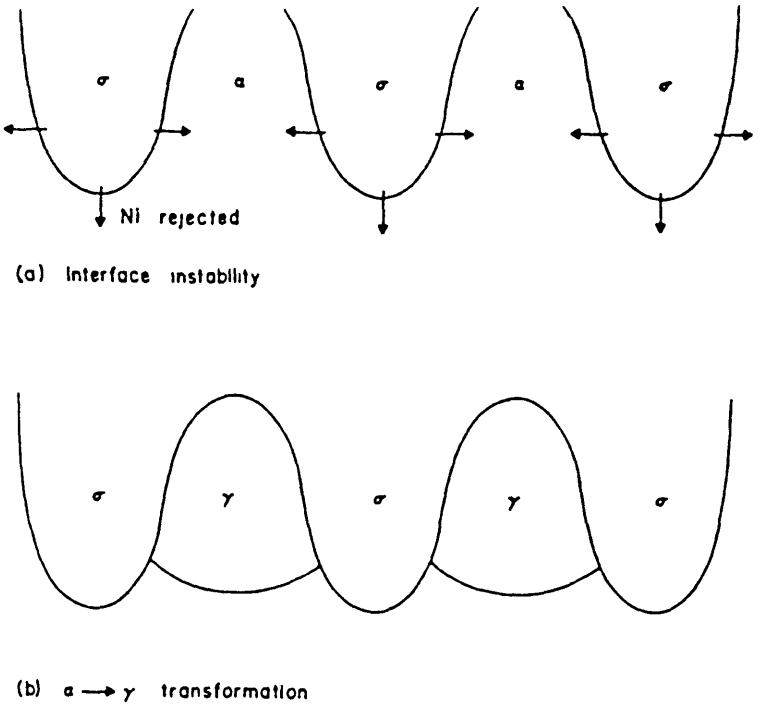

Model for austenite formation. (*a*) Development of dendritic morphology of sigma with rejection of nickel to interdendritic regions. (*b*) ferrite-to-austenite transformation

Ref. 233

Figure 116.

650°C isotherm of Cr-Fe-Ni system

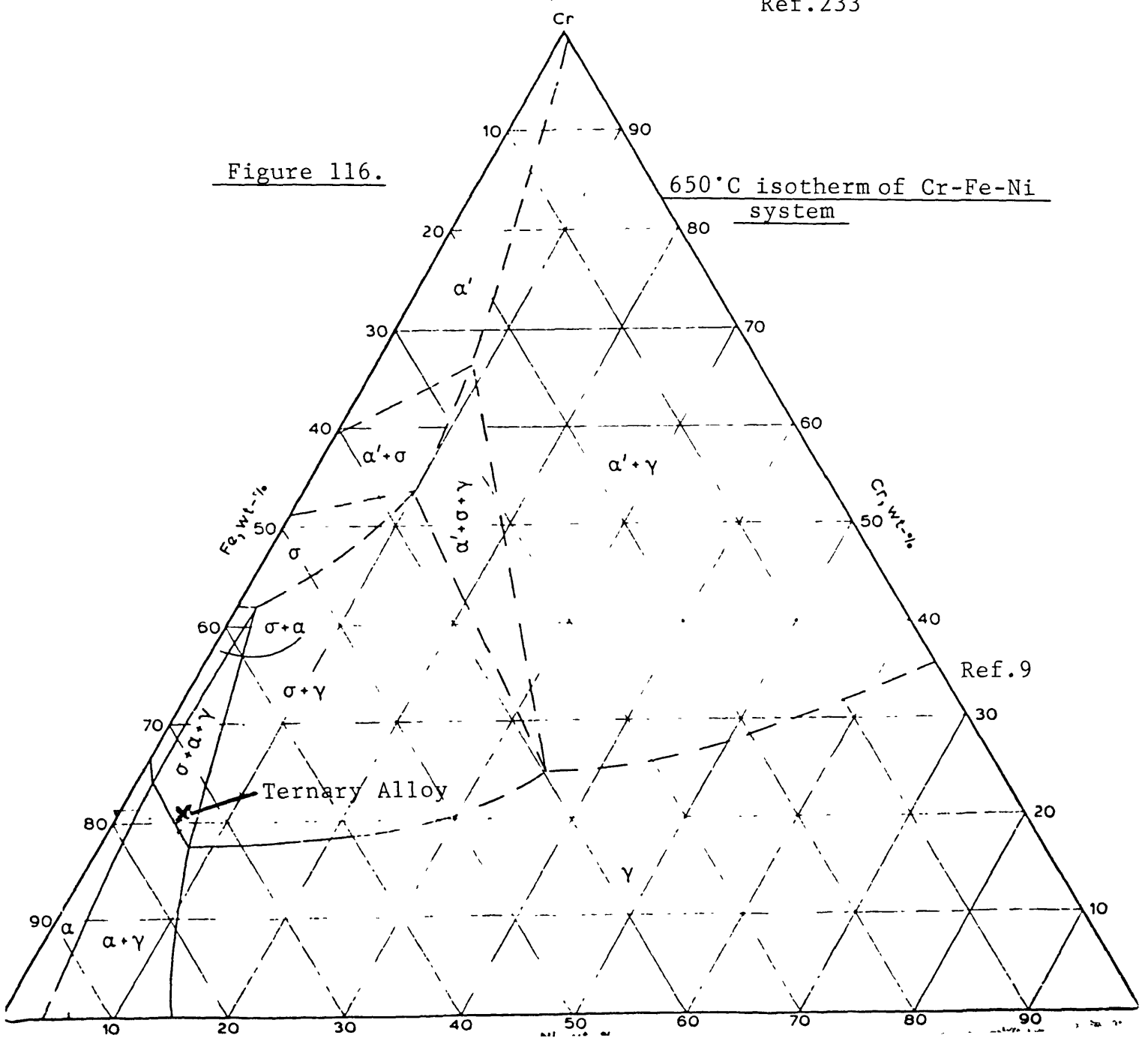

Ref. 9

800°C isotherm of Cr-Fe-Ni System.

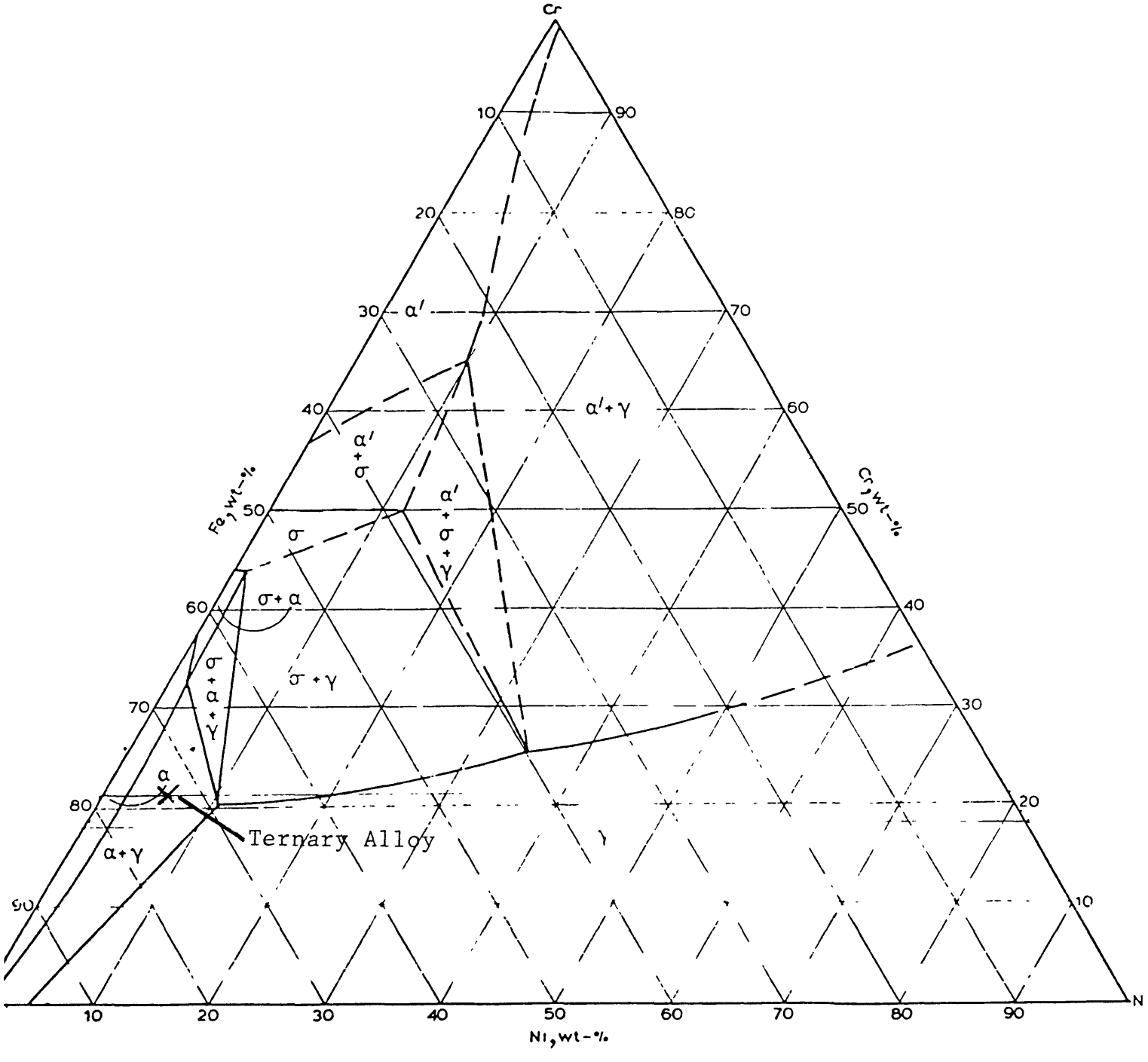

Figure 117. Ref.9

900°C isotherm of Cr-Fe-Ni system.

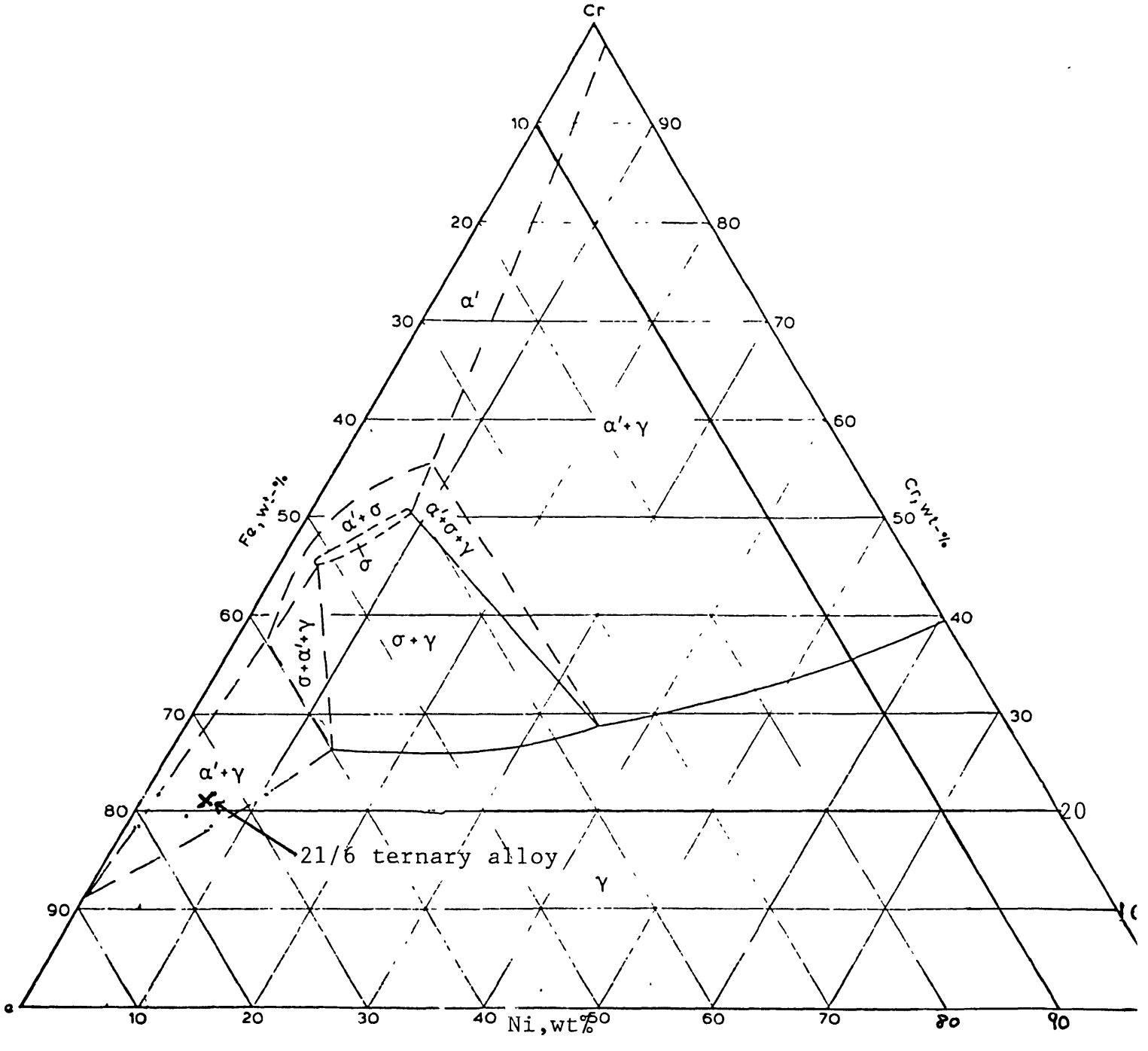

Figure 118.

Ref.9

and formation, displacing the γ-austenite solvus towards lower chromium contents below that predicted by the phase diagram. The purity of Fe used in this study is shown in Figure 50. Whilst typical impurity levels are: Si < 0.016, Mn 0.12 and Mo < 0.005wt%, are reasonably low, their combined effect might explain the accelerated formation of σ in the ternary and PGM containing alloys, not predicted by isotherms at 800°C and 900°C.

6.2.2. Compositional Effects

The effect of alloying elements on σ phase precipitation in ferrite + austenite duplex stainless steels whilst not extensively characterised in this work, has been the focus of attention in many studies (59,220, 224,225). Particular emphasis is made on the partitioning of alloying elements. Cr and Mo elements increase both the rate and the maximum amount of σ phase precipitation (224). An increase in Ni content reduces the maximum amount of σ phase precipitation, though the rate of precipitation will be accelerated (224). The effect of Ni can be explained in terms of the reduction in α-ferrite phase fraction before ageing, and its propensity to promote an enrichment of σ forming elements in the ferrite.

A limited amount of chemical data concerning partitioning of PGMs in aged specimens has been obtained in Figure 97. The analysed chromium contents of σ compared to σ compositions shown by the ternary isotherms in Figures 116-118 are consistently low. These results are very surprising since for example; the analysed σ compositions at 800°C/5 mins. ranged from 22.4 - 21.1wt%Cr and 5.9wt%Ni. These compositions lie in the two phase ($\alpha + \gamma$) field, well below the three phase ($\gamma + \sigma + \alpha$) phase triangle in Figures 116-118. The lowest σ composition predicted by the 800°C isotherm (Figure 118) is at ≈22%Cr, 12%Ni. The ternary nickel content of σ in this study is ≈6wt%Ni - half that predicted by the 800°C isotherm. This places considerable doubt on the validity of analysed σ compositions in this study, since they are significantly low in both Cr and Ni; being nearer to α compositions in the $\alpha + \gamma$ phase field. Hence, microprobe EDS analysis has not permitted conclusive chemical analysis of σ in this study. A possible source of error is attributed to inadequate phase contrast to conclusively differentiate between γ_2 and α grains adjacent to σ grains. STEM would permit more conclusive microanalysis and phase identification.

As previously mentioned the amount of α present at the temperature where the duplex structure was established, generally exceeds the equilibrium amount present at about 600-800°C. Ageing in this temperature range therefore results in a reduction in α content via an $\alpha \rightarrow \gamma$ transformation, where γ is denoted γ_2 (59). This γ_2 phase has approximately the same composition as the bulk γ and as such it is nickel-rich and chromium-poor, relative to the surrounding α (212). This aids the nucleation of Cr-rich and Ni-poor phases, such as σ phase. Both diffusion controlled nucleation and growth and martensitic γ_2 have been identified (211). Solomon (212) performed STEM analysis of γ_2 precipitates in Uranus 50 alloy annealed at 1375°C (Figure 95). Figure 95 shows that the γ_2 precipitates were enriched in Ni and Cu relative to the matrix and deficient in Fe, Cr and Mo. Like Solomon's (212) observations, results in this investigation show γ_2 to nucleate and grow prior to σ precipitation, and σ precipitation thereafter is associated with pre-existing α/α and α/γ_2 phase boundaries (see Figures 96, 98 and 99).

The acceleration of σ phase precipitation with PGM containing alloys (Figure 101), can be explained by taking into account the partitioning of PGMs in the duplex structure. For 1250°C solution treated alloys it should be noted that the increase in γ-austenite fraction, as a result of the presence of Pt, Pd or Ru, enriched the σ forming element, Cr, in the α-ferrite phase (Figures 85-87). This suggests that the rate of σ phase precipitation will increase with increasing PGM content, but that, the maximum amount of σ phase precipitation will be reduced because of the decrease in α-ferrite phase fraction. This is indeed reflected in Figure 100, where a larger proportion of σ phase is present in the Ru containing alloy than the Pd. This is as a consequence of a larger ratio of γ/α associated with the Pd alloy as compared with the Ru alloy. However, the Pd alloy has the greater acceleration of σ at relatively short times, in Figure 101, and is a consequence of a stronger partitioning to γ of Pd, causing the ferrite to be additionally enriched in Cr. It is probable then, that the effect of PGMs on σ precipitation in duplex stainess steels in relation to compositional effects, is indirect. The effect of Pd to accelerate sigma phase formation in the early stages of precipitation is attributable to its strong synergistic partitioning with Cr, whilst the larger volume fraction of ferrite associated with the Ru alloy, assists σ precipitation in its later stages.

Comparing the analysed elemental concentrations of Cr in σ (in Figure 97) with σ compositions shown by ternary isotherms (Figures 116-118), shows the Cr levels of σ to be significantly low in this present work. This cast considerable doubt on the credability of these results, compared to predicted isothermal compositions. However, one source of error, which would result in these low Cr levels, is the close association of γ_2-austenite and σ during ageing, such that precise analysis of σ phase may not be possible by microprobe EDS analysis due to the close proximity of γ_2-austenite.

6.2.3. Sigma Precipitation Kinetics

The curves in Figure 101 show the logarithmic function of precipitation rate against temperature. This relation may be expressed by the following analytical equation:

$$J = A(T)[\exp-(\Delta G^* + Q)/kT] \qquad (218)$$

where J is the precipitation rate, A(T) is a constant depending on temperature of ageing (or annealing) of the steel, ΔG^* is the change in free energy due to the formation of a nucleus, Q is the activation energy of the σ-phase precipitation process, k is the Boltzmann constant, and T is the absolute temperature. At temperatures lower than that at which the σ-phase precipitates at the highest rate, the value of ΔG^* is very small. Hence the rate of σ-phase precipitation represented in the lower ends of the "c" curves in Figure 101 may be written as: $J = A \exp - (\frac{Q}{kT})$.

The precipitation kinetics of sigma in stainless steels have been shown to conform to the Johnson-Mehl equation (218,219) for the kinetics of isothermal diffusion-controlled precipitation. The generalised equation related to this transformation in metals is given as:

$$X = 1 - e^{-(kt)^n}$$

where X = fraction (of sigma in the present work), transformed in time t, n and k being constants. This equation has been applied in the treatment of diffusion-controlled precipitation (203) and shown by Ham (226-228) to closely approximate to the time dependence of precipitation for a fraction of the reaction time. This equation yields:

$$\text{loglog}\frac{1}{1-X} = n \log t + n \log k - \log 2.3$$

If the reaction conforms to the Johnson-Mehl (218,219) equation, a graph of $\text{loglog}\frac{1}{1-X}$ versus log t is linear; n and k obtained from the slope and intercept respectively are the time exponent and rate constant.

These parameters describe how the sigma precipitation reaction proceeds. The term (1-x), is a measure of the untransformed α-ferrite phase. Figure 119 summarises the values of n in the Avrami (229,230) equation which may be observed in various experimental conditions. The values for n and k in this investigation are shown in Figure 103. The n values are more than 1, lying between 3.6 and 1.3. According to Christian (218) (see Figure 119) n values < 1 correspond to a diffusion controlled growth of σ particles growing from α/α or α/γ interfaces into α, as thick 'platelets'. These 'plates' of sigma are said to grow after complete 'edge impingement', that is as the σ front advances into Cr-rich regions, the region adjacent to it will become depleted in Cr until the volume from which σ is drawing solute atoms from, i.e. Cr, is not able to provide sufficient solute to sustain growth in that direction. This is what occurs at α/α or α/γ_2 grain boundaries which are rich in Cr, observed in this investigation in Figures 96, 98 and 99. Discrete σ particles nucleate and grow along Cr-rich grain boundaries until the grain boundary volume from which they are drawing solute Cr form, begin to overlap (impinge). Growth then proceeds into α phase by the 'thickening' of these σ grains (see Figure 111). The question then arises; could this 'thickening' process give rise to a lamellar arrangement of γ + σ phases in Figures 107 and 108? The arrangements of phases, as described by n-values (Figure 103) in this investigation indicate a structure derived from a eutectoid decomposition, since according to Christian (218) n would need to be at least 1 for such a transformation. This confirms the postulation of many authors (214-217) of a eutectoid decomposition of $\alpha \rightarrow \sigma + \gamma$ occurring in the Fe-Cr-Ni system. None of these authors, e.g. Mahara et al (216,217) have reported n and k values derived from a $\log\log\frac{1}{1-x}$ vs. log t plot to substantiate their claim. Whilst it is unclear how or why a 'thickening' of σ plates can give rise to a lamellar structure, such arrangements of σ and γ phases have been undoubtedly cited in the literature and are observed in the present investigation. J. Chance et al (231) have investigated a duplex alloy, 25Cr-7Ni-2Mowt% cooled slowly from 700-950°C and report that as σ forms in the ferrite, the surrounding matrix is enriched in nickel and denuded of chromium. As a result, a sympathetic nucleation of σ and γ occurs, which gives rise to a lamellar structure.

Figure 119 Values of n in kinetic law $X = 1 - \exp(-kt^n)$

(a) Eutectoidal reactions:	n 1-4
(b) Diffusion controlled growth: Conditions	n
Needles and plates of finite dimensions, small in comparison with their separations.	1
Thickening of long cylinders (needles), e.g. after complete edge impingement.	1
Thickening of very large plates, e.g. after complete edge impingement.	1/2
Segregation to dislocations (very early stages only).	2/3

Ref. 218.

Figure 120 Calculated n and k values from Ref. 64.

Temperature ^oC	Slope n	k minutes^{-1}	k arbitrary Unit
700	0.56	2.88×10^{-5}	100
750	0.53	1.26×10^{-5}	45
600	0.50	1.04×10^{-5}	36
800	0.53	8.91×10^{-6}	32
850	0.71	2.34×10^{-6}	8

A value of n less than 1 has been reported by Harper (232) and documented by other workers for a diffusion controlled nucleation and growth of sigma on dislocations (64,203,218). Beetge and Robinson (64) report that this growth takes place by the migration of solute atoms, e.g. Cr, to dislocations, and that subsequent growth of sigma occurs by the 'thickening' of such regions. Such a process as indicated in Figure 119, clearly occurs in the very early stages of precipitation, $t < 5$ mins, and as such was not identified in this investigation.

In Figure 102 it is evident that variations exist for the precipitation of sigma in the experimental alloys 21Cr-6Ni and 21Cr-6Ni-2Ru, as indicated by the change in slope, n. The values of n and k in Figure 103 obtained at 900°C, where the precipitation of sigma occurs relatively quickly are greater than values obtained from Beetge and Robinson (64) in Figure 120. In Figure 102 the very steep slopes observed are indicative of an interface controlled precipitation of sigma with time, associated with a eutectoid transformation of $\alpha \rightarrow \gamma + \sigma$ phase. Beetge and Robinson (64) also propose an arbitrary parameter, k, in Figure 120, which they equate to a 'reaction rate'. Unfortunately, this cannot be strictly correct, as two derivations have been used, i.e. log log $\frac{1}{1-X}$, to obtain it, and it therefore should be considered as a very qualitative term to describe how a reaction proceeds. k values have been calculated in this study, and are shown in Figure 102. The PGM containing alloy has a reaction constant, k 2.3 times greater at 900°C than 800°C, whilst in the ternary alloy, 21Cr-6Ni, it is 5 times greater at 950°C, than 800°C. Although a direct comparison is not possible, the implication is that the presence of PGMs, Ru in this instance, accelerates σ precipitation; the effect increasing with ageing temperature up to 900°C.

The Avrami (229) equation (often in the form $f = 1 - \exp(-kt^n)$) provides a reasonable approximation for the growth kinetics in the early stages of sigma precipitation in this study. However, Ham (226,227) emphasises, that it does not have any fundamental significance on diffusion limited transformations, except as an approximation for small times. Moreover, the experimental value of n is of limited value since the growth law does not distinguish between particles of various shapes growing initially from small dimensions (218).

6.2.4. Substructural Transformations

In the present study the precipitation of sigma in duplex steels assists the onset of a variety of substructural transformations in ferrite (Figures 104-112). Firstly, at the ferrite/sigma interface, the growth of sigma appears to increase the dislocation density, Figures 110 and 111, clearly induced by stresses resulting from transformation strains. These dislocations were observed in Figures 110 and 111 for the 21/6/2Pd alloy aged at 650°C for 168 hours. Studies have shown that the recovery of these dislocations into observed subgrain structures is due to the thermal activation provided by elevated ageing temperatures (64,233). Secondly, regions of the ferrite transform to austenite. For this to occur it is evident that thermal activation must be sufficient for long range diffusion, and, the partitioning of alloying elements necessary for austenite transformation. Chemical analysis of aged samples in Figure 97 show this process to proceed and promote chemically, local regions of austenite. The formation of sigma depletes ferrite of Cr, in addition Ni and Pd are probably rejected from the growing sigma phase. The atomic structure of Ni, Pd and Ru would be expected to raise the average electron concentration of an alloy such that sigma phase formation is favoured (234-236). Therefore, Ni, Pd and Ru are not expected to be major components of sigma phase and their rejection enhances the likelihood of austenite stabilization, promoting austenite formation adjacent to sigma, as is in fact observed in Figures 107 and 108. Figure 115 shows schematically a proposed (233) two step process by which this observed sigma-austenite morphology may develop. The first step may involve the development of a sigma-ferrite interface in a manner similar to dendritic growth. Diffusion of Cr to sigma and Ni and PGMs from the sigma-ferrite interface into the interdendritic regions occur at this stage. Without the diffusion-limiting constraints of the interdendritic regions and the large interfacial areas per unit volume associated with the branched growth of the sigma phase, it is not probable that PGMs could build-up to a concentration sufficient for sigma formation. Striking evidence for the validity of the proposed model is seen in Figures 107 and 108. Maehara et al (216,217) further report on this lamellar morphology of sigma which appears in Figures 107 and 108. For a duplex alloy Fe-25Cr-7Ni-3Mo solution treated at 1250°C and aged between 700°C and 950°C sigma particles were observed to nucleate at ferrite/austenite interfaces and grow into ferrite grains, thereafter a decomposition of

ferrite into sigma and austenite phases occurred with a resultant lamellar morphology of sigma and austenite. They postulate the precipitation process of sigma phase in duplex stainless steels as $\alpha \rightarrow \sigma + \gamma$.

Although no systematic transmission electron microscopy has been done in this study, light microscopy has not provided evidence of a eutectoid transformation in the early stages of sigma precipitation; i.e. <250 mins. However > 250 mins. lamellar aggregates of γ and σ are present, but their prior transformation sequence, was not evident. A sympathetic transformation of $\alpha \rightarrow \sigma + \gamma$, has however been identified as the reaction mechanism (231).

6.2.5. Hardness Variations

The development of hardness with time and temperature is shown in Figure 113. For the ternary alloy 21Cr-6Ni in Figure 113a, hardness values increased from 200 to 285 with increasing amounts of sigma. The peak hardness occurring in approximately 40 mins. at 800°C is consistent with a peak transformation of σ at this temperature. Thereafter hardness falls very sharply. The behaviour is particularly incongruous, since there are no clear microstructural features, readily observable to explain it. However, the behaviour is likely to be associated with instability in α' or α phases, via:

$\alpha' \rightarrow \gamma$; recovery and reversal

or $\alpha \rightarrow \gamma_2$; equilibration

After ≃ 100 minutes of ageing, a levelling off of hardness is achieved for each temperature consistent with a saturation of sigma precipitation and occurrence of γ_2-austenite.

The Pd containing alloy in Figure 113b developed hardness values between 205-280; the maximum hardness achieved is at the annealing temperatures of 950°C. The curves 650°C to 950°C all show an initial softening before increased hardness. The minimum of these curves coincide with minimas of σ contents in Figure 100 prior to rapid transformation. This early softening is likely to be associated with an initial equilibration of austenite and ferrite fractions and annealing of strain-induced martensite within γ-austenite.

Similar characteristics are observed for the Ru containing alloy in Fig. 113c. However in the Pd alloy a somewhat anomalous effect exists for the 950°C curve which lies above the 900°C curve. This contradicts values

for σ content in Figure 100 and 101 which indicate faster precipitation at 900°C than 950°C; and therefore higher hardness values are expected. However, comparison of photomicrographs in Figure 114 reveals that the 950°C specimen contains sigma in a fine irregular form at grain boundaries. The sigma developed at 900°C, on the other hand, is present as a more continuous coalesced structure at ferrite grain boundaries. It is probably this difference in sigma morphology, rather than the relative amount at the two temperatures, which accounts for the difference in hardness.

6.2.6. Effect of Thermal History and Strain

The effect of a 1250°C solution treatment temperature received by alloys in this study is an important consideration on the subsequent precipitation of sigma, since Roberts (237) has reported that an increase in the solution annealing temperature causes an increase of ferrite content and a change in chemical composition; raising its chromium and molybdenum percentages. Both variations will have a marked influence on the subsequent phase precipitations. Maehara et al (238) also report that a relatively small retardation of the σ precipitation by increasing the preheating temperature in the α + γ duplex phase region is experienced for alloys 25Cr-7Ni-3Mo and 23Cr-6Ni. They further investigated (238) the effects of thermal history prior to ageing, noting a significantly large retardation of σ phase by (a) heating in the single phase region > 1350°C or (b) remelting > 1550°C and furnace cooled to 1400°C before water quenching. These retardation effects were attributed to the homogenisation of alloying elements by heat treatments in (a) and (b).

In the present study, experimental alloys were water quenched after annealing; whether this enhanced σ precipitation by introducing local regions of thermal strain and dislocations, is inconclusive. However, Maehara et al (238) report that σ precipitation is indeed enhanced by water quenching before ageing by the introduction of lattice defects, acting as potent sites for precipitation, (though these defects were not identified).

It is worth mentioning, finally, the significant effect of strain induced by hot or cold working or even water quenching on σ precipitation. These variables have been shown to enhance σ nucleation and growth (59,221,225,238-240). In duplex steels this enhancement is very important in view of practical applications (238).

The $\alpha \rightarrow \sigma$ transformation, further produces a volume contraction which is measurable by dilatometry. Typical results by Maehara et al (238) are shown in Figure 121. They report that σ phase precipitation is avoidable by increasing the cooling rate above 20-30°C/min. The practical consequence is that with air cooling of plate sections, about 20 mm is the maximum thickness that can be produced without difficulty. It seems unlikely from this study that Pd or Ru would improve these production variables as a consequence of inherently increased σ precipitation rates.

Effect of cooling rate on σ precipitation.

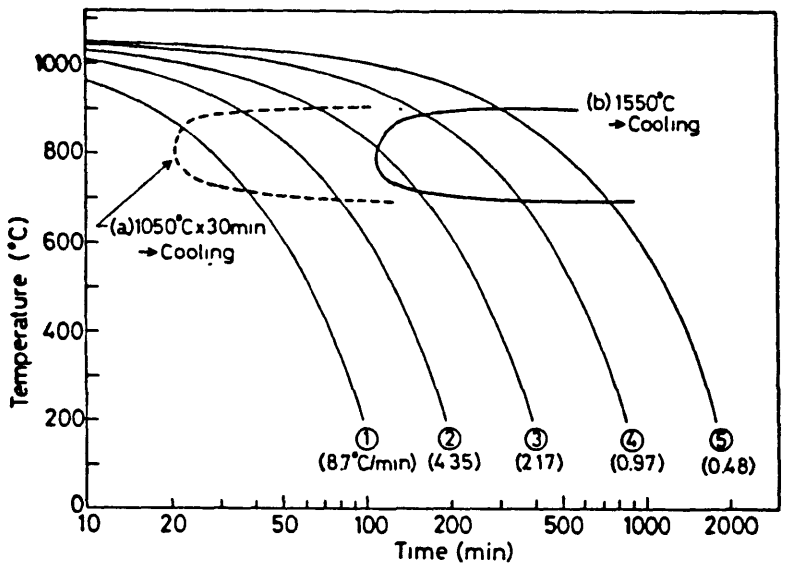

CCP diagrams for the σ phase precipitation; (a) after heating at 1 050 °C and (b) after remelting at 1 550 °C, where the time is counted after cooling curve described in the figure crossed 1 050 °C.

Alloy Composition-0·02C,0·94Mn,0·49Cu,6·64Ni,25·3Cr

Figure 121. Ref.216

CHAPTER 7

Martensite: formation and structure

Phase transformations occur in order to lower the energy of a body. Or to put it another way...

'Its a very funny thought that, if Bears were Bees,
They'd build their nest at the bottom of trees.
And that being so (if Bees were Bears),
We shouldn't have to climb up all those stairs'

(A.A. Milne)

7.1. Results

7.1.1. Effect of PGMs on Bulk Martensite

In this section of work the austenite stability will be discussed. The term, 'stability', will be used to refer to the propensity of metastable γ transforming to martensite.

The fraction of γ-austenite transformed to α'-martensite has been determined by measuring the ferromagnetic ($\alpha' + \alpha$) content of annealed and deformed alloys by magnetic balance measurements and subtracting the equilibrium volume fraction of α determined by point counting. The fraction of $\gamma \rightarrow \alpha'$ in ternary and PGM modified alloys annealed at 1250°C and cooled rapidly to room temperature is shown in Figure 122.

Figure 122.

% $\gamma \rightarrow \alpha'$ In Ternary and PGM Containing Alloys Determined by Magnetic Balance and Point Counting Measurements of α, γ and α' Phases

Alloy	%$\gamma \rightarrow \alpha'$	Alloy	%$\gamma \rightarrow \alpha'$
21Cr-6Ni-Fe bal.	69	18Cr-6Ni-Fe bal.	63
21Cr-6Ni-2Pt-Fe bal.	21	18Cr-6Ni-2Pt-Fe bal.	43
21Cr-6Ni-8Pt-Fe bal.	10	18Cr-6Ni-8Pt-Fe bal.	3
21Cr-6Ni-2Ru-Fe bal.	12	18Cr-6Ni-2Ru-Fe bal.	61
21Cr-6Ni-8Ru-Fe bal.	9	18Cr-6Ni-8Ru-Fe bal.	29
21Cr-6Ni-2Pd-Fe bal.	3	18Cr-6Ni-2Pd-Fe bal.	59
21Cr-6Ni-8Pd-Fe bal.	3	18Cr-6Ni-8Pd-Fe bal.	1

In all cases the additions of Pt, Pd and Ru to the ternary alloys result in a decrease in the fraction of austenite transformed to martensite at room temperature. In the 21Cr-6Ni alloy series the additions of PGMs to the ternary alloy series, both at the 2 and 8 wt% level, substantially reduced the α' fraction; the 21Cr-6Ni-8Pd alloy in particular contained a negligable α' content compared to $\simeq$69% in the ternary alloy. Pt and Ru are less effective at stabilizing austenite than Pd, with Ru being intermediate to Pd and Pt. In the 18Cr-6Ni alloy series, Ru at the 2 and 8 wt% level is the least effective PGM at inhibiting α'-martensite formation, whilst Pt confers the greatest stability at the 2% level and Pd at the 8% level.

The % of γ transformed to α'-martensite in alloys deformed at room and liquid nitrogen temperatures, was also determined by the above procedure and results are presented in Figures 133 and 134.

7.1.2. Microstructural Features

The amounts and distribution of martensite are illustrated in Figures 123-131. Figure 123 shows α'-martensite generated in metastable γ for the 21Cr-6Ni alloy. This α'-martensite forms within bands of γ as laths having a 'blocky' appearance. Figure 124 shows these laths of α'-martensite to have $[\bar{1}11]_{\alpha'}$ and [001] variants shown in the HRDFs. Figures 125 and 126 show light and TEM micrographs of the duplex alloy, 21Cr-6Ni-8Ru annealed at 1250°C and water quenched. Figure 125a shows the γ phase (60%) as the matrix, containing α grains. Within the austenite phase are regions of overlapping stacking faults and transformation to ε- and α'-martensites seen in Figures 125b and c. The α'-martensite (identified in Figure 126) is seen as faulted parallel-sided plates growing from and within bundles of ε-martensite. Figure 126 shows these α'-martensite plates as a $[110]_{\alpha'}$ variant. The α'-martensite plates also have ledge-like steps running across them. Figure 126(d) shows all four, α', α, γ and ε phases co-existing together in this duplex alloy. In particular an α'-martensite "embryo" grain (53) is seen to nucleate and grow within a bundle of ε-martensite. Figures 127 and 128 show light and TEM micrographs of the 18Cr-6Ni-8Ru alloy. Large faulted polyhedral grains of γ-austenite predominate (Figure 127a), although the TEM micrograph in Figure 127b shows grains of untransformed γ. The TEM micrograph in Figure 128a shows an "embryo" of α'-martensite lying in a bundle of ε-martensite with the following relationship:

$$[1\bar{2}10]_{\varepsilon} // [1\bar{1}0]_{\gamma}$$
$$(0001)_{\varepsilon} // (111)_{\gamma}$$

Figure 128c shows additional transformed regions to contain stacking faults and ε-martensite. The SADP pattern shows 2 variants of hcp ε-martensite precipitates forming on the $(\bar{1}1\bar{1})$ and $(11\bar{1})$ fcc planes. The orientation relationship in each case is a variant of:

$$(0001)_{\varepsilon} // (111)_{\gamma} \equiv (\bar{1}1\bar{1})$$
$$[\bar{2}110]_{\varepsilon} // [0\bar{1}1]_{\gamma}$$

Figure 129 shows α'-martensite structures generated in the 18Cr-6Ni-8Pd alloy. Large grains of austenite exist containing surface martensite (188). This surface product, identified by SEM, exhibits significant surface relief, and is in the form of lens-shaped needles with a central midrib. Within the bulk material, this alloy shows the conventional α'-martensite laths having a high dislocation density, and identified in the SADP in Figure 129(d). The effect of Pd and Ru on the M_s temperature in the 21Cr-6Ni alloy series is shown in Figure 132. The ternary alloy has an M_s of 229°C, whilst the M_s for the Ru alloy was substantially lower at 146°C. The M_s for the 21Cr-6Ni-2Pd alloy was not readily observed.

Figure 123. Alloy: 21Cr-6Niwt%
Condition: Light and TEM micrographs of 1250°C annealed alloy cooled rapidly to room temperature.

(a) The light micrograph shows α-martensite generated within the austenite phase as parallel regions of striations.

(b) The TEM micrograph identifies the regions of striations in γ above, as bands of martensite plates within the transforming austenite. However, no clear evidence of untransformed γ is present in this micrograph.

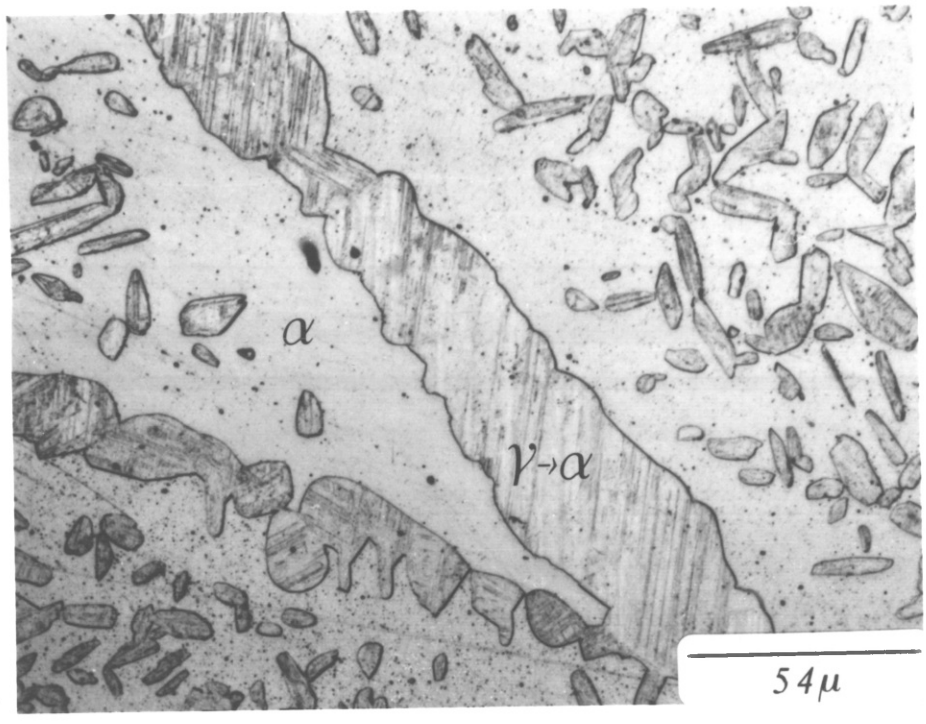

a

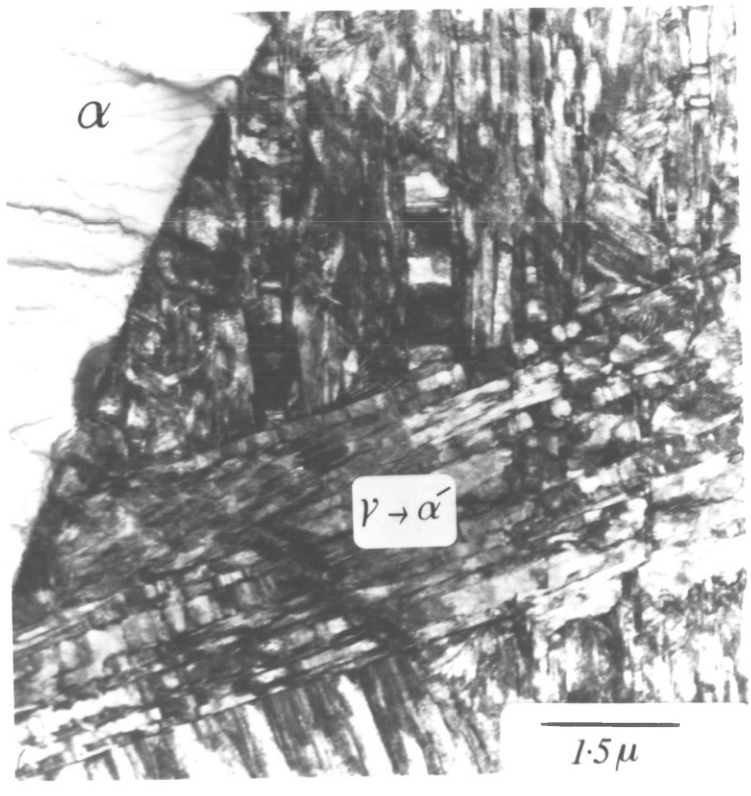

b

Figure 124. Alloy: 21Cr-6Niwt%
Condition: TEM micrograph of 1250°C annealed alloy cooled rapidly to room temperature.

(a) TEM micrograph. The metastable γ-austenite shows transformation to 'laths' of α-martensite containing a high dislocation density.

(b) SADP from bright-field area in (a), identifying α' variants: $[\bar{1}11]_{\alpha'}$ and $[001]_{\alpha'}$.
No γ-austenite is indicated. $2\lambda L = 5.29 \text{Å cm}$

(c) HRDF identifying the $[\bar{1}11]_{\alpha'}$ variant.

(d) HRDF identifying the $[001]_{\alpha'}$ variant.

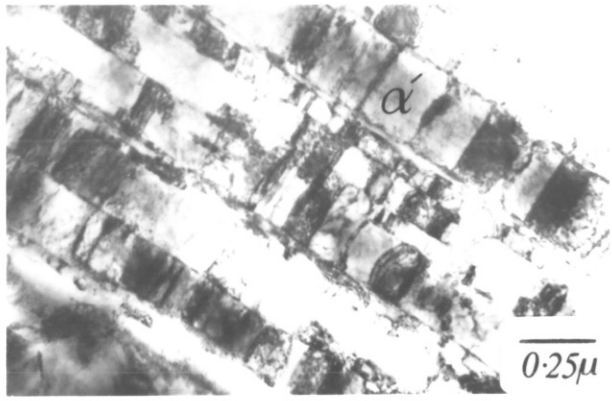

a

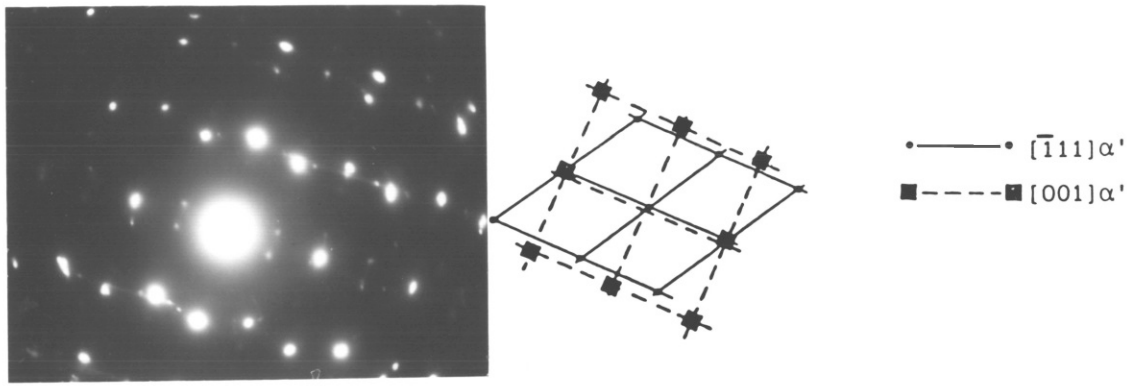

b

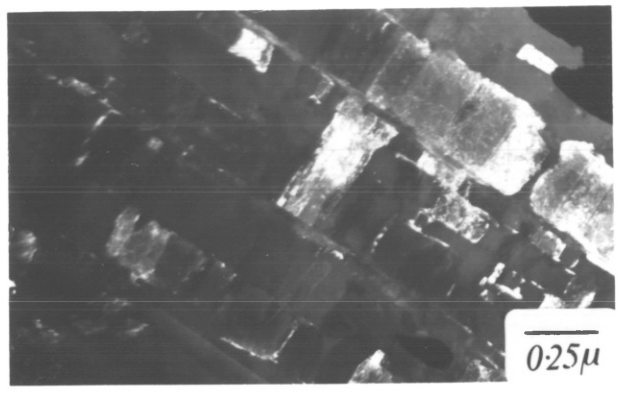

c

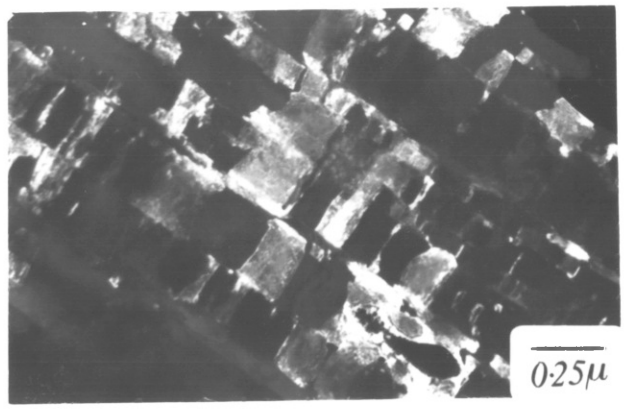

d

Figure 125. Alloy: 21Cr-6Ni-8Ruwt%
Condition: Light and TEM micrographs of alloy annealed at 1250°C and rapidly cooled to room temperature.

(a) The light micrograph shows grains of α in an γ matrix.

(b) The TEM micrograph shows that the austenite phase contains regions of slip, bundles of ε-martensite and parallel sided plates of α'-martensite. The α' phase was identified in the SADP in Figure 126(a).

(c) The TEM micrograph shows an area of austenite containing a high density of overlapping stacking faults.

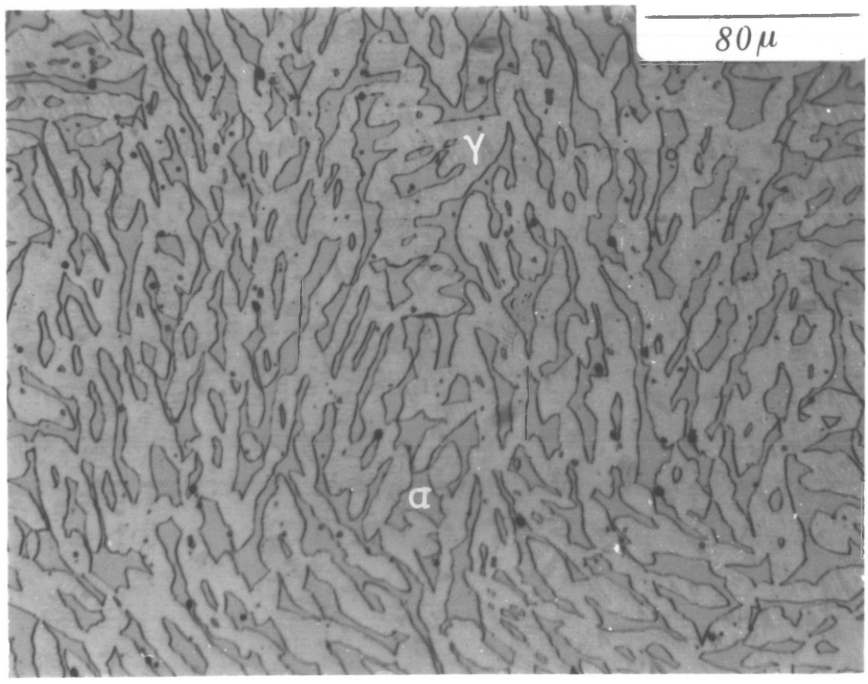

a

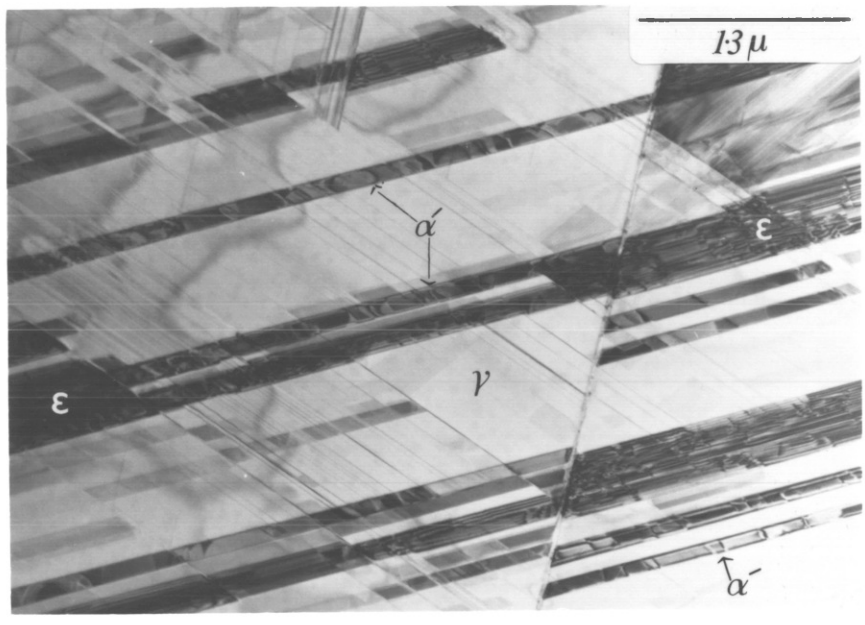

b

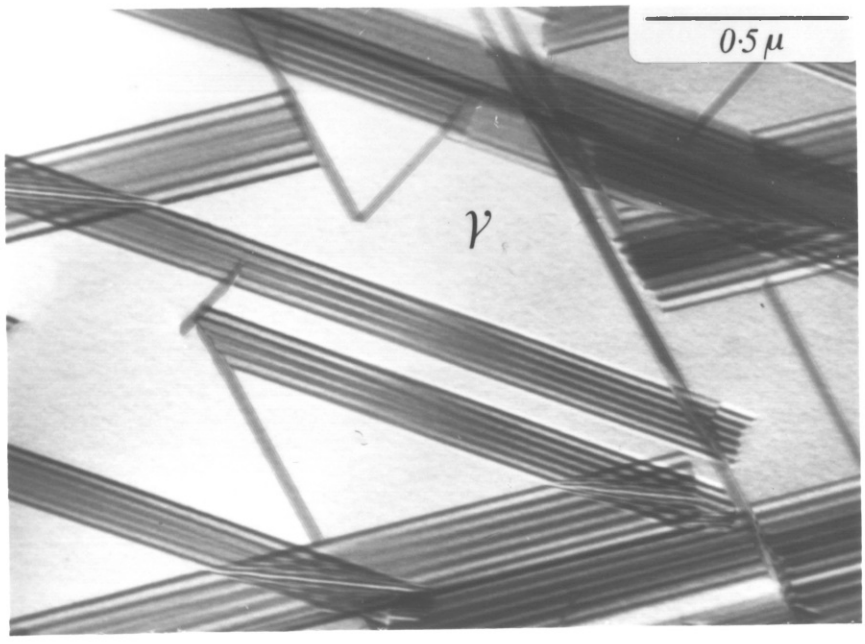

c

Figure 126. Alloy: 21Cr-6Ni-8Ruwt%
Condition: TEM micrographs of alloy annealed at 1250°C and rapidly cooled to room temperature.

(a) The TEM micrograph shows variants of α'-martensite in austenite. The martensite plates contain ledges running across them, (possibly associated with dislocations).

(b) The SADP from the area in (a) identifies the α'-martensite plates lying in an austenite matrix with $[110]_{\alpha'} // [\bar{1}11]_{\gamma}$. The HRDF in (c) originates from a $\{\bar{2}\bar{2}0\}_{\alpha'}$ reflection. $2\lambda L = 5.29$ Å cm

(c) The TEM micrograph shows grains of α, γ, ε and α-martensite co-existing together. The α'-martensite is seen as an 'embryo-like' grain within ε-martensite.

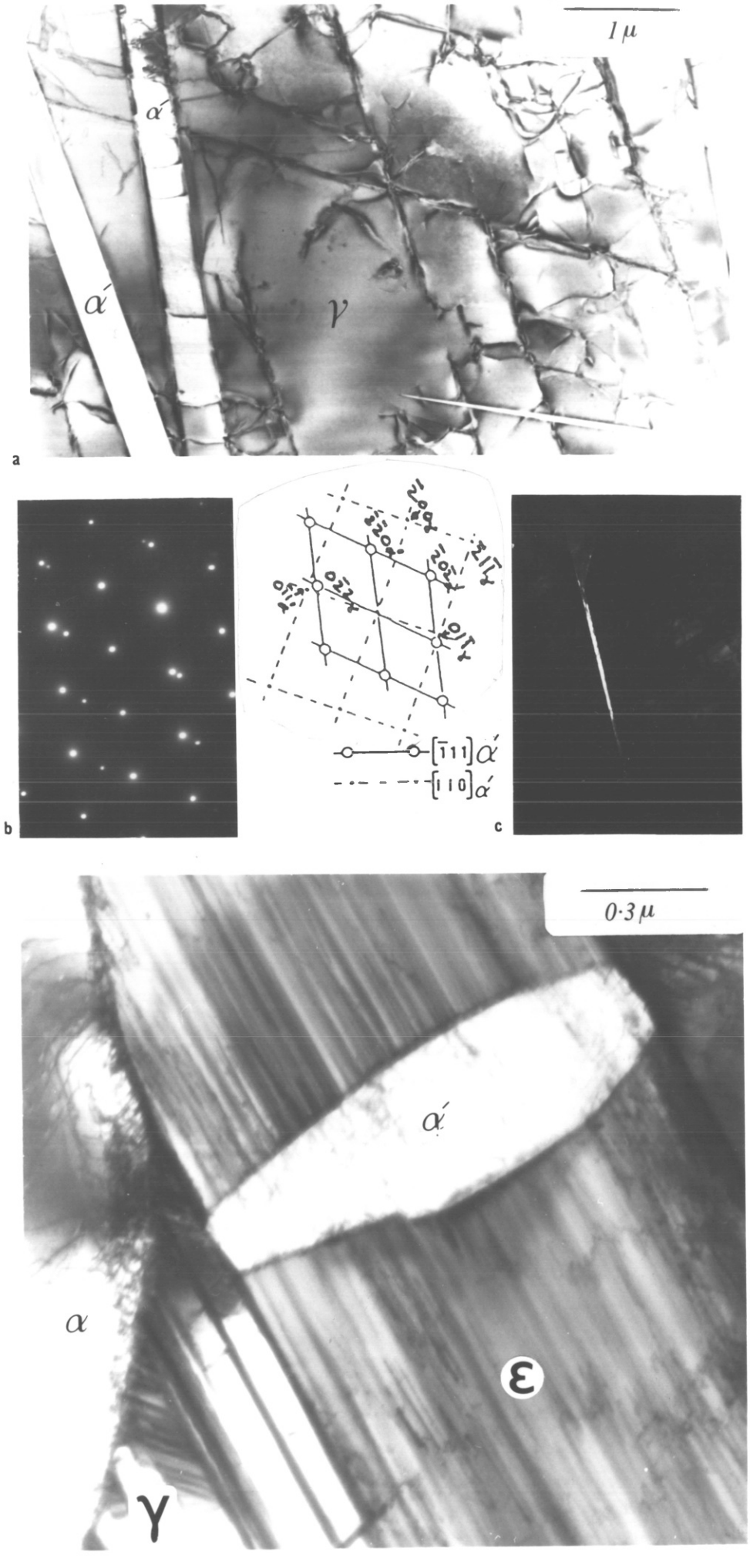
1 μ
α′
α′
γ
a
b
c
[1̄11]α′
[110]α′
0·3 μ
α′
α
ε
γ

Figure 127. Alloy: 18Cr-6Ni-8Ruwt%
Condition: Light and TEM micrographs of alloy annealed at 1250°C and rapidly cooled to room temperature.

(a) The light micrograph shows large grains of austenite containing faults.

(b) The TEM micrograph shows grains of untransformed austenite.

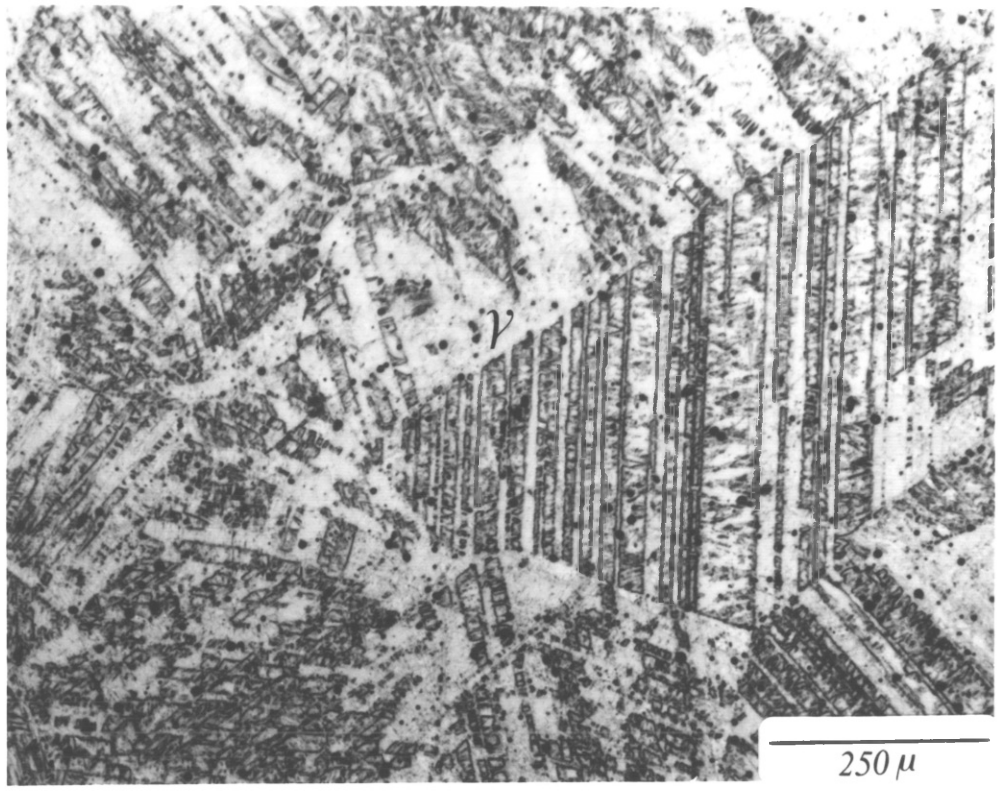

a

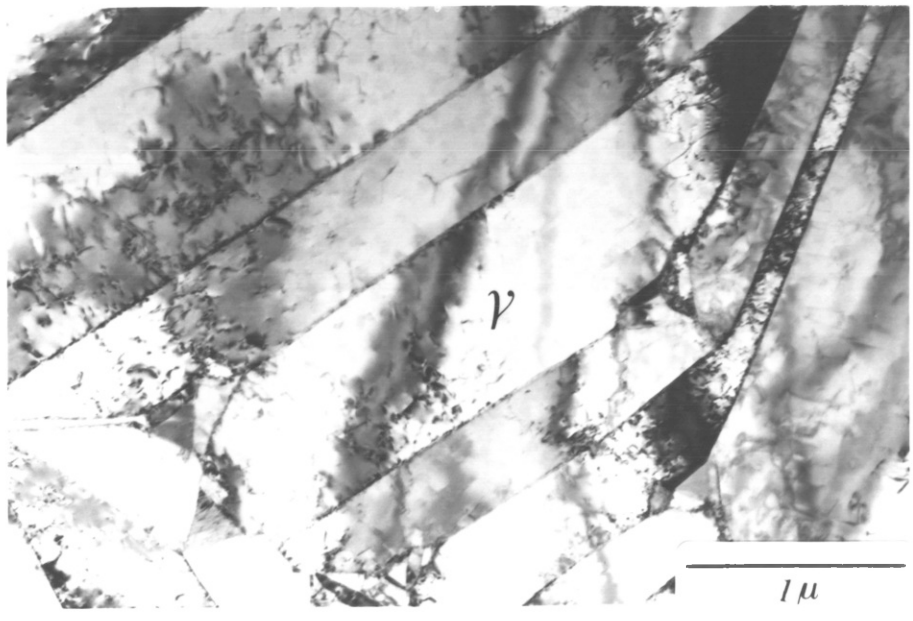

b

Figure 128. Alloy: 18Cr-6Ni-8Ruwt%
Condition: TEM micrograph of alloy annealed at 1250°C and rapidly cooled to room temperature. ($2\lambda L = 5.29$ Å cm)

(a) The TEM micrograph shows α'-martensite lying within a band of γ-austenite transformed to ε-martensite.

(b) The SADP from the area in (a) identifies γ and ε-martensite phases, with $[1\bar{2}10]_\varepsilon // [1\bar{1}0]_\gamma$
$(0001)_\varepsilon // (111)_\gamma$.

(c) The TEM micrograph shows austenite to contain stacking-faults and variants of ε-martensite.

(d) The SADP shows 2 variants of hcp precipitate forming on the $(\bar{1}1\bar{1})$ and $(11\bar{1})$ fcc phases. The orientation relationship in each case is a variant of $(0001)_\varepsilon // (11\bar{1})_\gamma$
$[\bar{2}110]_\varepsilon // (011)_\gamma$
The hcp ε-martensite is in the form of thin overlapping plates producing streaking of this diffraction pattern.



a

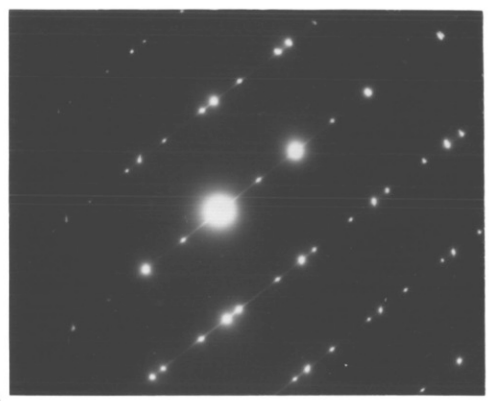

b

ά

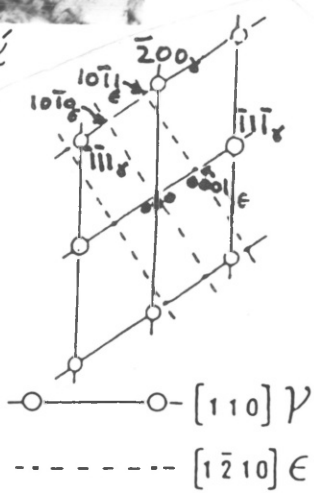

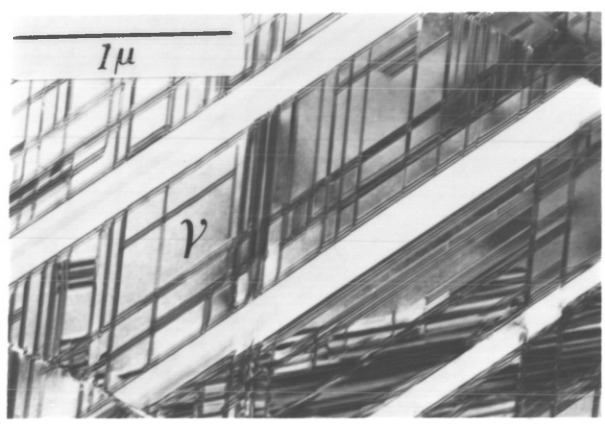

c

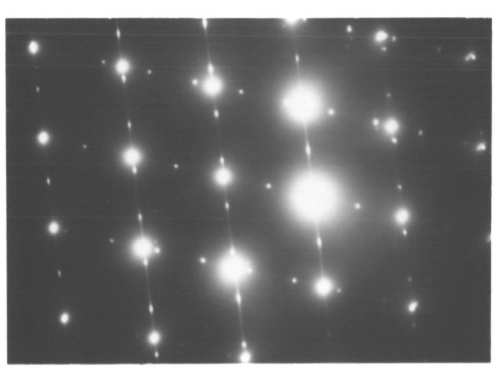

d

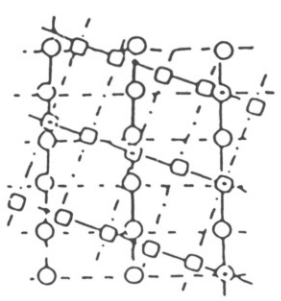

[110] γ
[1$\bar{2}$10] ε
[1$\bar{2}$10] ε

Figure 129. Alloy: 18Cr-6Ni-8Pdwt%
Condition: The micrographs are of the alloy annealed at 1250°C and rapidly cooled to room temperature.

(a) The light micrograph shows large grains of γ-austenite containing substantial numbers of needles.

(b) The SEM micrograph identifies the needles on the surface of austenite grains to have significant surface relief and to contain a midrib.

(c) The TEM micrograph shows austenite to contain α'-martensite in the form of laths.

(d) The SADP of the area in (c) originates from the α'-martensite laths identifying a: $[\bar{1}11]_{\alpha'}$ variant. ($2\lambda L = 5.29$ Å cm).



a

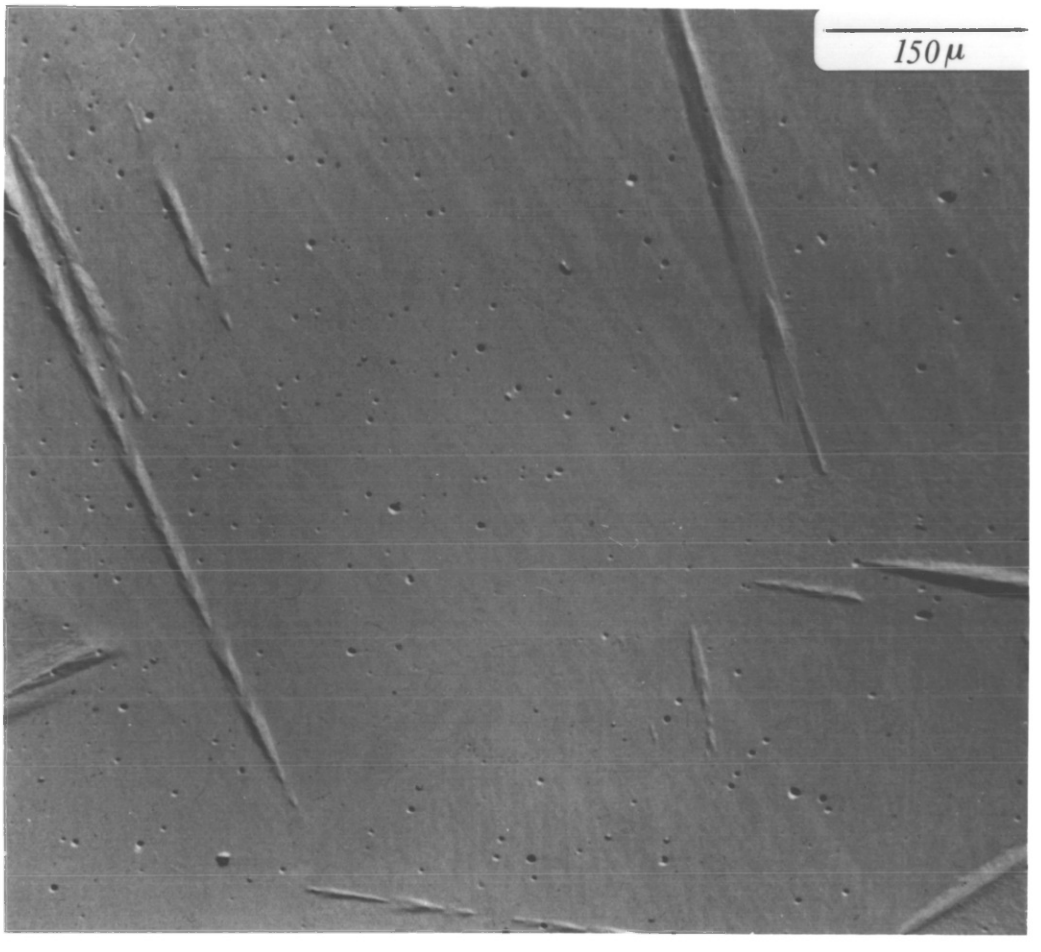

b

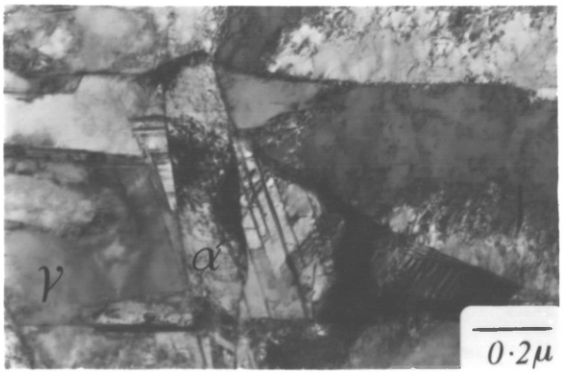

c

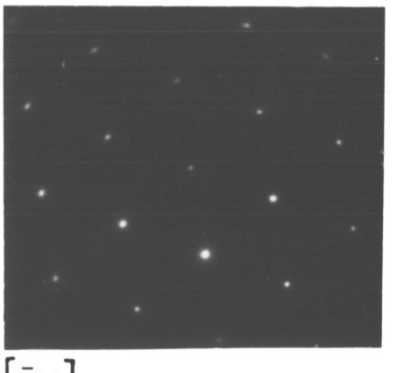

d

$[\bar{1}11]_{\alpha'}$

Figure 130. Alloy: 18Cr-6Ni-8Ruwt%
Condition: TEM micrograph of alloy annealed at 1250°C and rapidly cooled in liquid nitrogen. ($2\lambda L = 5.29$ Å cm)

(a) The TEM shows bands of γ-austenite transformed to α'-martensite.

(b) The SADP identifies the bands of α'-martensite within austenite having a $[111]_{\alpha'}$ variant.

(c) The SADP identifies bands of untransformed γ having a $[\bar{1}23]_{\gamma}$ variant.

(d) The TEM micrograph shows bands of α'-martensite in the above alloy deformed by 75% at room temperature.

(e) The SADP identifies the grains of α'-martensite in (d).

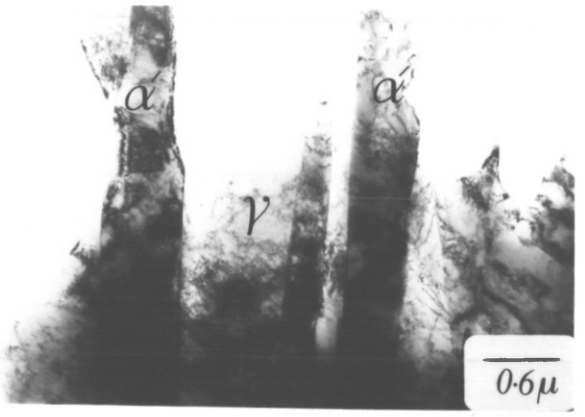

a

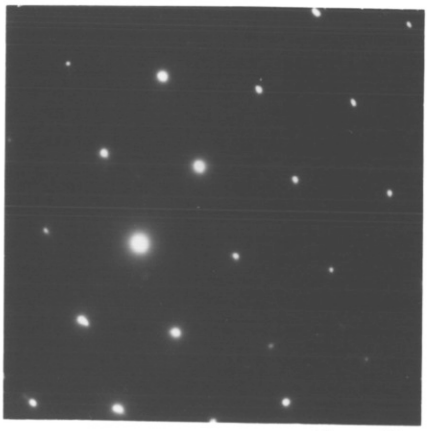

b

$[\bar{1}11]_{\alpha'}$

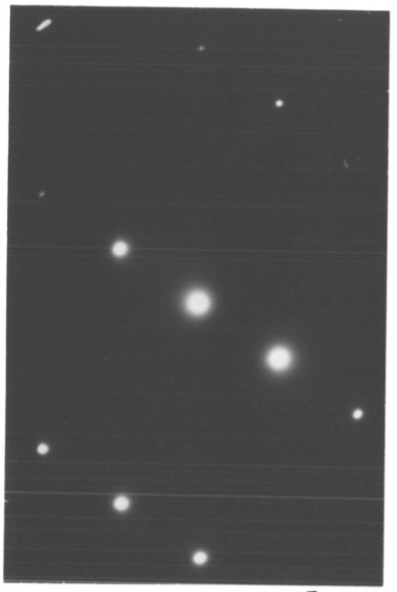

c

$[\bar{1}23]_{\gamma}$



d

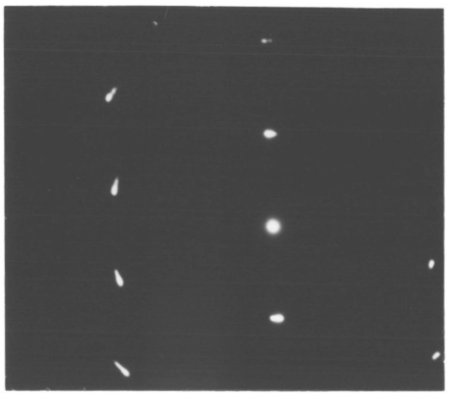

e

$[\bar{1}13]_{\alpha'}$

Figure 131. Alloy: 18Cr-6Ni-8Pdwt%
Condition: The TEM micrographs are of the alloy deformed by 64% at -196°C.

The TEM micrographs in a, c, d and e show alternate bands of deformation induced [$2\bar{1}\bar{1}3$] twin related ε-martensite, with twinning occurring on the {$10\bar{1}1$} reflection. Within each band are additional twins and faults, seen in d, and e HRDFs.
(Since the SADP is not precisely on zone, diffraction angles are not ideal).



a

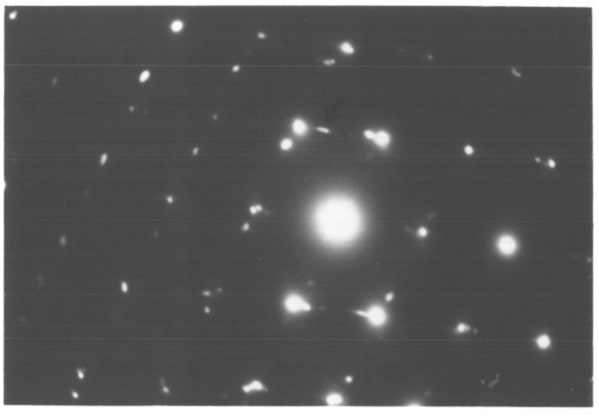

b $[2\bar{1}\bar{1}3]\varepsilon$ + twin on $\{10\bar{1}1\}$



c

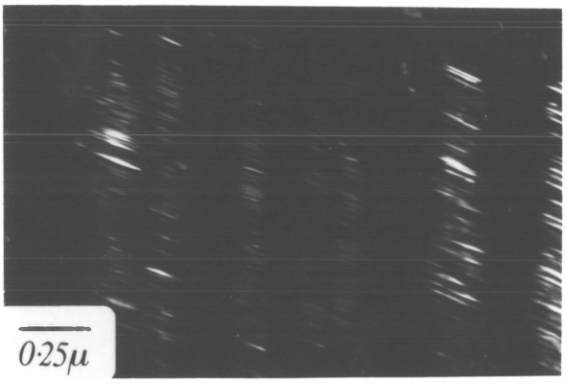

d

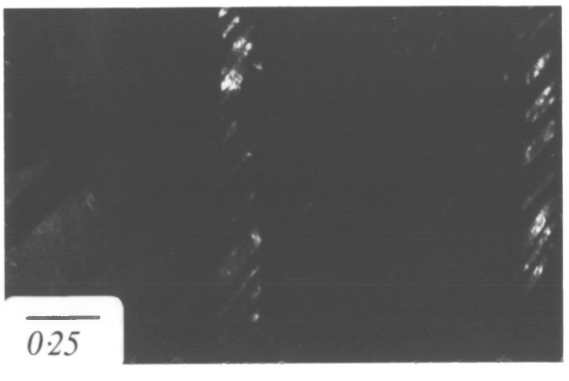

e

Figure 132. Dilatometry Curves showing change in Length, ΔL, as a Function of Temperature in Duplex Alloys. -----corresponds to the M_s Temperature for $\gamma \rightarrow \alpha'$.

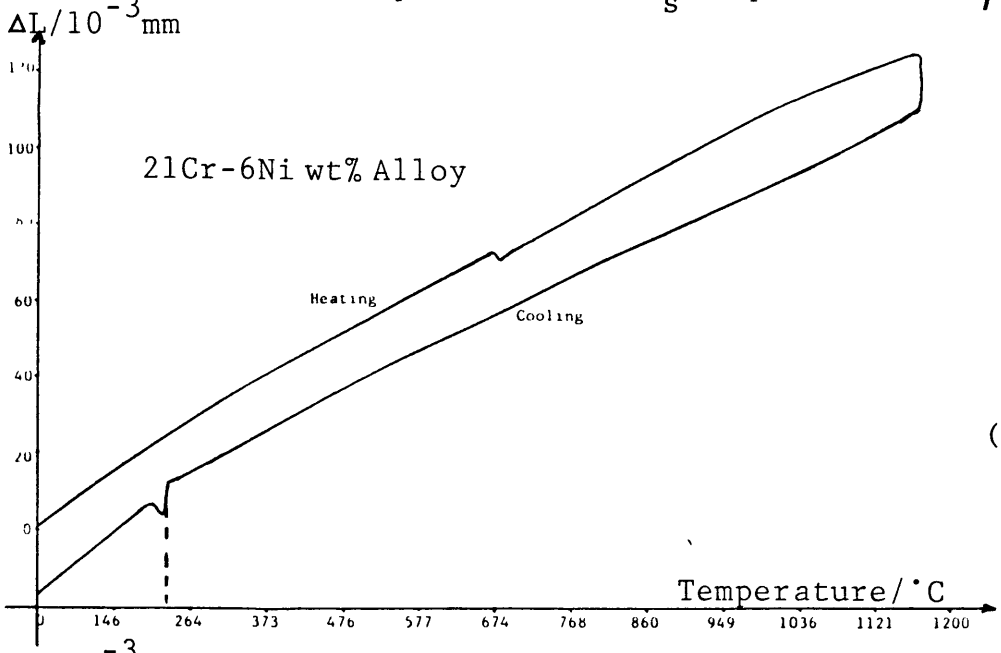

(a)

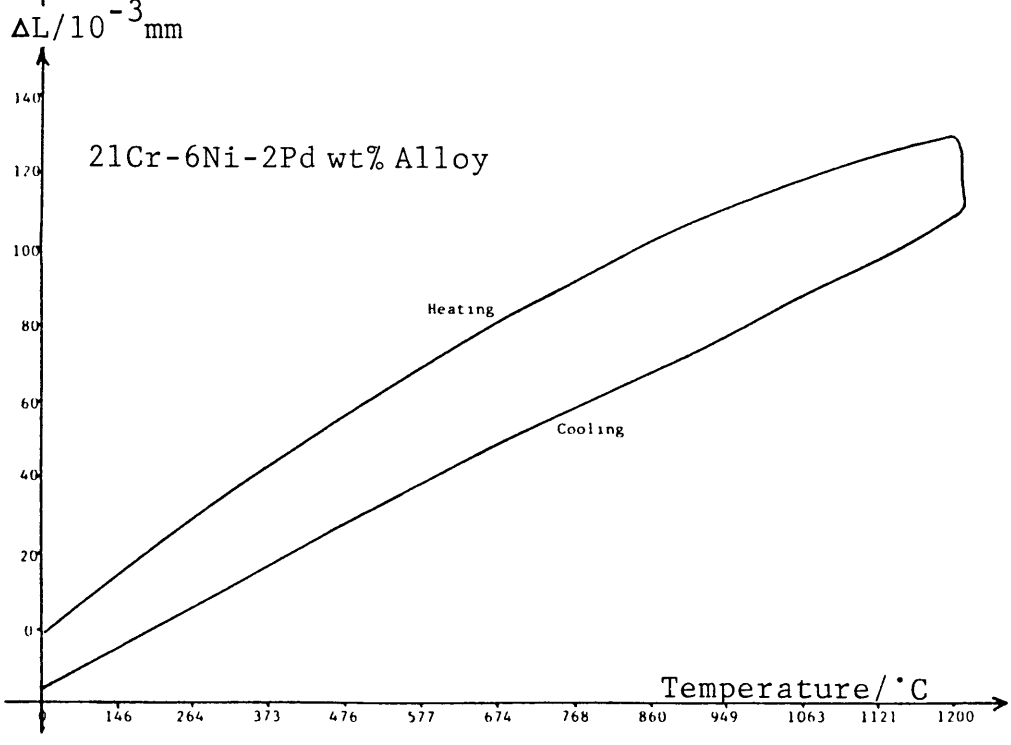

(b)

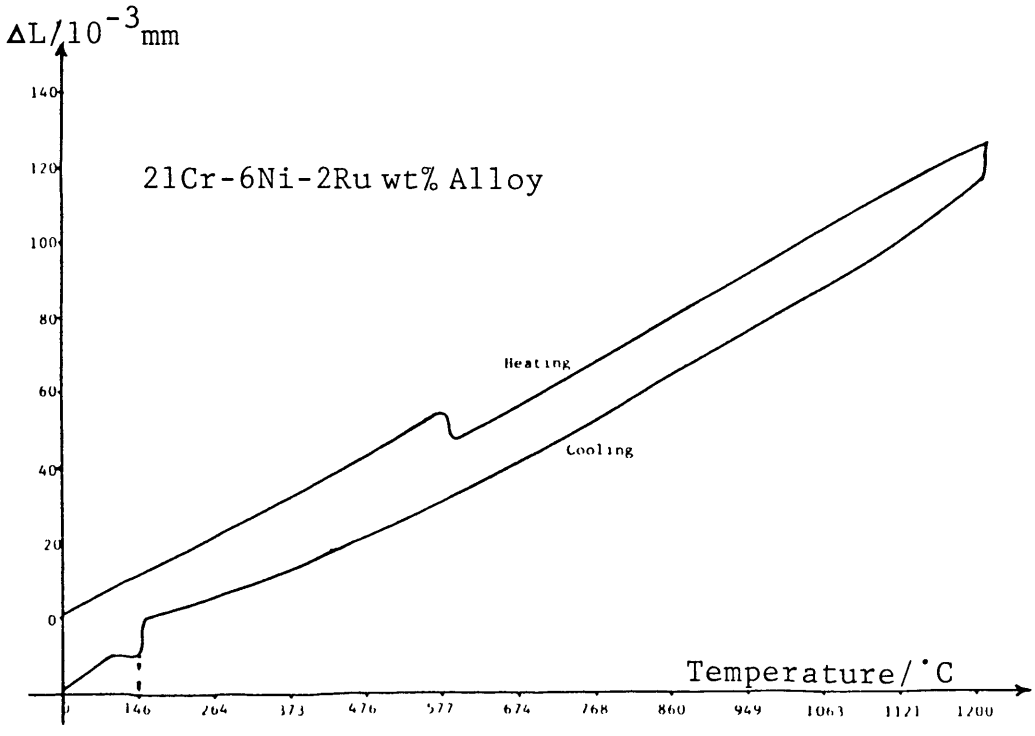

(c)

7.1.3. Effect of PGMs on Strain-Induced Martensite

(i) Room Temperature Deformation

18Cr-6Ni alloy series - Figure 133a.

The deformation of all alloys by rolling causes an increase in the fraction of γ-austenite transformed to α'-martensite as identified by magnetic balance measurements and point counting. This increase in martensite content obeyed a sigmoidal (241) relationship for Pt and Ru containing alloys reaching a saturation plateau, typically after a true strain of 0.6, the ternary alloy reaching its martensite saturation at a strain of ≈10%. The Pd containing alloys at the 2 and 8wt% level however, obeyed a linear relationship of increasing amounts of α'-martensite with strain (up to 150% deformation for the 18Cr-6Ni-2Pd alloy). The amounts of α' generated in the Pd containing alloy are substantially decreased compared to the ternary alloy indicating that Pd is a potent stabilizer of γ, restricting martensite formation even at high strains. The amounts of α'-martensite generated in the Ru containing alloys exceed that in the ternary alloy after ≈30% deformation eventually levelling off at ≈50% deformation. This suggests that whilst Ru marginally increases the volume fraction of γ at the annealing temperature of 1250°C it does not produce a concommitent increase in austenite stability.

21Cr-6Ni alloy series - Figure 133b.

The deformation of all alloys (except alloy 21Cr-6Ni-8Pd) causes a sigmoidal (241) increase in α'-martensite content reaching a saturation plateau after ≈50% deformation. The 21Cr-6Ni-8Pd alloy has a linear increase in α'-martensite content which shows no evidence of decline with strains in excess of 140% deformation, suggesting that still further amounts of α' may be generated with strain. The level of α'-martensite in all PGM containing alloys was significantly lower than in the ternary alloy, typically being ≈40% less at saturation. Increasing the level of Ru from 2 to 8wt% causes an increase in α' content of ≈34% to 44% at the saturation plateau.

(ii) -196°C Deformation

21Cr-6Ni alloy series - Figure 134a.

The deformation of all alloys (except alloy 21Cr-6Ni-8Pd) in this series results in a sigmoidal (241) increase in α'-martensite with

Figure 133.

$\%\gamma \rightarrow \alpha'$ as a Function of Strain-ϵ, induced by rolling at room temperature.

A

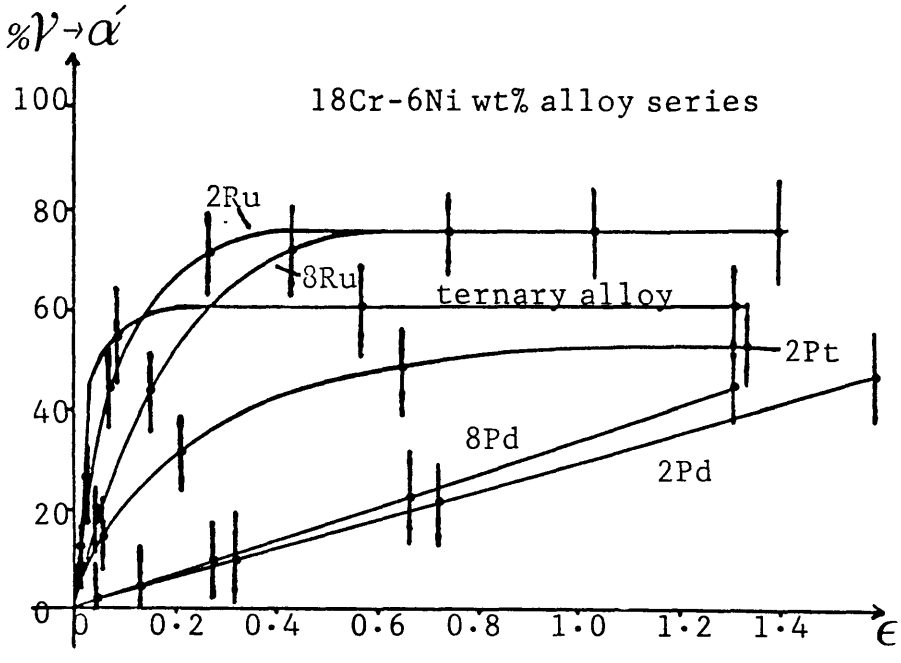

B

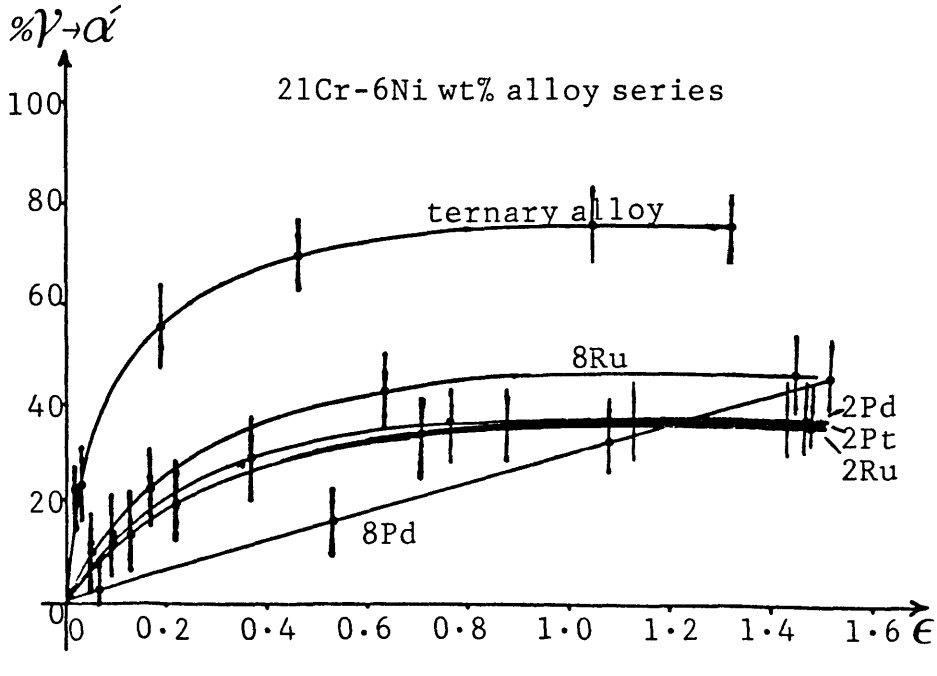

Figure 134.

$\%\gamma \rightarrow \alpha'$ as a Function of Strain-ϵ, induced by rolling at -196°C.

A

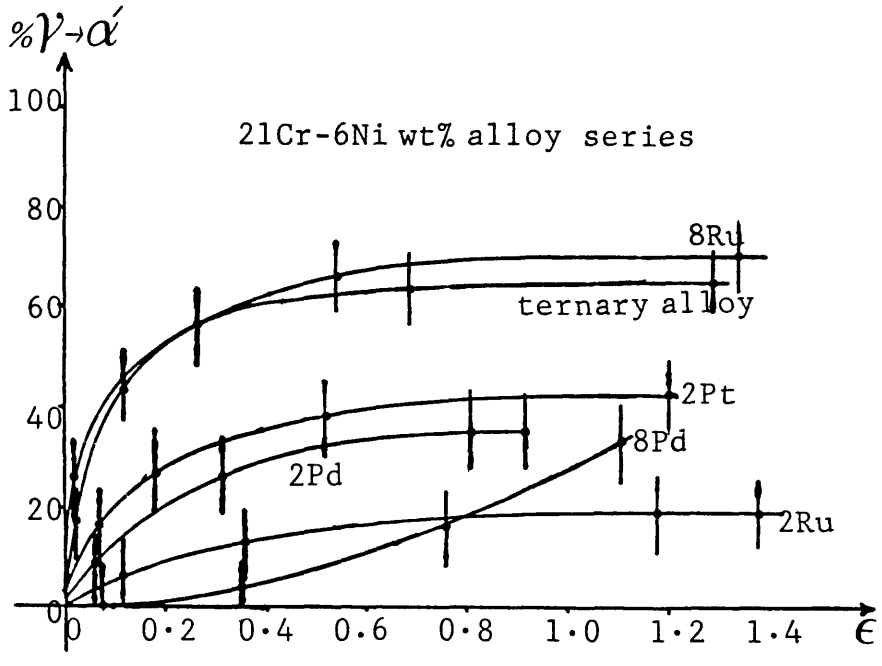

B

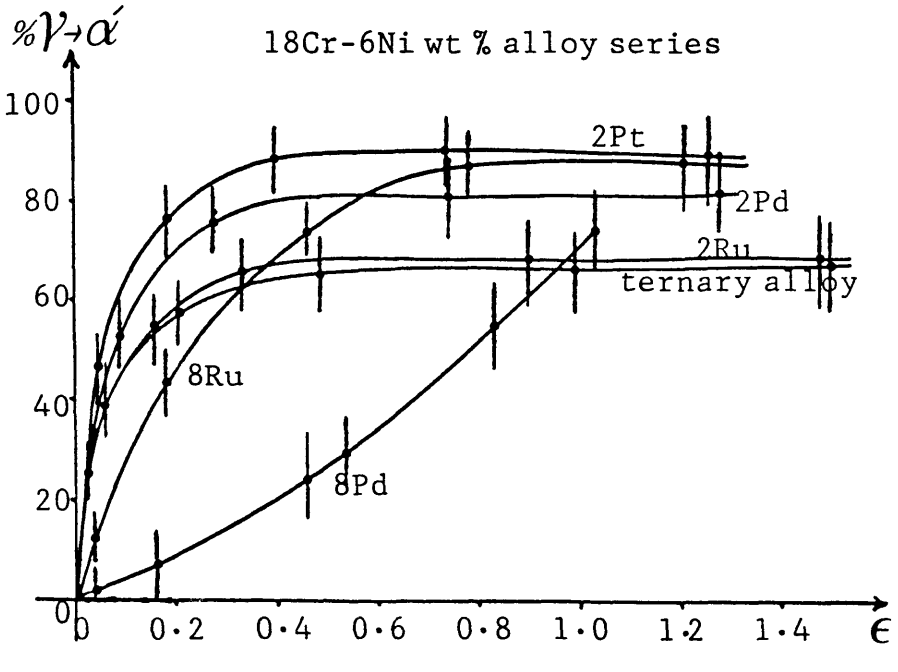

increasing strain ε, reaching a saturation plateau after ≈60% deformation. The 21Cr-6Ni-8Pd alloy has an increasing percentage of $\gamma \rightarrow \alpha'$ with increasing strain (which is non-linear) up to 110% deformation. No observation of a levelling off in α' content was evident, suggesting that the predominant mode of deformation in this alloy at these high strains, is α' formation whilst at strain <40% extensive slip and twinning are likely to be generated within austenite. At the 2wt% PGM level the amounts of α' generated with strain are significantly less than in the ternary alloy. Ru confers the greatest γ stability and Pt the least, whilst Pd is intermediate. As at room temperature, the behaviour of the 21Cr-6Ni-8Ru alloy is such that at true strains in excess of 40% deformation, the levels of α' exceeds that in the ternary alloy, associated with limited γ stability.

18Cr-6Ni alloy series - Figure 134b.

The generation of α'-martensite with increasing strain at this temperature reflects the instability of γ phase. For all alloys (except 18Cr-6Ni-8Pd) increasing strain produces a sigmoidal (241) increase in strain-induced martensite. However, at the 2wt% PGM level each PGM containing alloy has increased α' contents over the ternary alloy after ≈30% deformation, this being the strain at which a saturation plateau is achieved. The 18Cr-6Ni-8Ru alloy also exceeds the α' content in the ternary alloy after ≈40% deformation. It is expected that alloys containing 2 and 8wt% Ru should exceed α' contents in the ternary alloys as the behaviour was observed and explained for deformation at room temperature. The only reasonable explanation for the behaviour of alloys 18Cr-6Ni-2Pd and 18Cr-6Ni-2Pt is that in addition to increased γ contents and concommitent decrease in stability, there is the effect of the low deformation temperature. Angel (241) reports that for a given alloy there is an abrupt change in γ stability within a narrow temperature range. McReynolds (242) identified this temperature as M_d - the temperature of transition from slip to martensite formation as the primary mechanism of deformation. It has been suggested (49) that M_d is a better measure of austenite phase stability than M_s. However, M_d as defined above is difficult to determine experimentally, and therefore is outside the scope of this study.

Figure 135. Alloy: 21Cr-6Ni-2Pdwt%
Condition: Light micrographs of
1250°C annealed alloy air cooled.

(a) The light micrograph shows the above alloy deformed by 34% at room temperature. The ferrite phase (dark) is discontinuous within the γ phase, and is elongated parallel to the rolling direction.

(b) The light micrograph shows the α/γ grain boundaries to be highly serrated and irregular. The ferrite phase has deformed inhomogeneously.

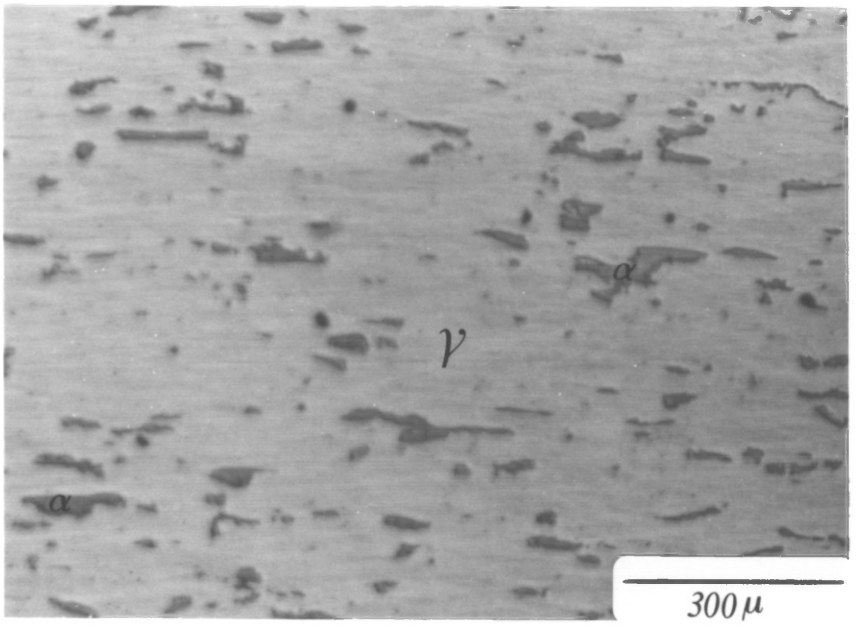

a

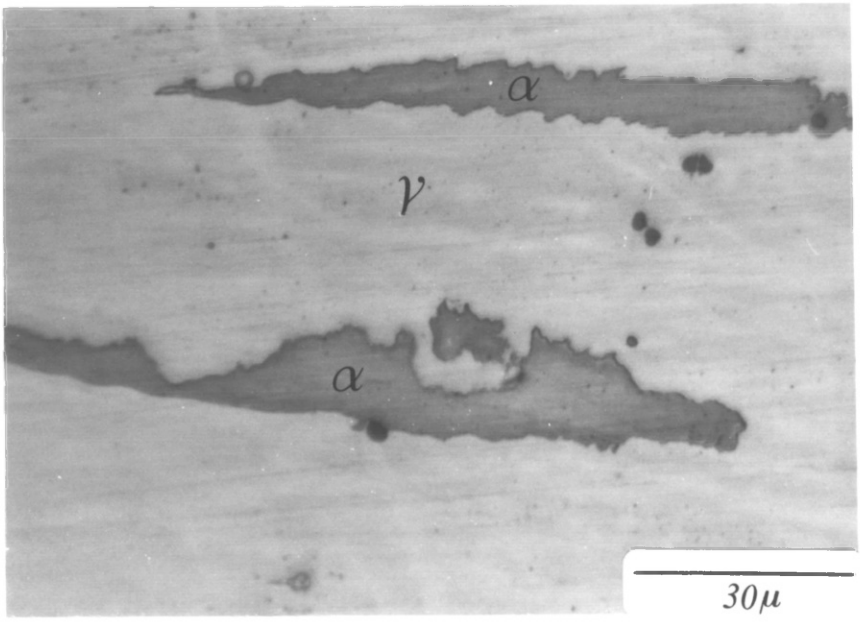

b

Figure 136.

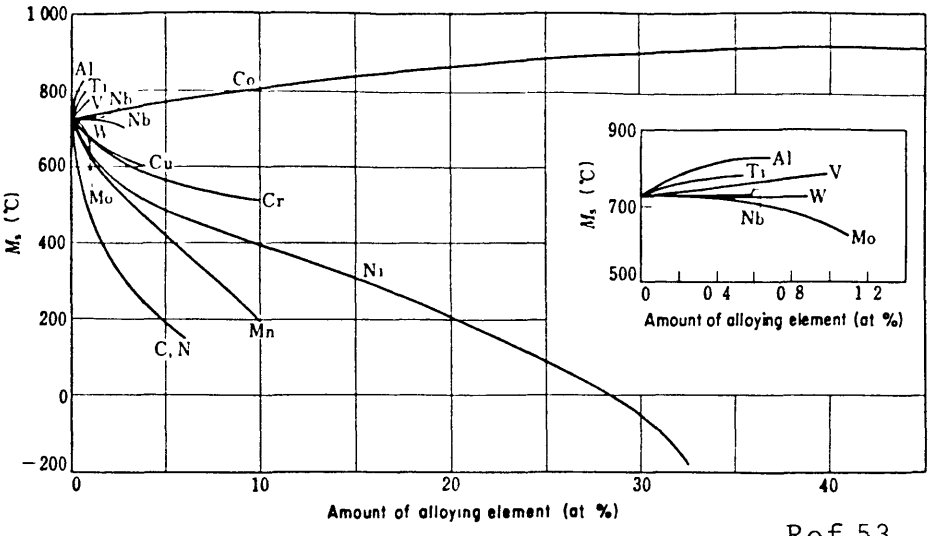

(a)

M_s temperatures of Fe-base binary alloys

Ref. 53

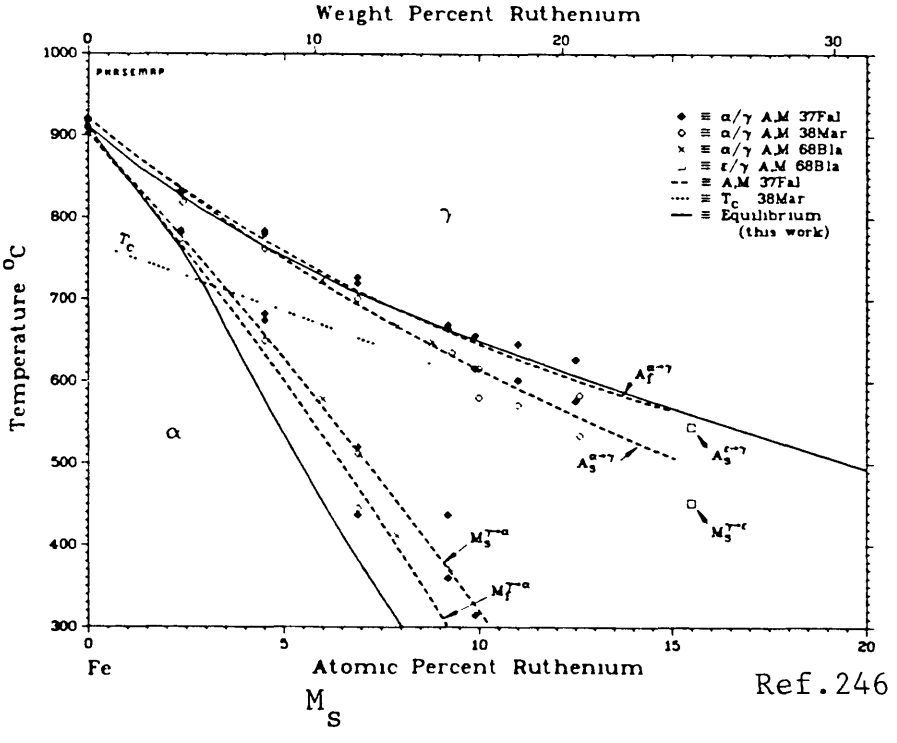

(b)

M_S

Ref. 246

Fe-34 wt% Pd =187°C Ref. 247

Fe-53 wt% Pt =-3°C "

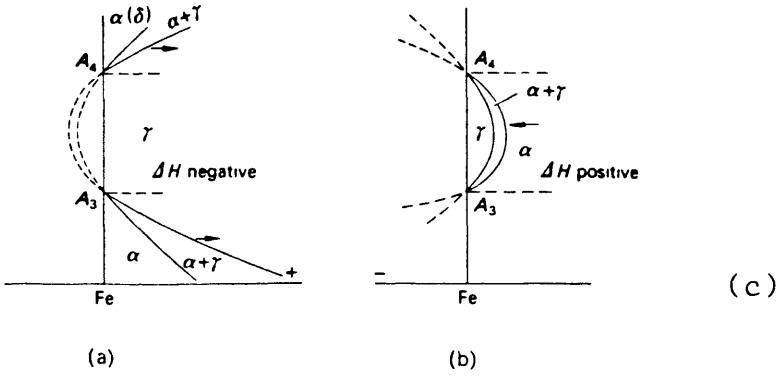

(c)

Two basic phase diagrams a ΔH negative $H_a > H_\gamma$ γ favoured b ΔH positive $H_a < H_\gamma$ α favoured

7.2. Discussion

7.2.1. Effect of PGMs on Bulk Martensite: M_s, T_o, SFE, and $\Delta H^{\alpha' \rightarrow \gamma}$

Results in Figure 122 indicate that the amounts of α' formed in these PGM containing duplex alloys is strongly dependent upon the austenite composition. Since the amount of α' formed in a PGM containing alloy is always less than the ternary it may reasonably be inferred that Pt, Pd, Ru confer increased stability upon the γ phase with respect to α'-martensite formation. For the 21Cr-6Ni alloy series (see Figure 122) at the 2 and 8% alloying level the inhibition of α' formation is comensurate with: Pd > Ru > Pt. For the 18Cr-6Ni series, at the 2% alloying level: Pt > Pd > Ru whilst at the 8% level Pd > Pt > Ru. The γ-austenite phase in these duplex steels, like most austenite, is metastable at low temperatures (53). The temperature at which this $\gamma \rightarrow \alpha'$ transformation occurs, the M_s temperature depends on the exact alloy composition, but is often below room temperature (24). Dilatometry measurements in the present study in Figure 132, show the 21Cr-6Ni and Ru alloys to have M_s values of 229 and 146°C respectively. The Pd alloy had an M_s value not far above room temperature not determined by dilatometry. These observations are consistent with magnetic balance measurements for this alloy series, in Figure 122, showing Pd and Ru to be highly potent γ stabilizers. Using tie-line data from the austenite phase at 1250°C, values for M_s for alloys containing PGMs have been determined from:

Steven and Haynes (243) - $M_s(^oC) = 561 - 474C - 33Mn - 17Cr - 17Ni - 21Mo + (10Co + 7.5Si)$

Andrews (244) - $M_s(^oC) = 539 - 423C - 30.4Mn - 12.1Cr - 17.7Ni - 7.5Mo + (10Co - 7.5Si)$

Recently an examination and review of the validity of existing empirical formulae for the calculation of the M_s temperature in steels was made by Kung and Rayment (245). They established that the above formulae give very good approximations for steels with < 7wt% alloying elements. Kung and Rayment (245) show that the standard deviation ($|\Delta \bar{M}_s|$) for Andrews (244) and Steven and Haynes (243) equations are only 13.4 deg. and 17 deg. respectively. Using tie-line data from the present work, M_s values for the alloys shown below are compared with dilatometry measurements.

Figure 137.

Alloy/wt%	M_s/°C		
	Stevens and Haynes	Andrews	Measured
21Cr-6Ni	147	207	229
21Cr-6Ni-2Ru	102	170	146
21Cr-6Ni-2Pd	94	164	-

There exists considerable variation between the M_s value calculated according to Stevens (243) and that of Andrew (244) from γ tie-line measurements in the present work. The M_s values measured by dilatometry in the present work also differ markedly from both of these empirically derived values, the ternary alloy is significantly higher, and the Pd and Ru alloys have much lower values than predicted by

Andrew (244) at, or just above, room temperature. The actual effect of Pd and Ru have not been included in the Stevens/Haynes (243) and Andrews (244) equations. This would probably account for the differing M_s values from these empirical equations. However, the dilatometry measurements conclusively establish that both Pd and Ru alloying additions depress the M_s temperature in Fe-Ni-Cr alloys. This is fully consistent with the variation in M_s with increasing amounts of Pt, Pd and Ru in Fe. Figure 136b shows this variation for the Fe-Ru (246) system with values of M_s also indicated for Pt (247) and Pd (247). In the present study it has already been shown in a previous chapter that the presence of PGMs causes an increase in the level of nickel partitioning to the austenite phase. The depression in M_s can therefore be related to compositonal variations:

1) the synergistic behaviour of Pd and Ru with Ni such that γ is stabilized with the enrichment of Ni. (The austenite composition in the 21Cr-6Ni-2Ru alloy is 19.2Cr-7.1Ni-2.5Ruwt%, in the 21Cr-6Ni-2Pd alloy it is 19.5Cr-7.3Ni-2.7Pd wt%.), and,

2) the inherent stabilizing effect of Pt, Pd and Ru themselves on γ-austenite as indicated by the Fe-PGM systems in Figure 136(b).

The amounts of α'-martensite forming in the 21/6, 21/6/2Pd, and 21/6/2Ru in alloys in Figure 122 indicate that Pd lowers the M_s temperature further than Ru. This is consistent with the proposals of (1) and (2) above. As has already been reported by Honeycombe (24) and Cottrell (15), Pt, Pd and Ru belong to the steel alloying elements

that 'open up' the γ-field. (This is not strictly true, since Ru only 'expands' the γ-field). Elements which expand and open the γ-loop will reduce $\Delta H^{\alpha' \rightarrow \gamma}$ at a constant temperature and lower T_o while elements which favour α-formation will increase $\Delta H^{\alpha' \rightarrow \gamma}$ at a constant temperature, and raise T_o (24). Whilst ΔH values for Pd and Ru alloys are not widely reported, Matveeva et al (248) reports a value of 0.53 kJ mol^{-1} for Pt, this compares with ΔH for Ni of -8.4 kJ mol^{-1} suggesting that Ni confers greater stability upon γ than Pt. This might be inferred from magnetic balance measurements from the 21Cr-6Ni alloy series (Figure 122) in particular, which show all Pt containing alloys (at a given alloying level) to contain the highest fractions of α' compared to Pd and Ru alloys. The magnetic balance measurements also suggest that $\Delta H^{\alpha' \rightarrow \gamma}$ for Pd and Ru would be negative, consistent with their being γ stabilizers having values comparable to Ni.

The distinct role of Pt, Pd and Ru on the γ-austenite SFE may not be commented upon due to the absence of experimental data. However, the occurrence of deformation twins in the following section is considered to be a direct consequence of the austenite exhibiting a low SFE rather than as a pre-requisite to the formation of α'-martensite.

7.2.2. Martensite: Structure, Morphology and Orientation

The destabilisation of austenite may yield two phases by martensitic transformation:

- the bcc, ferromagnetic, α'-martensite phase which forms with a volume dilation of $\simeq$2.5% (249).
- the hcp, paramagnetic, ε-martensite phase involving a volume contraction of $\simeq$0.8% (249). Both phases have been identified in this study by TEM, the α' was further identified by magnetic balance and dilatometry measurements. The ε-martensite is seen to have an hcp structure in Figure 128 forming as plates having $\{111\}_\gamma$ habit planes and obeying a rational orientation relationship with the γ matrix where the close packed planes and direction of each phase are parallel as shown below:

$$(111)_\gamma // (0001)_\varepsilon$$
$$[1\bar{1}0]_\gamma // [1\bar{2}10]_\varepsilon$$

The occurrence of ε-martensite in the present study has predominately been prior to α'-martensite, the α' forming often within bundles of ε-martensite, seen in Figures 126(d) and 128(a). M. Harmelin et al (249) have proposed that in Fe-Ni-Cr alloys containing <72% Fe, extensive

transformation takes place below M_s according to the sequence $\gamma \rightarrow \varepsilon \rightarrow \alpha'$ such that α' forms only in bands ascribed to ε, and not in the residual austenite. The significance of Pt, Pd and Ru additions on this sequence is that they favour ε-martensite formation before α' forms, particularly in the 18Cr-6Ni series; when PGMs are present in Figures 126 and 128, implying that the austenite stacking fault energy is decreased in the range of 5-60 mJm^{-2} - typical in Fe-Ni-Cr alloys (24).

The occurrence and distribution of α' in annealed alloys has been identified by TEM in Figures 123-129. Two orientation relationships between the γ and α' phases have been reported by various authors (53, 149). These are the Kurdjumov-Sachs (K-S) and Nishiyama-Wasserman (N-W) relationships, two variants of which are:-

K-S	N-W
$(111)_\gamma // (011)_{\alpha'}$	$(111)_\gamma // (011)_{\alpha'}$
$[\bar{1}01]_\gamma // [\bar{1}\bar{1}1]_{\alpha'}$	$[1\bar{1}0]_\gamma // [100]_{\alpha'}$
$[\bar{1}2\bar{1}]_\gamma // [\bar{2}1\bar{1}]_{\alpha'}$	$[11\bar{2}]_\gamma // [0\bar{1}\bar{1}]_{\alpha'}$

The K-S relationship has been established in the present work. Figures 124 and 126 show α'-martensite laths and plates having the following variants: $[\bar{1}11]_{\alpha'} // [001]_{\alpha'}$ and $[111]_\gamma // [110]_{\alpha'}$ in alloys 21Cr-6Ni and 21Cr-6Ni-8Ru respectively.

The α' in the 18Cr-6Ni-8Pd is seen as laths in Figure 129c. In addition Figures 129a and b shows the surface relief of what can only be inferred as lens-shaped martensite needles. Breedis (182) has suggested that steels which form such surface martensite would also form martensite within the bulk, of a different morphology to the lath type, which is termed 'massive' martensite. However, no indication could be found for this type of martensite within the bulk of the alloy - 18Cr-6Ni-8Pdwt%.

The C-content of the alloys used in this work, is low, being 0.02 wt% (from Fe spec.). The bcc structure for α'-martensite observed in the present work is consistent with the low C-content (53,54). The lath morphology is shown to be expected. However, the α'-martensite in the 21Cr-6Ni-8Ru duplex alloy in Figures 125 and 126, is in the form of bcc lenticular plates < 0.5μm in width, not the conventional lath type.

7.2.3. Strain-Induced Martensite

(i) Introduction

It has been shown that martensitic transformation in stainless steels are strongly promoted by an applied plastic deformation in a range of temperatures above M_s - the temperature for spontaneous transformation (242, 250-252). The nucleation process can be significantly modified when the transformation occurs as a result of plastic deformation of the parent phase (252). Such processes are often complex involving twinning in the austenite and both fcc → hcp and fcc → bcc martensitic transformations occurring during deformation (189). Further on the generation of strain-induced martensite, it is well established that shear band intersections can be very effective strain induced nucleation sites (189, 253, 254). The operative shear bands can be in the form of ε(hcp)-martensite, mechanical twins, or dense stacking fault bundles, all being promoted by a low SFE (255). The mechanisms by which these shear band intersections can produce bcc martensitic 'embryoes' is well reported (189,256).

(ii) Effect of PGMs, Pt, Pd and Ru

The most important question to address in this study, is whether the alloying additions of Pt, Pd and Ru PGMs to duplex steels confer not only an increase in γ phase fraction, but a concommitent increase in γ stability? The significance of this may be illustrated by considering the behaviour of some Pt and Ru containing alloys in Figures 133 and 134. Additions of Pt to the 18Cr-6Ni and 21Cr-6Ni alloy series at the 2 wt% level result in a decrease in the fractions of α'-martensite generated with strain at room temperature in Figure 133. The effect is greatest in the 21Cr-6Ni alloy and indicates that Pt confers increased stability on γ-austenite such that both the amount and rate at which martensite forms with strains are decreased. Pt confers increased stability by altering the γ phase composition, such that in the 21Cr-6Ni alloy, γ has a composition of 19.3Cr-7.0Ni-2.7Pt wt% and in the 18Cr-6Ni alloy, 17Cr-5.9Ni-2.7Pt wt%. These observations are highly significant for a number of reasons. Firstly, it suggests that not only is the maximum percentage of $\gamma \rightarrow \alpha'$, decreased (by 10% in the 18Cr-6Ni alloy and 14% in the 21Cr-6Ni alloy series), but that the induced strain must cause a change in the microstructural deformation processes, i.e. the local strain in γ is not accommodated just by α' formation, but probably

increased slip, twinning and ε-martensite formation. Secondly, it indicates that accompanying increased γ phase content there is a concommitent increase in γ phase stability for additions of 2 wt% Pt. In contrast to the ternary alloys containing 2 wt% Pt, is the behaviour of alloys containing Ru. The effect of most elements on the stability of austenite is to inhibit the formation of martensite, see Figure 136a (53). For example Cr, an α-ferrite forming element, acts as a strong γ- stabilizer in the same way as nickel. However, in the present work, Ru alloying additions in particular, do not consistently follow this behaviour. Additions of 2 and 8 wt% Ru to the 18Cr-6Ni ternary alloy deformed at -196°C and room temperature, and the addition of 8 wt% Ru to the 21Cr-6Ni ternary alloy deformed at -196°C results in an increase in the percentage of $\gamma \rightarrow \alpha'$ with increasing strain compared to the ternary alloys (see Figures 133 and 134b). The rates of reaction are however not increased in these Ru alloys. It is the γ composition in these alloys which dictates its stability, this is altered by Ru such that in the 18Cr-6Ni alloy, γ has compositions of 18.3Cr-6.3Ni-2.31Ru and 18.5Cr-6.0Ni-8.5Ru wt% and in the 21Cr-6Ni ternary alloy, 19.2Cr-7.1Ni-2.50Ru wt%. Clearly Ru in these γ compositons does not confer substantial austenite stability.

Angel (241) reports that in the final stages of strain-induced transformations, 3 fundamental processes of deformation are operative: martensite formation, slip in the austenite and slip in the martensite, and that there is a transition of deformation by slip and twinning to that of α'-martensite with decreasing deformation temperature. Microstructural evidence from the present work (Figure 131) suggests however that this transition is delayed with alloying additions of Pd in particular such that deformation by twinning predominates to lower temperatures and higher strains, rather than α' formation. Figure 131 shows this for an alloy 18Cr-6Ni-8Pd deformed at -196°C by 64%. The TEM bright field shows bands of twin related ε-martensite as identified by the SADP running from top to bottom. Within each twin band are additional internal twins and faults shown in the HRDF micrographs.

In Figure 134b, PGM containing alloys, 18Cr-6Ni-2Pt, 18Cr-6Ni-2Pd, 18Cr-6Ni-2Ru and 18Cr-6Ni-8Ru have higher α' contents than the ternary alloy with increasing strain. Hence, as previously mentioned, whilst the fraction of austenite is increased by 2 wt% Pt, Pd, Ru and 8wt% Ru, the inherent stability of the γ phase, controlled by its composition, is

Figure 138. Assessment of the variation of $\gamma \rightarrow \alpha'$ and rate of Transformation in Duplex Alloys in Figs.133 & 134. PGM alloys are compared to ternary alloys.

21Cr-6Ni ALLOY SERIES

		$\%\gamma \rightarrow \alpha'$	Reaction Rate	Austenite Composition/wt%
Room Temperature Deformation	2Ru	↓	↓	19·2Cr-7·1Ni-2·5Ru
	2Pd	↓	↓	19·5Cr-7·3Ni-2·7Pd
	2Pt	↓	↓	19·3Cr-7·0Ni-2·7Pt
	8Ru	↓	↓	20·1Cr-6.6Ni-8·6Ru
	8Pd	↓	↓	20·5Cr-4·1Ni-8·2Pd
-196°C Deformation	2Ru	↓	↓	19·2Cr-7·1Ni-2·5Ru
	2Pd	↓	↓	19·5Cr-7·3Ni-2·7Pd
	2Pt	↓	↓	19·3Cr-7·0Ni-2·7Pt
	8Ru	↑	↓	20·1Cr-6·6Ni-8·6Ru
	8Pd	↓	↓	20·5Cr-4·1Ni-8·2Pd

18Cr-6Ni ALLOY SERIES

		$\%\gamma \rightarrow \alpha'$	Reaction Rate	Austenite Composition/wt%
Room Temperature Deformation	2Ru	↑	↓	18·3Cr-6·3Ni-2·3Ru
	2Pd	↓	↓	18·5Cr-6·0Ni-2·3Pd
	2Pt	↓	↓	17·0Cr-6·0Ni-2·7Pt
	8Ru	↑	↓	18·5Cr-6·0Ni-8·5Ru
	8Pd	↓	↓	18·7Cr-6·0Ni-8·0Pd
-196°C Deformation	2Ru	↑	↑	18·3Cr-6·3Ni-2·3Ru
	2Pd	↑	↓	18·5Cr-6·0Ni-2·3Pd
	2Pt	↑	↑	17·0Cr-6·0Ni-2·7Pt
	8Ru	↑	same as ternary	18·5Cr-6·0Ni-8·5Ru
	8Pd	↓	↓	18·7Cr-6·0Ni-8·0Pd

where ↓ represents a decrease in the fraction or rate of α' formed with increasing strain compared to the ternary alloy and ↑ is the converse.

not necessarily maintained or increased. This explains the effect of PGMs in both alloy series in Figures 133 and 134, and is related to austenite chemical composition as follows:
Hence it can be stated from Figure 138 that:
1) Of the 3 PGMs in the 21/6 alloy series, Ru confers the greatest γ stability at the 2 wt% level for deformation at room and -196°C temperatures whilst Pd is the most effective γ stabilizing PGM at the 8wt% level with increasing strain.
2) Of the 3 PGMs in the 18/6 alloy series, Pd confers the greatest γ stability at the 2 and 8 wt% level for deformation at room and -196°C temperatures. (Although the 18Cr-6Ni-2Pd alloy is intermediate to Pt and Ru alloys at strains > 0.6ε for deformation at -196°C and this stability is less than the ternary alloy). These statements may be related to γ composition in Figure 138.

Martensite Kinetics

The kinetics of martensite transformation has been shown to obey a sigmoidal relationship of nucleation and growth with strain and % martensite (241). A stimulating effect occurs at low strains while at higher strain levels, a decreasing rate of transformation occurs. The regime of the lower strain level will depend on alloy composition and temperature of deformation.

Angel (241) has proposed a model of the following form:

$$\ln \frac{f}{1-f} = n \ln \varepsilon + k$$

where f = fractional amount of martensite formed.
ε = true strain.
n and k are constants; n is independent of temperature and alloying composition, while k is dependent on these parameters. A more detailed equation is that proposed by Olson and Cohen (255) as follows:

$$f = 1 - \exp\{\beta - (1 - \exp[-\alpha\varepsilon])\}^{n}$$

where f = fractional amount of martensite formed
ε = strain
n = a fixed exponent
α and β are temperature-dependent parameters.
α defines the coarse band (twinning, hcp) formation, while β is proportional to the probability that an intersection of shear bands will form an embryo.

18Cr-6Ni wt% alloy series. Figure 139.

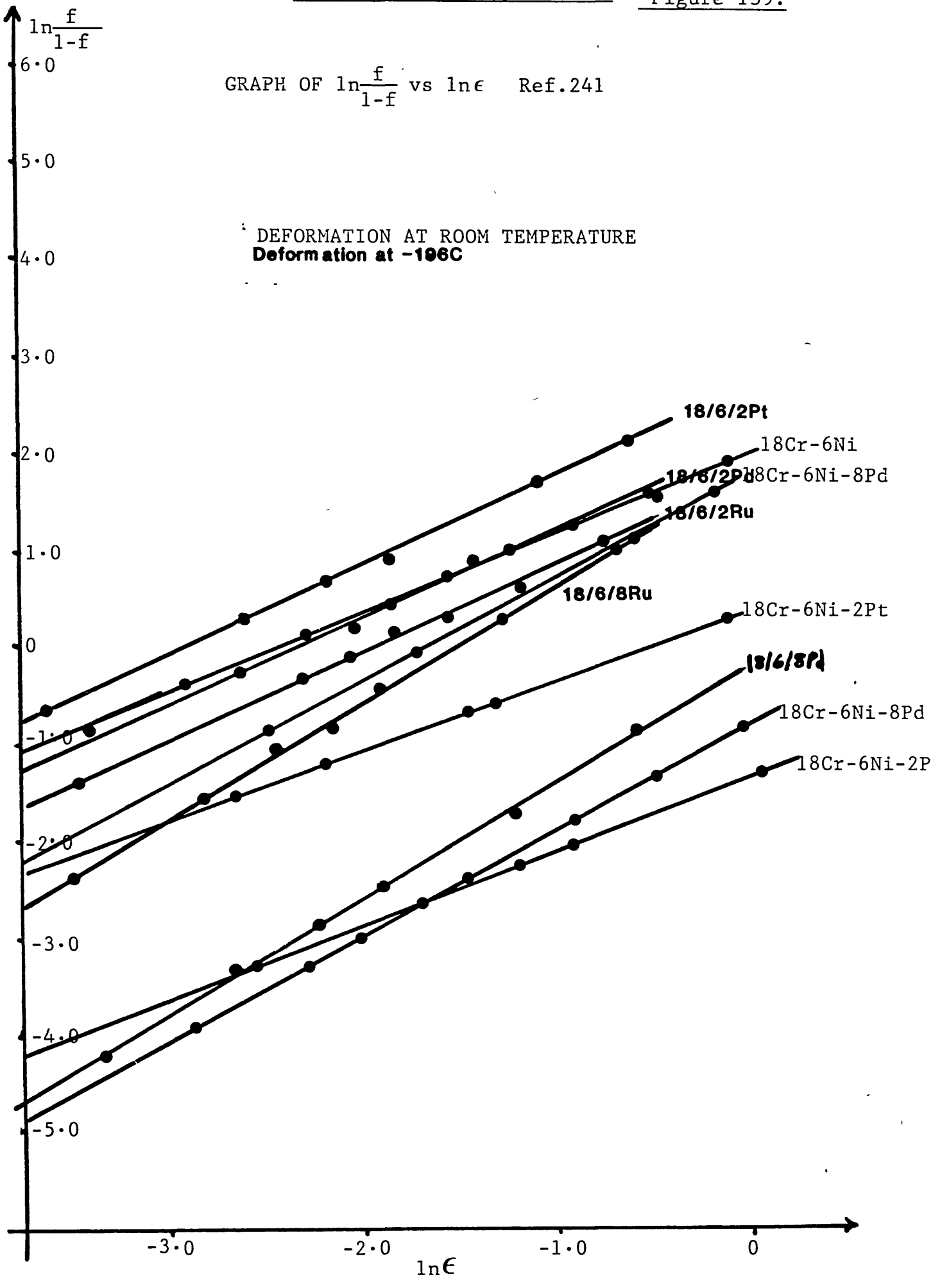

18Cr-6Ni wt% alloy series. Figure 139.

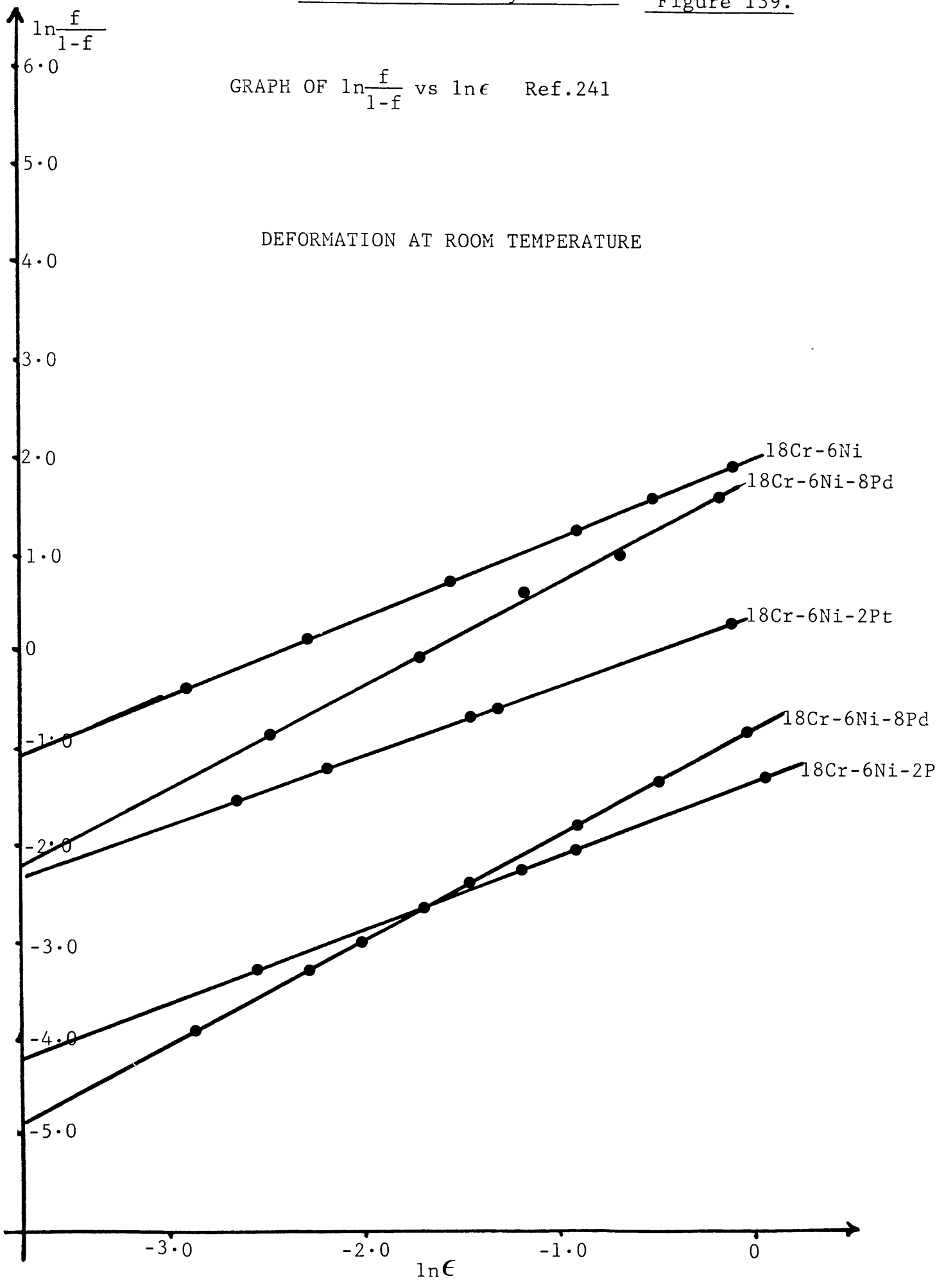

21Cr-6Niwt% alloy series. Figure 140.

GRAPH OF $\ln\frac{f}{1-f}$ vs $\ln\epsilon$ Ref.241

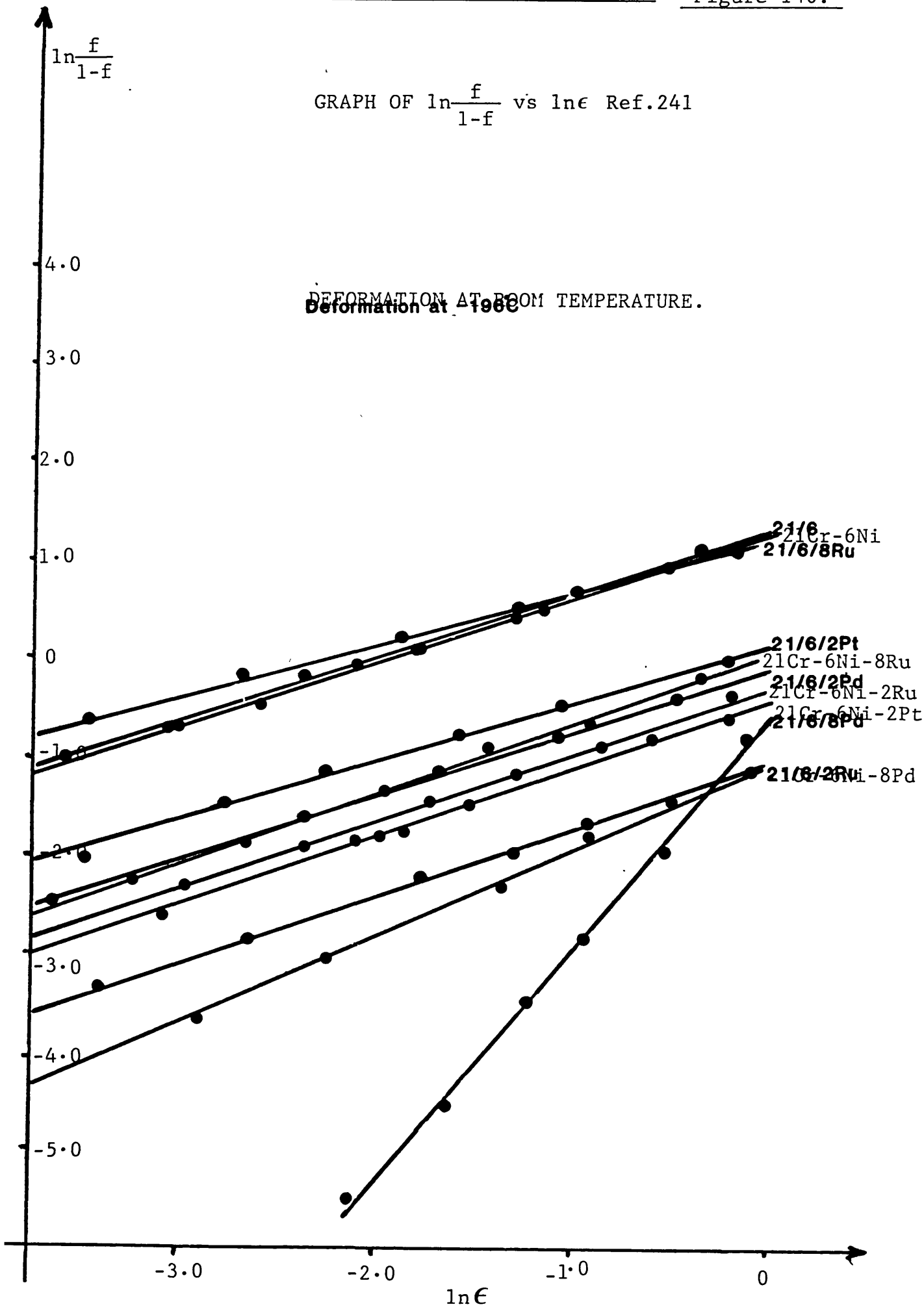

21Cr-6Niwt% alloy series. Figure 140.

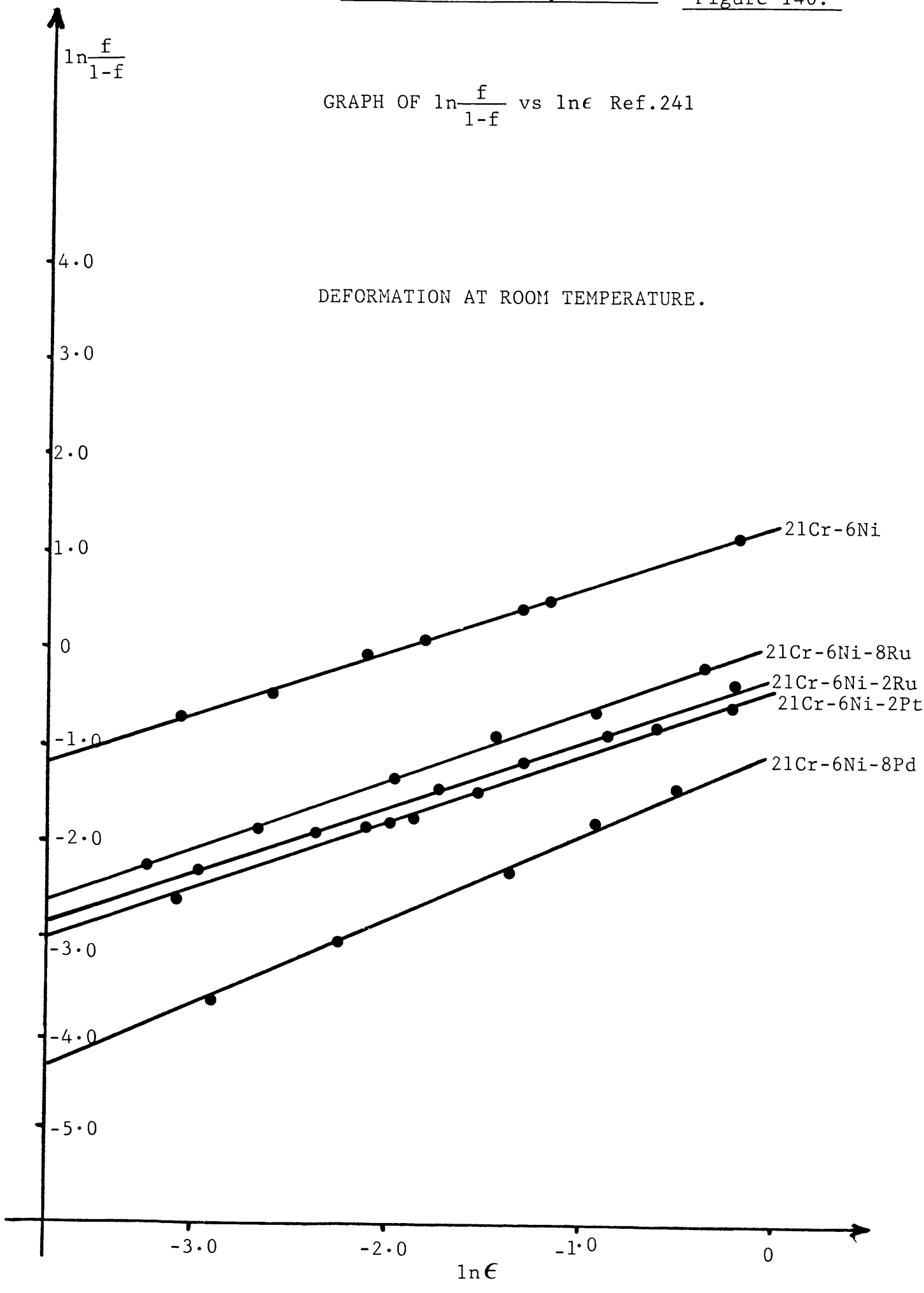

In this investigation it is considered satisfactory to apply the simpler Angel (241) equation to experimental data in Figures 133 and 134. This is shown in Figures 139 and 140. The graphs of $\ln \frac{f}{1-f}$ vs $\ln\varepsilon$ are seen to be straight lines; the n-values (slopes) for the 21Cr-6Ni alloy series deformed at room and -196°C temperature vary between 0.67 and 1.25 except the 21Cr-6Ni-8Pd alloy deformed at -196°C which has a slope of 2.4. n values for the 18Cr-6Ni alloy series vary between 0.72 and 1.25. Angel (241) reports a value of 3 for n. The difference may be related to the difference in the calculation of f as done in the present work and by Angel (241). Angel (241) assumed a limiting value of the transformation, M_T, and calculated f as $\frac{M}{M_T}$ where M is the degree of transformation at lower strains. In the present work, f is the % of martensite formed, this gives lower n values. These analyses indicate that the kinetics of deformation induced martensite in PGM modified duplex steels obey a sigmoidal relationship between the martensite formed and strain. However, analysis of the data in Figures 133 and 134 strictly requires knowledge of the development of true strain in the γ phase not the 'overall' strain of the duplex material (as determined in the present work). The austenite phase probably accommodates a greater proportion of the strain than does the α-ferrite phase.

7.2.5. Microstructural Features

The microstructural variations during rolling and refrigeration in PGM containing alloys have been identified by light and transmission electron microscopy in Figures 130, 131 and 135. Figure 130 shows structures developed in the 18Cr-6Ni-8Ru alloy subsequent to treatment in liquid nitrogen at -196°C and identified by TEM. Regions of austenite are separated by alternate bands of α'-martensite. 75% deformation at room temperature results in ectensive transformtion to bands of α'-martensite shown in the TEM micrograph of Figure 130d. Figure 131 shows structures generated in the 18Cr-6Ni-8Pd alloy deformed at -196°C by 64%. The TEM bright field shows bands of hcp faulted twins, as identified by the SADP, running from top to bottom and containing thin-overlapping plates of hcp ε-martensite as shown by the HRDFs.

In Figure 135, the 21Cr-6Ni-2Pd alloy is shown by the light micrographs. Deformed by 35% at room temperature, the ferrite phase is seen to be discontinuous and elongated parallel to the rolling direction

within the γ phase. The α/γ grain boundaries are highly irregular and serrated, the ferrite phase deforming inhomogeneously.

CHAPTER 8

Physical Properties

'These alloys are so far like the present ones
that some of the noisiest authorities
insist in their being received for good or
for evil in the superlative degree of comparison
only.'

H.D. Solomon and T.M. Devine Jr.

8.1. Results

In this investigation, the tensile, oxidation and corrosion properties of selected PGM modified duplex steels are presented and discussed. The alloys studied, were 21Cr-6Ni, 21Cr-6Ni-2Pd, 21Cr-6Ni-2Pd, and a commercial alloy Uranus 50.

8.1.1. Tensile Properties

In the first instance the tensile properties are presented as stress-strain curves. The subsequent effect of σ-sigma phase precipitation on these properties is also investigated. Hardness values, in addition, are presented for alloys in Figure 148, in the as-cast and annealed conditions.

Figure 141 typifies values of 0.2% proof stress, tensile strength, and % elongation developed in the above alloys in annealed and aged conditions. Each value was obtained from an average of 3 measurements.

Figure 141

Alloy	Condition	0.2% σ_{PS}/MN/m^2	UTS/MN/m^2	Elongation
Uranus 50	Annealed at 1250°C	458	713	21
Uranus 50	" + 700°C Age	490	617	19
21/6	"	333	743	26
21/6	" + 700°C Age	467	681	6
21/6/2Pd	"	382	709	23
21/6/2Pd	" + 700°C Age	426	786	12
21/6/2Ru	"	329	615	30
21/6/2Ru	" + 700°C Age	355	634	15

In the annealed condition, Figure 142, the Pd containing alloy developed a significant improvement in 0.2% proof stress compared with the ternary alloy, but showed a lower tensile strength and marginally lower ductility. The Ru containing alloy, however, is significantly less strong with a marginal decrease in tensile strength over the ternary alloy. The ductility in the Ru containing alloy is greater than the base alloy. The effect of ageing at 900°C on the 0.2% proof stress and % elongation is also considered. These results are shown in Figure 143. The effect on proof strength is not substantial with a gradual increase in 0.2% proof stress with time in Figure 143a, consistent with the precipitation of sigma phase. The effect on ductility in Figure 143b is however, more significant; the commercial duplex alloy Uranus 50 loses significant

Figure 142. Stress-Strain Characteristics of Duplex Alloys Annealed at 1250°C.

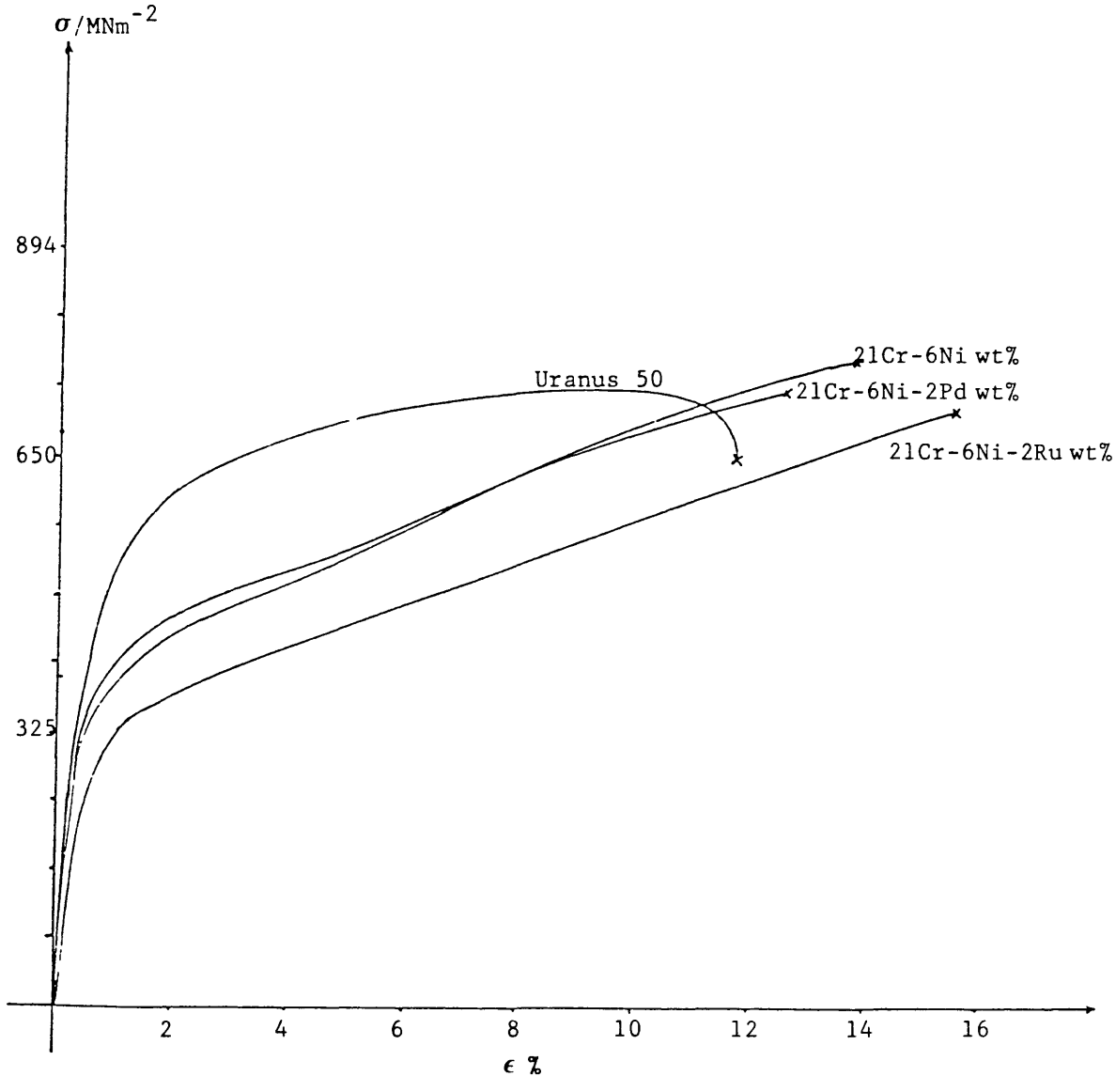

Figure 143. The Effect of Sigma Precipitation, Ageing at 900°C, On Ductility and Strength in Duplex Steels.

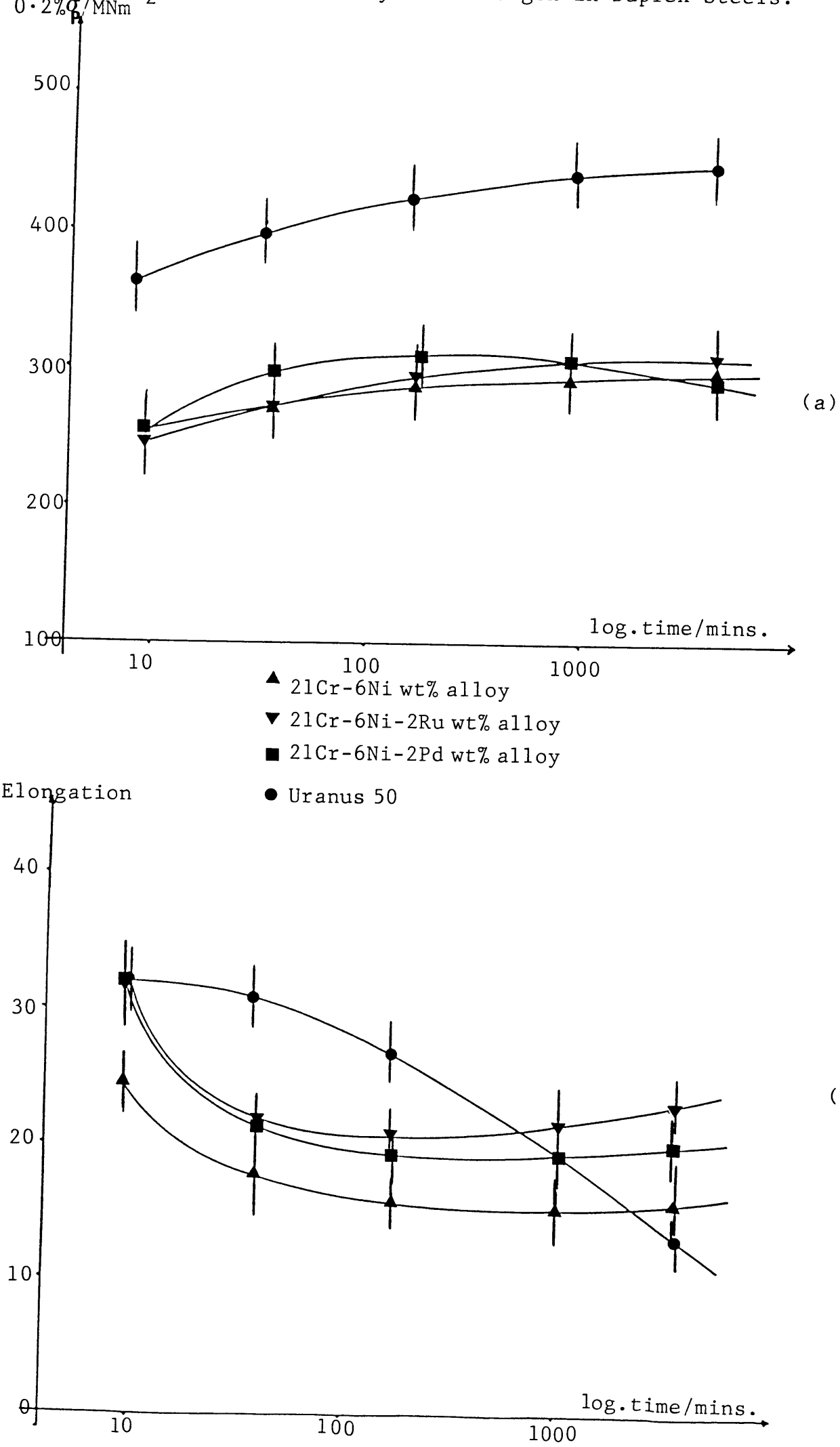

Figure 144 Stress-Strain Characteristics of Duplex Alloys Annealed at 1250°C and Aged at 700°C(10mins.).

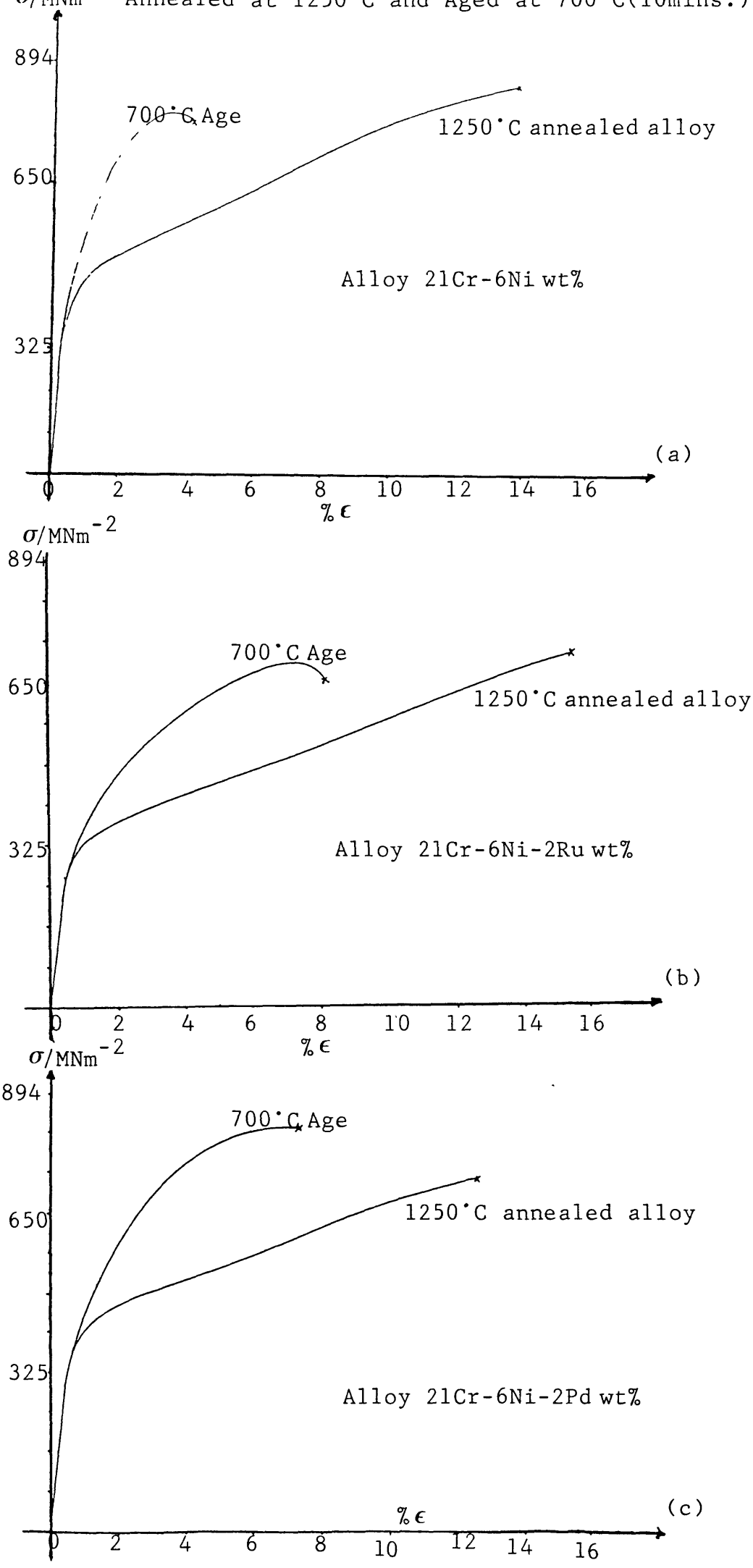

ductility, whilst the decrease in % elongation shown by the experimental alloys, proceeds less quickly with time, generally levelling off in ductility after ≃100 mins. These results are consistent with the findings of many authors who report that σ precipitation has a deleterious effect on room temperature toughness (60-63). The effect of ageing at 700°C for 10 mins. is shown in Figure 144 as a substantial loss in ductility and considerable increase in work hardening. This is believed to be associated with the transformation of metastable austenite to martensite, prior to testing on cooling rapidly from 700°C. Further strain-induced martensite is generated during tensile straining. Figure 145 further shows this loss in ductility at 700°C, the alloys being aged at 650°C, 700°C, 800°C, 900°C and 950°C for 10 mins. After 700°C ageing there is a general increase in % elongation associated with the rapid precipitation of γ_2-austenite prior to σ precipitation. Alloys Uranus 50 and 21Cr-6Ni reach a plateau after ≃ 10 mins. ageing at 800°C, whilst the Pd and Ru containing alloys show a rising ductility up to 950°C due to a greater stabilization of γ_2-austenite with increasing temperature.

Figures 146 and 147a show the banded γ + α duplex structure in these experimental alloys. Figure 146a shows a section through a tensile specimen subsequent to testing. The fracture profile is seen to be highly irregular, indicating crack propagation to have been assisted by either microcracks transverse to the tensile direction or crack propagation along ferrite grain boundaries and austenite twin interfaces. Figures 146b and c show these twins within austenite, together with strain-induced martensite. Prior to deformation the γ phase contained a negligible amount of α' seen in Figure 147a.

The banded structure developed in annealed alloys is shown in Figure 147a. The subsequent tensile deformation at room temperature results in a fracture surface seen in the SEM micrograph (Figure 147b) which is fully consistent with a duplex structure. Areas of fibrous dimple fracture are associated with the ductile γ phase whilst regions of cleavage are associated with the brittle α phase. Ageing of the ternary alloy and those containing Pd and Ru at 700°C (10 mins) results in an essentially brittle fracture in Figures 147c and d due to the transformation of $\gamma \rightarrow \alpha'$. The brittle fracture facets in Figure 147d have a fibrous appearance on their surface associated with the deformation of γ phase.

Figure 145.

(a) The effect of ageing temperature on the tensile ductility of Duplex stainless steels.

(b) Alloy 21Cr-6Niwt%
The light micrograph shows γ partially decomposed to α'-martensite on rapid cooling to room temperature from 700°C.

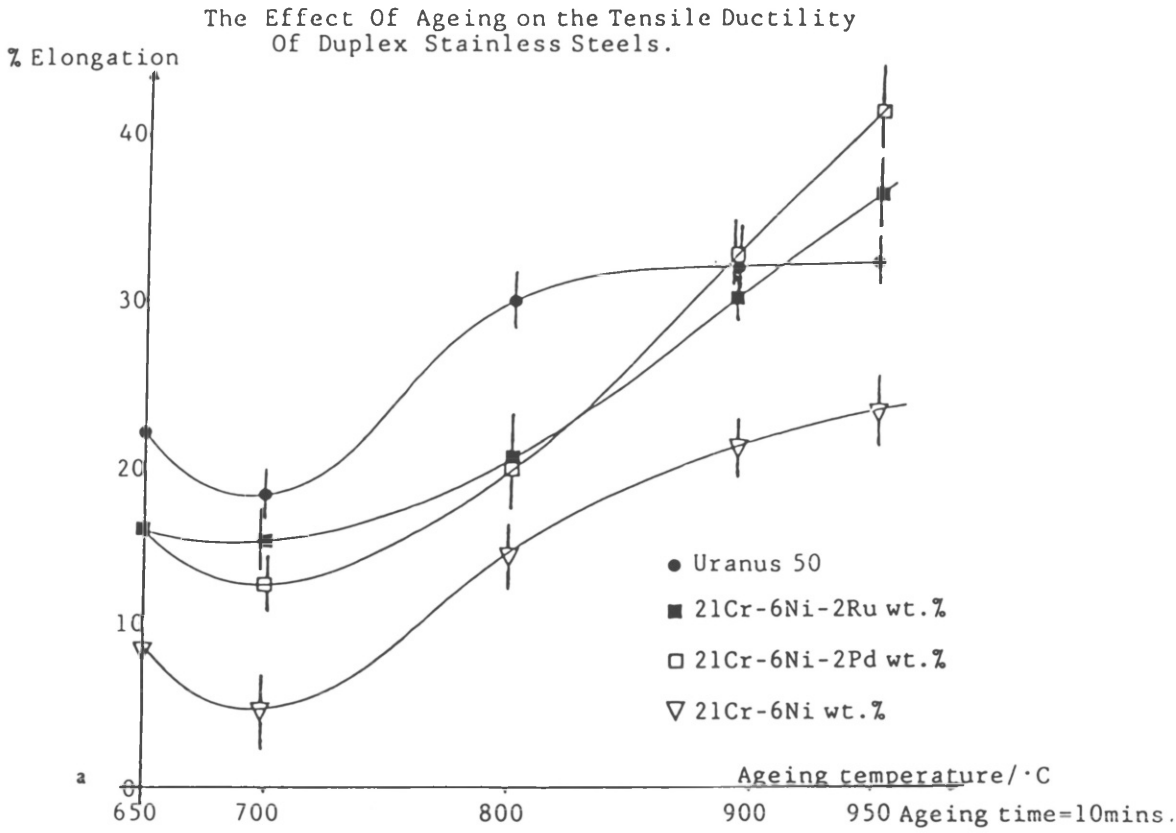
The Effect Of Ageing on the Tensile Ductility
Of Duplex Stainless Steels.
% Elongation
40
30
20
10
0
650
700
800
900
950
Ageing temperature/·C
Ageing time=10mins.
● Uranus 50
■ 21Cr-6Ni-2Ru wt.%
□ 21Cr-6Ni-2Pd wt.%
▽ 21Cr-6Ni wt.%

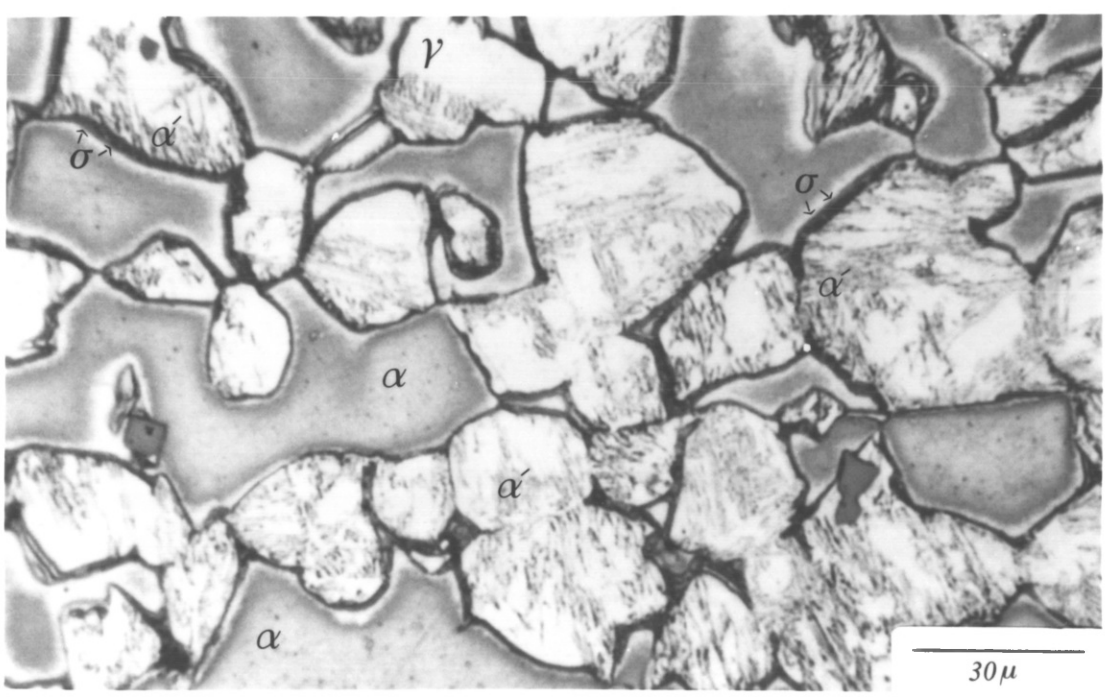
γ
α′
σ
σ
α′
α
α′
α
30μ

Figure 146. Cross-sections of tensile specimens 21/6/2Ru, fractured at room temperature.

(a) Light micrograph shows highly convoluted fracture cross-section. The microstructure shows bands of α and γ phases.

(b) The light micrograph shows bands of γ and α. γ shows evidence of strain-induced martensite.

(c) In addition to martensite formation within austenite, there is evidence of twinning, as indicated by the light micrograph.

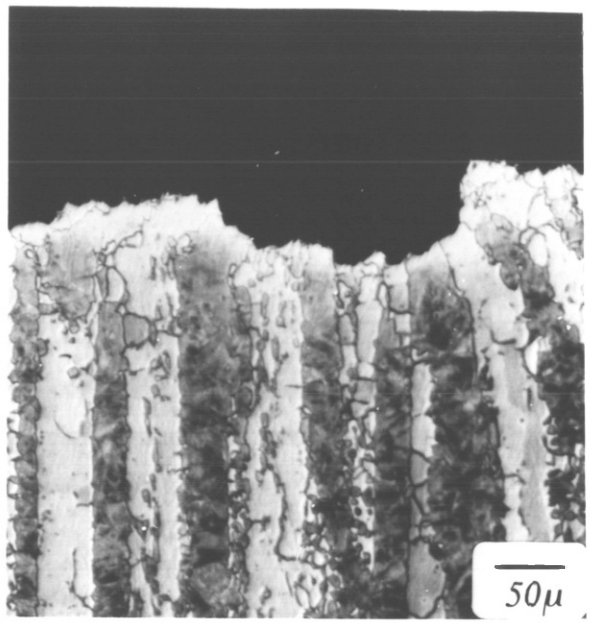

a

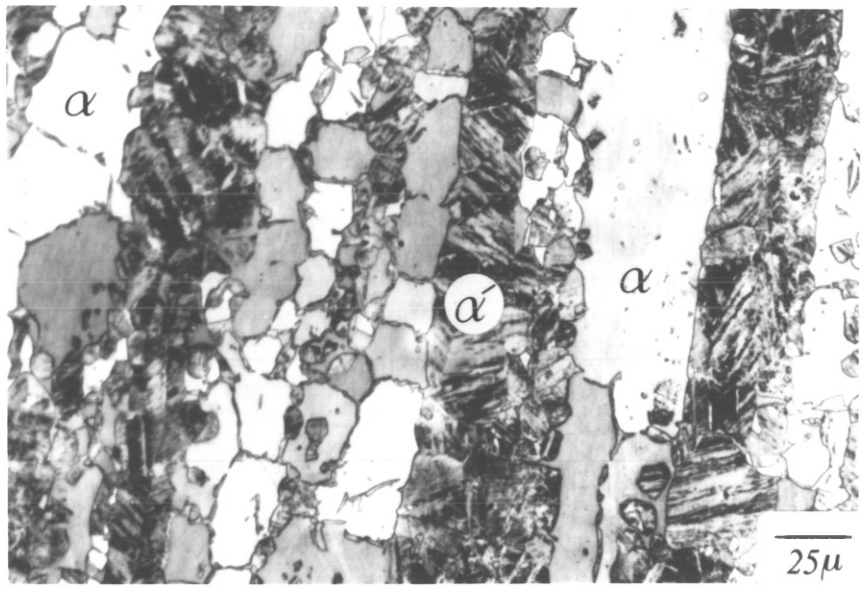

b

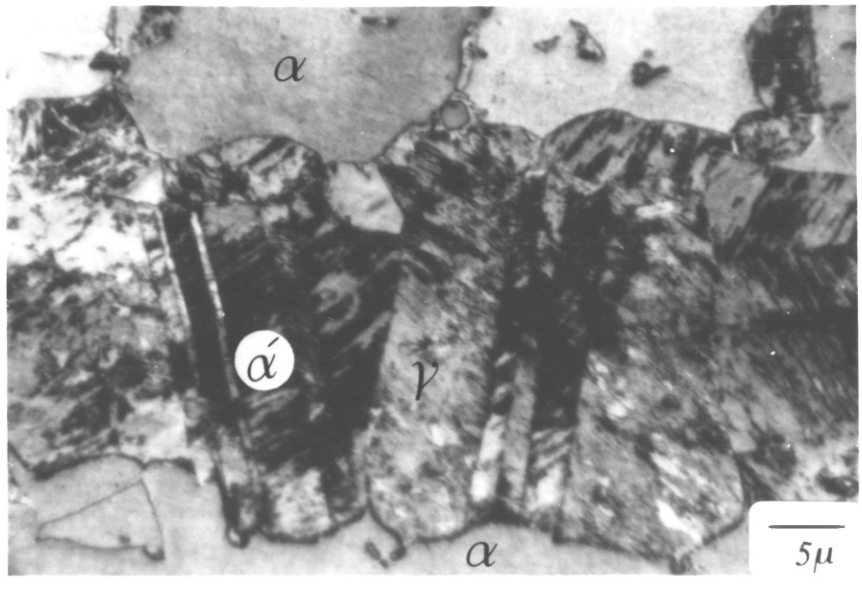

c

Figure 147. (a) Alloy 21Cr-6Niwt% annealed at 1250°C, shows bands of α and γ phases.

(b) SEM fractography of the 21Cr-6Ni-2Pd alloy deformed at room temperature shows ductile fibrous regions associated with the γ phase. The cleavage facets are associated with the brittle α phase. The micrograph also shows non-metallic inclusions inside dimples.

(c) SEM fractography.
Subsequent ageing of alloy 21Cr-6Ni-2Pd at 700°C produces a brittle fracture.

(d) SEM fractography. Cleavage facets in aged alloy have a fibrous appearance associated with the austenite phase.

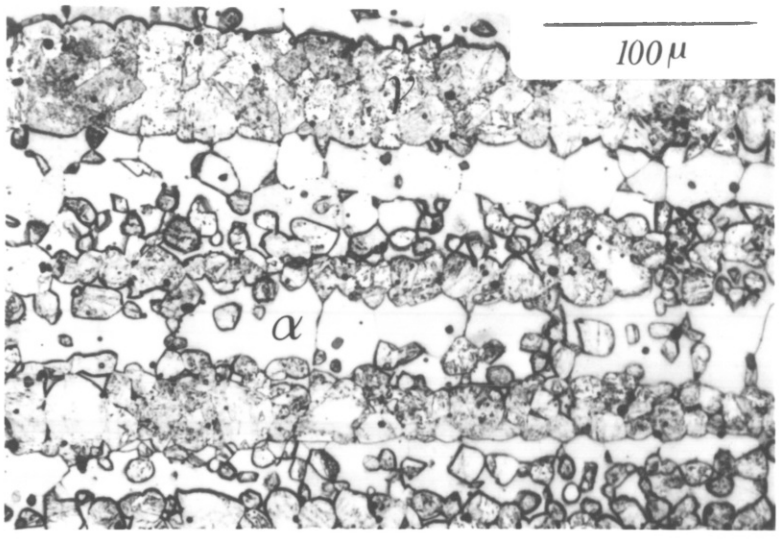

a

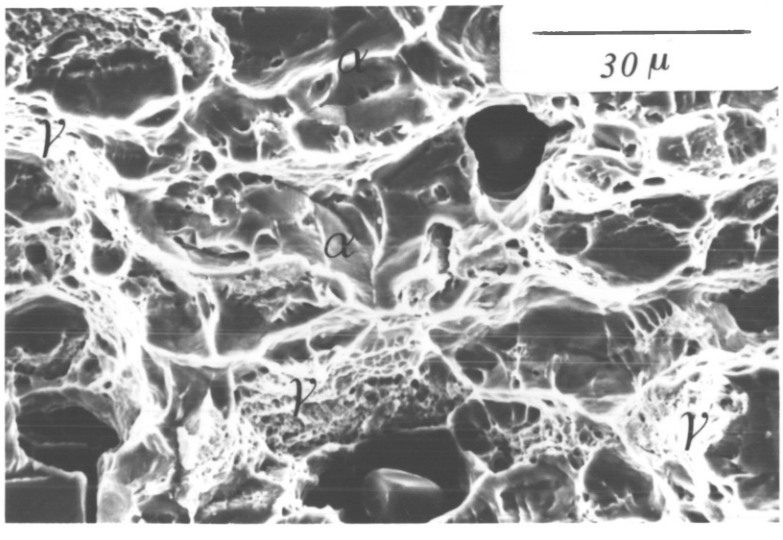

b

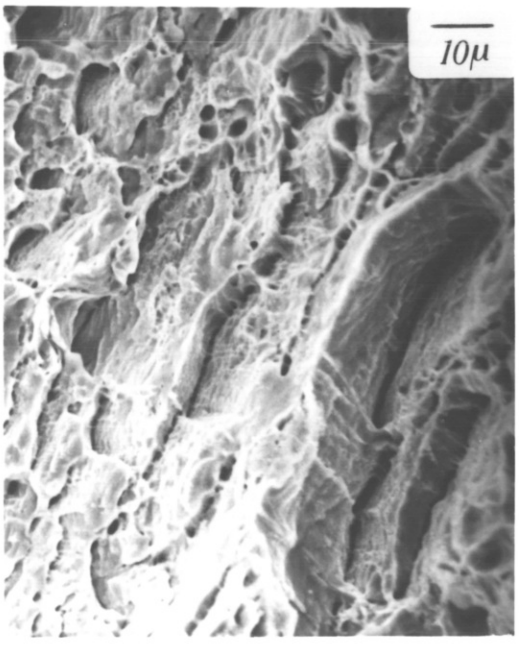

c

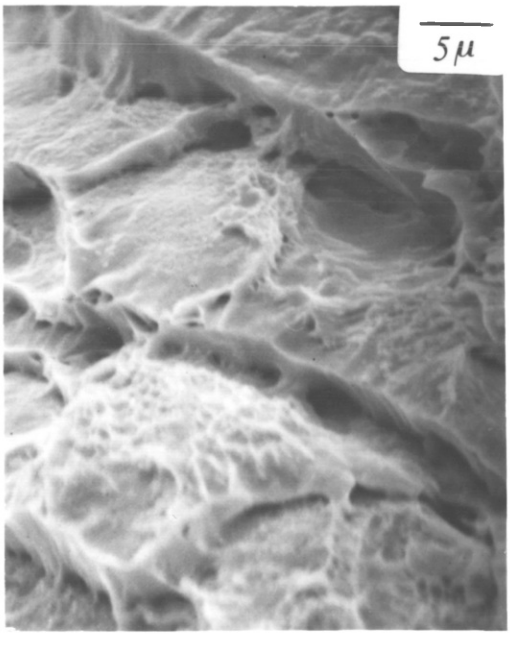

d

8.1.2. Hardness Variations

(i) As Cast Alloys

Figure 148 shows the hardness values developed in as-cast alloys. The highest hardness values are for alloys which have solidified ferritically, e.g. 18/6/2Ru ∿251. Those alloys containing primary dendrites of γ-austenite have lower H_v values consistent with the softer γ phase, e.g. 18/6/8Pd ∿ 149.

(ii) Annealed Alloys

The hardness values developed in alloy series, 21/6 and 18/6 solution treated between 1000 and 1300°C are shown in Figure 148. These results are also presented graphically in Figures 149 and 150; the omission of alloys containing 5wt% PGM means that trends shown between 2 and 8wt% are inexact.

Figure 148. Vickers Hardness Measurements

	Condition			
		Annealing temperature/°C		
Alloy	As Cast	1000	1250	1300
21/6	192	224	223	233
18/6	229	228	209	276
21/6/2Pt	213	209	217	206
21/6/8Pt	225	180	189	216
18/6/2Pt	239	241	234	253
18/6/8Pt	189	179	213	183
21/6/2Ru	209	223	218	210
21/6/8Ru	247	210	237	225
18/6/2Ru	251	305	281	283
18/6/8Ru	229	232	236	242
21/6/2Pd	240	201	219	196
21/6/8Pd	161	144	180	181
18/6/2Pd	237	270	277	297
18/6/8Pd	149	142	158	149

Annealing times ranged from 24 to 70 hours.

For the 18/6 alloy series in Figure 149, the maximum hardness developed at the 2wt% PGM level comes from Ru at 1000 and 1250°C and from the Pd containing alloy at 1300°C. At this PGM level, it is noted that with a rising temperature 1000 to 1300°C, Pd alloys show a gradual increase in hardness, whereas Ru hardness values, decrease.

Figure 149. Hardness Variations in the 18Cr-6Ni alloy Series as a Function of PGM Alloying Addition. (Alloys were anneald for 24 to 70 hours).

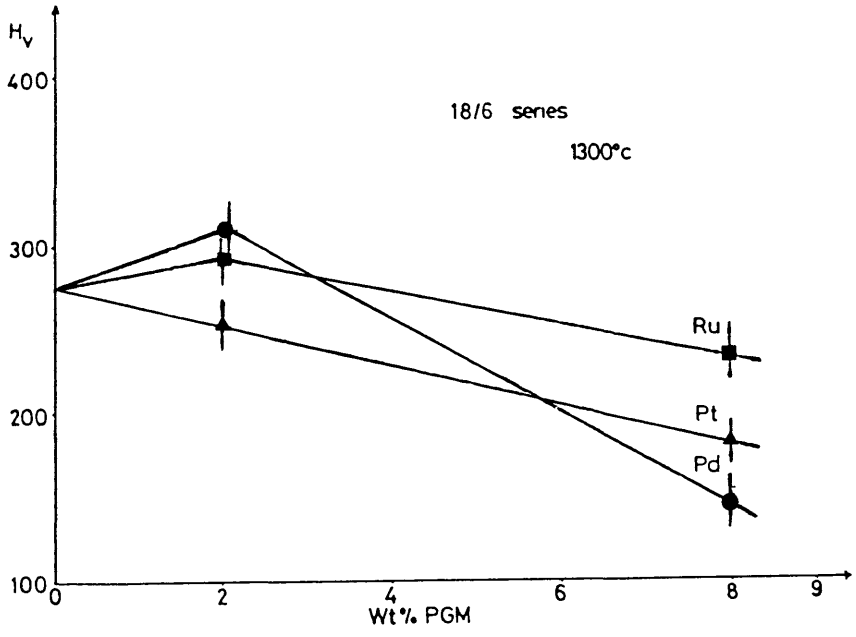

(a)

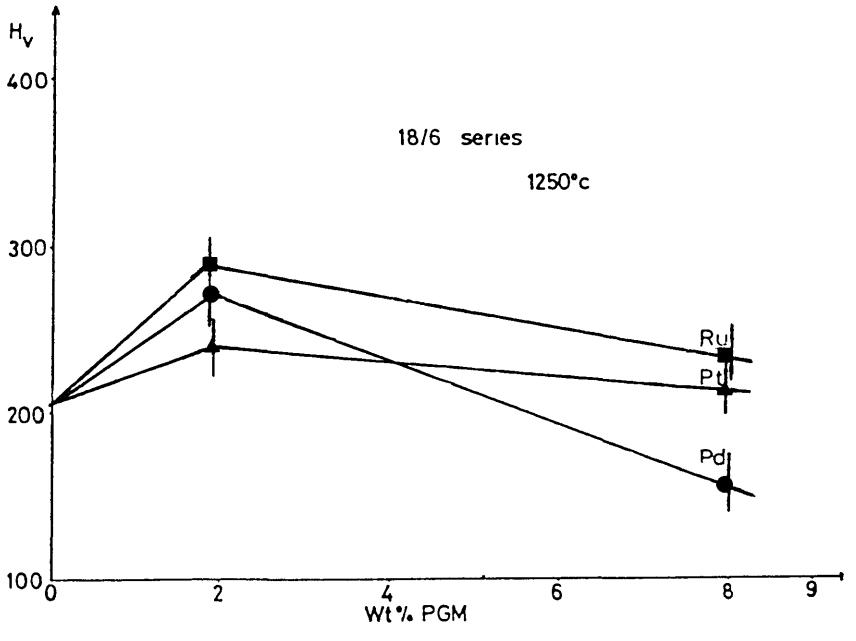

(b)

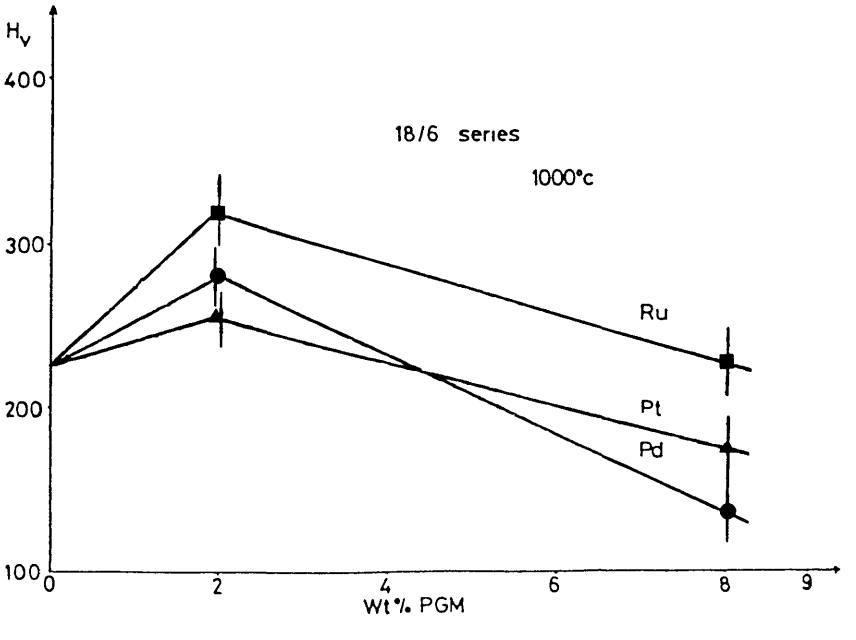

(c)

Figure 150. Hardness Variations in the 21Cr-6Ni alloy Series as a Function of PGM Alloying Addition. (Alloys were annealed for 24 to 70 hours).

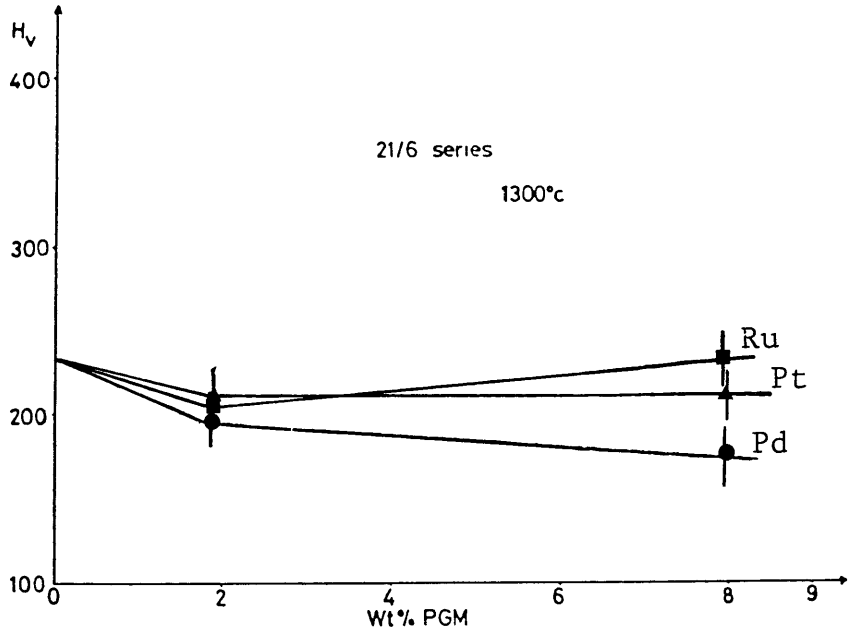

(a)

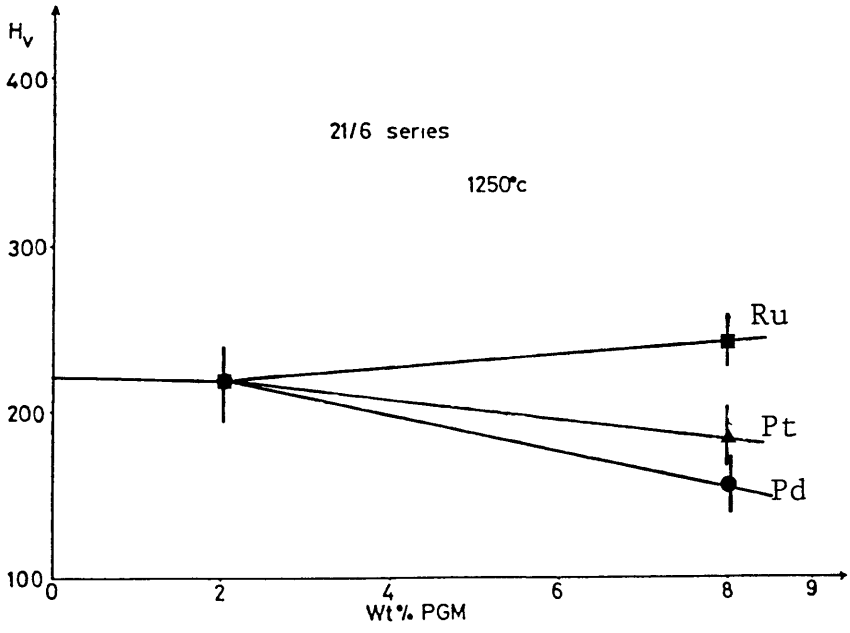

(b)

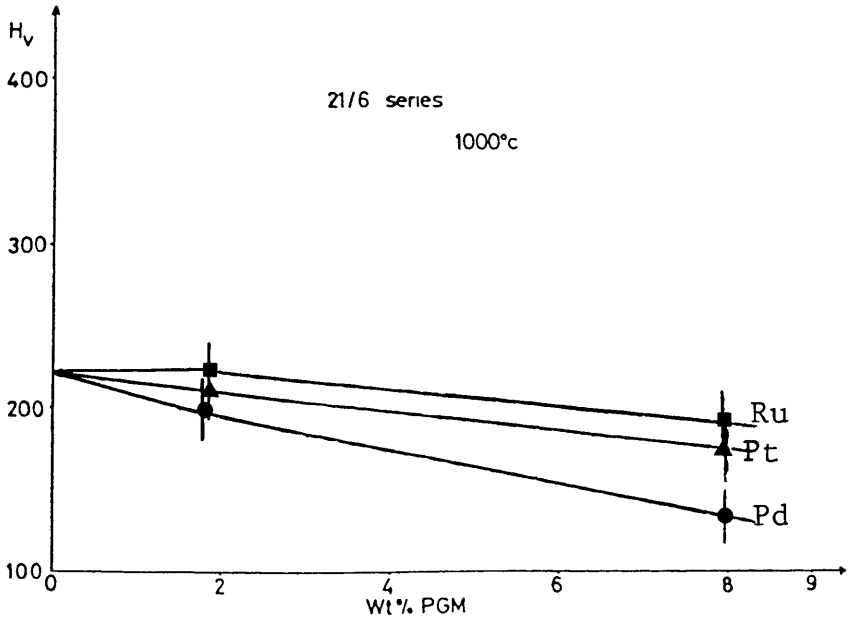

(c)

Figure 151.

(a) Isothermal oxidation behaviour of alloys 21Cr-6Ni, 21Cr-6Ni-2Pd, 21Cr-6Ni-2Ru at 1000°C in air, result in essentially linear oxidation rates.

(b) Light micrograph of oxide cross-section in alloy 21Cr-6Ni-2Ru showing the oxide nearest the alloy substrate. The oxide/alloy interface is non-uniform and contains regions of porosity and internal oxidation.

(c) Light micrograph of oxide cross-section in alloy 21Cr-6Ni-2Pd. The oxide scale above the region of porosity nearest the substrate, is seen here to be a two-phase structure.

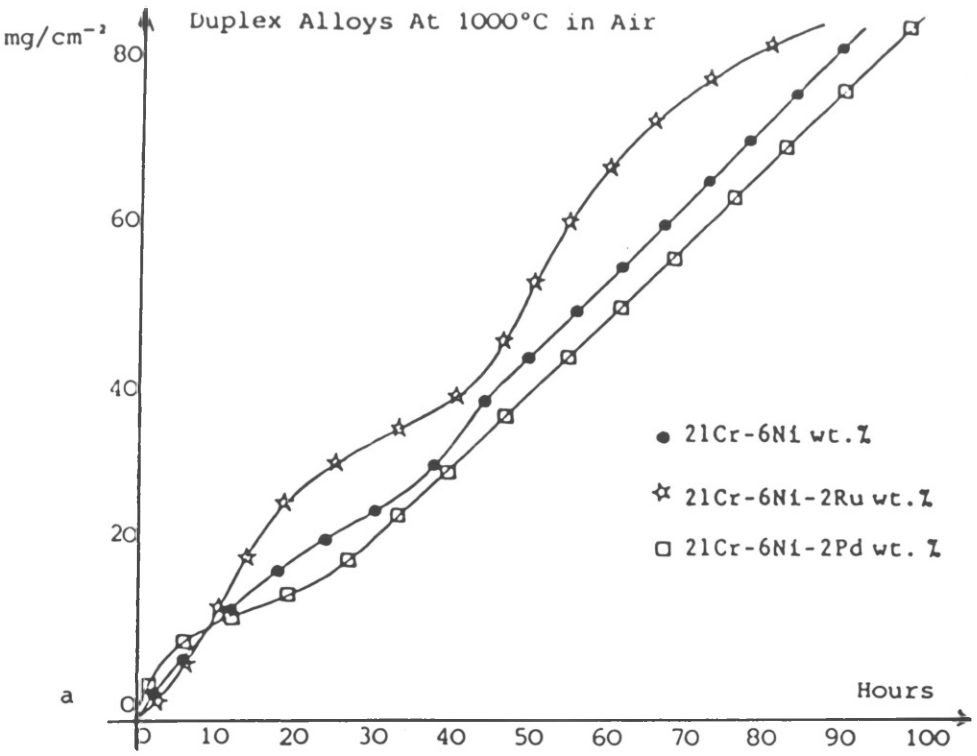
Duplex Alloys At 1000°C in Air
mg/cm⁻²
80
60
40
20
0
Hours
0
10
20
30
40
50
60
70
80
90
100
● 21Cr-6Ni wt.%
☆ 21Cr-6Ni-2Ru wt.%
□ 21Cr-6Ni-2Pd wt.%

a

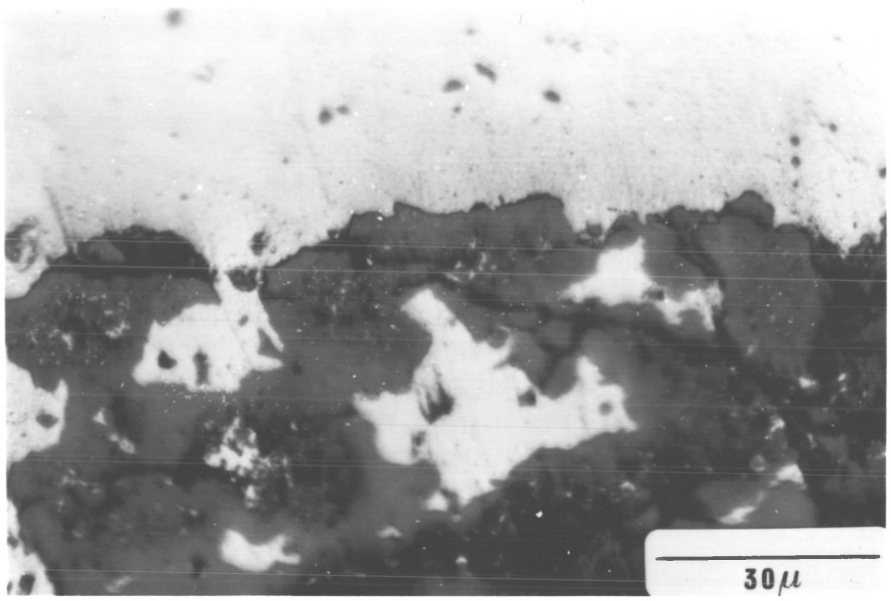
30μ

b

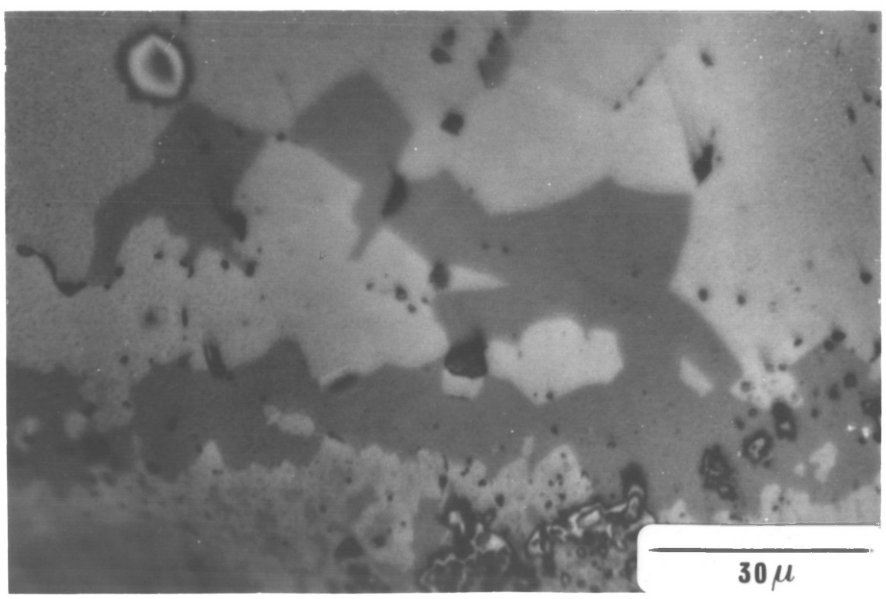
30μ

c

The 18/6/2Pt alloy has a hardness value of 241 at 1000°C rising to 253 at 1300°C and hence Pt contributes the least amount of hardening at this alloying level. At the 8wt% PGM level, hardness significantly falls at each annealing temperature to the lowest value for the Pd containing alloys. The Ru containing alloys however remain relatively high, e.g. 242, being less affected by increasing temperature. Increasing levels of Pt up to 8wt% causes a general decrease in hardness at each solution temperature, but Pt is intermediate to Ru and Pd at this alloying level.

At the 2% PGM level Ru > Pd > Pt (except at 1300°C)

At the 8% PGM level Ru > Pt > Pd

For the 21/6 alloy series in Figure 150, the predominant trend is a decrease in hardness with increasing additions of PGM, although with increasing annealing temperature, this effect is lessened.

At the 2 and 8% PGM level Ru > Pt > Pd.

8.1.3. Isothermal Oxidation Behaviour

This section of the present study aims to present and discuss some features of the isothermal oxidation behaviour of PGM modified duplex steels. Alloys 21Cr-6Ni, 21Cr-6Ni-2Pd and 21Cr-6Ni-2Ru were isothermally oxidised in air at 1000°C for 100 hours, and were characterised by very high oxidation rates. Figure 151a shows this behaviour to conform to a linear oxidation rate. The Ru containing alloy has an essentially higher oxidation rate than the 21Cr-6Ni ternary alloy whilst the Pd containing alloy is marginally lower. The oxide scales in the three alloys studied were morphologically similar consisting of a grey-black outer scale. A schematic cross section through the oxide developed in these alloys is shown in Figure 152 below. All alloys showed protrusions rich in iron growing through a granular scale rich in Cr identified qualitatively by X-ray EDS analysis in Figure 153.

Schematic section through oxide films developed at 1000°C in air.

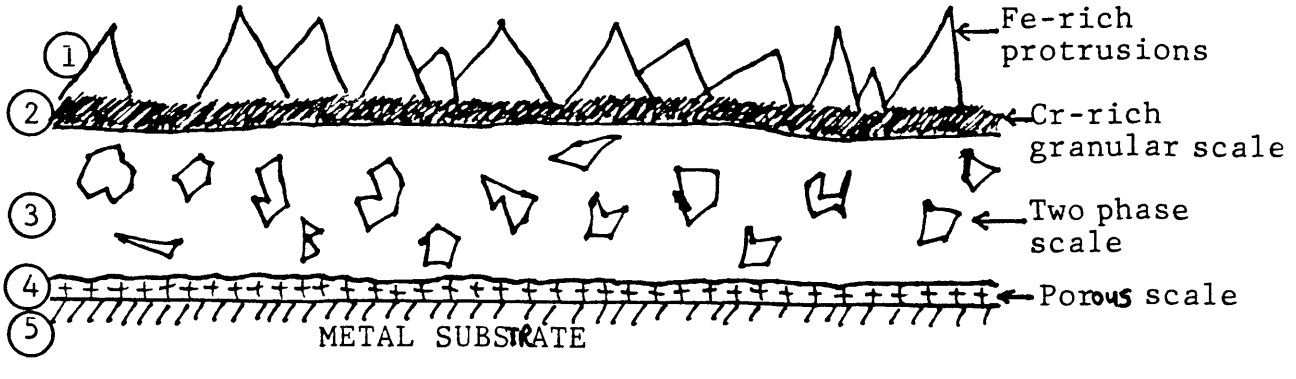

Figure 152.

EDS analysis also revealed that the concentration of Pd and Ru in the outer scale was low, being ≈0.4wt%. The oxide scale beneath the Cr-rich granular scale was observed in Figure 151c and Figure 154b as a two-phase consolidated structure suggesting that it was a nickel or chromium spinel. The scale immediately adjacent to the metal substrate in these alloys revealed extensive porosity and some evidence of internal oxidation. Figures 153 and 154 show SEM micrographs of the oxide surface developed in the above alloys. They identify 3 constituent regions, namely Fe-rich protrusions and a Cr-rich granular scale above a third phase. These regions correspond to regions (1), (2) and (3) shown in Figure 152 and described previously. Since the morphologies in the ternary and PGM containing alloys were essentially similar, and microchemical characterisation was minimal it seems unlikely that any conclusive effects of PGMs to modify isothermal behaviour in these steels can be established.

Figure 153.

(a) The isothermal oxidation (1000°C, 100 hours) of alloy 21Cr-6Ni-2Ru produces an oxide scale which shows Fe-rich protrusions growing through a Cr-rich granular scale, as indicated by the SEM micrograph.

(b) X-ray EDS analysis of the oxide scale in the above alloy shows a low concentration of Ru and relatively high concentrations of Cr and Fe on the oxide surface.

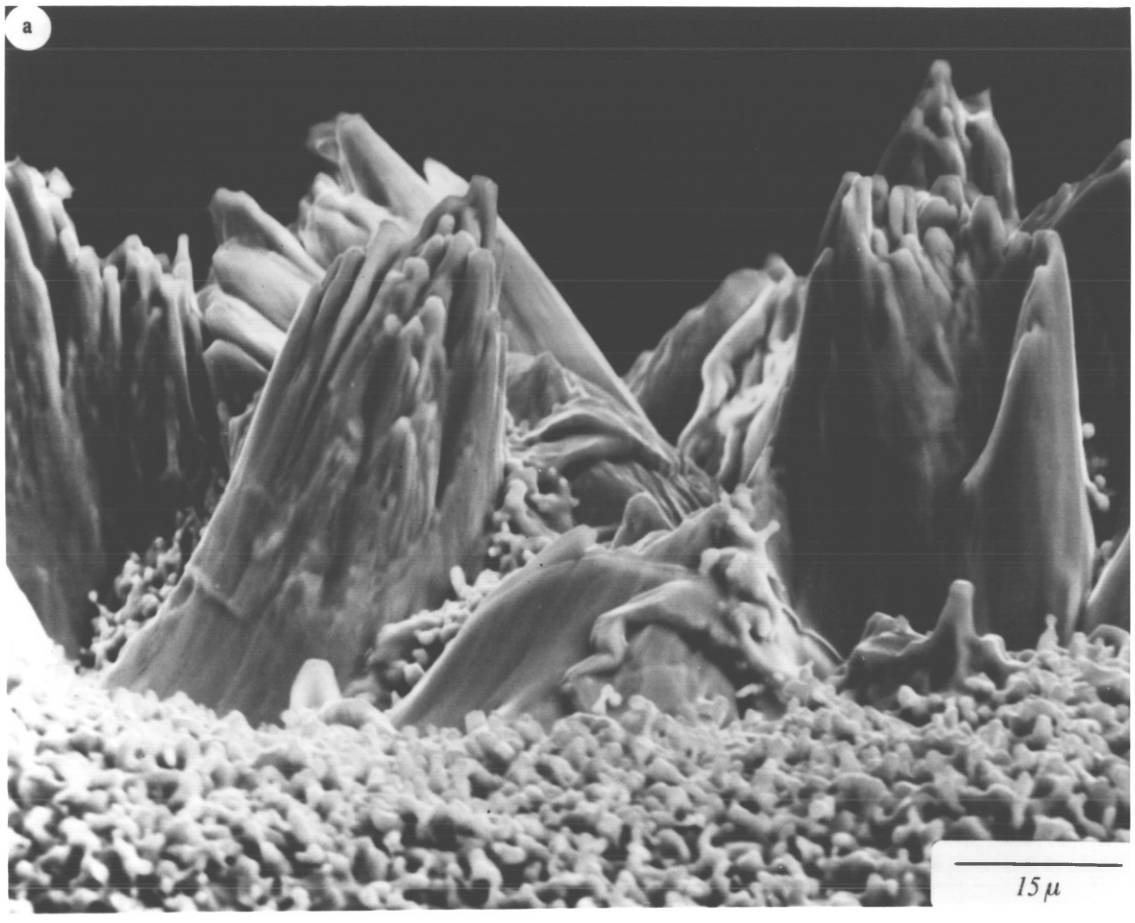
a
15 μ

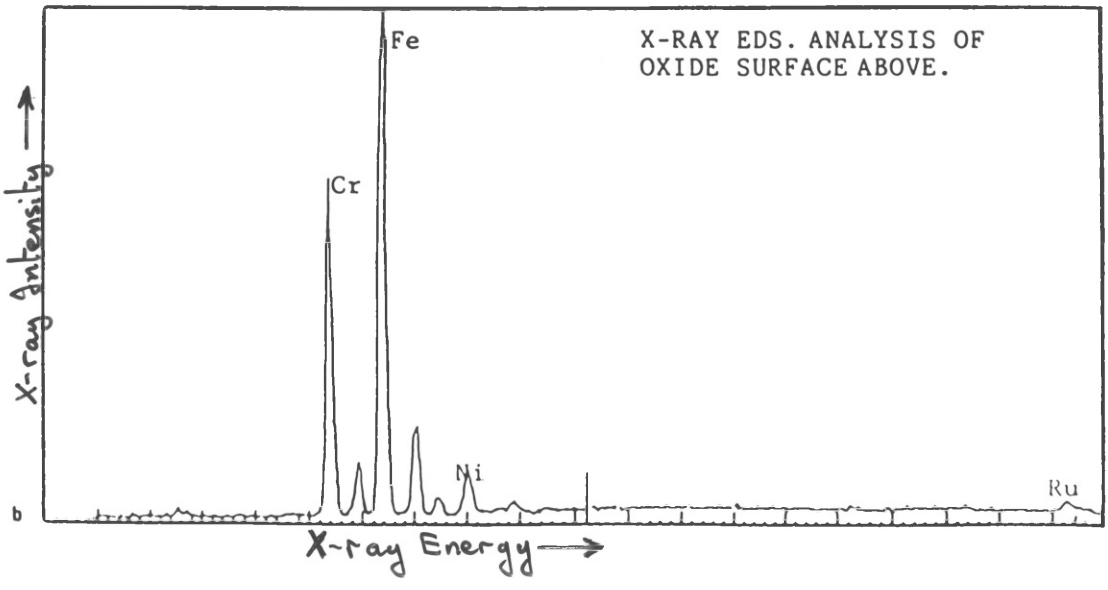
X-RAY EDS. ANALYSIS OF
OXIDE SURFACE ABOVE.
Fe
Cr
Ni
Ru
X-ray Intensity
X-ray Energy
b

Figure 154.

(a) The SEM micrograph shows a planar view of Fe-rich protrusions and Cr-rich granular scale in alloy 21Cr-6Ni oxidised in air at 1000°C for 100 hours.

(b) Alloy 21Cr-6Ni-2Pd oxidised in air at 1000°C for 100 hours. A third phase (M) lies beneath the Cr-rich scale (B) and Fe-rich protrusions (A).

(c) The SEM micrograph shows the alloy in (b) to have regions of extensive cracking as a result of thermally induced stresses produced on cooling to room temperature.



a



b



c

8.1.4. Anodic Polarisation Behaviour

It is well proven that platinum group metal additions to Fe-based alloys improve general corrosion resistance when subjected to a variety of acidic media (111,112). The accepted basis for this behaviour is associated with the high exchange current density for the cathodic reaction on the PGM in question (112). A stimulation of the cathodic reaction raises the anodic potential and allows rapid passivation of the surface. This will only hold true as long as the alloy itself is capable of passivation and at the accelerated rates of anodic dissolution involved (111).

As a consequence of these effects it is apparent that even low levels of PGM addition would be sufficient to have marked effects on corrosion properties, and in particular the polarisation characteristics of Fe-based alloys. The anodic polarisation characteristics of experimental duplex alloys, 21Cr-6Ni, 21Cr-6Ni-2Pd, 21Cr-6Ni-2Ru and palladium modified Uranus 50 are presented in Figures 155 and 156. These figures show the various effects of Ru and Pd on the peak current density at the critical passivation potential, i_{cpp}, the current density necessary to sustain passivation, i_{min}, and the potential at which passivity breaks down (transpassivity), E_t in N.H_2SO_4 at 25°C. A schematic representation of these values is shown in Figure 157.

Both Pd and Ru containing alloys have similar characteristics as compared with the base alloy 21Cr-6Ni. A notable effect observed during polarisation was the ability of ruthenium and palladium to induce self-passivity and in general, to reduce the current density over the potential range of passivity. Clearly, palladium and ruthenium play key roles in modifying the anodic reactions, and in particular, influencing the behaviour of the passivating film. Additionally, both ruthenium and palladium containing alloys reduce the peak current density, i_{cpp}, at the critical passivation potential E_{cpp}.

Figure 156 shows the effect of Pd on the anodic polarisation characteristics of a commercial duplex alloy, Uranus 50 in 1N.H_2SO_4. The significant effect of 8wt%Pd on this alloy was to substantially lower the current density over the range of passivity, from $\simeq 10^3$ to $\simeq 10^1$ microA/sq.cm. which was consistent with the reported effects of Pd in steels (112).

Figure 155. Anodic Polarisation Characteristics of Duplex Alloys Containing Pd and Ru in deaerated 1N.H_2SO_4 at 25°C.

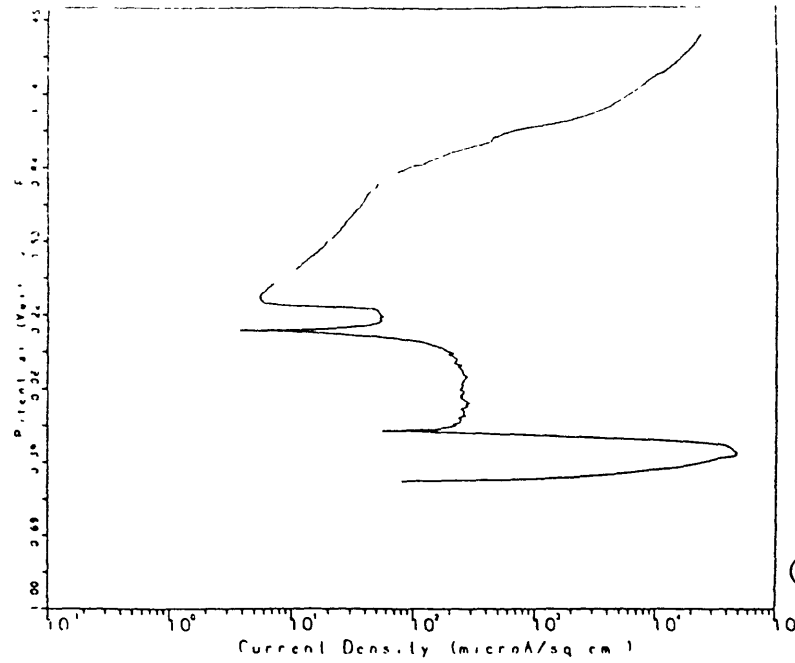

Alloy 21Cr-6Ni wt%

(a)

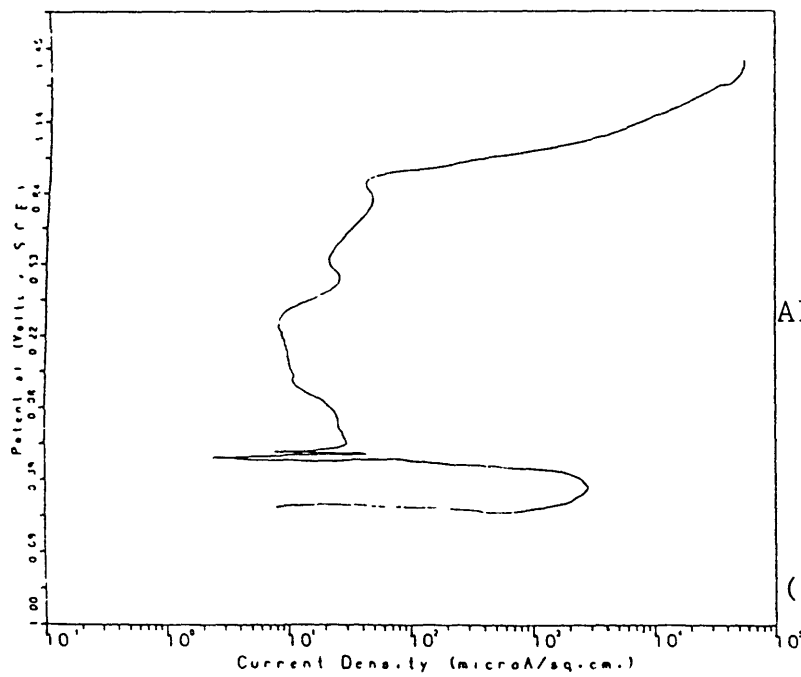

Alloy 21Cr-6Ni-2Ru wt%

(b)

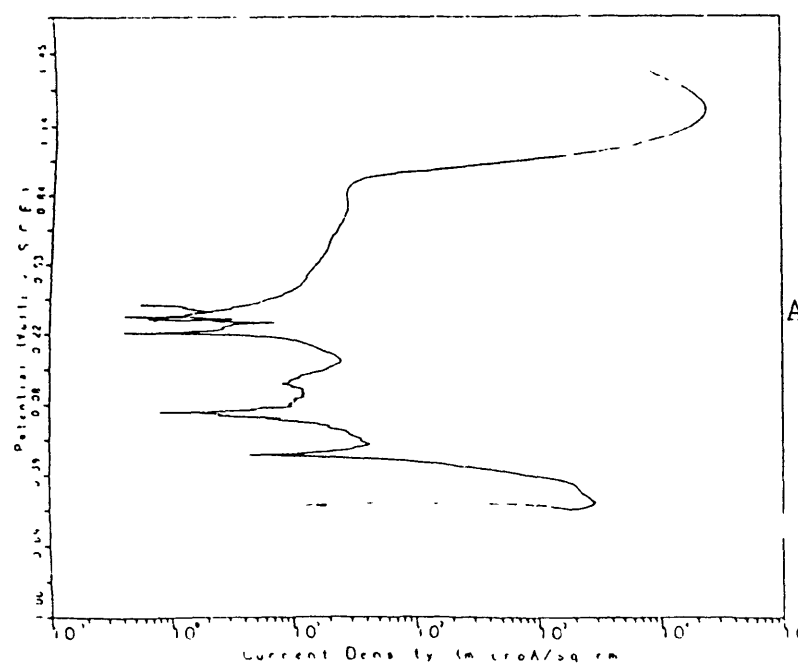

Alloy 21Cr-6Ni-2Pd wt%

(c)

Anodic Polarization Characteristics of Modified Uranus 50 steel in deaerated 1N.H_2SO_4 at 25°C.
Figure 156.

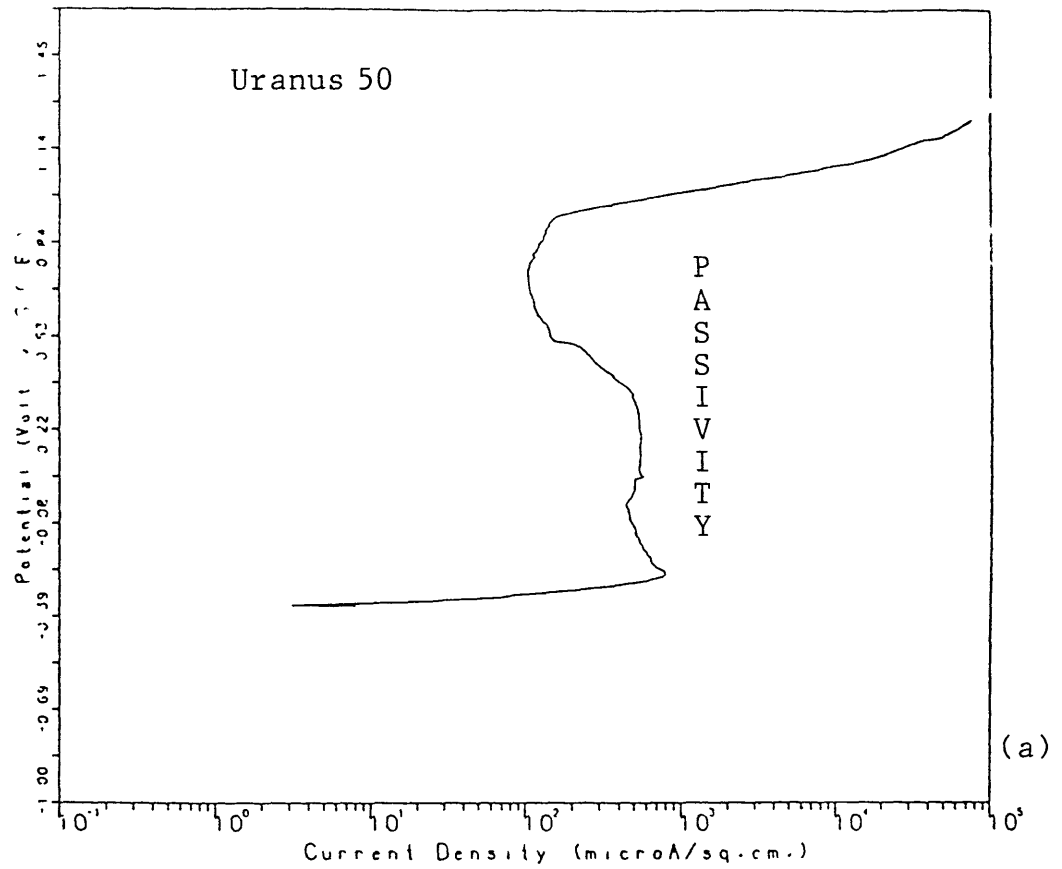

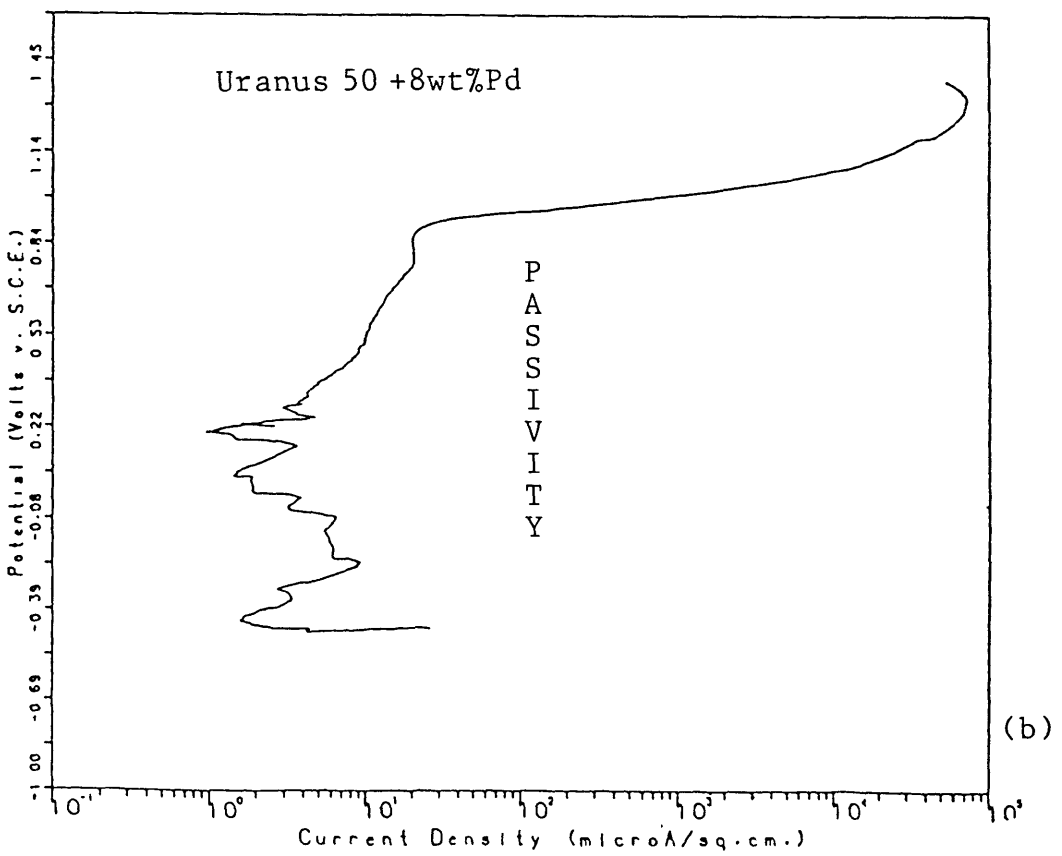

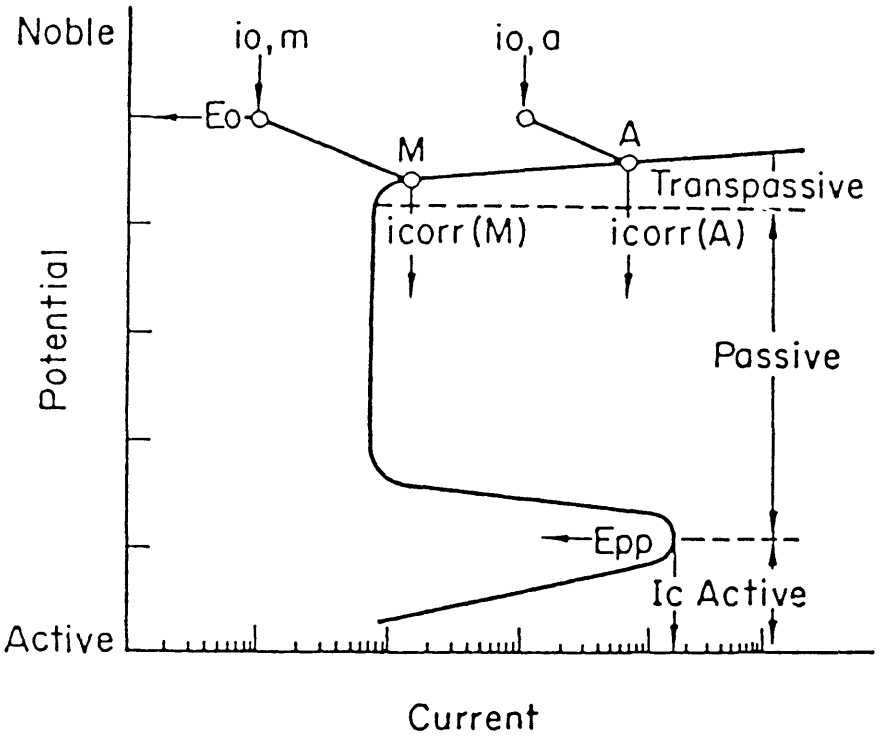

Effect of noble metal additions to the corrosion reaction of chromium. In non-oxidizing acids the metal is passive. In oxidizing acids it is raised into the transpassive region . $i_{0,m}$ and $i_{0,a}$ are the exchange current densities for the cathodic reduction reaction on the metal and alloy surface respectively. $i_{corr\,(M)}$ and $i_{corr\,(A)}$ are the corrosion rates of the metal and alloy respectively.

Figure 157. Ref.258

8.2. Discussion

8.2.1. Tensile Behaviour

(i) Variables affecting stress-strain characteristics

It is evident from the literature discussed (59) that many factors act to determine the mechanical properties of a duplex stainless steel, even when it is in its optimum, unembrittled condition. The amount of α and γ present, the morphology of the α and γ phases, the orientation of the α and γ with respect to applied stresses or fracture paths, and the exact composition of both the α and γ phases, all play an important role in determining the mechanical properties (59). Furthermore, this role may vary with temperature and strain rate, causing what might be a favourable situation in one condition to be unfavourable in another (59). In this investigation it is therefore dangerous to try to use data from PGM containing alloys to predict quantitatively the behaviour of another duplex alloy containing a differing amount of PGM. However, the data in the literature (59) and results from this investigation together may serve as a guide to the effect of PGM additions.

Figure 158a has marked the position of the ternary alloy in this study reinforcing that it is a two-phase structure belonging to the duplex steel alloys, whose tensile behaviour is intermediate to ferritic/austenitic and martensitic steels in Figure 158b.

(ii) Effect of composition and microstructure

The tensile strength and proof stress have been related to compositional and microstructural parameters in γ-austenitic steels containing ferrite, by the following regression equations:

$$0.2\%\ \text{proof stress} = 15.4[4.4 + 23(C) + 1.3(Si) + 0.24(Cr) + 0.94(Mo) + 1.2(V) + 0.29(W) + 2.6(Nb) + 1.7(Ti) + 0.82(Al) + 32(N) + 0.16(\text{ferrite}) + 0.46d^{-\frac{1}{2}}]\ /MN/m^2 \quad (257)$$

$$\text{and Tensile strength} = 15.4[29 + 35(C) + 55(N) + 2.4(Si) + 0.11(Ni) + 1.2(Mo) + 5.0(Nb) + 3.0(Ti) + 1.2(Al) + 0.14(\text{ferrite}) + 0.82t^{-\frac{1}{2}}]\ / MN/m^2 \quad (257).$$

where ferrite is the percentage of ferrite, d is the mean linear intercept of the grain diameter (mm), t is the twin spacing (mm) and the brackets indicate the alloying addition in wt%.

Figure 158.

(a)

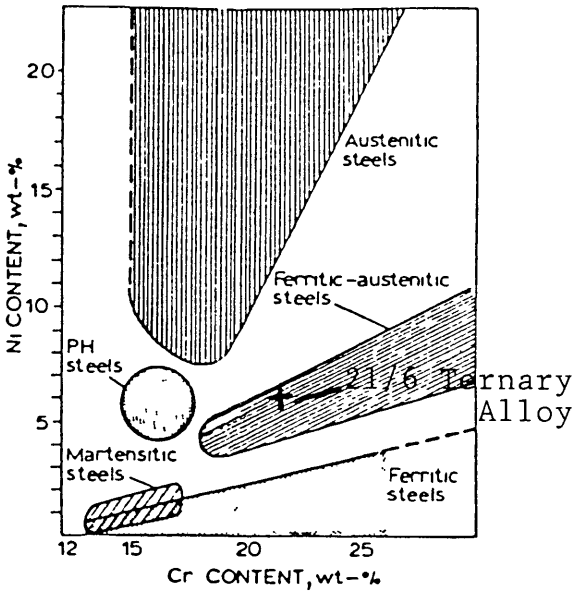

Relation between nickel and chromium contents of stainless steels and type of steel. PH steels are precipitation-hardening steels

Ref.2

(b)

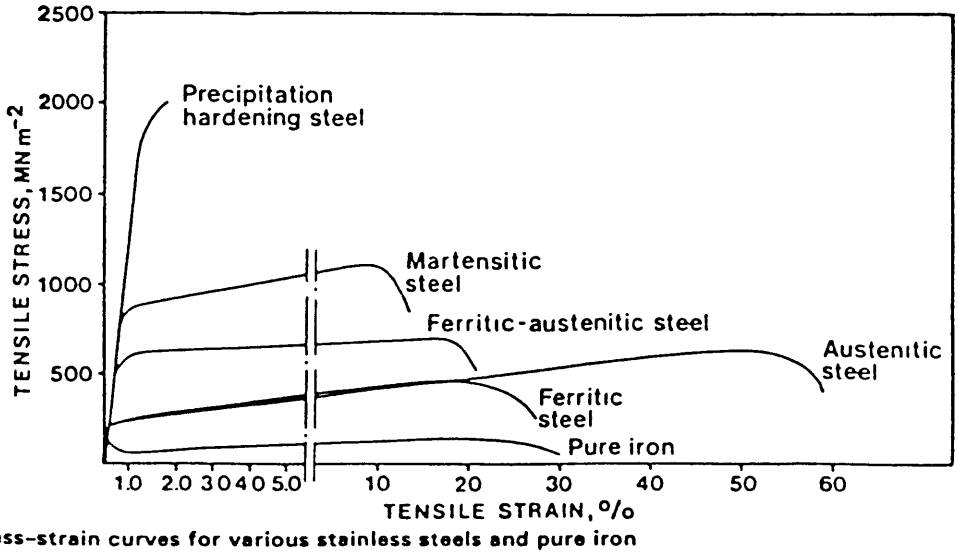

Tensile stress-strain curves for various stainless steels and pure iron

Ref.2

Unfortunately no measurement of twin spacings, t, was made for the alloys in this study to permit correlation between the observed tensile strength and that predicted by the regression equation. Proof stress values have however been calculated using measured austenite tie-line compositions in the present work, and are:

Figure 159.

Alloy	0.2% σ (proof stress)/MN/m^2	
	Calculated	Observed
21Cr-6Ni	364	333
21Cr-6Ni-2Pd	335	382
21Cr-6Ni-2Ru	346	329

(iii) Effects of prior martensite and solid-solution strengthening

The strengthening achieved by Ru and Pd alloying additions may be established by comparing the observed mechanical properties (in this instance the proof stress) with those calculated on the basis of the regression analysis in Figure 159. The difference between the calculated and observed values reflect the effect of the added variables, Pd and Ru. The values of ΔP, which is the difference between the observed and calculated 0.2% proof stress, are:

$\Delta P = +47$ for a 2 wt% Pd addition

and $\Delta P = -17$ for a 2 wt% Ru addition.

Therefore Pd has a solid-solution hardening effect of 23.5 MN/m^2 per 1 wt% Pd. Ru has a solid-solution 'softening' effect of -8.5 MN/m^2 per 1 wt% Ru.

A cautionary comment is made on these findings since ferrite has a yield stress higher than austenite and recent analysis (157) indicates that strain concentration in the softer austenite phases causes it to work-harden to a strain greater than the nominal 0.2%, and therefore gives a higher proof stress value. The prior martensite content must also affect the value of 0.2% proof stress. However, both Pd and Ru containing alloys contain <15% martensite prior to tensile straining (see Figure 122) - this has been shown to have an insignificant effect on proof stress (46). Indeed, up to 35% martensite prior to straining does not affect the 0.2% proof stress - up to 20% martensite prior to straining may actually lower the 0.2% proof stress because of internal

stresses produced (46). Because of the low strains involved at the proof stress, very little martensite forms, and consequently has little effect on the proof stress. When more than ≃35% martensite is present prior to straining, the 0.2% proof stress increases with increasing martensite content (46). This may be due in part to the martensite being highly stressed, and the austenite and the martensite being differentially stressed during tensile testing.

(iv) Effect of PGMs on proof stress

The results in Figures 141 and 142 establish that Pd and Ru alloying additions cause a respective increase and decrease in the 0.2% σ proof stress of a 21Cr-6Ni duplex alloy. The following variables will now be discussed to explain these variations in proof stress.

Grain Size

It should be emphasized that the grain size will depend on both the alloy composition and solution treatment and/or hot working conditions (157). In the present investigation, the ternary alloy, 21Cr-6Ni and those containing Pd and Ru were hot-rolled at 1000°C prior to the 1250°C anneal to produce a banded structure of γ and α grains in Figure 147a. The grain size developed in these alloys was $d \simeq 0.04mm^{-\frac{1}{2}}$, with negligible differences between the three alloys. Therefore variations in proof stress cannot be simply explained in terms of differing grain sizes.

While an increase in proof stress can be achieved by decreasing the γ grain size, the intensity of the grain size strengthening in austenite is only about half that achieved in ferrite (157). This means that to achieve a given increment, a more pronounced grain refinement is required in austenite than in ferrite (46,59,157).

Ferrite Content

The fraction of ferrite in alloys 21Cr-6Ni, 21Cr-6Ni-2Pd, and 21Cr-6Ni-2Ru was 60, 45 and 50% respectively and clearly constitutes an important variation. Increasing amounts of ferrite are known to cause a decrease in the γ grain size and hence an increase in 0.2% σ proof stress (157). However, this is not borne out in this study since the grain size in each alloy was approximately the same. In addition, despite a relatively smaller fraction of α associated with the Pd containing alloys it has a proof stress which exceeds both the ternary and Ru containing alloys and that predicted by the regression equation. The implication is that the solid solution strengthening

Figure 160.

(a) TEM micrographs in (a) and (b) show the co-existence of α-ferrite stringers and γ-austenite in the 21Cr-6Ni-2Pd alloy annealed at 1250°C. The ferrite phase generates fringes into γ from the α/γ phase boundaries.

(b) The TEM micrographs in (c) and (d) of the above alloy show grains of α-ferrite and α'-martensite. The α' is identified by the HRDF in (d) using $\{110\}_{\alpha'}$ reflection from the SADP. ($2\lambda L = 5.29$ Å cm).

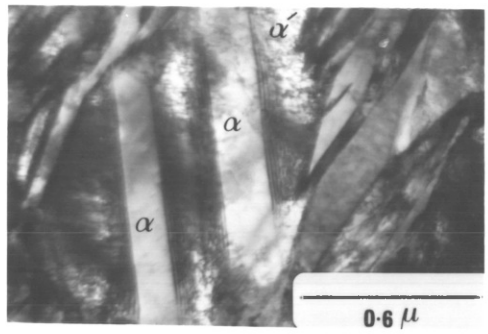

a

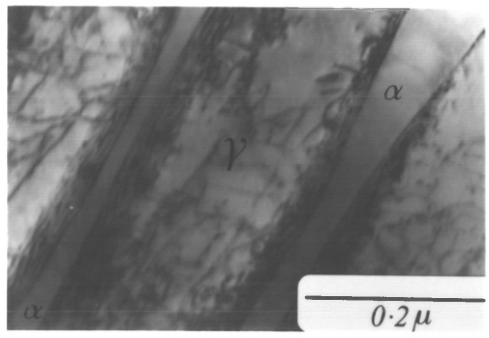

b

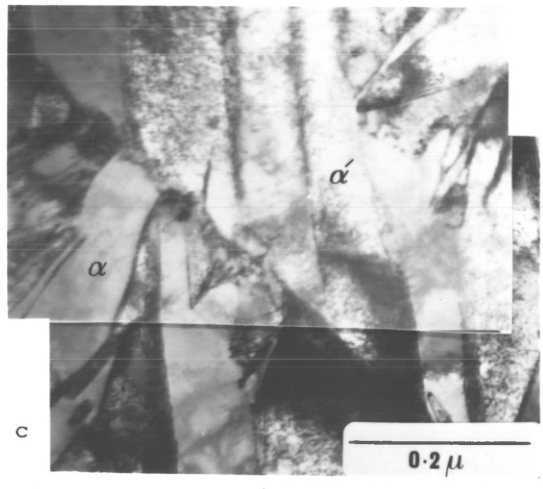

c

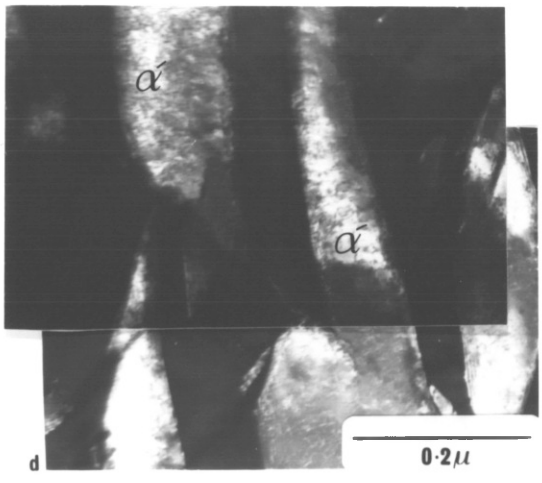

d

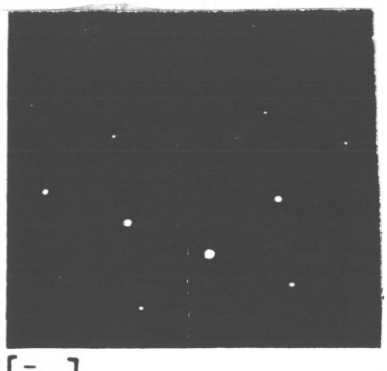

e

$[\bar{1}11]_{\alpha'}$

effect of Pd in γ (and α) greatly exceeds the expected loss in strength associated with a smaller α fraction of 45% compared with 60% in the ternary alloy. Ru is observed to have a negative solid solution strengthening effect (as borne out by the regression equation) since it should have a 0.2% proof stress higher than the Pd containing alloy by dint of a 50% ferrite content.

The strengthening effects of ferrite itself are important and significant. This is because:
a) There is partitioning of elements, Pd and Ru between the austenite and ferrite phases introducing solid solution hardening into both phases.
b) Ferrite occurring as either longitudinal stringers, e.g. Figure 160 a and b, or bands in the duplex structure acts as a fibre-strengthener (157).
c) Due to the differences in coefficients of expansion between austenite and ferrite phases, dislocations are generated in the austenite phase near to the ferrite which increases the austenite strength (157). Such dislocations are readily seen in this investigation in Figure 160. However, according to Irvine et al (157) (and observed in Figure 160), the dislocation density generated by the α and γ phases seem rather too small to cause significant increases in proof stress.

Solid Solution Strengthening

The effect of various elements on the change in lattice parameter of austenite per atomic % alloying elements and the strengthening coefficient on the same basis, are shown in Figure 161. Increasing lattice distortion leads to an increased solid-strengthening for ferrite stabilizing elements and interstitials solutes, e.g. C and N (46,157). However, austenite stabilizers, e.g. nickel, show negligible strengthening (46). Despite this, the evidence in this investigation indicated by the regression equation suggests that Pd (an austenite stabilizer) has a significant solid-solution strengthening effect accorded by the lattice distortion.(Pd and Ru have atomic radii of 137 and 135 pm respectively). Ru partitions only slightly to γ, and is shown to have a negligible solid solution-hardening effect in this study. The regression analysis calculated in Figure 159, allows for the strong sinergistic effect of Pd with . Pd increasing the partitioning of Cr to ferrite. Ni has not been used in the regression analysis since its effect is known to be negligible (46).

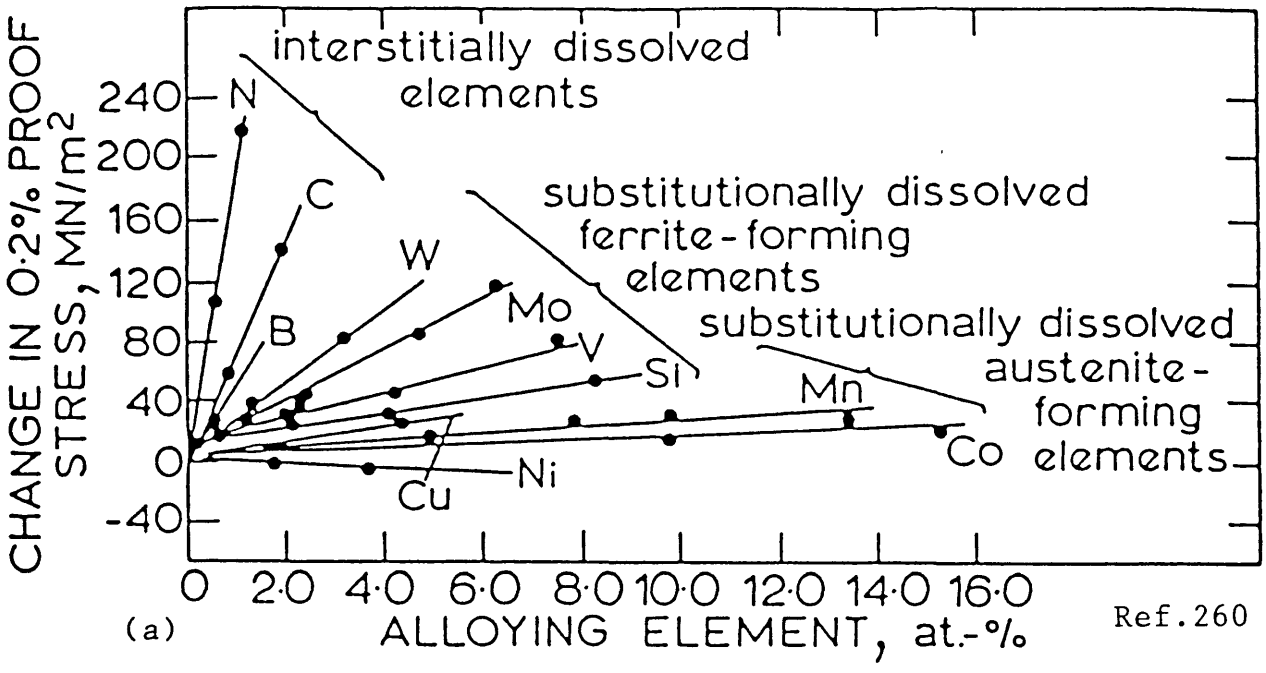

(a) Ref.260

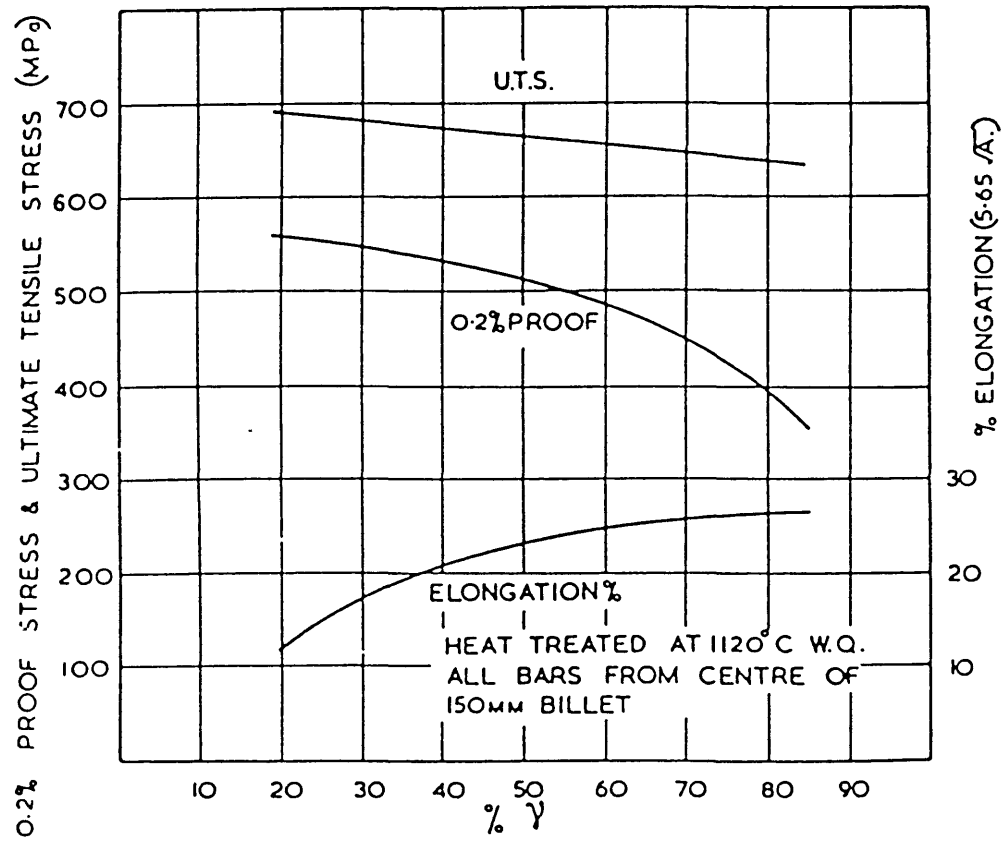

(b)

The effect of α/γ phase balance on the room temperature thick section tensile properties.
Alloy composition-25Cr, 0·04C, 0·1N_2, 2Mo, 3-9Ni wt% Ref.231

Martensite

It is unlikely that any martensite was formed during the tensile test in the steels used for the regression analysis up to strains of 0.2%. Consequently the 0.2% proof stress value for these steels will not be influenced by the formation of strain-induced martensite. Moreover as already mentioned Irvine et al (157) have reported that up to 35% martensite prior to deformation does not significantly affect the proof stress.

(v) Effect of PGMs on Tensile Strength

The various factors controlling the tensile strength in these PGM modified duplex steels will now be discussed. Regression analysis was not possible since austenite twin spacing was not measured.

The effect of PGMs, Pd and Ru on the tensile strength of a duplex ternary alloy 21Cr-6Ni is shown in the true strain-true stress curves in Figure 141 and Figure 142. The ternary alloy has a UTS of 743 MPa, whilst the Ru and Pd alloys have lower values of 615 and 709 respectively. The effect of ferrite content is similar to its effect on the 0.2% proof stress, (though its magnitude is smaller) as shown by Figure 161b and reported by Irvine et al (157) i.e. a decrease in ferrite content decreases tensile strength values. Consequently the additions of Pd and Ru (which decreases the percentage of ferrite) result in a fall in the tensile strength compared to the ternary alloy. However, the Pd containing alloy is expected to have the lowest UTS value consistent with a ferrite volume fraction of 45% - that its UTS is intermediate to the Ru and ternary alloys suggests an added strengthening mechanism. The most important variable controlling the tensile strength, is the twin spacing in the austenite phase which is controlled by the stacking fault energy, SFE, which also dictates the work hardening rate (157). The implication for the above observations is for the 21Cr-6Ni-2Ru alloy to have a marginally higher SFE than the 21Cr-6Ni-2Pd alloy. This creates only a small number of dissociated dislocations and aids cross slip. This results in a higher work hardening rate for the Pd containing alloy as is in fact seen in Figure142- this increases the tensile strength.

The effect of prior martensite content on the tensile strength is complex (157) but depends on the stability of the austenite and increases linearly according to: tensile strength $MN/m^2 = 15.4[T_c + 120+0.82t\%M)]$ (261)

where T_c = tensile strength from regression equation, and
%M = Percentage of martensite prior to tensile testing.

In all cases the ductility (Figures 141 and 142) does not vary greatly with PGM additions although it is interesting to note that Ru increases ductility somewhat. This observation is in contrast to the reported literature (112), which suggests that PGMs have a detrimental effect on the ductility of steels. The behaviour of the 21Cr-6Ni-2Ru alloy in the present study may be associated with the generation of strain-induced martensite, since as shown in the previous chapter, in Figure 133, at this level of alloying addition, Ru retards α' formation marginally more than Pd with increasing strain, and would therefore be comensurate with increased ductility.

(vi) Effect of PGMs on the Strain-hardening Exponents

The stress-strain curve of many metals in the region of uniform plastic deformation can be expressed by the simple power curve relation:

$$\sigma = k\varepsilon^n \qquad (262)$$

where n is the strain-hardening exponent and k is the strength coefficient. These values of n and k are shown in Figure 162 determined from solution treated and aged alloys in this investigation.

Figure 162.

Alloy	Condition	n exponent	k MPa
21/6	Annealed at 1250°C	0.26	1906
21/6/2Ru	"	0.23	1413
21/6/2Pd	"	0.22	1585
21/6	Annealed and Aged at 700°C	0.48	3020
21/6/2Ru	"	0.38	1259
21/6/2Pd	"	0.40	1622

The γ-austenite in the duplex structure of these alloys is metastable and transforms to martensite during plastic deformation. This transformation is illustrated in Figures 146b and c. Within γ there are twinned regions containing martensite. Figure 162 shows that the addition of Pd and Ru alloying elements results in a decreased work hardening exponent. This suggests that Pd and Ru additions increase the stacking fault energy of the austenite, and confer increased γ stability for a given deformation. The n values in Figure 162 indicate that Pd has a marginally stronger effect than Ru in reducing strain (work) hardening. However, there are two factors influencing the

extent of work hardening:

a) The stacking fault energy of the austenite determined by the composition (24).

b) The stability of the austenite.

It is the austenite stability which has the largest effect on n (24) (i.e. $\gamma \rightarrow \alpha'$ transformation). This then further suggests that Pd and Ru have the largest effect on the work hardening of duplex steels by conferring increased austenite stability. The implications are, for situations and applications where austenite stability and sustained ductility are essential, e.g. deep drawing. The following general requirements are necessary for good deep drawing behaviour (46):

a) The grain size should be coarse.

b) There should be a low work-hardening rate, i.e. a high stacking fault energy and enhanced γ stability. This can be achieved by high nickel or copper contents, and by keeping nitrogen and carbon to a minimum.

c) Solid-solution hardening should be at a minimum.

Ageing at 700°C considerably increases the work hardening exponent n in Figure 162, and is shown in the stress-strain curves in Figure 144. This increase in n is not solely due to σ precipitation as it is reported that σ does not affect this parameter (263). Figures 144 and 145 show that the increase in n is due to α'-martensite formation within the austenite phase, the effect being greatest for the ternary alloy.

As mentioned earlier the metastable nature of the austenite phase enables it to transform to martensite when deformed. This transformation plus strain hardening of austenite before transformation and the strengthening effect of the martensite formed during the transformation, is complex but contributes appreciably to the alloys plastic behaviour. Ludwigson and Berger (264) proposed a model for such behaviour. If strain is designated by e, then the volume fraction of martensite VFM resulting from the application of a particular strain is given by:

$$VFM = \left(1 + \frac{e^{-B}}{A}\right)^{-1}$$

and the true stress σ resulting from a particular strain is given by:

$$\sigma = k[\ln(1+e)]^{n}(1-VFM) + C(VFM)^{Q}$$

k and n describe austenite strain hardening discussed in the earlier part of this section: k is termed the austenite strength factor and

n is termed the austenite strain-hardening index. A measures the propensity to transform and B measures the autocatalytic nature of the martensitic transformation. C and Q express the strengthening effect of the martensite formed: C is the martensite strength factor and Q is the martensitic strengthening index. The above relationships provide a reasonable measure for compositional variations on strain-hardening and strain-induced martensite.

(vii) Ageing Characteristics

The effect of ageing on the mechanical properties of duplex steels, particularly the deleterious effects on toughness, is well documented (60-63), and shown in Figure 163. In this investigation the effect on 0.2% proof stress, % elongation, and strain-hardening exponent are examined when alloys 21Cr-6Ni, 21Cr-6Ni-2Pd, and 21Cr-6Ni-2Ru are aged between 650 and 950°C. Results are shown in Figures 143-145, 147. Figure 143 shows the effect of ageing at 900°C on 0.2% proof stress and % elongation. The behaviour is consistent with the precipitation of σ phase in reducing ductility and having a minimal effect on σ_{PS}. The ternary alloy and those containing Pd and Ru show a slight increase in proof stress values with increasing ageing time at 900°C. The effect of σ precipitation in Uranus 50 is also shown. The Pd alloy has a slightly decreasing proof stress at times greater than 1000 minutes. The behaviour may be explained by σ precipitation at short times, whilst the Pd containing alloy develops a large fraction of γ_2 with time which marginally reduces strength levels. The effect on % elongation in Figure 143b is slightly more marked with a loss in ductility between 10 and 100 minutes; thereafter ductility levels off only increasing slightly in the Ru containing alloy after ≃1000 minutes. The commercial duplex alloy experiences a substantial reduction in ductility compared to the 3 experimental alloys, losing a third of its ductility after ≃7000 minutes ageing at 900°C. The loss in ductility in these alloys is associated with the embrittling effect of σ precipitation (60-63) having a greater effect on % elongation than 0.2% proof stress. The decrease in elongation to fracture is greatest for the ternary alloy and least for the Ru containing alloy, the Pd alloy being intermediate. The fact that both the PGM alloys maintain higher ductilities is associated with inherent higher γ volume fractions at this temperature conferring more ductility.

The Effect of Aging on the Tensile Properties In Duplex Steels.

Specimen No	Orientation	Annealing Temp	Aging Conditions	σ_y (2%) Ksi	σ_y (2%) MPa	σ_{uts} Ksi	σ_{uts} MPa	Strain to Max Load %	$\frac{\Delta A}{A}$ %
40	L	1375 °C	None	69 4	478 5	85 3	588 1	2 3	26 3
36	L	1375 °C	700 °C-0 167 hr	98 6	679 8	115 6	797 0	10 7	41.6
407	L	1375 °C	700 °C-0 5 hr	100 5	692.9	107 5	741 2	10 0	42.0
462	T	1375 °C	700 °C-2 hr	90 4	623 3	112 6	776 4	6 5	31.0
37	L	1375 °C	700 °C-8 hr	96 8	667 4	114 6	790 1	11 3	37 4
464	T	1375 °C	700 °C-24 hr	96 1	662 6	157 0	1082 5	5.9	15 0
38	L	1375 °C	700 °C-100 hr	33 4	230 3	36 9	254 5	1 9	*
42	L	1375 °C	600 °C-0 5 hr	75 6	521 2	100 2	690 9	14 9	58 7
43	L	1375 °C	600 °C-8 hr	103 5	713 6	136 2	939 1	9 5	56 5
1061	L	1150 °C	None	56 0	386 1	87 0	599 8	27.0	80 0
1075	L	1150 °C	600 °C- 0 167 hr	65 5	451.6	98 8	681 2	31 9	76.6
1076	L	1150 °C	600 °C-1 hr	68 3	470 9	99 5	686 0	30 3	70 4
1077	L	1150 °C	600 °C-24 hr	73 4	506 1	106 7	735 7	27.2	60 5
1078	L	1150 °C	600 °C-100 hr	72 7	501 3	108 8	750 2	24 6	59 7
449	L	1100 °C	700 °C-0 5 hr	53 6	369 6	91 7	632 3	29 2	74.2
473	T	1100 °C	700 °C-0 5 hr	50 7	349 6	97 8	647 3	29.1	67.3
450	L	1100 °C	700 °C-2 hr	50 7	349 6	93 7	646 0	31 0	73.2
475	T	1100 °C	700 °C-2 hr	56 3	388 2	99 5	686 8	28 0	64 0
474	T	1100 °C	700 °C-24 hr	58 3	402 0	112 3	774 3	11 9	16 0
404	L	1100 °C	700 °C-24 hr	60 0	413 7	102 5	706 7	9 0	21 0
1079	L	1150 °C	700 °C-100 hr	82 9	571 6	116 5	803 2	6 5	23 2

* Failure in the specimen shoulder

BULK ALLOY COMPOSITION AND COMPOSITION OF α AND γ PHASES FOR A SPECIMEN FABRICATED AND HEAT TREATED AT 1150 °C (HEAT NO. 83826)

	Composition[a], Percent by Weight												
	Fe	Cr	Ni	Mo	Cu	Mn	Si	C	N	S	P	B	Ti
α	65 3±0 1	24 0±0 1	5 3±0 1	3 1±0 1	1 1±0 1	0 66±0 080	0 40±0 02		.		..	...	...
γ	68 1±0 5	19 5±0 1	8 3±0 1	2 0±0 1	1 6±0 1	0 59±0 03	0 44±0 02	.	.	...	..	..	...
Bulk Alloy	Balance	21 08	7 38	2 39	1 33	0 62	0 45	0 032	0 071	0 021	0 022	0 003	<0.01

a Bulk alloy composition (average of mill certification and laboratory analysis).

Figure 163. Ref.212

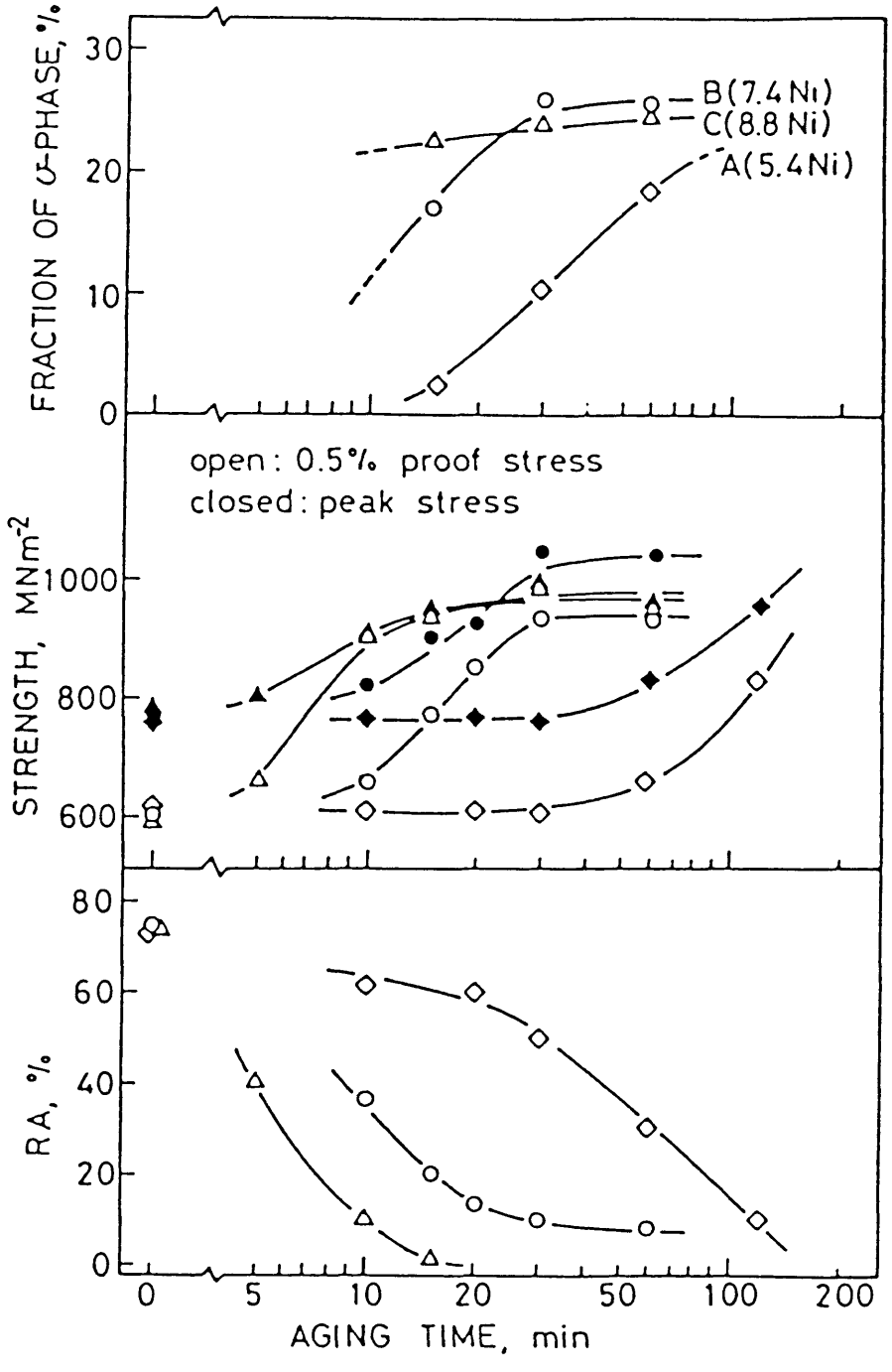

Variation of σ-phase volume fraction and room-temperature tensile properties with aging time at 1 073 K; specimens solution treated at 1 323 K for 30 min, water quenched, and aged in salt bath

Steel	C	Si	Mn	P	S	Cr	Mo	Ni	Cu	N	W	/wt%
A	0·024	0·45	0·81	0·009	0·005	24·4	2·76	5·47	0·38	0·130	0·21	
B	0·028	0·44	0·78	0·010	0·005	24·3	2·74	7·27	0·39	0·137	0·20	
C	0·022	0·46	0·79	0·010	0·005	24·1	2·78	8·79	0·39	0·128	0·22	

Figure 164. Ref.265

Maehara et al (265) have determined the effect of ageing time at 800°C on the room temperature tensile properties of steels relating these to the fraction of σ-phase formed in Figure 164. With increasing ageing time, the strength of each steel increased, but the ductility decreased in keeping with the progress of ferrite decomposition; $\alpha \rightarrow \sigma + \gamma$. The authors (265) commented that such variations were reduced markedly by decreasing the nickel content. Figure 163 lists duplex tensile results from Solomon (212) of specimens aged at 600°C and 700°C. Ageing the duplex structure (established at 1130°C) does not appreciably influence the tensile properties of the $\alpha + \gamma$ duplex structure unless a considerable amount of sigma phase is produced which occurs at 700°C after 24 hours, when the tensile ductility is greatly reduced. Ageing of these at 600°C and 700°C also produces α' (bcc Cr-rich precipitate) and γ_2 phases. This caused an increase in yield strnegth, UTS, strain to maximum load and % reduction in area, compared to a ferritic steel. In the present investigation the effect of phase precipitation on the tensile ductility is shown graphically in Figure 145. Ageing for 10 minutes between 650°C and 950°C shows the three experimental alloys and Uranus 50 to initially lose ductility at 700°C before increasing with γ_2 precipitation and tending to level off for the ternary and Uranus 50 alloys up to 950°C. This marked effect is seen more readily in Figure 144, where the substantial loss in ductility at 700°C (10 mins.) is also observed to be associated with a rapid increase in work hardening. The precipitation of σ-phase does not give an adequate explanation for this behaviour since the TTT C-curves in Figure 101 show that <5% σ is present in these alloys at 700°C (10 mins.). The strain hardening exponent, n for these alloys aged at 700°C for 10 minutes (Figure 162), confirms that extensive work hardening in the γ phase (212) is attendent with this loss in tensile ductility. Solomon and Devine (263) have shown that the strain hardening exponent, n, is not altered when σ precipitates in the α phase. This is not surprising since the work hardening of duplex steels is determined primarily by the γ phase. Microstructural evidence in Figures 145 and 146 show that γ has become unstable and strain induced martensite forms giving rise to the rapid work-hardening and loss in tensile ductility seen in Figure 144.

(viii) Mode of Failure

The mode of fracture and failure of annealed tensile specimens was

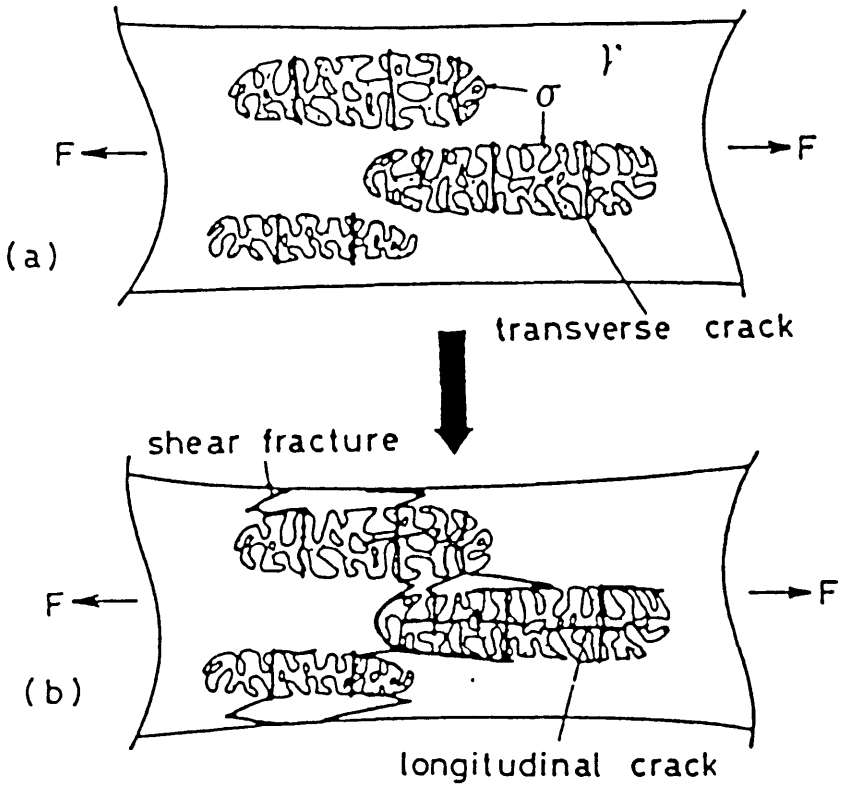

a initiation; *b* propagation

Proposed mechanism of microcrack development during low-temperature deformation in structure consisting of thin austenite and σ-phase–austenite cellular layers

Figure 165. Ref.255

fully consistent with the duplex structure. For the ternary alloy and those containing Pd and Ru, there were ductile, fibrous regions of γ separated by α grains which had failed in a more brittle manner revealing cleavage facets (Figure 147b). The metastable behaviour of austenite during tensile testing was evident, and Figure 146 shows this transformation of $\gamma \rightarrow \alpha'$. Whether the transformation of the austenite to martensite plays an important role in preventing cleavage is hard to say. The ability of the austenite to transform to martensite would be helpful in that the volume expansion would tend to relieve the hydrostatic tensile stresses ahead of a crack. This effect might help to some extent in preventing the initiation of cleavage (59). The implication for Pd and Ru alloying additions is for increased austenite stability and hence less resistance to cleavage in α grains. Floreen and Hayden (155,156,159) have noted that the major effect of austenite in a duplex structure is to prevent the propagation of cleavage cracks by either blunting or delaying crack propagation.

The irregular convoluted nature of the cross-section of the tensile specimen suggests that either (a) the longitudinal crack propagation, parallel to the tensile straining, is accompanied by transverse microcracks linking α and metastable γ phases, or (b) crack propagation through the duplex structure is aided by delamination of twin and grain boundaries perpendicular to the tensile direction. The explanation in (b) seems most likely as no evidence of transverse microcracks was established. Floreen and Hayden (155,156,159) have, however, observed transverse microcracks in duplex structures. Their occurrence increased with decreasing test temperature, and followed either the ferrite or the ferrite/austenite interfaces. It is believed that if the duplex structure were orientated perpendicular to the tensile direction, failure and fracture would occur by the delamination of α and γ phase bands. Solomon and Devine however report that duplex steels do not exhibit a marked tensile anisotropy (59).

Ageing the alloys in the present investigation at 700°C results in a brittle fracture seen in Figure 147. Cleavage facets predominate resulting from martensite transformation in austenite, and as such does not substantiate reports (156,159) that martensite formed in γ prevents cleavage failure. In the present investigation it was difficult to assess the effect of σ on the fractography of aged specimens, though its presence does result in a loss in ductility at 900°C in

Figure 143. Maehara et al (265) have proposed a model for this failure of aged duplex structures containing σ shown in Figure 165. Transverse microcracks across the σ-phase/austenite cellular structure form in the initial stage of deformation, Figure 165a, and these microcracks are linked by large cracks which are formed by either the brittle fracture of the cellular structure or the decohesion of the matrix/cellular structure interfaces parallel to the tensile direction. The final fracture, Figure 165b, takes place by the shear fracture of thin austenite layers. The tensile ductility is obviously dependent on the prior morphology of austenite/ferrite duplex structure and Maehara et al (265) propose that ductility is improved by either increasing the thickness of the austenite layers prior to σ precipitation or by ensuring that there is a homogeneous and fine distribution of σ-phase in the parent austenite phase.

8.2.2. Hardness Variations

(i) As-Cast Alloys (see Figure 148)

The variation in hardness for as-cast alloys is fully consistent with the structure and distribution of α and γ phases. Alloys, 18/6/2Pt, 21/6/8Ru, 18/6/2Ru and 21/6/2Pd have the highest H_V values consistent with a ferritic mode of solidification such that the structure is dominated by ferrite grains with γ occupying α grain boundaries. (Ferrite has a hardness value of ≃260 and austenite ≃230 (217).) The structures which have solidified austenitically, e.g. 18/6/8Pt, 18/6/8Pd and 21/6/8Pd are dominated by primary γ dendrites with ferrite occupying intercellular spaces. These structures consequently have lower hardness values.

(ii) Annealed Alloys (see Figures 149 and 150)

As suggested from the results, the hardness values for the 18/6 series show that:

a) at the 2% PGM level, Ru > Pd > Pt (except at 1300°C).

b) at the 8% PGM level, Ru > Pt > Pd

For the 21Cr-6Ni alloy series, the greatest increase in hardness is achieved by: Ru > Pt > Pd.

These variations in hardness are dictated by the volume fraction of phases such that the Ru containing alloys are dominated by the harder ferrite phase whilst Pd and Pt alloys are dominated by the softer, γ-austenite phase.

8.2.3. Anodic Polarisation Characteristics

The most notable effect of Ru and Pd noble metals on the anodic polarisation characteristics of alloys 21Cr-6Ni and Uranus 50, is a general shift in the pitting potential, and a lowering of the current density necessary to achieve and maintain passivity in the solution of 1N.H_2SO_4 at 25°C in Figures 155 and 156. Whilst these movements are significant, of themselves they cannot be said to be more than marginal in improving corrosion resistance in these steels. However, they are fully consistent with findings of other workers (111,112).

Related to the observed anodic polarisation characteristics, is the formation of microcathode sites on the metal surface, by the additions of PGM. This process will raise the anode potential to induce passivity by increasing the cathodic reaction of hydrogen evolution. The convoluted section of the anodic polarisation curves (Figure 156) over the passive potential regime does indeed suggest a certain degree of instability of the passivating film, indicative of the formation of noble microcathodic sites. Further to this phenomena, was the observation that when a PGM containing alloy was initially immersed in the acid solution, the alloy potential was found to be negative, but changing over a period of a few hours to a positive potential. Thus the significant effect of Pd and Ru on these duplex alloys is improving the efficiency of the cathodic reaction, and in particular as suggested by Hoar (134) the corrosion performance of these alloys in non-oxidising media is considerably modified by virtue of the unique behaviour of PGMs in reducing the hydrogen overpotential.

8.2.4. Isothermal Oxidation Behaviour

(i) Effect of Alloy Compositions on Oxidation Behaviour

On the basis of the type external scales produced during oxidation, Croll and Wallwork (151) classified the ternary Fe-Ni-Cr alloys into four broad composition ranges as follows:

I, Alloys containing <20% Cr and <20% Ni whose external scales are characterised by an outer layer of Fe_2O_3 and inner layer of $Ni_xFe_{(3-x)}O_4$ spinel: the oxidation rates are very high.

II, Alloys containing <20% Cr and 20-60%Ni. Alloys of this type exhibit lower oxidation rates than type I alloys and are characterised by the formation of complex external scales consisting of 'islands' of Fe_2O_3, $NiFe_2O_4$ spinel and NiO in this order from the scale/atmosphere interface.

III, Alloys containing <20%Cr and <60%Ni. This group of alloys oxidises at a slower rate than either the type I or II alloys. The major components of these scale are an inner and outer layer of NiO between which is a thin layer of stoichiometric $NiFe_2O_4$ spinel.

IV, Alloys containing >20%Cr. These alloys are characterised by very slow oxidation rates. This is due largely to the formation of scales, consisting primarily of chromic oxide.

It should be stressed that the divisions between the ranges are only approximate and there may be some overlapping of oxidation behaviour for those alloys whose compositions lie close to the edge of a range. A diagramatic summary of the above classification is given in Figure 166. The ternary alloy composition in this investigation, 21Cr-6Niwt%, is marked and its position lies marginally in IV, near the border of range I.

Results in Figure 151 show that the isothermal oxidation behaviour of alloys in this investigation to follow more closely than expected, the behaviour of alloys in range I. These alloys are characterised by very high oxidation rates conforming to a linear oxidation rate. The actual ternary alloy composition lies marginally in range IV of Figure 161, defined by Croll and Wallwork (151), but the oxidation behaviour is clearly at variance with the behaviour of these alloys which show a parabolic rate oxidation. However, Croll and Wallwork (151) do indicate that considerable overlap of behaviour does exist for alloys near to the border of ranges as is the case in this study, since iron oxide protrusions (typical in Range I) do give way to a granular Cr-rich scale (typical in Range IV) in Figure 154.

(ii) Effect of Pd and Ru

The isothermal oxidation of alloys 21Cr-6Ni and 21Cr-6Ni-2Ru and 21Cr-6Ni-2Pd at 1000°C in air has produced essentially a linear oxidation rate, described by the linear rate equation: $x = k_L t + C_L$ (266)

where x = oxide thickness

k_L = linear rate constant

C_L = constant.

This equation is observed under conditions where a phase boundary process is the rate determining step for the reaction (266). Superimposed on this rate, particularly for the Ru alloy in Figure 151a, is a parabolic thickening film which is continually fracturing.

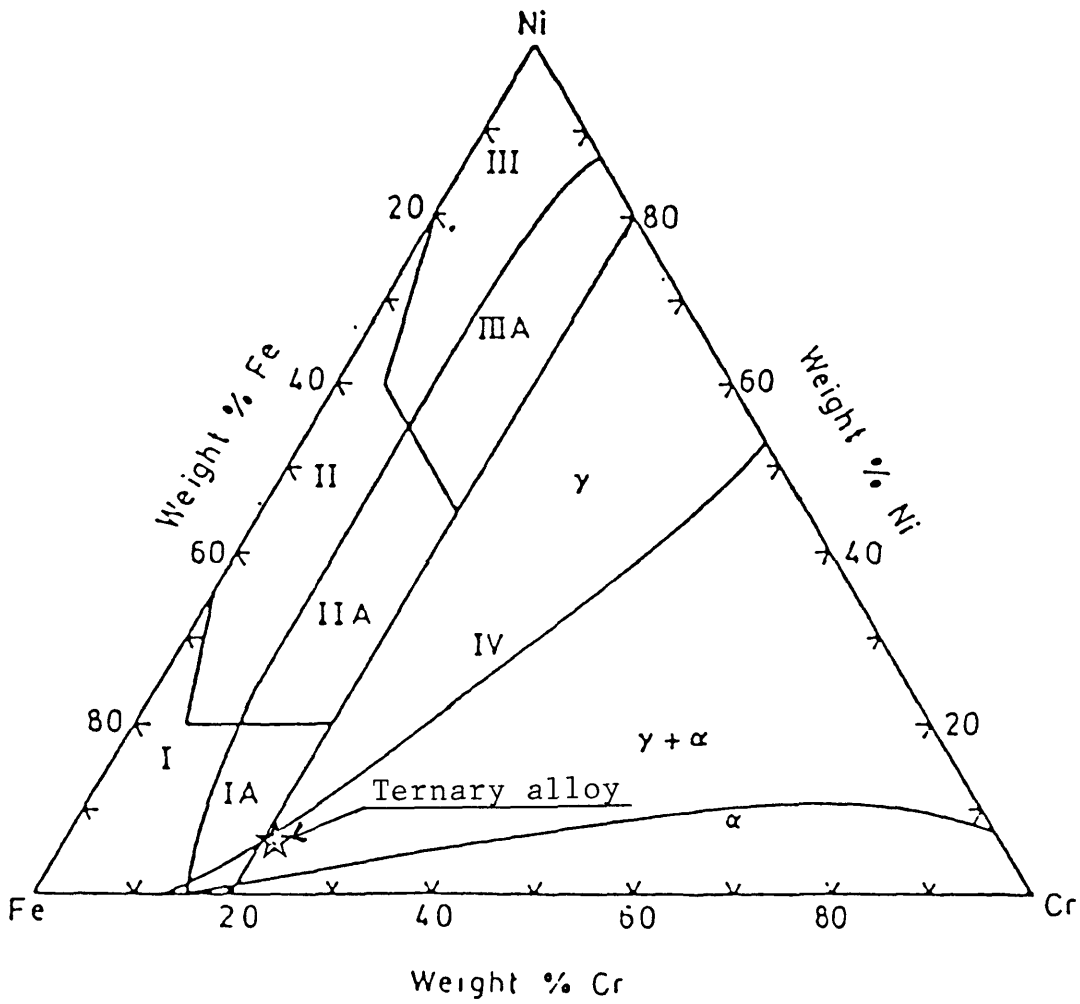

Diagrammatic classification of the Fe–Ni-Cr alloys into types I, II, III and IV

Figure 166. Ref.161

The effects of Pd and Ru in this investigation are not substantial; the Ru containing alloy having a marginally increased oxidation rate and the Pd alloy having a reduced rate compared to the ternary alloy. These observations are consistent with the oxidation behaviour of Ru and Pd metals which have different oxidation rates governed by their affinities for oxygen (267). Ru oxidises more rapidly than Pd by the formation of highly volatile gaseous species. The implication is for duplex steels containing Ru to have increased oxidation conferred by the formation of volatile RuO_3 or RuO_4 which have high partial pressures. Whereas Pd up to $\simeq 1000^{o}C$ develops a much more stable oxide PdO, with a low partial pressure and a resultant low oxidation rate. Concerning duplex steels, Holm et al (268) have shown that Cr is more mobile in the ferrite phase than the austenite, and that the oxide formed on the ferrite phase constituent has an outer surface rich in Fe, but whose lower part is Cr-rich. This suggests that a critical effect of Pd and Ru PGMs on the isothermal oxidation of duplex steels will be whether they increase or decrease the mobility of chromium in the ferrite phase; such that the oxide forming on the ferrite phase grows faster than that on the austenite phase.

This would lead to the depletion of one of the phases in the parent metal substrate and the faster growing oxide could lift the slower forming (and thus thinner) oxide layers, off the surface, leading to porosity. Figure 151b shows that such porosity is prevalent in the Ru containing alloy which has undergone considerable breakaway during isothermal oxidation. In addition, since the growth of oxides is governed by a non-stoichiometry of ionic species (266) an important factor influencing oxidation rates, will be whether Pd or Ru increase the defect structure of Cr_2O_3 or Fe_2O_3 oxides creating n- or p-type defects and thereby increasing the mobility of Fe^{2+} or Cr^{3+} ions, increasing the oxidation rate. This study has shown that Ru marginally increases oxidation rates whilst Pd decreases them in duplex steels; the observed behaviour cannot be conclusively explained, but the above proposals are thought to be significant.

CHAPTER 9

Conclusions and Proposals for Future Work

My pen is at the bottom of a page
which being finish'd, here the story ends;
Tis to be wish'd it had been sooner done,
But stories somehow lengthen when begun.

(Byron)

1. The solidification reactions and subsequent solid state changes of alloys 18Cr-6Niwt% and 21Cr-6Niwt% is altered by additions of PGMs. At the 2wt% level, Pt, Pd and Ru additions cause an increase in the volume fraction of Widmanstatten γ precipitating by a solid state reaction at primary α-ferrite grain boundaries. The alloys all solidify ferritically. At the 8wt% alloying level, Pt and Pd promote an austenitic mode of freezing, whilst Ru-containing alloys develop primary grains of ferrite. Often associated with austenitic freezing of PGM containing alloys, is a divorced eutectic of $\alpha + \gamma$ phases formed during the terminal stages of freezing. The implications of these findings are for situations where weld stability are required; Pt and Pd PGMs in particular, are likely to promote hot-cracking by favouring austenitic freezing.

2. At the 2wt% level, Pt, Pd and Ru have only marginal effects on the shape distribution and volume fraction of austenite, and generally increase the γ phase content in the temperature range 1000 - 1300°C. At the 8wt% PGM level austenite is the primary phase, with in general Pt > Pd > Ru in promoting austenite formation. Pt, Pd and Ru partition to the austenite phase with Ru partitioning less strongly than Pd and Pt. The partitioning of these PGMs is accompanied by: (a) an increase in the level of nickel partitioning to the austenite phase, (b) an increase in the level of chromium partitioning to the ferrite phase. This synergistic behaviour of PGMs with Cr and Ni is quite marked, and dictates much of the structural and property behaviour studied in the present work, e.g. the variations in austenite stability, σ formation and tensile behaviour.

3. The addition of 2wt%Pd and Ru to the duplex ternary alloy 21Cr-6Niwt% results in an increased rate of precipitation of sigma phase over the temperature range 650 to 950°C from 5 minutes to 5 days ageing. This is due to the synergistic effect of Pd and Ru to increase the level of Cr partitioning to α-ferrite. The much reported eutectoid decomposition of $\alpha \rightarrow \sigma + \gamma$ appears to be correct since analysis by the Johnson-Mehl/Avarami equation in the present work indicate n values to be more than 1, consistent with the growth of 'thickening' sigma plates via a eutectoid growth of σ and γ phases. The precipitation of lamellar mixtures of phases in the present work has been identified as a sympathetic nucleation and growth of $\gamma + \sigma$ phases from α phase.

4. The effects of PGMs on bulk martensite formation in duplex steels in the present work are as follows. Pt, Pd and Ru additions confer increased stability on austenite. In the 21Cr-6Niwt% alloy series, Pd > Ru > Pt at the 2 and 8wt% level. In the 18Cr-6Niwt% alloy series Pt > Pd > Ru at the 2% level whilst at the 8% level Pd > Pt > Ru. The effect of PGMs on austenite stability is a consequence of depressed M_s temperatures and lowering $\Delta H^{\alpha' \rightarrow \gamma}$ (and hence lower T_o) to more negative values. Specifically these effects are due to (1) the synergistic behaviour of Pd, Pt and Ru with Ni such that γ is stabilized by enrichment in Ni, and (2) the inherent stabilizing effect of Pt, Pd and Ru themselves in γ. The effect of PGMs on the γ SFE was inconclusive as no microstructural measurements were made, but the extensive occurrence of hcp ε-martensite in particular, suggests that the SFE was low, typically $\sim$15 mJm^{-2}. The occurrence of ε-martensite prior to α'-martensite in alloys containing 8wt% PGM suggests the γ SFE is lowered by such additions. Rational orientation relationships were identified for structures containing martensite. Although the conventional α'-martensite predominated in PGM containing alloys, surface and plate martensites are identified in alloys 18Cr-6Ni-8Pd and 21Cr-6Ni-8Pd respectively. The kinetics of strain induced α' in PGM containing alloys follow a sigmoidal relationship between strain and $\%\alpha'$ formed. Of the three PGMs studied, in the 21Cr-6Ni alloy series, Ru confers the greatest γ stability at the 2wt% level for deformation at room and -196°C whilst Pd is the most effective PGM at the 8wt% level, stabilizing γ with increasing strain. Of the 3 PGMs in the 18Cr-6Ni alloy series, Pd confers the greatest γ stability at the 2 and 8wt% levels for deformation at room and -196°C temperature.

5. The isothermal oxidation of alloys 21Cr-6Niwt%, 21Cr-6Ni-2Pdwt% and 21Cr-6Ni-2Ruwt% at 1000°C in air has produced essentially a linear oxidation rate. The effects of Pd and Ru are not substantial, the Ru containing alloy having a marginally increased oxidation rate and the Pd alloy having a reduced rate compared to the ternary alloy. These variations are believed to be due to the inherent higher oxidation rate of Ru and lower oxidation rate of Pd. It is recommended that a fundamental scientific study be made to identify precisely where PGMs are located and enriched during the formation of a stable chromic oxide scale in Fe-Ni-Cr alloys. In addition the synergistic effect of Pt, Pd and Ru on the mobility of Cr, possibly increasing the defect structure of Cr_2O_3 or Fe_2O_3 oxides, is considered highly significant and worthy of detailed characterisation.

6. The most notable effect of Ru and Pd on the anodic polarisation characteristics of alloys 21Cr-6Niwt% and Uranus 50 is a general shift in the pitting potential and a lowering of the current density necessary to achieve and maintain passivity in a 1N H_2SO_4 solution at 25°C. The accepted basis for this behaviour is associated with the high exchange current density for the cathodic reaction on the noble metals in question. Although these effects are interesting, of themselves, they do not constitute further lengthy studies. Moreover, reported literature suggests that there can be no justification in pursuing a detailed investigation into the effects of Pt and Pd on the corrosion performance of steels. However, the effect of Ru on the stress corrosion cracking resistance of duplex steels in chloride environments may be beneficial on a cost effective and performance basis, and therefore worthy of attention.

7. The variations in hardness of as-cast and annealed PGM containing alloys are dictated by the volume fractions of α and γ phases, such that Ru containing alloys are generally harder, being dominated by the harder α phase. The Pd and Pt alloys are dominated by the softer γ phase, and have lower hardness values.

8. The tensile behaviour of alloys 21Cr-6Niwt%, 21Cr-6Ni-2Pdwt%, 21Cr-6Ni-2Ruwt% and Uranus 50 indicate that the effects of Pd and Ru on proof stress are marginal. Pd increases the proof stress in ternary alloys due to a substantial solid solution strengthening effect, whilst Ru causes a decrease in proof stress. Both Pd and Ru PGMs decrease the UTS due largely to a reduction in α' compared to the ternary alloy. The Pd alloy has a higher UTS than the Ru alloy associated with a higher SFE and increased γ stability. Ru causes a marginal increase in ductility in the ternary alloy due to a retardation of strain-induced martensite. Pd, however, causes a decrease in ductility consistent with the reported effect of PGMs in steels. Pd and Ru increase the stability of γ - the strain hardening exponent, n, reduced by both elements, indicates that Pd has a marginally stronger effect than Ru in reducing strain-hardening in γ.

Ageing the above alloys, at 700°C for 10 minutes and rapidly cooling to room temperature, increases n in each alloy due to the transformation of metastable γ to α'. Such thermal treatment shows how extensive work-hardening in the γ phase is attendant with a marked loss in ductility.

Ageing for times of up to 5 days between 650 and 950°C results in σ precipitation, this produces a reduction in room temperature ductility and marginal increase in proof stress. The loss in ductility in PGM containing and ternary aged alloys is associated with the embrittling effect of σ. The decrease in ductility with ageing is greatest for the ternary and Uranus 50 alloys. Both PGM containing alloys maintain higher ductilities than the ternary alloy due to inherent higher γ volume fractions.

Of possible interest for future work is the effect of up to 2wt%Ru on the strength and ductility of high ductility, TRIP steels. Whilst strength levels are not necessarily improved by Ru, ductility may be increased by reducing strain hardening in γ and retarding strain-induced martensite. This control of transformation kinetics together with a beneficial corrosion influence from Ru, may make it a candidate alloying addition to high strength, high ductility TRIP steels, in their use as implant materials, where high mechanical integrity and all round corrosion resistance to body fluids is of vital importance. The detrimental effect of σ precipitation would therefore warrant further investigation.

REFERENCES

1. M.J. Matthews: The Metallurgist and Materials Technologist, pp.205-210, (May 1982).
2. R. Kiessling: Metals Technology, 11, pp.169-180, (May, 1984).
3. M. Kowaka et al: Sumitomo Search, 15, pp.64-77, (Nov. 1976).
4. S.O. Bernhardsson et al: NACE, Corrosion 80, paper 14, pp.1-28.
5. G. Herbsleb and R.K. Popperling: NACE, Corrosion 80, paper 13, pp.1-21.
6. C.W. Corti et al: Platinum Metals Review, 24, 1, pp.2-11, (Jan. 1980).
7. R.G. Wing and I.R. McGill: Platinum Metals Review, 25, 3, pp.2-13, (July 1981).
8. A.G. Knapton: Platinum Metals Review, 23, 1, pp.2-13, (Jan. 1979).
9. V.G. Rivlin and G.V. Raynor: Int. Met. Rev., No. 1, pp.21-38, (1980).
10. F.A. Shunk: 'Constitution of binary alloys', 2nd Suppl., New York, (1969).
11. R.P. Elliott: 'Constitution of binary alloys', 1st Suppl., McGraw-Hill, (1976).
12. M. Hanson and K. Anderks: 'Constitution of binary alloys', McGraw-Hill, (1958).
13. R. Rant et al: Z. Metallk., 54, pp.549-552, (1963).
14. A. Kaussumann and K. Jassen: Z. Metallk., 54, pp.504-510, (1963).
15. A. Cottrell: 'An Introduction to Metallurgy', pp.514-16, (1967).
16. T.F. Connelly and E.D. Copenhanur: 'Bibliography of magnetic materials and tabulation of magnetic transition temperatures', IFI/Plenum, (1972).
17. A.H. Sully and E.A. Brandes: 'Chromium', pp.77-82, 2nd edition, Butterworths (1967).
18. W.B. Pearson: 'A handbook of lattice spacings and structure of metals and alloys', 2, Pergamon Press, (1958).
19. E. Saristsky et al: 'Physical Metallurgy of PGMs', translated by I.V. Savin, MIR Pub., Moscow.
20. F. Muller and O. Kubaschewski: 'High temperature pressures', 1, pp.543-551.
21. P. Payet et al: Mem. Sci. Rev. Metall., 69, 11, pp.775-783, (1972).
22. E. Schurmann and J.Branckmann: Arch. Eisenkitenwes., 48, 1, pp.3-7, (1977).
23. W. Hume-Rothery: 'The structure of alloys of iron', chap. 5, (1966).

24. R.W.K. Honeycombe: 'Steels, microstructure and properties', Pub. by E. Arnold, (1981).
25. N.R. Roshan et al: 'New investigations of constitution diagrams of metallic systems, pp.190-196, Pub. by Nanka, Moscow, (1971).
26. E.M. Savitsky et al: 'Palladium alloys', Pub. by Primary Sources, New York, (1969).
27. M. Sundaresen et al: Zh. Fiz. Khim., pp.2462-66, (1963).
28. J. Crangle and J.A. Shaw: Phil. Mag., 7, pp.207-12, (1962).
29. R.A. Buckley and H. Hume-Rothery: J. Iron and Steel Inst. (Lond.) 193, pp.61-62, (1959).
30. E.C. Bain and W.E. Griffiths: Trans. AIME, 75, pp.166-213, (1927).
31. O. Kubaschewski and L.E.H. Stuart: J. Chem. Eng. Data, 12, 3, pp.418-420, (1967).
32. S.W. Gilby and G.R. St. Pierre: Trans. AIME, 245, pp.1749-1758, (1969).
33. A.P. Lyubimov et al: Nauch. Doklady Vyssh. Shkoly. Met., 1, pp.7-10, (1958).
34. L. Kaufman and H. Nessor: Z. Metallak., 64, 4, 24, pp.249-257, (1973).
35. L. Kaufman and H. Nessor: Metall. Trans., 5, 7, pp.1617-1621, (1974).
36. F. Kralikand and K. Kovarova: Kovove Mater., 10, pp.380-381, (1972); 11, pp.6-15, (1973).
37. J. Vrestal et al: ibid., 14, pp.481-489, (1976).
38. J.W. Pugh and J.O. Nisbet: Trans. AIME, 188, pp.268-76, (1950).
39. F.N. Rhines: 'Phase diagrams in Metallurgy', pp.151-53, McGraw-Hill, (1956).
40. F. Wever and W. Jellinghans: Mitt. Kaiser. Wilhelm. Inst. Eisenforsh, 13, pp.98-109, (1939).
41. C.H.M. Jenkins et al: ibid., 136, pp.187-222, (1937).
42. Scheider and Climax Molybdenum Co.: J. Foundry Trade, 108, p.562, (1960).
43. P.E. Price and N.J. Grant: Trans. AIME, 215, pp.635-37, (1959).
44. M. Hasebe and T. Nisihiyama: 'Applications of phase diagrams in Metallurgy and Ceramics', 2, pp.910-954, NBS. Special pub. 496, (1978).
45. J.W. Schultz and H.F. Merrick: Metall. Trans, 3, pp.2479-2483, (1972).

46. F.B. Pickering: Int. Met. Rev. (Dec. 1976).
47. K.E. Thelming: 'Steel and its heat treatment', Bafor Handbook, (1975).
48. F.C. Monkman et al: Met. Prog., 71, p.94, (1957).
49. G.H. Eichmann and F.C. Hull: Trans. ASM, 45, p.77, (1953).
50. T. Angel: ibid, 173, p.165, (1954).
51. K.W. Andrews: Metal Treatment, 19, pp.452-489, (1952).
52. B. Holms et al: B.Sc. Research Prod./PM5762.12.72/A, (June, 1972).
53. Z. Nishiyama: 'Martensitic transformations', (1978).
54. C. Zener: Trans. AIME, 167, p.550, (1946).
55. T. Williams: Proc. 6th Int. Cryogenic Eng. Conf., Grenoble, 337, (May, 1976).
56. E.C. Rollason: 'Metallurgy for Engineers', pp.258-60, 4th edition, (1973).
57. L. Columbier: Mo in stainless steels, Climax Molybdenum Company, (1968).
58. H. Weigend and M. Domk: Arch Eisenhenwin, 33, p.55, (1962).
59. H.D. Solomon and T.M. Devine, Jr.: 'Duplex stainless steels', Conf. proc. ASM edited by R.A. Lula, pp.693-756 (1983).
60. L.-Å. Norstrom et al: Z. Werkstoffech, 12, pp.229-234, (1981).
61. M.A. Snirnov et al: SB. Nauchin. Tr Chelyabinsk Politekh Inst. 229, pp.113-117, (1979).
62. A. Hoshino et al: Trans. Natl. Res. Inst. Met. (Japan), 22, pp.185-195, (1980).
63. Y. Maehara et al: J. Iron Steel (Japan), 67, pp.577-586, (1981).
64. F.G.E. Beetge and F.P.A. Robinson: Metals and Materials, 7, 9, pp. 408-413 (Sept. 1973).
65. J.S. Kasper: Acta Metallurgicia, 2, pp.455-461, (1954).
66. J. Hochmann et al: Metaux Corrosion Industries, 591-529, pp.390-423, (1974).
67. H.D. Solomon and L.M. Levinson: Acta Met., 26, pp.429-442, (1978).
68. H. Hochmann and P. Jolly: Mem. Sc. Rev. Met., 70, p.117, (1973).
69. C.S. Tedmon et al: Met. Trans., 1, p.2043, (1970).
70. W.O. Binder et al: Trans. ASM, 41, p.1301, (1949).
71. H. Smith and D.R.F. West: Met. Tech., 1, p.295, (1974).
72. S.R. Thomas and Gilkrauss: Trans. AIME, 239, p.1136, (1967).
73. A.M. Parshin and N.E. Vasil'kov: Met. Sci. Int. treatment, 21, 2, pp.44-48, (Jan.-Feb. 1979).

74. C.S. Tedmon and D.A. Vermilyea: Met. Trans., 1, p.2043, (1970).
75. T.M. Devine: J. of the Electrochemical Society,
76. F.R. Beckitt: J. Iron and Steel Inst. (Lon.), p.632, (1969).
77. P. Combrade et al: Materiaux et Techniques, No. 9/10, p.1, (Sept.-Oct. 1977).
78. J. Hochmann et al: 'Propcites des Aciers Inoxydables Ferritiques a Teneur Elevee en Chrome, Ductiles et des Aciers Austens Ferritiques', Editions Metaux, (1975).
79. F.C. Hull: Welding J., 46, pp.3995-4095, (1967).
80. Y. Arate et al: Trans. JWRI, 5, pp.35-51, (1976).
81. F. Matsuda et al: Trans. JWRI, 8, pp.105-112, (1979).
82. J.C. Lippold and W.F. Savage: Welding J., 58, pp.362S-374S, (1979).
83. J.C. Lippold and W.F. Savage: Welding J., 59, pp.485-585, (1980).
84. M.J. Cieslak and W.F. Savage: Welding, J., 59, pp.136S-146S, (1980).
85. S.A. David et al: Welding J., 58. pp.308S-336S, (1979).
86. C.D. Lundin et al: Welding J., 59, pp.226S-232S, (1980).
87. N. Suutala et al: Met. Trans., 10A, pp.512-514, (1979).
88. N. Suutala et al: Met. Trans., 10A, pp.1183-1190, (1979).
89, N. Suutala et al: Met. Trans., 11A, pp.717-725, (1980).
90. N. Suutala et al: Welding J., 60, pp.92S-93S, (1981).
91. T. Takalo et al: Met. Trans., 7A, pp.1591-1592, (1976).
92. T. Takalo et al: Met. Trans., 10A, pp.1173-1181, (1979).
93. M.J. Cieslak et al: Welding J., 61, pp.1S-8S, (1982).
94. G. Blanc and R. Tricot: Mem. Sci. Rev. Metall., 68, pp.735-53. (1971).
95. O. Hammer and U. Svensson: Mets. Soc., pp.401-10, (1979).
96. O.J. Pereira and J. Beech: Univ. of Sheffield, Dept. of Metallurgy.
97. J. Hertier and J. Levy: Mem. Sci. Rev. Met., (Sept. 1976).
98. N. Suutala and T. Moisio: Solidification Tech. in Foundry and Casthouse, Mets. Society 1980, p 49.
99. Jerkontoret: 'A guide to the solidification of steels' Stockholm, (1977).
100. J.E. Trueman: Int. Met. Rev., No. 6, (1981).
101. 'Corrosion resistance of the austenitic chromium-nickel stainless steels in marine environments', Int. Nickel Ltd.
102. L. Colombier and J. Hochmann: Aciers moxydables aciers refractories, Paris, (1965).
103. 'Corrosion resistance of the austenitic chromium-nickel stainless steels in clean environments', Int. Nickel Ltd.

104. E. Brauns et al: Stahl U. Eisen, 84, p.798, (1964).
105. L.L. Shreir: Corrosion metal/3nvironment.
106. M. Streicher: Corrosion, NACE, 30, 3, pp.77-91, (1974).
107. M. Smialowski et al: Corrosion Sci., 9, p.123, (1969).
108. G. Eklund: J. Electrochemical Soc., 121, p.467, (1974).
109. P.E. Mauning et al: Corrosion, 35, p.151, (1979).
110. P. Hronsky and D.J. Duquette, Corrosion, 38, p.63, (1982).
111. R.P. Gore: Johnson Matthey Research Group, (June, 1983).
112. R.P. Gore: Johnson Matthey Research Group, (Oct.-Dec., 1981).
113. N.D. Tomashov et al: Zh. Fiz. Khim., 23, 3, (1949).
114. N.D. Tomashov et al: Dokl. Akad. Nauk SSSR, 89, 1, p.121, (1953).
115. N.D. Tomashov et al: Dokl. Akad. Nauk SSSR, 88, 6, p.1023, (1953).
116. N.D. Tomashov et al: Trudy In-ta Fiz. Khim. Akad. Nauk SSSR, 4, p.159, (1955).
117. N.D. Tomashov et al: Akad. Nauk SSSR, 68, (1956).
118. N.D. Tomashov et al: Akad Nauk SSSR, 17 (1956).
119. N.D. Tomashov et al: Plenum Press NY, Chap. III, (1967).
120. N.D. Tomashov et al: Prot. Metals, 6, pp.380-90, (1970).
121. N.D. Tomashov et al: Tshchigrinskaya, German Werkstoffe Korrosion, 27, 9, p.636, (1976).
122. N.D. Tomashov et al: Zashchita Metallov., 16, 2, pp.105-112, (1980).
123. N.D. Tomashov et al: Zashchita Metallov, 13, 1, pp.10-16, (1977).
124. N.D. Tomashov et al: Prot. Met., 9, 3, pp.289-292, (1973).
125. N.D. Tomashov et al: Prot. Met., 9, 6, pp.616-618, (1973).
126. P. Monnartz: Metallurgia, 8, 7, p.161, (1911).
127. N.D. Tomashov et al: Zashchita Metallov., 9, 3, pp.314-318, (1973).
128. M. Streicher: Plat. Met. Rev., 21, pp.51-55, (1977).
129. G.J. Biefer: Canad. Metall. Quart., 9, 4, pp.537-550, (1970).
130. G.J. Biefer and V.S. Agarwala: Corrosion, 28, 2, pp.64-74, (1972).
131. Van Rooyen: 1st Int. Conf. on SCC, Butterworths, (1962).
132. Nato Conf. on the Theory of SCC in Alloys, (1971).
133. A.G. Knapton: Tech. mem. (met-grp.), No. 79, JM. Research Laboratories, Wembley, (1971).
134. T.P. Hoar: Plat. Met. Rev., 2, p.117, (1958).
135. G. Parkin: 'High-strength steels', The Iron and Steel Inst. p.87, (1962).
136. N.D. Tomashov et al: Zashchita Metallov, 6, 4, pp.425-27, (1970).
137. J. Hochmann et al: NACE, conf. proc. Unieux-Firminy, France, 5, p.956, (1973).

138. S. Shimodeira et al: ibid, p.1003.
139. R.W. Latanison and R.W. Staehle: NACE, conf. proc., p.215, Houston, (1959).
140. H.E. Hänninen: Int. Met. Rev., No. 3, (1979).
141. G. Chaudron: US/Euraton Programme, Project No. 293, Eurae reports 1749 and 1804.
142. M.A. Streicher: Corrosion, 30, 3, pp.77-91, (1974).
143. R.W. Staehle et al: Corrosion, 26, pp.451-486, (1970).
144. N.A. Neilsen: 'Hydrogen Induced Cracking of Low Strength Stainless Steels, (1972).
145. J. Montuelle and M. da Cutina Belo: NATO Conf. on Theory of SCC in Alloys, Enciera, Portugal, (1971).
146. G.C. Wood: Corrosion Sci., 2, p.173, (1961).
147. H.J. Yearian et al: Corrosion, 12, p.561t, (1956).
148. G.C. Wood and T. Halgkiess: J. Electrochem. Soc., 113, p.319, (1966).
149. G.C. Wood et al: J. Iron Steel Inst. (Lon.), 202, 685, (1964).
150. M.G. Hobby and G.C Wood: Oxidation of Metals, 1, 1, pp.23-54, (1969).
151. J.E. Croll and G.R. Wallwork: Oxidation of Metals, 1, 1, pp.55-71, (1969).
152. Saller et al: Batelle Mem. Inst., BMI, p.1017, (1955).
153. J.E. Truman and K.R. Pirt: BR. Corrosion J., 13, 3, pp.136-141, (1978).
154. A. Htun: Lon. Univ., Dept. of Metallurgy, (1982).
155. H.W.Hayden and S.FloreenTrans. ASM. 61, pp.489-499, (1968).
156. H.W. Hayden and S. Floreen: Trans. ASM, 61, pp.474-488, (1968).
157. K.J. Irvine et al: J. of Iron and Steel Inst., 207, p.1017, (1969).
158. R.C. Gibson and J.H. Brophy: 16th Sagamore Army Materials Research Conf. Ultra fine grain metals, edited by J.J. Burke and V. Weiss pp.377-394.
159. S. Floreen and H.W. Hayden: Trans. AIME, 239, pp.1405-1407, (1967).
160. J.A. Rinebolt and W.J. Harris: Trans. ASM, 43, pp.1175-1201, (1951).
161. E.A. Loria: Trans. ASM, 58, pp.221-23, (1965).
162. N.S. Stoloff: Fourth annual symp. on Fundamental Phen. in the Material Sciences, pp.197-245, Plenum Press, NY, (1967).
163. Metals Handbook: 85h edition, ASM, 1, p.424.
164, R.C. Gibson et al: ASM Trans., Q, 60, p.3, (1967).
165. H.F. Merrik: Tech. paper 691, The Int. Nickel Company, (1969).
166. B. Ahlbolom and R. Sandstrom: Int. Met. Rev., No. 1, pp.1-27, (1982).

167. A. Jarvinen: Jernkontorets forstning, report D47, (1972).
168. R.H. Kahn: 'The hot deformation of austenite', Am. Inst. MMPE, pp.457-498, (1977).
169. O. Karling: Licarbete Tekniska Hogskolan otnas, (1968).
170. K. Skuin et al: Nene Hutte, 18, pp.663-667, (1973).
171. L.G. Ljungstrom: Scand. J. Metall., 8, pp.95-96, (1979).
172. A. Gittins et al: Manuf. Eng. Trans., 2, pp.199-207, (1973).
173. H.W. Hayden et al: Trans. ASM, 60, pp.21-28, (1967).
174. W. Lumb and R.C. Gibson: Steel Int., pp.105-111, (1969).
175. W.A. Backofen et al: Trans. ASM, 57, pp.980-990, (1964).
176. D.H. Avery and W.A. Backofen: Trans. ASM, 58, pp.551-562, (1965).
177. R.C. Gibson et al: Trans. ASM, 61, pp.85-93, (1968).
178. H.W. Hayden and J.H. Brophy: Trans. ASM, 61, pp.542-549, (1968).
179. R. Gibson: 'Handbook of stainless steels' Chap. 8, McGraw-Hill, (1977).
180. R.D. Doherty: Met. Sci., 8, p.132, (1974).
181. M. Blicharski: Met. Sci., 18, pp.92-98, (1984).
182. J.F. Breedis et al: Met. Trans., 230, p.2, (1964).
183. I. Tamura et al: J. Jpn. Inst. Metals, 33, p.1376, (1969).
184. R.G. Davis and C.L. Magee: Met. Trans., 2, p. 1939, (1971).
185. R.G. Davis and C.L. Magee: Met. Trans., 1, p.2927, (1970).
186. H.M. Otte: Acta Met., 5, p.65, (1957).
187. B. Cina: Acta Met., 6, p.748, (1958).
188. M.W. Bowkett and D.R. Harries: Special Pub., AERE, Harwell, (1978).
189. F. Lecroisey and A. Pineau: Met. Trans., 3, (1972).
190. D.V. Laptev and D.R.F. West: Met. Tech., (1977).
191. K. Wasaka and T. Nakamura: J. Mat. Sci., 12, p.10, (1977).
192. K. Wasaka and T. Nakamura: J. Mat. Sci., 12, p.7, (1977).
193. P.C. Maxwell: Met. Trans., 5, p.1319, (1974).
194. H. Smith: Lond. Univ., Department of Metallurgy, (1968).
195. P. Weiss and R. Forrer: Ann. Phys., 10, 12, p.279, (1929).
196. K. Guy: Lond. Univ., Department of Metallurgy, (1981).
197. H. Thier: DVS-Berichte, Band 41, DVS GmbH, Dusseldorf, pp.100-106, (1976).
198. V. Kujanpaa et al: Met. con., 12, pp.282-285, (1980)
199. L-Å. Nordström and S. Malm: Scand. J. Met., 7, pp.31-33, (1978).
200. J. Stjerndahl and C-Å. Dacher: Scand. J. Met., 9, pp.217-224, (1980).
201. G.L. Leone and H. W. Kerr: Weld. J., 61, pp.13s-21s, (1982).

202. D.R.F. West: 'Ternary Equilibrium Diagram', pp.83-87, 2nd Edition (1982).
203. R.W. Cahn: 'Physical Metallurgy', pp.318-327, (1965).
204. H.D. Solomon: 'Embrittlement of Welds', 25, edited by C.L. Briant and S.K. Banerji, Academic Press.
205. J.C. Borland: Brit. Welding J., 8, pp.526-540, (1961).
206. H. Homma et al: Welding J., 58, pp.277s-282s, (1979).
207. E.J. Morgan-Waren and M.F. Jordan: Mets. Tech., 1, pp.271-278, (1974).
208. M. Simpson: Welding Res. Inst., 7, pp.177-193, (1977).
209. T. Ogawa and E. Tsunetoomi: Welding J., 61, pp.82s-93s, (1982).
210. L. Pryce and K.W. Andrews: JISI, 195, pp.415-417, (1960).
211. P.D. Southwick and R.W.K. Honeycombe : Met. Sci., pp.253-261, (1980).
212. H.D. Solomon: 'Duplex stainless steels', Conf. proc. ASM edited by R.A. Lula, pp.41-69, (1983).
213. T. Thorvaldeson et al: 'Stainless steels' 84', Met. Soc., Sweden, (1984).
214. Lu Shi Ying: 'Stainless steels' 84', Met. Soc., Sweden, (1984).
215. G.W. Lorimer et al: 'Stainless steels '84', Met. Soc., Sweden, (1984).
216. Y. Maehara et al: Trans. ISIJ, 23, pp.240-246, (1983).
217. Y. Maehara and Y. Ohmori: Trans. ISIJ, 24, pp.60-68, (1984).
218. J.W. Christian: 'The theory of transformations in Metals and Alloys' pp.471-95, (1965).
219. J.K.L. Lai Meshkat: Met. Soc., 12, p.415, (1978).
220. J. Shao and E.S. Machlin: Met. Trans., 10A, pp.585-590, (1979).
221. U.O. Osuoji: Lon. Univ., Department of Metallurgy, (1980).
222. L. Pryce et al: ibid., 184, 3, pp.289-301, (1956).
223. A.M. Talbot and D.E. Furman: ibid., 45, pp.429-442, (1953).
224. Y. Maehara: Met. Sci., 17, pp.541-547, (1983).
225. J. Barick: Met. Trans. A, 14A, pp.635-641, (1983).
226. F.S. Ham: J. Phys. Chem. Solids, 6, p.335, (1958).
227. F.S. Ham: Quart. J. Appl. Math, 17, p.137, (1959).
228. F.S. Ham: J. Appl. Phys. 30, 915, p. 1518, (1959).
229. M. Avrami: J. Chem. Phys. 7, p.1103, (1939).
230. M. Avrami: J. Chem. Phys., 9, p.177, (1941).
231. J. Chance et al: 'Duplex Stainless steels' Conf. Proc. ASM, edited by R.A. Lula, pp.371-398.
232. S. Harper: Phys. Rev., 83, p.709, (1951).
233. E.L. Brown: Met. Trans. A, 14A, pp.791-800, (1983).

234. C.T. Sims and W.C. Hagel (Eds.): 'The Superalloys', J. Wiley and Sons, NY, (1972).
235. M.S. Dean and W.J. Plumbridge: Nucl. Energy, 21, 2, pp.119-135, (1982).
236. W. Wallace: Met. Sci., 9, pp.547-549, (1975).
237. R. Roberti and W. Nicoderni: Avesta Stainless steel Bull., 2, pp. 14-17, (1982).
238. Y. Maehara et al: Trans. ISIJ, 23, pp.247-255, (1983).
239. K. Kumada: Bull. Japan Inst. Metals, 2, p.261, (1963).
240. A.J. Lena and W.E. Curry: Trans. ASM, 47, p.193, (1954).
241. T. Angel: ISIJ, pp.165-174, (May, 1954).
242. A.W. McReynolds: J. Appl. Phys., 20, pp.806-907, (1949).
243. W. Stevan and A.G. Haynes: J. Iron and Steel Inst., 183, p.341, (1956).
244. K.W. Andrew: J. Iron and Steel Inst., 203, p.721, (1965).
245. C.Y. Kung and J.J. Rayment: Met. Trans. A, 13A. pp. 328-331, (1982).
246. L.J. Swartzendruber and B. Sundaman: Bull. of Alloy Phase Diagrams, 4, 2, pp.155-160, (1983).
247. R.G. Davis and C.L. Magee: Met. Trans. 2, pp.1939-1947, (1971).
248. N.M. Matveeva et al: Proc. of th Int. Conf. on Martensitic Trans., pp.377-382, Leuven, Belgium, (1982).
249. M. Harmelin et al: Proc. of the Int. Conf. on Martensitic Trans., pp.467-472, (1982).
250. E. Scheil: Z. Anorg. Allgem. Chem, 207, p.21, (1932).
251. D.J. McAdam et al: Trans. ASM, 41. p.609, (1949).
252. R. Lagneborg: Acta Met., 11, p.547, (1963).
253. J.A. Venables: Phil. Mag., 7, p.35, (1964).
254. P.L. Manganon and G. Thomas: Mat. Trans., 1, p.1577 (1970).
255. P.L. Manganon and G. Thomas: Met. Trans., 6A, pp.791-795, (1975).
256. G.B. Olson and M. Cohn: J. Less common Mets., 28, p.107, (1972).
257. K.J. Irvine et al: JISI, 195, p.385, (1960).
258. J.C. Scully: 'The fundamentals of Corrosion', p.123, pub. by Pergamon Press, (1975).
259. N.D. Greene et al: J. Electrochemical Soc., 108, p.836, (1961).
260. K.J. Irvine et al: ibid., 199, p.153, (1961).
261. K.J. Irvine and F.B. Pickering: 'High-alloy steels', 34, London, The ISIJ, (1964).
262. G. Dieter: 'Mechanical metallurgy', McGraw-Hill, (1976).
263. H.D. Solomon and T.M. Devine: Micon '78, ASTM STP 672, pp.430-461, (1979).

264. D.C. Ludwigson and J.A. Berger: JISI, (Jan. 1969).
265. Y. Maehara et al: Mets. Tech., 10, pp.296-303, (Aug. 1983).
266. N. Birks and G.H. Meier: 'Introduction to high temperature oxidation of metals' Pub. by E. Arnold Ltd., (1983).
267. J.C. Chaston: Plat. Met. Rev., 19, 4, pp.135-140, (1975).
268. R. Holm et al: Scanning electron microscope, 4, pp.1465-1473, (1982).

ACKNOWLEDGEMENTS

I should like to express my sincere thanks for the guidance shown by Dr. H.M. Flower and Dr. D.R.F. West, under whose supervision this work was conducted.

I am grateful for the friendship shown by all my colleagues in the Electron Microscopy Group of the Metallurgy Department, and the technical expertise of Mr. G. Briers has been gratefully appreciated.

Thanks are also extended to Mrs. G. Flower for the excellent typing of this thesis, and to Mr. J. Rossdale for the reproduction of the photographic pages.

The financial support of the Science and Engineering Research Council and Johnson Matthey Co. Ltd. is gratefully acknowledged, and I wish to thank Professor D.W. Pashley for the provision of research facilities.

Finally, I would like to express my gratitude to my wife, Gillian, for her patience and understanding.

APPENDIX

ESTIMATION OF MARTENSITE CONTENT USING A MAGNETIC RING BALANCE

INTRODUCTION

Among the methods which have been used for measuring the martensite content of steels are quantitative metallography, X-ray diffraction, electrical resistivity and various magnetic techniques.

Quantitative metallography is inherently slow and tedious, and requires great care in the choice of the areas of the specimen to be examined if they are to be representative of the complete sample. Difficulty may be experienced in distinguishing between the martensite and other phases present, and a false value of the percentage martensite present may result from over-etching; espeically at high levels of martensite content when small areas of retained austenite are easily obscured.

A second absolute method for martensite determination is by the measurement of the integrated intensities of X-ray reflections. The accuracy is known to fall off seriously when the specimen contains less than about 70% martensite.

Electrical resistivity and most 'low-field' magnetic properties are influenced by grain-size, internal stresses, cracks and the size and distribution of particles comprising the aggregate. However, the specific saturation magnetic intensity, σ , is insensitive to such factors and is a direct function of the proportional amounts of each phase present in the alloy and their respective σ values. The contribution of austenite can usually be neglected as it is paramagnetic, and so the saturation intensity of the aggregate gives a direct measure of the ferromagnetic, α' , martensite content. The measurement of σ is useful for tempering studies as well as for martensite content determinations. It is a rapid technique capable of a high degree of accuracy and requires only moderate care in specimen preparation.

THEORY

The magnetic balance measures the force on a ferro-magnetic specimen placed in a non-uniform magnetic field with constant field gradient produced by an electromagnet.

The specimen is placed in a position of constant field gradient where it experiences a force equal to $M \cdot dH/dX$ in the direction of the field gradient (i.e. vertically downwards). The operating conditions are such that the downward movement is sufficiently small to ensure that the

specimen remains in the region of constant dH/dx, M, the saturation magnetic moment of the specimen, equals J_S V = σ m where V is the volume, m the mass of the specimen and J_S the saturation magnetization, σ is thus defined as the saturation magnetic moment per unit mass but usually called the specific magnetic intensity.

The force of the specimen is then given by: $F = \sigma m \, dH/dx$.

If σ is in c.g.s. units, m in grams, H in oersteds and x in centimetres, then F is given in dynes. Thus a specimen of pure iron of mass 0.1 gm in a typical field gradient of 900 oersted/cm will experience a force of approximately 20 grams.

The force F, exerted on the specimen produces a downward displacement, D, which is balanced by the elastic distortion of the ring from which it is suspended. The following relationship is obtained:

$D \propto F \propto m \, \sigma \, dH/dx$; therefore $D = Km\sigma$

where K is a constant for the apparatus used under standard conditions. Hence, although an absolute value of σ is not obtained, an accurate comparison can be made between the σ values of two specimens. The apparatus is therefore calibrated by measuring the deflection due to a specimen of known mass prepared from material of known σ. Pure iron is the obvious choice as its σ value is both accurately known and is comparable with that of substantially martensitic steels. Hence

$$\frac{D_s}{D_{Fe}} = \frac{K, m_s, \sigma_s}{K, m_{Fe}, \sigma_{Fe}} = \frac{m_s, \sigma_s}{m_{Fe}, \sigma_{Fe}}$$

If the specimen, s, contains only one ferromagnetic phase, then its magnetic response can be attributed entirely to this phase with little error. The saturation intensity of the specimen as a whole, σ_s, is related to that of the ferromagnetic phase, σ_M, by the relationship:

$$\sigma_s = \sigma_M \frac{\%M}{100}$$

Substitution in the previous equation gives:

$$\frac{D_s}{D_{Fe}} = \frac{m_s \, \sigma_M \, \%M}{m_{Fe} \, \sigma_{Fe} \, 100}$$

hence

$$\%M = \frac{D_s \, m_{Fe} \, \sigma_{Fe} \, 100}{D_{Fe} m_s \, \sigma_M} = \frac{D_s}{m_s \, D_{Fe}} \times C \quad \text{(where C = constant)}$$

The displacement of a standard iron specimen, D_{Fe}, is measured each time to check the calibration. Thus when C has been evaluated for a particular composition, the martensite content of a specimen is found merely by measuring its mass and its displacement under the standard conditions.

CALCULATION OF σ_M

An evaluation of σ_M for a particular composition can be made by taking into account the effects of the various alloying additions on the value of σ_{Fe}. Chromium and nickel atoms substituted in the iron lattice contribute to the ferromagnetism.

1 mole Ni weights A_{Ni} gms and contains No molecules (atoms.

W_{Ni} gm of Ni contain $\frac{W_{Ni}}{A_{Ni}}$. No atoms

Thus, in 100 gm alloy, nickel contributes $\frac{W_{Ni}}{A_{Ni}}$. No atoms.

Similarly for Fe and Cr . . in gm of alloy the number of atoms of these three elements is:

$$\text{No} \quad \frac{W_{Cr}}{A_{Cr}} + \frac{W_{NI}}{A_{Ni}} + \frac{W_{Fe}}{A_{Fe}}$$

Each Cr atom contributes 0.22 Bohr magnetons.
Each Ni atom contributes 0.6 Bohr magnetons.
Each Fe atom contributes 2.2 Bohr magnetons.

Number of Bohr magnetons in 100 gm alloys is

$$\text{No} \quad 0.22\frac{W_{Cr}}{A_{Cr}} + 0.66\frac{W_{Ni}}{A_{Ni}} + 2.2\frac{W_{Fe}}{A_{Fe}}$$

Neglecting interactions between Ni, Cr and Fe and assuming other elements have merely a dilution effect, we can continue as follows, taking Alloy B as an example:

Number of Bohr magnetons in 100 gm of alloy is:

$$6.023 \times 10^{23} \quad \frac{0.22 \times 14.9}{52.0} + \frac{0.6 \times 8.7}{58.71} + \frac{2.2 \times 74.14}{55.85}$$

$$= 6.023 \times 10^{23} \times 3.072$$

The Bohr magneton, $\mu_B = \frac{eh}{4\pi m}$

where $e/m = 1.759 \times 10^7$ e.m.u.

and $h = 6.62 \times 10^{-27}$ erg. sec.

$$\mu_B = \frac{6.62 \times 10^{-27} \times 1.759 \times 10^7}{4}$$

$$= 9.266 \times 10^{-21} \text{ c.g.s. units}$$

Hence, saturation magnetization due to 100 gm of alloy

$= 6.023 \times 10^{23} \times 3.072 \times 9.266 \times 10^{-21}$

saturation magnetization due to 1 gm alloy, σ_M

$= 6.023 \times 10^{23} \times 3.072 \times 9.266 \times 10^{-21} \times 10^{-2}$

$\underline{\sigma_{M(B)}} = \underline{171.0 \text{ c.g.s. units}}$

Similarly for Alloy A, $\underline{\sigma_{M(A)}} = \underline{168.8 \text{ c.g.s. units}}$